The Characterisation of Magnetic Couplings and the Development of a Thruster Module for an ROV

M.Sc.(Eng.) Dissertation by Timothy P. Hope

Supervisor: Prof Gerald Nurick
Co-Supervisor: Tracy Booysen

University of Cape Town
Department of Mechanical Engineering

Robotics and Agents Research Laboratory

September 2015

Abstract

This dissertation focuses on the development of thruster modules and the characterisation of magnetic couplings for a **R**emotely **O**perated Underwater **V**ehicle (**ROV**). The dissertation begins with an introduction to the Seahog ROV developed at the University of Cape Town's **R**obotics and **A**gents **R**esearch **L**aboratory (**RARL**). The history, relevance and features of commercial ROVs are discussed in chapter two to introduce the reader to this form of underwater robotics. After this the dissertation is divided into two separate sections.

The first section, chapters three to eight, detail the mechanical and electrical modifications made to an existing, magnetically coupled, thruster module design. The objective of this section was to improve the thruster module in order to achieve performances that are similar to commercially available thrusters. The modifications included changes to the drivetrain, the design of new electronics and motor drivers and a reduction in weight of the module's housing. A fundamental analysis of the thruster module is presented, no **C**omputational **F**luid **D**ynamics (**CFD**) is provided as the propeller and kort-nozzle designs remained unchanged. Even though the improvements produced a reliable and efficient thruster module a greater understanding of magnetic couplings was required to produce a design that was as lightweight as commercial modules. Therefore the second section of this dissertation, chapters nine to twelve, implement and validate an analytical model to calculate the torque and slip characteristics of magnetic couplings.

The dissertation is concluded in chapter thirteen with recommendations that incorporate the knowledge gained in magnetic coupling design with the modifications made to the thruster module to produce a thruster design that is both efficient and light.

Dissertation Overview

An Introduction to the Seahog ROV

In 2009 the Department of Biological Sciences at the **U**niversity of **C**ape **T**own (**UCT**) approached the **R**obotics and **A**gents **R**esearch **L**aboratory (**RARL**) with a proposal to build them a **R**emotely **O**perated underwater **V**ehicle (**ROV**) to aid them with marine research. The Zoology Department currently uses divers to collect samples, take videos and locate and retrieve equipment. Compressed air scuba diving is limited to a depth of 40 m and the deeper the dive the less time the diver can remain at depth [1]. ROVs. are tethered underwater robots capable of transmitting live video to the operator, illuminating their environment and can dive deeper than divers. ROVs. are piloted by an operator at the surface and are manoeuvred by controlling thruster modules on the ROV. They are powered from the surface vessel via a tether and can therefore remain at depth for extensive periods of time. There are commercial ROVs. that suit the Department of Biological Sciences' needs however they are prohibitively expensive machines.

The RARL is currently developing its third generation ROV named the Seahog. The Seahog utilises a modular design therefore making it easy to upgrade and modify the robot's subsystems. The robot is controlled using five vectored thruster modules. A camera and light unit is mounted to a tilt tray allowing the operator to view above, below and in front of the ROV. The Seahog is powered from a **P**ower **S**upply **U**nit (**PSU**) with 400 VDC along the tether. The power pod converts this to a range of lower voltages that are used by the various subsystems. Fibre optics in the tether allows the operator to view live video and sonar feeds and enable the fast communication of commands and auxiliary data between the operator and the ROV.

In Figure A the cover and the buoyancy system have been removed from the Seahog ROV to show the robot's modules and subsystems.

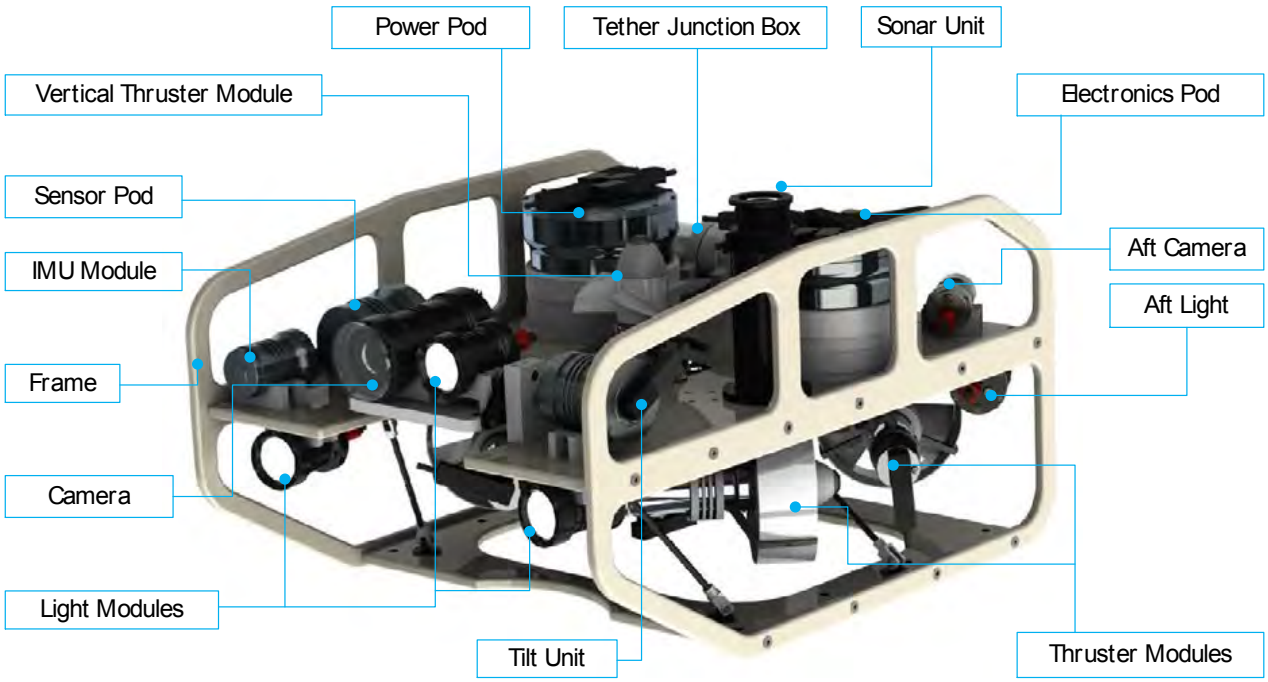

Figure A – The Seahog ROV

The Development of the Thruster Modules

The thruster modules were originally developed and tested in 2012 as part of a previous dissertation. When compared to commercial thruster modules they were found to be very inefficient and heavy. There were several reliability issues such as the overheating of the electronics and the regular loss of communication during operation. Four main areas of development for the thruster modules were identified as:

- increasing the efficiency of the drivetrain
- reducing the module's weight
- increasing the efficiency of the electronics
- and increasing the reliability of the communications

To improve the efficiency of the thruster, the drivetrain had to be better matched to the load. The load was defined as the magnetic coupling and the propeller. Test results from 2012 were used to characterise the load and select an appropriate gearbox reduction ratio. The single stage 3.5:1 gearbox was replaced with a two stage 12:1 gearbox.

The housing of the thruster module was overdesigned and constituted 41% of the module's weight. A more appropriate method for designing cylindrical pressure vessels subjected to external pressure was used. The design used to connect the electronics and motor housing was simplified and reduced in size. These two changes resulted in a 33% mass reduction in the thruster housing.

The electronics were completely replaced. A **b**rush**l**ess **DC** (**BLDC**) motor driver board was sourced from the motor manufacturer and a communications and control board was developed to interface the thruster module with the ROV. The communications and control board featured two embedded microcontrollers (one for communications and the other for motor control), protection circuitry, temperature sensors and motor driver power supply conditioning circuitry. Both boards fitted into the thruster housing. Interrupt based communications were implemented on the embedded processors and maintained communication throughout a 24 hour communications test.

With the change in gearbox and the improvement of the electronics the new thruster module produced nearly double the thrust it did previously and can be operated at full power without overheating. Table A shows the performance improvements for the thruster module and Figure B shows the modified thruster.

Table A – Performance Improvements of the ROV's Thruster Module

Specification	Previous	Modified	Units	% Change
Thrust at Maximum Power	32	63	N	+97%
Total Mass	4.8	4.2	kg	-12.5%
Thrust-to-Power Ratio	0.17	0.33		+97%
Thrust-to-Weight Ratio	0.68	1.51		+122%
Drivetrain Efficiency	0.17	0.66		+388%
Communication Speed	9600	115200	bps	+1100%

Figure B – Modified Thruster Module

Magnetic Couplings

The ROV must be able to operate in the high pressure environment that is found at 300 m below sea level. This pressure presents a dynamic sealing challenge regarding the sealing of rotating shafts. To overcome this issue the ROV uses magnetic couplings. Magnetic couplings transmit torque using magnetic forces and therefore no mechanical connection is required. This allows space for a separation membrane that is placed between the motor side of the coupling and the external environment. This membrane remains stationary relative to the coupling and therefore only static sealing is required.

The thruster modules utilise magnetic couplings and a camera tilt module, a manipulator module and potential sampling modules will use magnetic couplings to facilitate their actuation without the need for dynamic sealing.

The RARL built and tested two coaxial synchronous magnetic couplings, one that is currently used in the thruster module and one that was built for a development manipulator for the Seahog. These couplings proved to be over designed with the manipulator coupling producing over twice the pull-out torque that was expected. As a result of this excessive design, the couplings were larger and heavier than necessary. It was identified that a design tool was required to predict a magnetic coupling's pull-out torque in order to design efficient and lean magnetic couplings for the ROV.

Methods of modelling magnetic couplings were researched and an analytical model was implemented that suited the specific design limitations of the magnetic couplings that will be built for the ROV. The model's results correlated with the test results from the previous couplings built at RARL. To further validate the analytical model, several test couplings were built that had pull-out torques within the range of the current and future magnetic couplings that have and will be used for the ROV.

A test rig was manufactured that measured the angle of slip between the two couplings and the torque applied to the inner rotor of the coupling simultaneously. This allowed the entire torque vs. slip period of the couplings to be logged. Figure C shows the analytical model output range (the magnet strength is given as a range by the manufacturer) compared to the test results for three magnetic couplings utilising N48 magnets. The effects of varying the air gap and the effects of a stainless steel membrane were tested.

For couplings that had three to four pole pairs the analytical model's accuracy was within 10% of the test results and for two pole pair couplings the model's accuracy ranged from -5.88% to +23.21%. This accuracy was in the region of previously validated analytical models and, although not ideal, was an improvement from the previous design methods. The analytical model can be used to design magnetic couplings, especially couplings with three or more pole pairs.

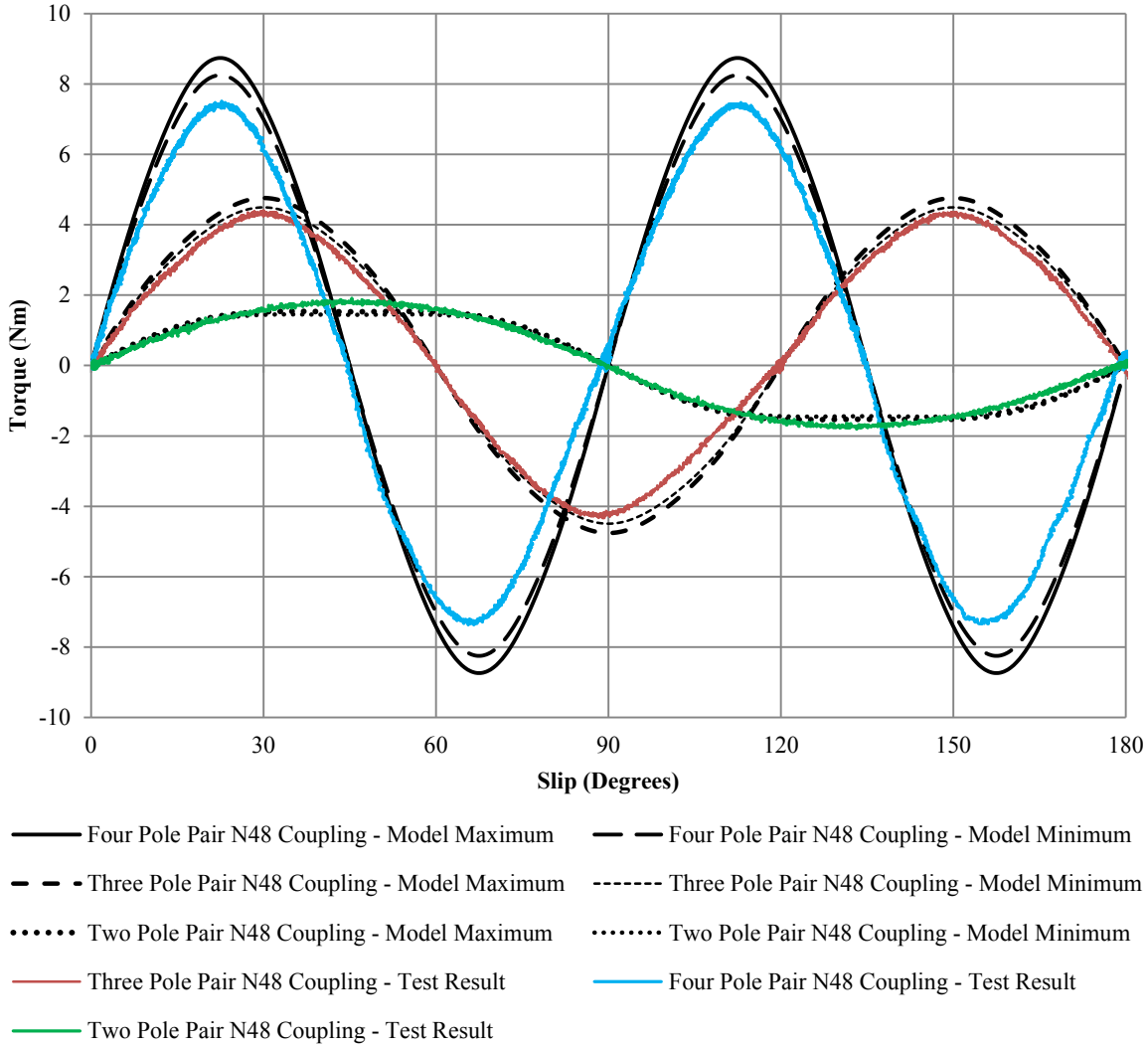

Figure C – N48 Magnetic Coupling Test Results vs. Analytical Model

Concluding Remarks

The thruster modules' drivetrain efficiency was nearly quadrupled and the thrust produced by the thruster module was nearly doubled. The overheating of the electronics and the loss of communications were both resolved and the weight of the module was decreased by 600 g therefore reducing the entire ROV's weight by 3 kg.

The magnetic coupling analytical model correlated with test results and therefore proved that it can be used as a design tool when designing magnetic couplings for the ROV. It was shown that the model had an error below 25% which is a significant improvement from the 225% previously achieved without the model.

By combining the knowledge gained from the modelling and testing of magnetic couplings the thruster module can be redesigned to incorporate a smaller coupling. This modification combined with a smaller housing design can reduce the module's weight to 2.7 kg. This weight reduction would make the thruster module competitive with commercial thrusters.

Plagiarism Declaration

This dissertation is submitted in complete fulfilment of a M.Sc.(Eng.) (Mechanical Engineering) at the University of Cape Town.

I know the meaning of plagiarism and declare that all of the work in the thesis, save for that which is properly acknowledged, is my own. Each contribution to, and quotation in, this dissertation from the work(s) of other people has been attributed, and has been cited and referenced according to the IEEE standard.

I have not allowed, and will not allow anyone to copy my work with the intention of passing it off as their own.

Signed by candidate

Timothy Patrick Hope

30-11-2015

Date

Acknowledgments

Firstly I would like thank the **C**ouncil for **S**cientific and **I**ndustrial **R**esearch (**CSIR**) for providing the funding for the project.

I owe great thanks to Tracy Booysen who offered to co-supervise this dissertation. Thank you for always being there, for your guidance and support.

I express my thanks to the following people who all played a part in helping me complete this project.

To Prof Gerald Nurick for offering to supervise the project.
To Trevor Cloete for voluntarily taking an interest in this dissertation and especially for his help in the later stages.
To Sam Ginsberg for his guidance and for probably the most crucial piece of advice I needed.
To Pierre Smith, the head of the workshop, for his patience, attention to detail, hard work and uplifting spirit.
To my colleagues, Roger and Max, I could not have asked for better engineers to work with on the "ol' Seahog". Thanks for the laughs and the help over the years.
To the RARL guys, for the good times, the coffee and the often random but nonetheless important advice.
And finally I owe my thanks to my family who have always given me their unwavering support.

Contents

List of Figures

List of Tables

List of Acronyms

ADC	-	**A**nalogue to **D**igital **C**onverter
AUV	-	**A**utonomous **U**nderwater **V**ehicle
BLDC	-	**B**rush**l**ess **D**irect **C**urrent
CAD	-	**C**omputer-**A**ided **D**esign
CFD	-	**C**omputational **F**luid **D**ynamics
CNC	-	**C**omputer **N**umerical **C**ontrol
CRC	-	**C**yclic **R**edundancy **C**heck
CSSF	-	**C**anadian **S**cientific **S**ubmersible **F**acility
CURV	-	**C**able-Controlled **U**nderwater **R**ecovery **V**ehicle
DAC	-	**D**igital to **A**nalogue **C**onverter
EMI	-	**E**lectro**m**agnetic **I**nterference
FEA	-	**F**inite **E**lement **A**nalysis
FEM	-	**F**inite **E**lement **M**ethod
GPIO	-	**G**eneral **P**urpose **I**nput / **O**utput
HDPE	-	**H**igh-**d**ensity **P**oly**e**thylene
IACS	-	**I**nternational **A**nnealed **C**opper **S**tandard
IC	-	**I**ntegrated **C**ircuit
JAMSTEC	-	**J**apan **A**gency for **M**arine-**E**arth **S**cience and **Tec**hnology
LARS	-	**L**aunch **a**nd **R**ecovery **S**ystem
Ma-Re	-	**Ma**rine **Re**search Institute
MBARI	-	**M**onterey **B**ay **A**quarium **R**esearch **I**nstitute
MISO	-	**M**aster **i**n **S**lave **o**ut
MOSFET	-	**M**etal-**O**xide **S**emiconductor **F**ield **E**ffect **T**ransistor
MOSI	-	**M**aster **o**ut **S**lave **i**n
PCB	-	**P**rinted **C**ircuit **B**oard
PI	-	**P**roportional **I**ntegral
PSU	-	**P**ower **S**upply **U**nit
RARL	-	**R**obotics and **A**gents **R**esearch **L**aboratory
ROV	-	**R**emotely **O**perated Underwater **V**ehicle
SPI	-	**S**erial **P**eripheral **I**nterface
TMS	-	**T**ether **M**anagement **S**ystem
UART	-	**U**niversal **A**synchronous **R**eceiver/**T**ransmitter
UCT	-	**U**niversity of **C**ape **T**own
USB	-	**U**niversal **S**erial **B**us
UUV	-	**U**nmanned **U**nderwater **V**ehicle

1 Introduction

Within the Department of Biological Sciences at the **U**niversity of **C**ape **T**own (**UCT**) the **Ma**rine **Re**search Institute (**Ma-Re**) conduct extensive research of marine organisms and the ocean's ecosystems. To collect samples, document marine life and retrieve and locate equipment Ma-Re primarily use divers. Diving is a hazardous task and divers can only remain at specific depths for limited periods of time to prevent nitrogen narcosis. The maximum depth a diver can reach using conventional compressed air scuba equipment is 40 m [1]. These limitations hinder Ma-Re in conducting research and put the lives of the divers at risk if deep and challenging dives are required to collect samples or retrieve equipment. Due to these limitations Ma-Re approached the **R**obotics and **A**gents **R**esearch **L**aboratory (**RARL**) in 2009 to build them a **R**emotely **O**perated underwater **V**ehicle (**ROV**) that can be used to aid their marine research.

ROVs. are tethered underwater robots that are controlled by an operator at the surface. An ROV's primary function is to send a live video feed to the operator and is manoeuvred by controlling thruster modules built into the ROV's frame. ROVs. can go deeper than divers and are powered from their respective surface vessel via a tether therefore being able to remain at depth for extensive periods of time. There are commercially available ROVs. that suit the Zoology department's requirements however these machines are prohibitively expensive therefore an economic solution was required.

Since 2009 the RARL has developed three generations of ROVs.. The first generation, the Challenger 1 (shown in Figure 1), featured a dynamic buoyancy module, five thruster modules and a dry electronics and camera hull. A manipulator arm was incorporated to retrieve solid samples and magnetically coupled syringes were designed to take water samples. This project was ambitious and for technical reasons was never operated underwater.

The second generation ROV, the Robin, was simplified and featured a dry camera and electronics hull like the Challenger 1 however it had three thruster modules, no manipulator or samplers and used a float block as opposed to a dynamic buoyancy system. This ROV was tested underwater. The dry hull design proved to be restrictive in improving the Robin ROV. For this reason and due to its small size continued development of the Robin was ceased.

The Challenger 1

The Robin

Figure 1 - First and Second Generation ROVs. Developed at RARL [2]

The third generation ROV currently being developed at the RARL is the Seahog. The design of this ROV is entirely modular and mimics designs commonly used by commercial ROV manufacturers. The modular design allows the robot to be progressively upgradable and modified for specific functions. The Seahog ROV is shown in Figure 2 with its key subsystems labelled in Figure 3. It is designed to operate to 300 m below sea level, record video, utilise sonar, take pressure, temperature and salinity measurements, and be capable of supporting a manipulator or sampling module.

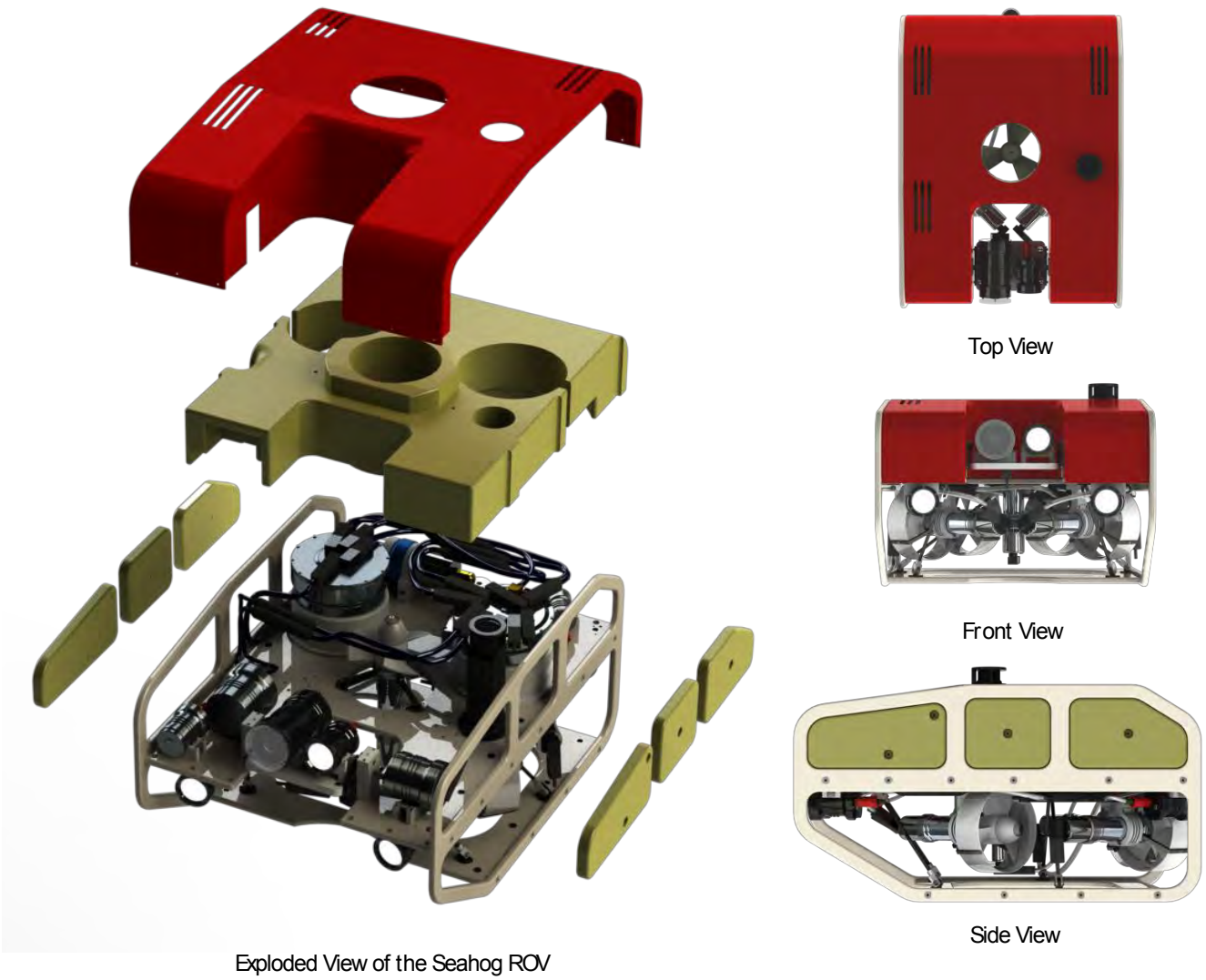

Figure 2 - The Seahog ROV

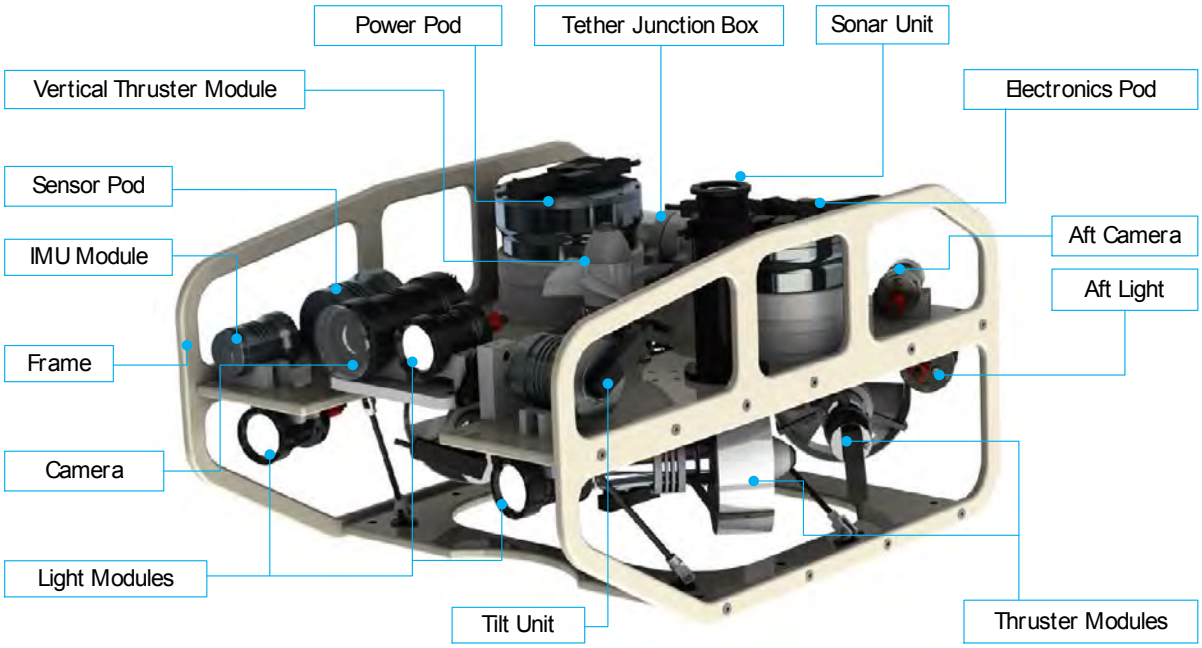

Figure 3 - The Seahog ROV with the Cover and Float Blocks Removed

The Seahog is powered by a **p**ower **s**upply **u**nit (**PSU**) that sends 400 VDC along the tether to the ROV's power pod. This power pod converts the 400 VDC to a range of lower voltages that are used by the ROV's subsystems. Data communication between the operator console and the ROV is done using fibre optics. This allows for live video and sonar streaming as well as all commands and auxiliary data communication.

The ROV is manoeuvred by five vectored thruster modules that control its movement in four degrees of freedom (surge, heave, sway and yaw). The thruster modules were originally designed in 2012 however they had several shortcomings. When analysed the main issues identified were:

- the inefficient production of thrust
- the excessive design of the housing which added weight
- the overheating of the electronics during operation
- and the regular loss of communications

Thruster reliability and efficiency is critical to the Seahog's effectiveness as they control the movement and position of the ROV. Because of the issues mentioned the thrusters were not usable and each shortcoming required an effective and economical solution.

Initially several commercial thruster modules were studied to better understand their features and performance capabilities. The Seahog's thrusters were then analysed and several modifications were made. The electronics were redesigned and the housings and drivetrains were modified. Due to significant initial investment in the thruster modules these modifications were considerate of costs and machining time. The modified thruster module was then put through a series of tests to evaluate its efficiency, performance and reliability.

A mechanical engineering challenge specific to ROVs. is reliable and efficient dynamic sealing of rotating shafts. To overcome this the Seahog utilises magnetic couplings. Magnetic couplings enable the transmission of torque without physical contact and therefore a membrane can be placed between

the motor side and load side of the coupling. This membrane separates the water from the inside of the module using a static seal therefore negating the need for high pressure dynamic shaft seals.

The thruster modules use magnetic couplings and the future camera tilt module, manipulator modules or sampling modules will use magnetic couplings. Previous magnetic couplings designed at the RARL were done according to weight and space constraints and no estimations of the couplings' maximum transmissible torque were done. This resulted in heavy and over designed couplings for their tasks.

This dissertation investigates methods used to model magnetic coupling torque vs. slip curves with the aim of developing a design tool to be used to design future couplings that are efficient and produce the intended torque for the application. An analytical model was implemented that suits the specific design characteristics of the couplings that will be built for the ROV. This model was validated for the torque ranges expected for future coupling designs and used magnets that were locally available.

2 Background Research

This chapter introduces ROVs by defining underwater vehicle classification in order to determine the functions and characteristics of ROVs and ROV systems. The history of ROVs is discussed in brief with several major historic challenges discussed. Finally the chapter takes a closer look at the various sub-systems found on ROVs that are of a similar size and functionality as the Seahog ROV.

2.1 An Overview of ROVs. and ROV Systems

2.1.1 Underwater Vehicle Categorisation

Underwater vehicles fall into two major categories; manned and unmanned vehicles. Within the unmanned underwater vehicle category there are two further sub categories; **A**utonomous **U**nderwater **V**ehicles (**AUVs.**) and **R**emotely **O**perated **U**nderwater **V**ehicles (**ROUVs.**, or, as known in industry, ROVs.) [3].

Figure 4 shows the various categories for underwater vehicles and touches on the various sub-categories of ROVs..

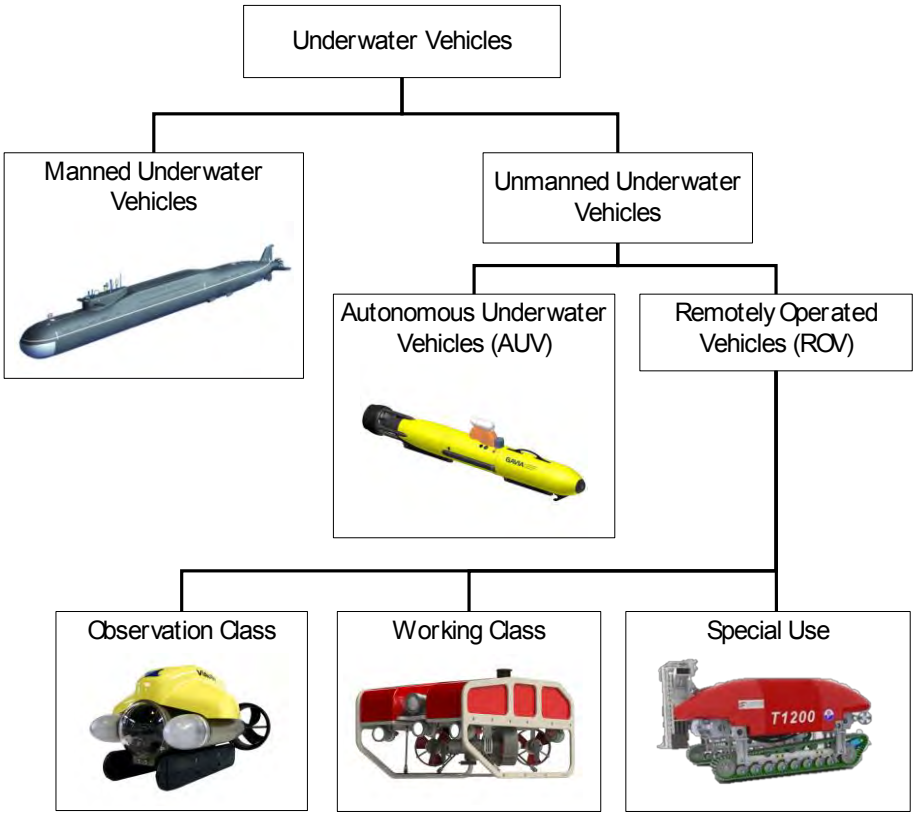

Figure 4 - Underwater Vehicle Categories [3]

There are several differences between AUVs. and ROVs.. An ROV is a submersible robot that is operated from the surface and sends real-time feedback to the operator via a tether. An AUV is an autonomous submersible robot that conducts a mission and provides the information to the operator once the mission is complete [4].

The US Navy refers to AUVs. as UUVs. (Unmanned Undersea Vehicles) and has the following definition of UUVs.:

Self-Propelled submersible whose operation is either fully autonomous (pre-programmed or real-time adaptive mission control) or minimal supervisory control and is untethered except, possibly, for data links such as fibre optic cable [5].

An ROV system can be described as a manoeuvrable underwater vehicle that sends a video feedback to the surface via a cable [3].

2.1.2 ROV System Components

A basic ROV system comprises of the ROV, tether, control station and controller. The ROV must be capable of manoeuvring underwater and be able to send a video feed to the surface for real-time feedback [3]. A basic observation class ROV system developed by *Video Ray LLC* can be seen in Figure 5.

Figure 5 - Basic ROV Components [6]

Larger ROV systems have dedicated surface PSU, **L**aunch **a**nd **R**ecovery **S**ystems (**LARS**) and **T**ether **M**anagement **S**ystems (**TMS**). TMS units can also incorporate a cage in which the ROV is lowered to the operating depth and the tether is then managed from the cage, this reduces the drag on the tether therefore allowing the ROV to manoeuvre more easily [3]. A large commercial ROV system can be seen in Figure 6.

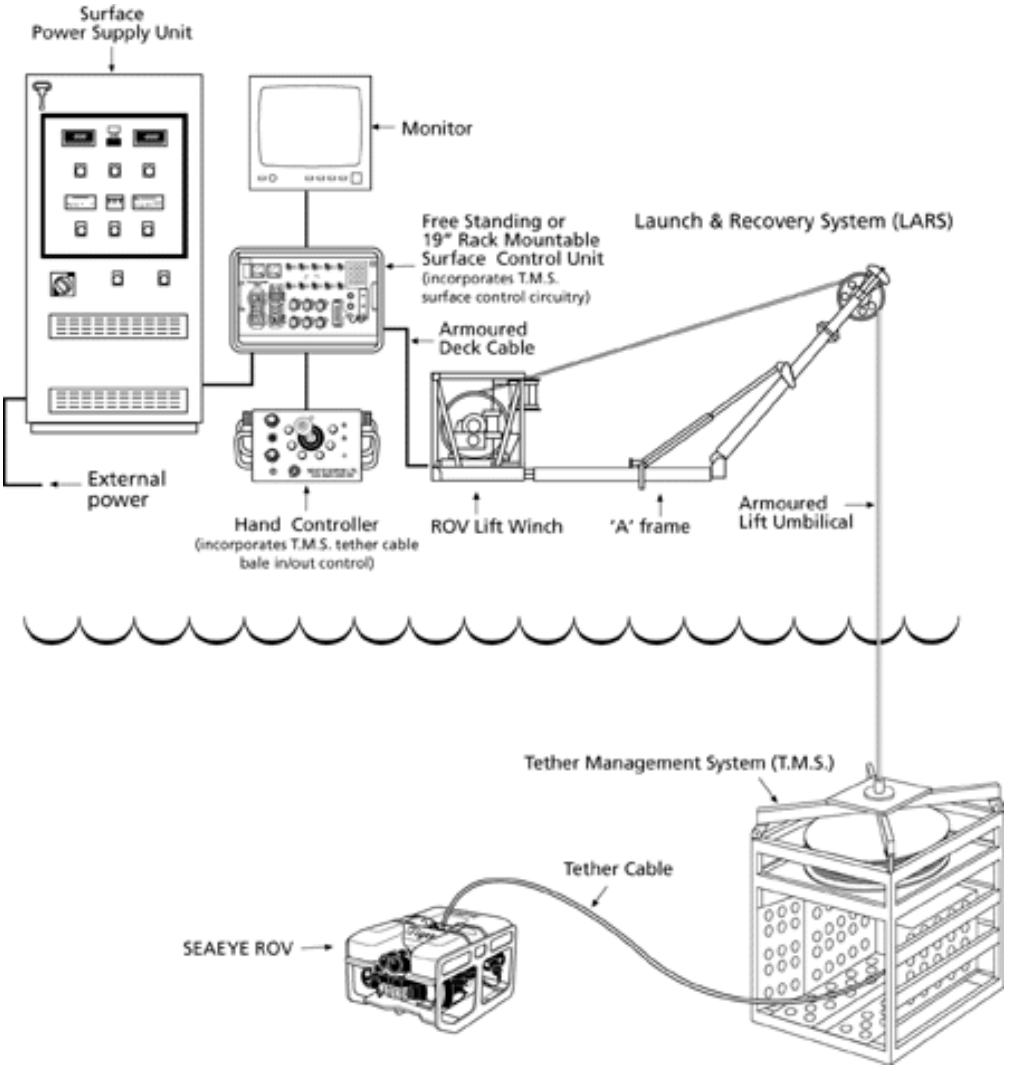

Figure 6 - Saab Seaeye ROV System Diagram [7]

2.2 A Brief History of ROVs.

The US Navy pioneered ROV development in the 1960s with their main concern being the retrieval of torpedoes lost on the seafloor. The US Navy achieved several milestones in ROV usage and effectiveness, two of those being:

- in 1966 the US Navy's Cable-**C**ontrolled **U**nderwater **R**esearch **V**ehicle (***CURV***) retrieved an atomic bomb off the coast of Spain at a depth of 869 m [8].

Figure 7 - US Navy's CURV ROV [8]

- in 1973 the *CURV III*, which had become a transportable and rapidly deployable system, was mobilised from San Diego to an offshore location near Cork, Ireland in order to assist with a submarine rescue mission. The CURV III attached a line to the *PICSES III* (a manned submersible with a crew of two) at a depth of 430 m. The submarine was pulled to the surface and the crew was saved [8].

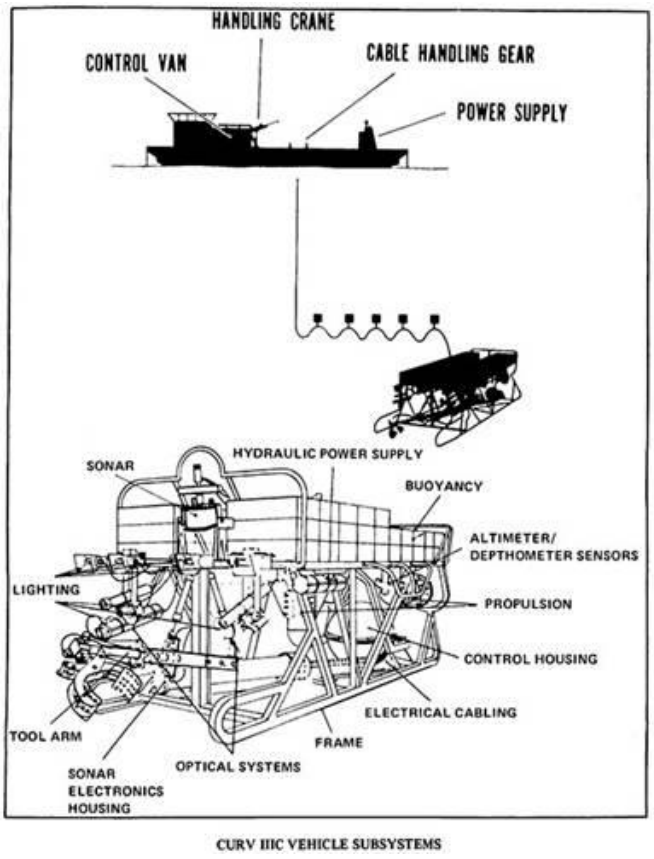

Figure 8 - US Navy's CURV III ROV System [8]

With these high-profile successes and the evident need for complex ROV systems the US Navy expanded its research to range from large ROVs. designed to attach pontoons to stricken submarines through to small hydraulically controlled observation class ROVs. [3].

Even with these developments and newly found capabilities ROVs. could not compete with manned submersibles and saturation divers in industry. Only with the advancements in electronics in the late 1970s, which provided the miniaturisation of components and increased reliability, did the privately funded ROV industry begin to emerge. From 1953 to 1974 85% of ROVs. were government funded, from 1974 to 1982, 96% of ROVs. were privately funded [3].

During the 1980s and 1990s the ROV industry began to expand rapidly due to the upturn in the offshore oil and gas industry. With oilfields being found in waters deeper than the capabilities of saturation divers the tasks fell to ROVs. for subsea installations and maintenance [3].

Figure 9 - JAMSTEC's Kaiko ROV [9]

The final and ultimate depth record was achieved by the **J**apan **A**gency for **M**arine-**E**arth and **Tec**hnology (**JAMSTEC**) with their ROV, Kaiko (Figure 9). On the 24th of March 1995 Kaiko reached the bottom of the Challenger Deep. The Challenger Deep is deepest known point in the Earth's oceans and Kaiko reached a recorded depth of 10911.4 m. Kaiko did not only break and effectively obliterate the deepest ROV dive record but during its 8 years of operation it made 250 dives, collecting 350 biological species. Of these species 180 were bacteria, some of which proved useful in cosmetics, semiconductor and omeg-3 fatty acid manufacturing [9].

2.3 Modern Applications and Relevance

As can be seen from the history of ROV development ROVs. are extensively used by militaries, for marine research and for commercial applications.

With increasing depth and pressure, conducting surveys and performing tasks below the ocean's surface becomes increasingly complex and dangerous.

2.3.1 Military Applications

For military applications ROVs. are used for sea mine countermeasures, ordnance retrieval, body recovery, accident investigations and harbour and vessel inspections [10].

2.3.2 Commercial Applications

In the oil and gas industry ROVs. are used to assist with the installation, operation, inspection and decommissioning of subsea structures such as blowout prevention valves and well head installations [11].

ROVs. are extensively used in the installation, maintenance and surveillance of subsea telecommunication cables [10].

2.3.3 Research and Exploratory Uses

ROVs. have explored hydrothermal vent fields in both the Pacific and Atlantic Oceans, conducted mid-water biological, acoustical and physical oceanography experiments. ROVs. have performed under-ice surveys in both the Arctic and Antarctic Oceans [12]. Other science applications include chemical oceanography and rock coring. The **M**onterey **B**ay **A**quarium **R**esearch **I**nstitute (**MBARI**), the **C**anadian **S**cientific **S**ubmersible **F**acility (**CSSF**) and JAMSTEC are home to typical research specific ROVs. [10].

2.3.4 Fundamental ROV Subsystems

This section describes the basics of ROV construction, function and performance. Examples of the subsections are displayed in Figure 10.

Frame

The frame of the ROV is the mechanical platform on which the modules that constitute the ROV are mounted to. Frames for ROVs. are generally made from plastic polymers or aluminium tubing. The two important criteria for frame materials are the strength and the density. An ideal frame is one which is light and strong and can manage the full weight of the ROV [3]. The frame shown in Figure 10 on the *Saab Seaeye Falcon* is made from polypropylene; this material is buoyant, corrosion resistant and easily machined [13].

Buoyancy

ROV parts are generally denser than water and because of this the ROV requires a buoyancy device to control vertical motion. Most ROVs. use the combination of a float block and vertical thruster to control this. The float block provides near neutral buoyancy to the ROV and the thruster module controls its ascent and descent. Dynamic buoyancy modules are rarely used due to their expense and mechanical complication [14]. In Figure 10 a float block forms the base of the *Saab Seaeye Falcon* and is manufactured from foam suitable for the depth rating of the ROV [13].

Propulsion and Thrust

To allow the ROV to manoeuvre in the water the vehicle requires mechanical actuation. On ROVs. this is achieved by using two or more thruster modules [3]. Thruster modules rotate a propeller that in turn provides thrust. By having multiple thruster modules in various orientations on the ROV one can control the movement of the ROV in several degrees of freedom. The number of degrees of freedom the ROV can be controlled in is determined by the number of thrusters and their respective orientations. Conventional ROVs. require high manoeuvrability in the horizontal plane and the ability to ascend and descend [15].

The Tether

The umbilical tether serves several functions. It provides a mechanical connection to the ROV in the case of ROV failure allowing the ROV to be easily retrieved. It allows the ROV to stay at the underwater work sight indefinitely as long as power is supplied from the surface and it allows real-time communication with the ROV [16].

Lighting

Seawater attenuates light rapidly due to scattering and absorption thus ROV's require on-board lighting. No significant sunlight penetrates beyond a depth of 200 m [3].

Camera Unit and Camera Tilt Unit

In order to receive visual images from the ROV a camera unit is required. Not all observation class ROVs. have a tilt unit connected to the camera, however on larger observation class ROVs. this is a standard feature [3]. The tilt unit allows the pilot to view what is below, in front of and above the ROV. Some tilt units as on the *Saab Seaeye Falcon* ROV (in Figure 10) have a built in slip coupling to protect the tilt mechanism and camera in case of obstruction in the tilt mechanism or a collision [13].

Power Pod and Electronics Pod

The power pod manages and distributes the various power requirements to the modules on the ROV. The electronics pod controls the communications and signal processing from the modules [2].

Manipulator Arm

The manipulator arm is often considered and designed to be an optional extra in the observation class ROV system. On light class or observation class ROVs., manipulator arms allow the pilot to perform basic tasks such as sample retrieval or cutting. More complex manipulators have multiple degrees of freedom, position control and force feedback [3].

Figure 10- ROV System Fundamentals – *Saab Seaeye Falcon* [13]

3 Overview of Commercial Thruster Modules

This dissertation investigated and modified the thruster modules built for the Seahog ROV therefore in this section various commercial thruster modules are evaluated to assess their features and specifications. The section is concluded with a summary of the features found on commercial thruster modules and a performance comparison.

3.1 *Saab Seaeye* Brushless DC Thrusters

Saab Seaeye was the first company to incorporate **b**rush**l**ess **DC** (**BLDC**) motors into thruster modules. To achieve this the thruster's electronics and control circuitry had to be developed to fit inside the thruster housing [17].

Features of the Saab Seaeye thrusters include: [18]

- closed loop speed feedback
- drive electronics contained inside the thruster housing
- high strength lightweight titanium shafts
- angular contact thrust bearings
- fouled propeller detector and reset circuitry
- under-voltage protection of the electronics
- pressure compensation for operation at full ocean depths

The thrusters used on the *Saab Seaeye Falcon* are the MCT01 thrusters (as seen in Figure 11). They incorporate magnetic couplings to transmit the torque from the drivetrain to the propeller. This eliminates the need for dynamic seals that require regular maintenance. They do not require oil for cooling or for pressure compensation and are therefore suitable for use in environmentally sensitive areas such as reefs and fisheries [18].

The larger thruster modules manufactured by *Saab Seaeye* use oil pressure compensation and tungsten carbide dynamic shaft seals [17]. Table 1 shows the key specifications of the Saab Seaeye MCT01 thruster module.

Table 1 - Saab Seaeye MCT01 Specifications [18]

Specification	Value	
Voltage	48	VDC
Current	3.25	A
Thrust at Max. Power	137.34	N
Max. Power	300	W
Weight in Air	4.3	kg
Weight in Seawater	2.5	kg
Depth Rating	1000	m
Control Signals	RS-485	
Connector	5 Way	

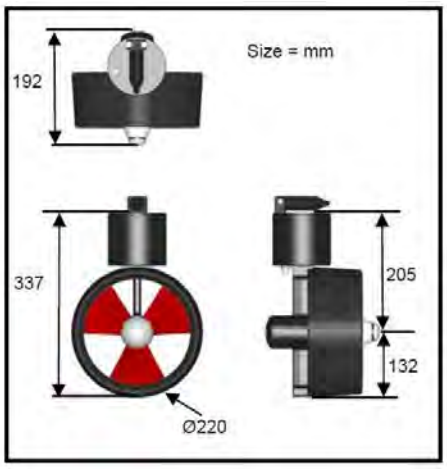

Figure 11 - Diagram of Saab Seaeye MCT01 Thruster [18]

3.2 Engtek SubSea Systems' Electric Thrusters

The Engtek thruster modules use rare-earth magnet BLDC motors. The motor drive and control circuitry is housed inside the thruster module. The propellers are manufactured from carbon-fibre and are designed to provide equal thrust in forward and reverse directions. No gearing is used between the motor and the propeller resulting in quieter and more efficient operation. The modules are sealed using a silicon carbide dynamic shaft seal [19].

Table 2 shows the specification of the SCE025 thruster module, the smallest thruster module from Engtek's range [19].

Table 2 - Engtek Subsea SCE025 Thruster Specifications [19]

Specification	Value	
Voltage	60	VDC
Current	3.1	A
Thrust at Max. Power	54	N
Max. Power	190	W
Weight in Air	2.5	kg
Weight in Seawater	1.9	kg
Depth Rating	150	m

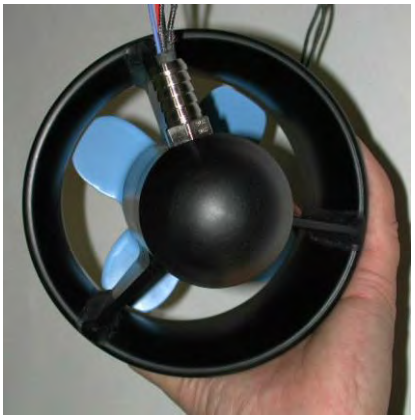

Figure 12 - Engtek Subsea SCE025 Thruster

3.3 Seamor Marine – 150 W Thruster

The Seamor Marine thrusters are built to be entirely modular with built in electronics and microcontroller that can feedback propeller speed, current draw, temperature and humidity for monitoring and control purposes. The drivetrain utilises a brushed Maxon motor and gearbox.

Seamor Marine propellers are injection moulded using carbon-fibre reinforced plastic. The thrusters are dynamically sealed using double ball seals. The housing is manufactured from anodised aluminium.

Figure 13 shows the overall dimensions of the 150 W thruster module. It is 247 mm long and has nozzle diameter of 126 mm.

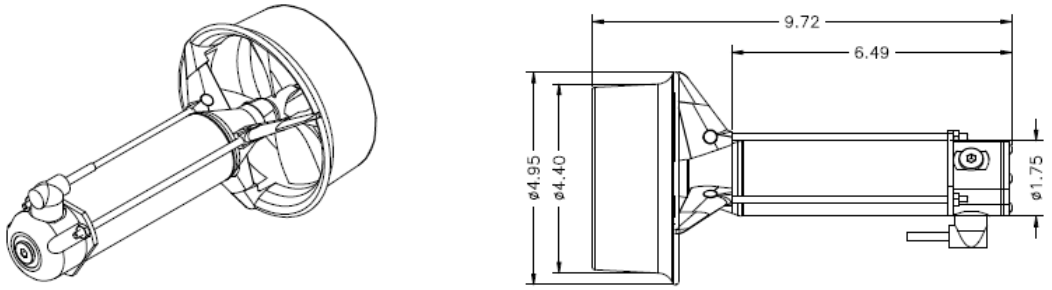

Figure 13 - Seamor Marine – 150 W Thruster (Dimensions in inches)

Table 3 - Seamor Marine - 150W Thruster Specifications

Specification	Value	
Voltage	24-48	VDC
Forward Thrust at Max. Power	44	N
Reverse Thrust at Max. Power	23	N
Max. Power	150	W
Weight in Air	1.2	kg
Depth Rating	300	m
Control Signals	RS-485	

Figure 14 - Seamor Marine's 150W Thruster Module

Table 3 shows the specifications for the 150 W thruster module. It can clearly be seen that the thruster was not designed to deliver equal forward and reverse thrust.

3.4 Chapter Summary

Three commercial thruster modules have been examined according to the information detailed in their respective product catalogues. Several different methods of sealing have been used ranging from dynamic seals to magnetic couplings. Two of the thruster modules utilise carbon fibre propellers implying that strength and the weight of the propellers are important factors.

Because these thrusters are not identical in specifications and performance two ratios were generated to compare the three essential performance indicators: thrust generated, power consumed and weight. Thrust-to-weight ratios and thruster-to-power ratios were calculated to compare the three modules; these can be seen in Figure 15.

The Saab Seaeye proves to be the best all-rounder with the highest thrust-to-power ratio and the second best thrust-to-weight ratio. It provides equal thrust in each direction and it does not utilise dynamic seals therefore improving maintenance and sealing reliability.

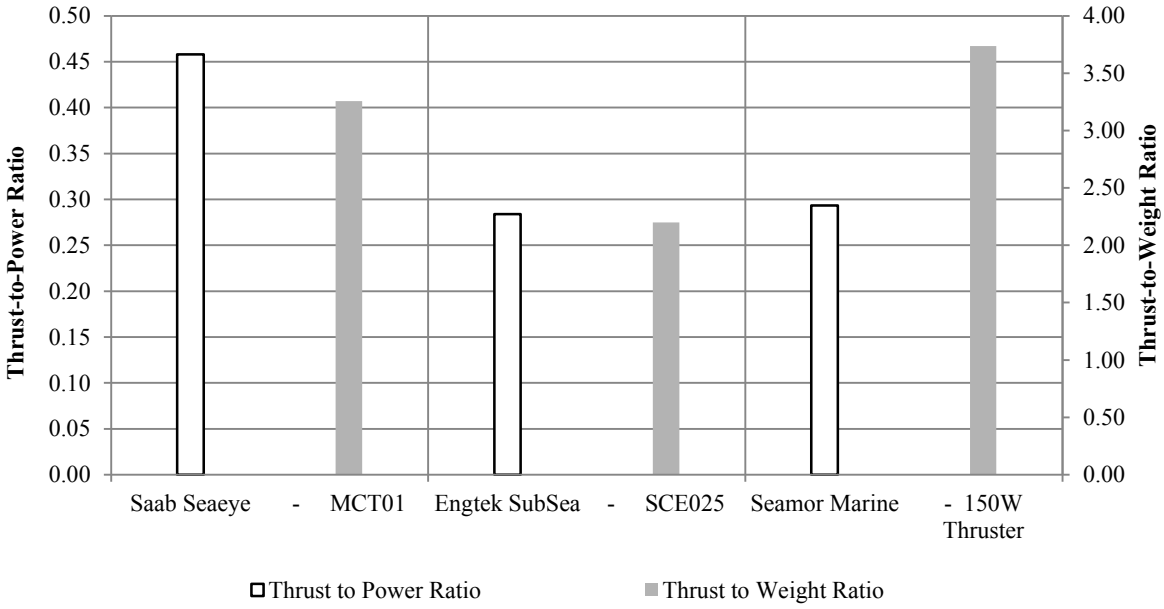

Figure 15 - Performance Comparison of Commercial Thrusters

An ideal thruster module for the ROV would:

- provide accurate closed loop speed control
- generate maximum thrust possible
- achieve equal thrust in forward and reverse directions
- consume as little power as possible
- weigh as little as possible
- operate at full power indefinitely without overheating
- require no oil pressure compensation
- only use static seals
- have a thrust-to-weight ratio and thrust-to-power ratio competitive with commercial thrusters

4 Thruster Module Analysis

The thruster module featured in this project was initially developed in the dissertation by T. Knight titled "The Development of the Steering and Propulsion and the Camera and Lighting Systems for an Observation Class Remotely Operated Underwater Vehicle".

This chapter discusses the previous work done and resulting technical and practical issues with the original thruster module.

4.1 Specifications and Features

The specifications of the thruster module are detailed below in Table 4.

Table 4 - Original Thruster Module Specifications [20]

Property	**Value**	
Mechanical		
Mass	4.8	kg
Maximum Thrust	35	N
Maximum Propeller Speed	550	rpm
Electrical		
Motor Supply Voltage	48	VDC
Motor Power Rating	120	W
Electronics Supply Voltage	5	VDC
Communication Protocol	RS-485	
Communications Speed	9600	bit/s

Other features included:

- overvoltage protection
- overcurrent protection
- reverse-bias protection
- temperature sensing on the motor housing
- quadrature encoder speed feedback
- addressable communications

4.2 Thruster Mechanical Layout

The thruster module incorporated a hermetic housing that mounted the kort-nozzle braces, the propeller and enclosed the electronics, motor, gearbox and magnetic coupling internal rotor. The external magnetic rotor was neatly incorporated into the base of the propeller. An exploded view of the module is shown in Figure 16.

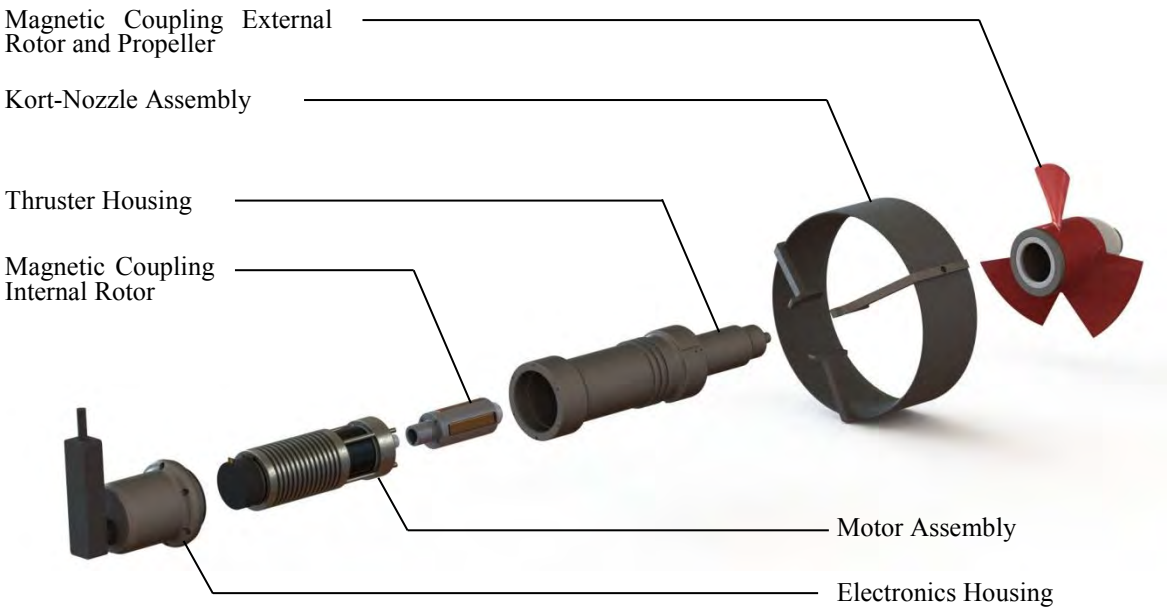

Figure 16- Exploded View of the Thruster Module[20]

The motor drivetrain selected was a BLDC *EC-max. 40*, 120W *Maxon* motor coupled to a 3.5:1 planetary gearbox. A four pole, neodymium magnet, magnetic coupling was used to transmit the torque from the motor to the propeller across the hermetically sealed thruster housing. The propeller design was modified from an existing commercial propeller made by *Vetus*.

The kort-nozzle, propeller and magnetic coupling performed as expected and no future work was recommended.

Modifications to the drivetrain were recommended as the maximum speed achieved by the thruster module fell far below the motor's efficient operating range therefore decreasing the efficiency of the thruster module [20].

4.3 Drivetrain Analysis

The determination of the thruster module drivetrain's efficiency at full power was done by comparing the input electrical power to the mechanical output power at the output of the planetary gearbox. The electrical input power *(P_{elec})* was calculated using equation 1, where supply voltage was *(V)* and current was *(I)*.

$$P_{elec} = VI \tag{1}$$

To determine the mechanical energy output of the drivetrain the output torque had to be calculated and multiplied with the output shaft's angular velocity. The motor output torque, τ, was calculated using the motor's torque constant *(K_m)* and current *(I)*.

$$\tau = I.K_m \tag{2}$$

The mechanical energy output of the motor *($P_{mech\ motor}$)* was calculated using the angular velocity *(ω)*, torque *(τ)* and the equation below.

$$P_{mech\ motor} = \tau . \omega \tag{3}$$

The efficiency of the planetary gearbox *(η_{gb})* was included; this is approximated by using the efficiency rating from the gearbox's specification sheet and is calculated as follows.

$$P_{mech} = \eta_{gb} . P_{mech\ motor} \tag{4}$$

The efficiency *(η)* for the thruster's motor drivetrain was calculated as follows:

$$\eta = \frac{P_{mech}}{P_{elec}} \tag{5}$$

Table 5 shows the results obtained for the previous thruster module. The original thruster module drivetrain had an efficiency of 17%.

Table 5 - Original Thruster Performance Analysis

Property	Symbol	Value	
Output Torque of Drivetrain	τ	0.558	Nm
Output Speed	ω	57.6	rad/s
Electrical Input Power	P_{elec}	190	W
Mechanical Output Power	P_{mech}	32	W
Thruster Drivetrain Efficiency	η	17	%

4.4 Mass Analysis

The original thruster module weighed 4.8 kg. There are five thruster modules on the ROV therefore contributing 24 kg to the total weight of the ROV. The ROV has been estimated to weigh 81.5 kg. This means the thrusters constituted 31% of the mass of the ROV as can be seen in Figure 17. When compared to commercial thrusters the thrust-to-weight ratio of the thruster module was worse than all of the thrusters reviewed.

Figure 18 shows the mass analysis for the thruster module, it can be seen that the housing weighed 1.99 kg, this made up 41% of the thruster's total weight meaning that the thruster housings constituted 12.3% of the total ROV's mass. The next heaviest sub-assembly was the drivetrain; this was 20% of the thruster module's mass. With future changes to the drivetrain being made to enhance performance rather than reduce weight the housing was identified as the sub-assembly with the greatest potential in which to reduce the weight.

ROV Mass Analysis

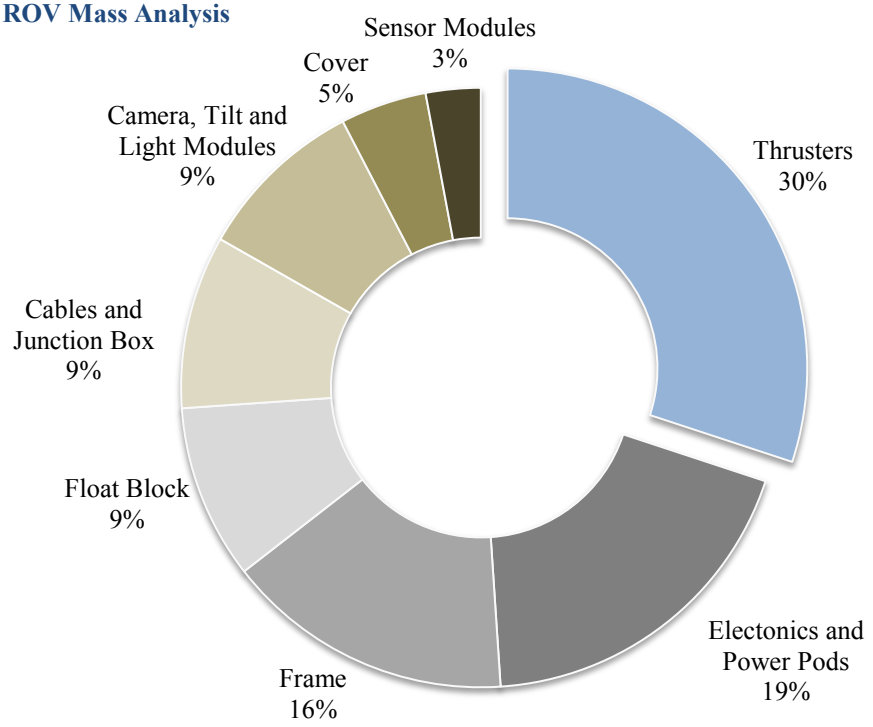

Figure 17 - ROV Mass Analysis

Single Thruster Module Mass Analysis

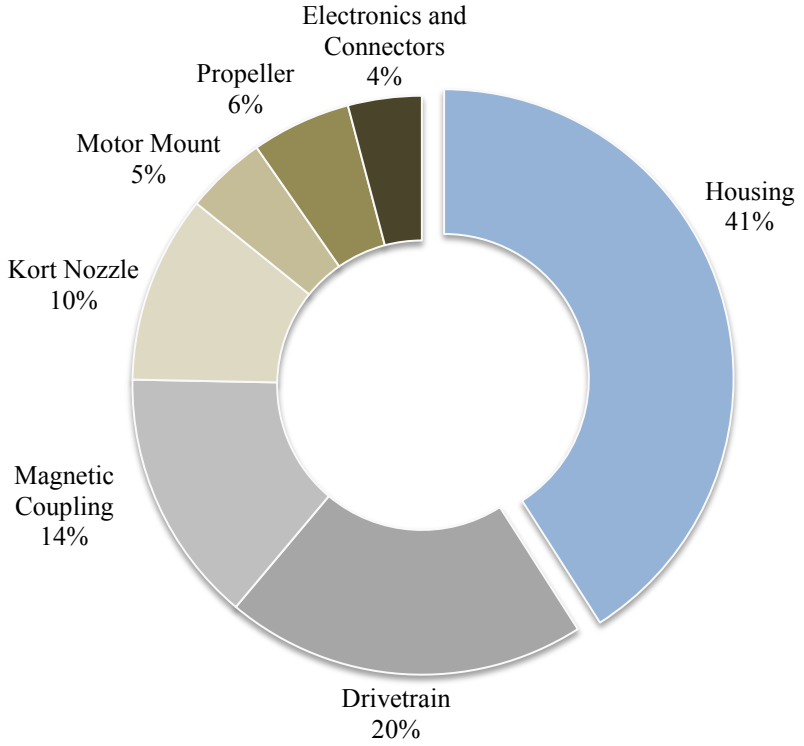

Figure 18 - Single Thruster Module Mass Analysis

4.5 Thruster Electronics

The electronics of the thruster module consisted of two sub sections; the central control unit and the motor controller board. Figure 19 shows an exploded view of the intended assembly of the electronics module.

4.5.1 Electronics Assembly

The actual application of this design was not fully implemented. The flexible plastic lining for holding the electronics was never made nor installed which increased the risk of the electronics conducting with the housing.

With there being two separate systems consisting of three **p**rinted **c**ircuit **b**oards (**PCB**) many wires were used to transmit power and signals between the boards. These wires were not taken into consideration during the design process.

The housing was designed with a smaller entrance diameter than internal diameter therefore creating a cavity; this is shown in the cross section of the part in Figure 20. This design makes assembly and disassembly difficult. Once the PCBs and wires were pushed into the housing the wires wrapped around the boards to get from either PCBs to other PCBs or from the Birns™ connector to the PCBs. This meant that the electronics and bunched wires filled the cavity and at times could not be removed without severing the wires. It was also found that wires had been directly soldered onto PCBs meaning that re-soldering was required when re-assembling a thruster module.

The foam inserts used to separate and electrically insulate the PCBs also served to thermally insulate them and therefore contributed to the overheating of the electronics.

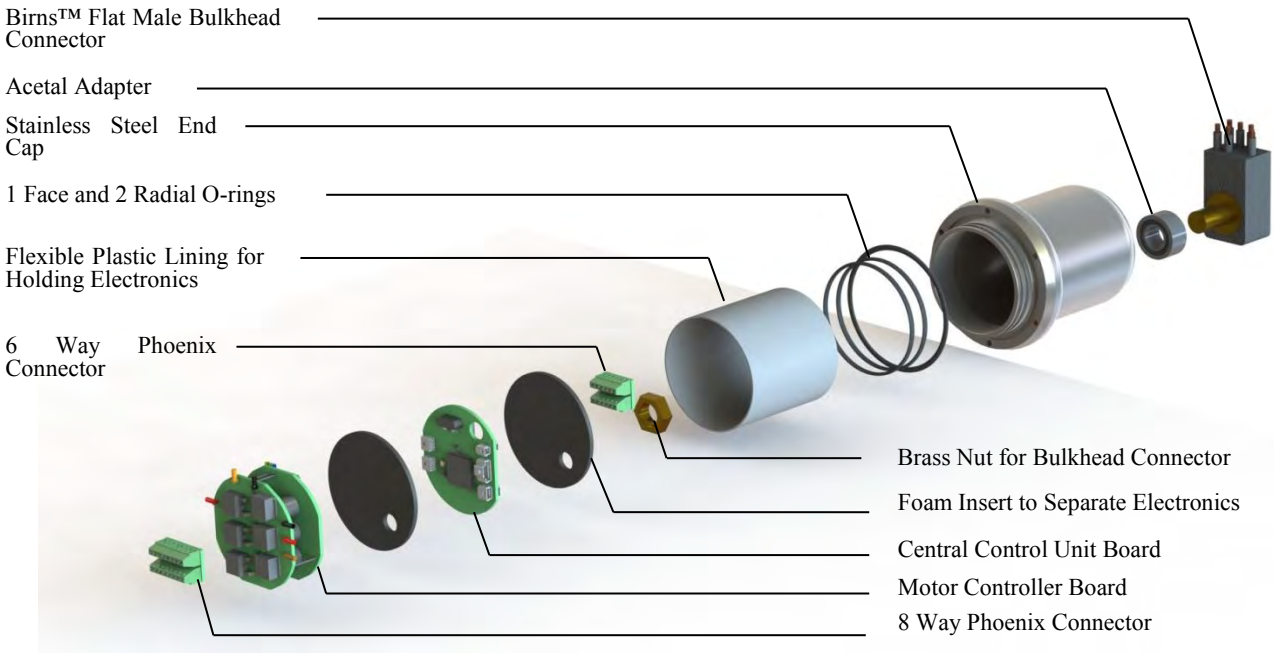

Figure 19 - Exploded View of the Intended Electronics Assembly [20]

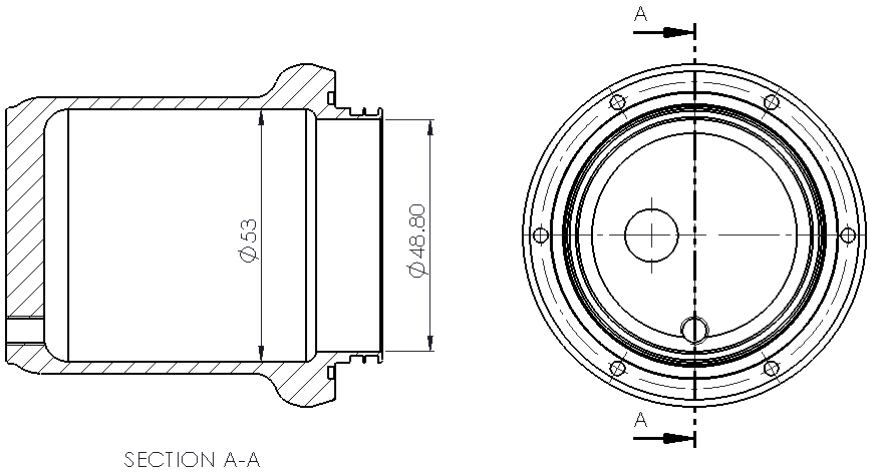

Figure 20 - End Cap Cross Section

4.5.2 Electronic Subsystems

The communications and sensing board was powered by 5 VDC generated in the electronics pod on the ROV. An *ARM ® Cortex™* M3 embedded microprocessor (LM3S8962 manufactured by Texas Instruments) was used to receive communications, send communications to the motor controller board and read and send back temperatures from sensors placed in the module.

Programming the LM3S8962

The embedded microprocessor was programmed using National Instruments' LabVIEW visual programming language. LabVIEW had a partially developed programming environment for the LM3S8962 therefore allowing one to code the processor using the graphical interface. This method of programming had one advantage; programming the processor was straight forward, graphical and quick. However this method did limit the processor's functionality. LabVIEW did not support the **U**niversal **A**synchronous **R**eceiver/**T**ransmitter (**UART**) communications interrupt and all communications had to be timer based. The LM3S8962 drew approximately 150 mA when programmed using LabVIEW and 15 mA when programmed in C-code using *Keil* (a development tool for ARM processors).

Timer Based Communications

The RS-485 serial communications were received via a MAX3485 IC placed on the central control unit that converted the RS-485 protocol into 0 V – 3 V UART logic acceptable for the embedded microprocessor's UART module. The microprocessor discriminated against the data packets received and only stored the data addressed to that module. Upon completing this task the microprocessor passed the data on via the **S**erial **P**eripheral **I**nterface (**SPI**) to the motor controller board.

Using timers as opposed to interrupts to receive and send communications meant that when the thruster module was initialised it had to be synchronised with the operator console software with regards to when communications were sent and received. This meant that the thruster had to be restarted several times when trying to establish connectivity to the operator console and was prone to eventually go out of sync with the operator control console therefore losing communication and requiring a restart. This was challenging when establishing communication with one thruster module, it would have been very challenging when attempting to establish communication with all five thruster modules.

Speed Feedback and Closed Loop Speed Control

The Maxon motor was fitted with a quadrature encoder module to provide accurate closed loop speed or position control capability. The LM3S8962 came with a quadrature decoder module and this was used to send back a 32-bit speed value to the operator console via the RS-485 network. The operators control station monitored the quadrature encoder values received over RS-485 and if the received value differed from the desired speed then step control was done to adjust the value sent to the thruster.

4.5.3 The Motor Controller Board

The motor controller board was developed to drive the Maxon 120 W 48 V BLDC motor. It received the desired speed and direction values via SPI from the central control board. The board implemented sensed BLDC motor closed loop control using the Hall effect switches built into the Maxon motor.

When operated at full power the **M**etal-**O**xide **S**emiconductor **F**ield-**E**ffect **T**ransistors (**MOSFET**s) used on the motor controller board heated up enough to melt the insulation of the wires that came into contact with them.

This overheating was investigated and attributed to shoot-through. The shoot-through was caused by **E**lectro**m**agnetic **I**nterference (**EMI**) generated from adjacent MOSFETs being switched on and off. This EMI induced a large enough potential difference over the gate and source to activate the MOSFET.

The motor controller board consists of two PCBs soldered together with wire, this design makes trouble-shooting, repair and component replacing very time consuming and difficult with de-soldering required.

4.6 Performance Comparison with Commercial Thruster Modules

To be able assess the overall performance of the thruster module a comparison with other thruster modules was done. The only information available was that of commercial thruster modules. In Chapter 3 an assessment with the limited information supplied by commercial thruster manufacturers was done. The thruster module was assessed in the same manor and both thrust-to-power and thrust-to-weight ratios were calculated. The results can be seen in Figure 21. The thruster module built by RARL performs poorly compared to commercial options with the worst power and mass efficiency of the four thrusters.

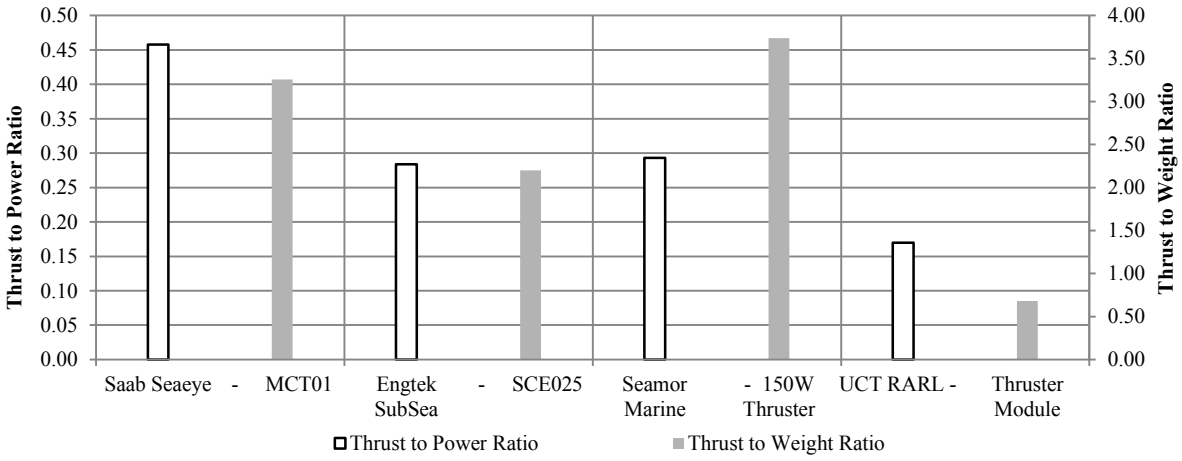

Figure 21 - Commercial Thruster Performance vs. UCT Thruster Performance

4.7 Thruster Module Analysis – Chapter Summary

The following sub-sections of the thruster module performed adequately and did not need to be replaced:

- the propeller
- the kort-nozzle
- the magnetic coupling

The following key issues were deemed detrimental to the thruster module's performance:

- the BLDC motor operating far below its optimal performance range
- the thrust-to-power ratio
- the thrust-to-weight ratio
- the inevitable loss of communications
- the rapid overheating of the electronics

5 Thruster Module Modifications

5.1 Introduction

Due to the initial investment in the thruster modules and the need to be economic in their modification not all the subsections were replaced.

This section details the modification of each subsection of the thruster modules that required improvements. It begins with the desired specifications and features of the completed thruster module. Each specification is followed with a justification. The modified subsections were analysed and redesigned. Where possible, estimated performance is predicted which will be compared to the test results in Section 6.

5.1.1 Mechanical Improvements Identified

The drivetrain's efficiency of 17% showed that the drivetrain output was not well matched to the load. The replacement of either the motor or the gearbox was required to improve the module's efficiency.

As the thruster modules' housings account for 12.3% of the weight of the entire ROV, changes in the housing were made. These changes, coupled with the modification of the drivetrain will aim to improve the thruster's thrust-to-weight ratio.

5.1.2 Electrical Improvements Identified

Since the development of this thruster module Texas Instruments had ceased production of the LM3S8962. Due to the unavailability of the microcontroller and the critical design flaws in the motor control board, the entire thruster electronics system was replaced as opposed to being modified. Interrupt based communications and efficient motor control were implemented to improve the reliability and efficiency.

5.2 Thruster Module Specifications

A desired thruster module for the ROV must be competitive with commercial thruster modules. Table 6 shows the intended specifications and features for the modified thruster module. Counter-intuitively, thrust generated is not listed as a specification as the maximum thrust possible is desired.

Table 6 - Thruster Module - Desired Specifications

Index	Design Requirement	Value
	Quantitative Specifications	
5.2.1	Thrust-to-Power Ratio	>0.28
5.2.2	Thrust-to-Weight Ratio	>2.2
5.2.3	Max. Reverse Thrust within % of Max. Forward Thrust	10%
5.2.4	Speed Error as % of Input Speed	1%
5.2.5	Communication Response Time	<10 ms
	Qualitative Specifications	
5.2.6	On-board Closed Loop Speed Control	Yes
5.2.7	Interrupt Based Communications	Yes
5.2.8	Can Operate at Max. Power Indefinitely	Yes
5.2.9	Temperature Feedback	Yes
5.2.10	Communication Failure Shutdown Procedure	Yes
5.2.11	Over Voltage, Over Current, Reverse Bias Protection	Yes

5.2.1 The thrust-to-power ratio must be competitive with the commercial thruster modules analysed in Section 3, this would require it to have a thrust-to-power ratio above 0.28 (that of the Engtek SubSea thruster module).

5.2.2 The same criteria from Section 5.2.1 apply to the thrust-to-weight ratio. The thrust-to-weight ratio should be greater than 2.2 (that of the Engtek SubSea thruster module).

5.2.3 It is desired to obtain symmetrical thrust from the thruster module to maximise positional control from the vectored thrusters on the ROV.

5.2.4 The thruster module will be speed controlled and therefore to obtain accurate speeds (and therefore accurate thrusts) the thruster module must be controlled to within a specified accuracy. The difference between the output speed and input speed had to be below 1% of the input speed.

5.2.5 An ideal thruster produces the exact speed at the exact moment required. Therefore this response time is crucial to the control of the ROVs. performance. A time of 10 ms was deemed achievable with the communication systems previously selected for the ROV's subsystems and fast enough for control purposes.

5.2.6 The ROV has been designed to incorporate distributed intelligence within the modules. Therefore as opposed to communicating the propeller speed back to the control station and doing closed loop speed control by the operator station with the corrected values being communicated back to the ROV (as was done in the previous thruster module) it is preferred to do the closed loop speed control at the thruster module. This will improve the closed loop response time by removing the intermediate communication steps and it will distribute the processing power of the ROV system.

5.2.7 As discussed in Section 4.5 the timer based communications proved to be unreliable. Interrupt based communications are essential to allow the thruster to continuously or intermittently communicate with the ROV at the discretion of the ROV control system and operator console.

5.2.8 The thruster module must be able to operate in water at full power continuously. This is essential for the vertical thruster which will be controlling the depth of the ROV and for the horizontal thrusters in the case of the ROV moving against or maintaining its position in a current.

5.2.9 Temperature feedback is essential for monitoring and potential trouble-shooting (in the case of unexpected performance reduction) when operating the ROV.

5.2.10 It is desired that if communications have failed or have been severed the ROV's thruster modules do not continue to produce thrust therefore avoiding uncontrolled manoeuvring conditions.

5.2.11 For reliability and robustness the electronics must have protection features to prevent operator error or accidents destroying the electronics. This protection includes over current protection for the motor controller if a foreign object were to obstruct the propeller and therefore rapidly brake the motor.

5.3 Thruster Module Drivetrain Modification

5.3.1 Introduction

In this section several steps were taken to select the optimum drivetrain for the thruster module. Initially the load was defined and discussed, then by using known relations and previous test data the load was characterised. Once a torque-speed curve was defined it was matched to different drivetrain assemblies that were available. The best expected combination was selected and new thruster module performance estimations were made.

5.3.2 Load Definition

It was ideal to obtain the expected torque and speed characteristics of the load to better match the output of the drivetrain to the load. In this case the load was defined as the magnetic coupling and the propeller as seen in Figure 22.

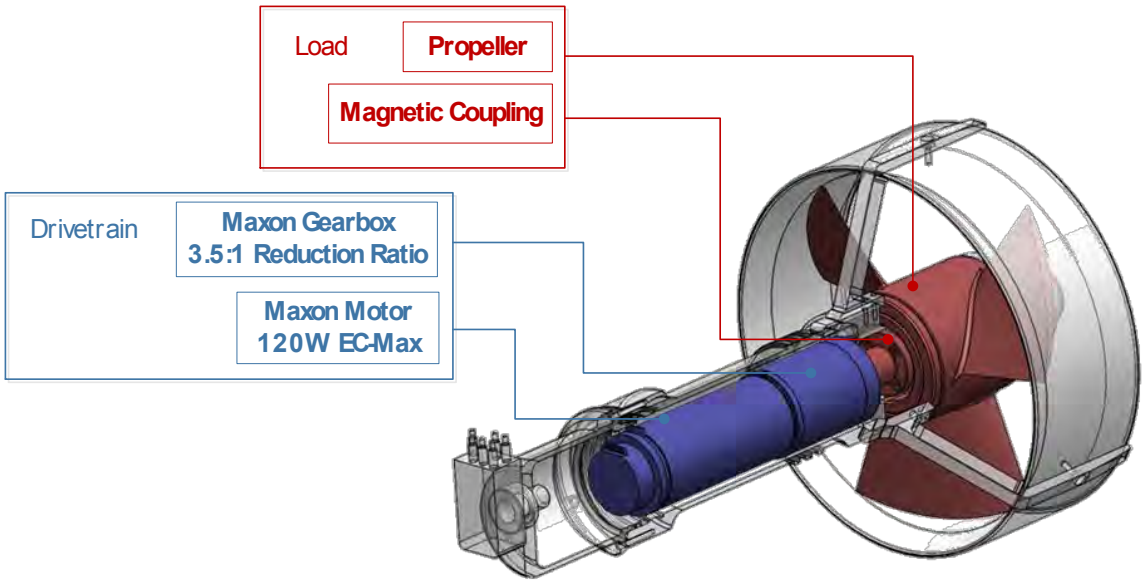

Figure 22 - Drivetrain and Load Segregation of Thruster Module

5.3.3 Load Characterisation

The steady-state relationship between torque and thrust is nearly linear [21]. The thrust produced by a shrouded propeller is approximated by equation 6 [21].

$$T = A\rho\eta^2 p^2 \Omega|\Omega| \tag{6}$$

Where A is the cross-sectional area of the shroud, ρ is the ambient fluid density, η is the efficiency of the propeller and p is the axial distance travelled by the propeller with one unit of rotation (1 radian), referred to as the pitch. The angular velocity of the propeller is given as Ω. The absolute value of Ω is used to preserve the sign of the thrust according to the direction of rotation of the propeller. From this equation we can see that thrust is proportional to the square of propeller angular velocity.

A, η and p are all characteristics of the propeller and shroud, ρ is the density of water. These values stay constant for the thruster. Equation 6 can be simplified to equation 7 where C_t is determined experimentally for a thruster and is called the proportionality constant [21].

$$T = C_t \Omega^2 \tag{7}$$

Figure 23 shows the thrust produced by the thruster module vs. the propeller speed squared. The linearly proportional relationship between thrust and propeller speed squared was evident, a best fit curve was used to approximate C_t which was equal to 0.0097. The data used to calculate the curve in Figure 23 was obtained by T. Knight [20].

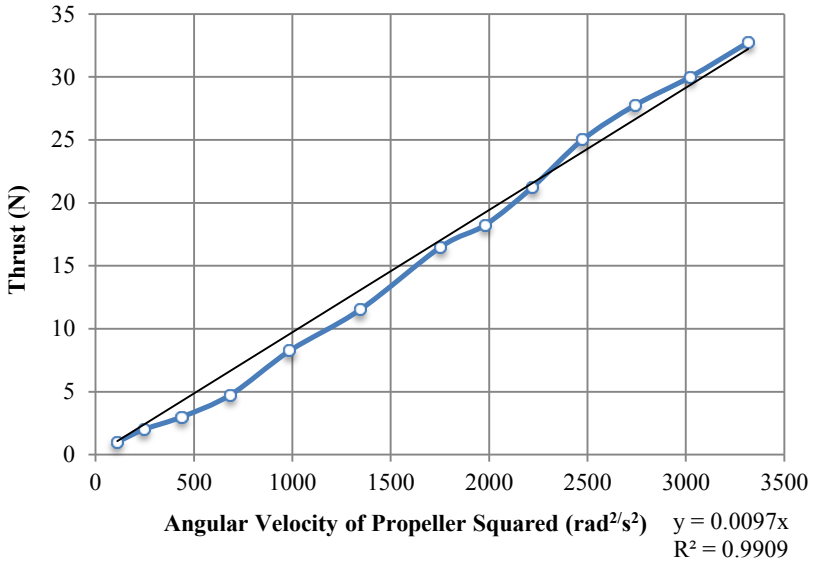

Figure 23 - Thrust vs. Propeller Speed Squared

The torque applied to the propeller was not measured however it was approximated by taking the motor current, I, the motor's torque constant, K_m, and applying equation 2 mentioned in Section 4.3.

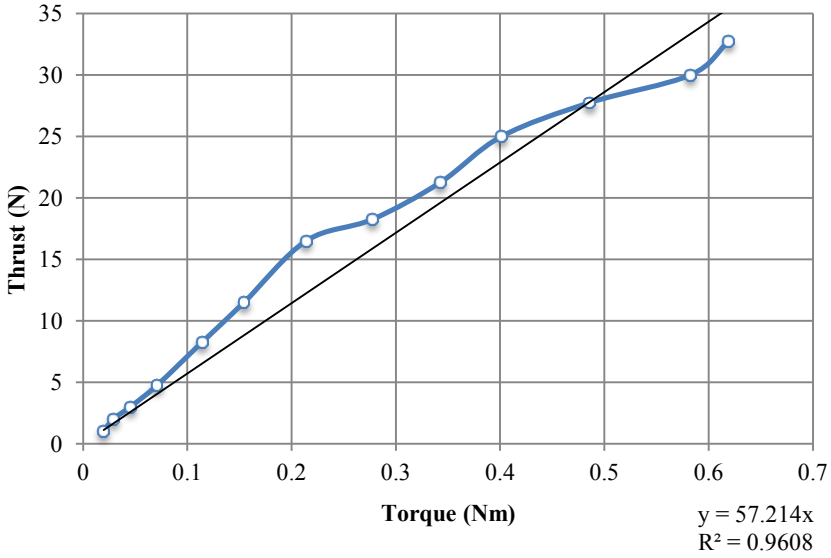

Figure 24 - Thrust vs. Approximated Torque

Figure 24 shows the thrust vs. approximated torque relationship and as stated previously the steady-state thrust and torque relationship is nearly linear. Therefore thrust can be written as a function of torque in equation 8.

$$T = K_t \tau \tag{8}$$

From the analysed thrust and current data a best fit curve was used to approximate K_t to be 57.214. Equating equations 8 and 7 gives us the torque as a function of angular velocity that defines the load (equation 9) and therefore can be used to select the most appropriate motor and gearbox combination to obtain maximum thrust from the thruster and efficiency from the drivetrain.

$$\tau = \frac{C_t}{K_t} \Omega^2 \tag{9}$$

5.3.4 Motor and Gearbox Comparison

The motor used was a 120W *EC-max.* BLDC Maxon motor and the specifications are shown in Table 7. This is the most powerful motor in Maxon's *EC-max.* range.

Table 7 – Maxon Motor Specifications [22]

***EC-max. 40* BLDC *Maxon* Motor**		
Specification	Value	
Part Number	283870	
Power Rating	120	W
Voltage Supply	48	VDC
Max. Continuous Current	4.06	A
No Load Speed	10100	rpm
Nominal Speed	9260	rpm
Nominal Torque	0.17	Nm
Max. Efficiency	85	%
Weight	720	g

The range of Maxon planetary gearboxes is detailed in Table 8. An alternative option to replacing the gearbox was to replace the motor for one of the same general specifications but that has a higher winding resistance and therefore a lower nominal operating speed. However new motors are significantly more expensive than new gearboxes and therefore this option was not deemed feasible and not pursued. Therefore the gearbox was changed to better match the drivetrain to the load.

Table 8 - Maxon Gearbox Specifications [22]

Planetary Gearhead 42C Gearboxes				
Part Details		Common Specifications	Value	
Part Number	203113	Number of Stages	1	
Reduction Ratio	3.5:1	Max. Continuous Torque	3	Nm
Part Number	203114	Max. Efficiency	90	%
Reduction Ratio	4.3:1	Weight	260	g
Part Number	260551			
Reduction Ratio	6:1			
Part Details		Common Specifications	Value	
Part Number	203115	Number of Stages	2	
Reduction Ratio	12:1	Max. Continuous Torque	7.5	Nm
Part Number	203116	Max. Efficiency	81	%
Reduction Ratio	15:1	Weight	360	g
Part Number	203117			
Reduction Ratio	19:1			

Figure 25 shows the maximum operating ranges of six drivetrain combinations (the Maxon 120W EC-max. motor coupled with each of the available gearboxes). The operating ranges were obtained from the motor's continuous operating torque-speed curve and then multiplied by the respective gearbox ratios and efficiencies. The load estimation obtained with equation 9 is plotted using the constant values obtained in the previous section. The ideal solution is to be as far along the estimated load curve as possible while being within the drivetrains' continuous operating range. Figure 25 shows the maximum speed reached by the original thruster module which correlates with the 3.5:1 gearbox selection.

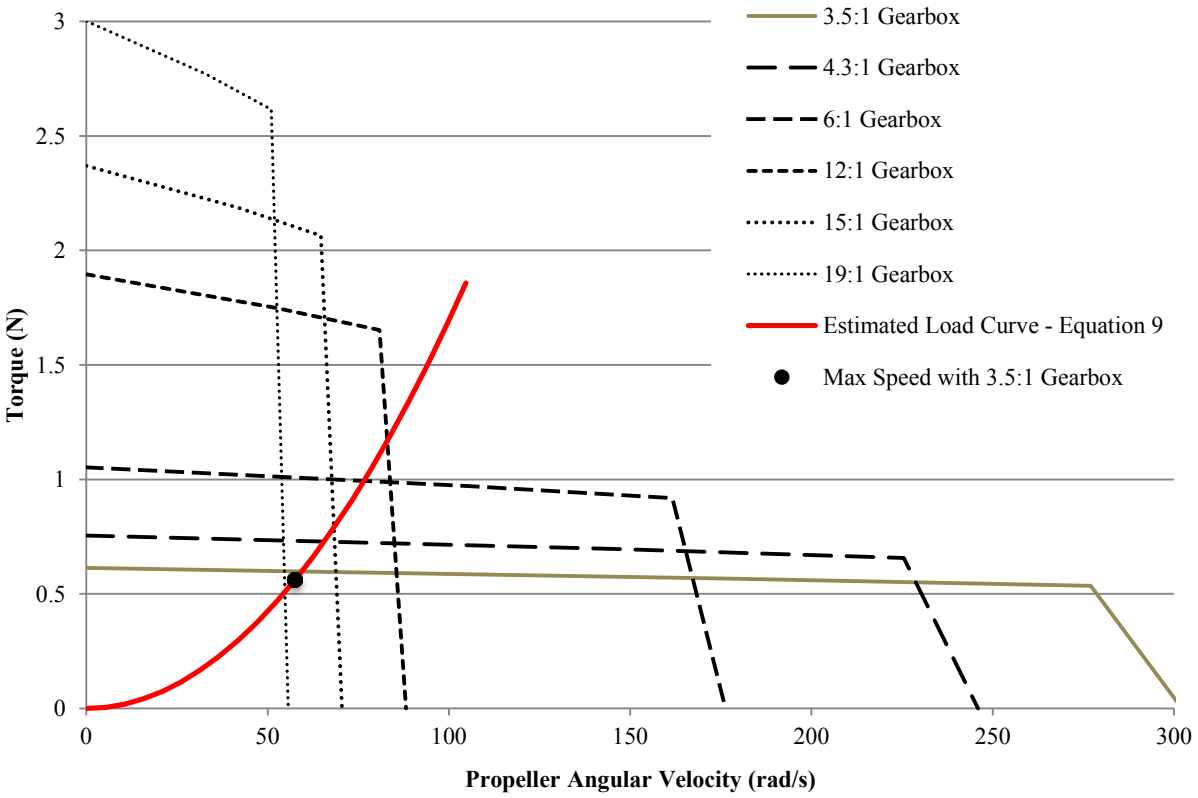

Figure 25 - Projected Load Curve vs. Available Gearbox Selections

5.3.5 Drivetrain Selection and Performance Estimations

From Figure 25 it can be seen that the 12:1 gearbox is best suited to the load. Even though the 12:1 gearbox is 100 g heavier and 9% less efficient than the 3.5:1 gearbox it allows the motor to get closer to its nominal speed and more efficient range. The estimated thruster performance with the 12:1 gearbox can be seen in Table 9. The efficiency was expected to increase from 17% to 76% and the thrust was expected to double from 34 N at 3.95 A to 68 N at 2.77 A.

Table 9 - Estimated Thruster Performance with 12:1 Gearbox

Description	Value	
Drivetrain Torque Output	1.206	Nm
Propeller Speed	800	rpm
Mechanical Output Power of Drivetrain	101	W
Current	2.77	A
Thrust Output	68	N
Drivetrain Efficiency	76	%

5.4 Thruster Housing Modification

5.4.1 Thruster Housing Review

As mentioned in Section 4.4 the thruster housings contribute 12.3% of the weight for the entire ROV. Figure 26 shows a cross section of the housing design. The motor housing is bolted to the electronics housing with six M3 bolts and statically sealed with one face seal and two radial seals. A pressure test to the equivalent depth of 450 m was conducted on the housings with the face seal removed, the two radial seals proved to be adequate and a recommendation was made to remove this seal [20].

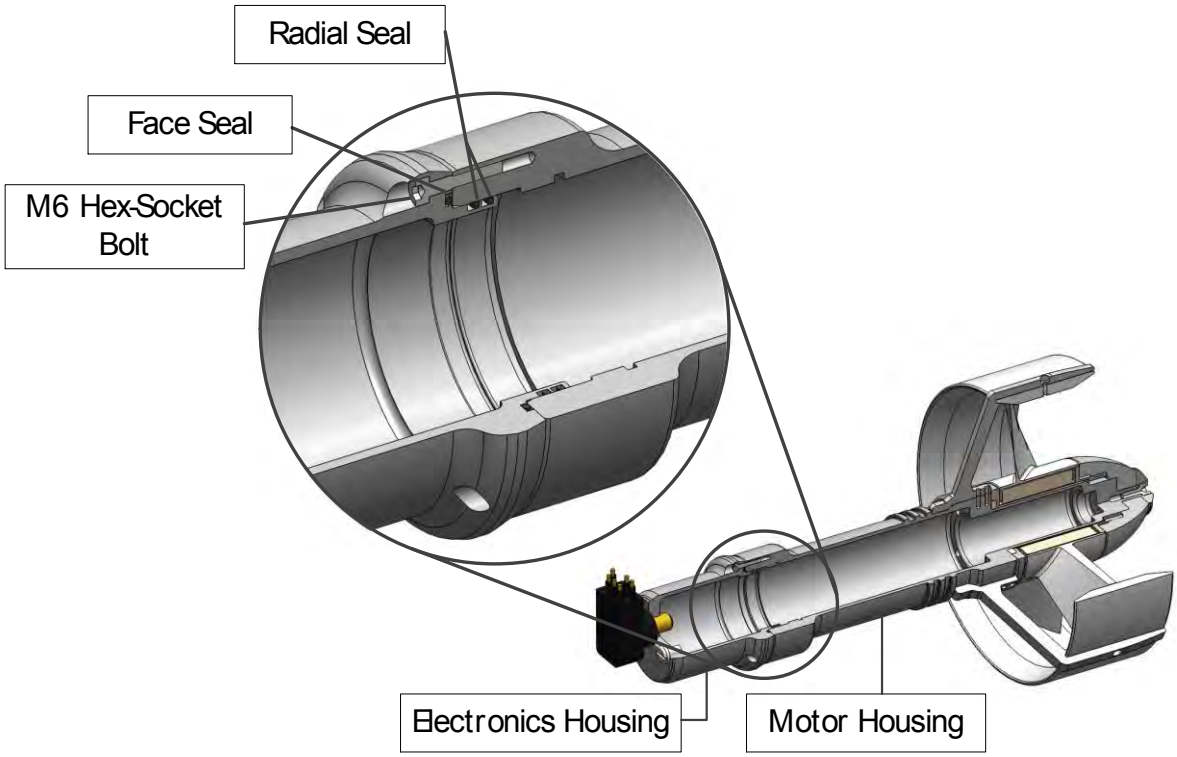

Figure 26 - Thruster Housing – Connection Design Diagram

The functions of the thruster housing are:

- to protect the electronics and drivetrain from water ingress
- to structurally protect the electronics and drivetrain from the pressures experienced at depth
- to serve as the magnetic coupling membrane
- to mount the propeller and kort-nozzle

An ideal thruster housing weighs as little as possible, does not collapse at the maximum operating depth and is corrosion resistant.

The thruster housings are manufactured from stainless steel 316. Stainless steel 316 is an austenitic chromium-nickel stainless steel that contains molybdenum. The molybdenum increases the material's corrosion resistance and its resistance to pitting in chloride solutions (such as seawater) therefore stainless steel 316 is commonly used for marine applications [23]. Stainless steel 316 has a 0.2% yield stress of 290 MPa therefore it is strong enough to use in high pressure situation without making the wall thickness impracticably large.

The method used by T. Knight to calculate the housing wall thickness is detailed in *Mechanics of Materials 1* in the chapter "Thin Cylinders and Shells" [24].

Several issues exist with this method and the assumptions made:

- this method is generally used for cylinders exposed to internal pressures [24]
- a yield strength of 205MPa was used for stainless steel 316 (instead of 290 MPa) [23]
- for conservative simplification of the calculation the housing was assumed to be infinite in length [20]

These choices contributed to the wall thickness being excessively thick and therefore increased the weight of the housing.

5.4.2 Preferred Method to Calculate Housing Wall Thickness

For vessels under external pressure a preferred method is detailed in the *Manual for the Design of Ferrous and Non-Ferrous Pressure Vessels and Tanks* in the chapter "Cylindrical Vessels under External Pressure". The US Experiment Model Basin method is recommended for the design of pressure vessels that are shorter than the critical length. The critical length is defined as the minimum length beyond which the resistance of the tube to collapse due to external pressure is independent of the length of the tube [25].

For its respective dimensions the thruster housing is shorter than the critical length and therefore the US Experimental Model Basin Method was used. The method, formula and calculations can be found in Appendix A.

The maximum operational depth is defined as 300 m. The parameters used to calculate the housing were:

- Maximum depth – 450 m
- Safety factor of 2
- Fluid density of sea water – 1029 kg/m^3

These were the same parameters used by T. Knight and R. de Smidt to design the other modules for the Seahog. The calculations resulted in a 1.3 mm decrease in wall thickness from 2.5 mm to 1.2 mm.

5.4.3 Housing Connection Design

A large portion of the weight of the housing is located where the electronics housing and motor housing fasten together. The use of six M3 hex-socket bolts and the face seal required a flange design which consequently added material.

An alternate method of fastening the housings was designed. This method is shown in Figure 27 and Figure 28. The design utilises a stainless steel connector ring that is located on the electronics housing and mates with a thread turned onto the motor housing. A locating key was used to prevent the two housings rotating relative to each other. This design removes the flange required for the bolts and the face seal. This method of connecting the housings was adapted from designs used to connect logging tools used to log oil and gas exploration wells in the oil and gas industry.

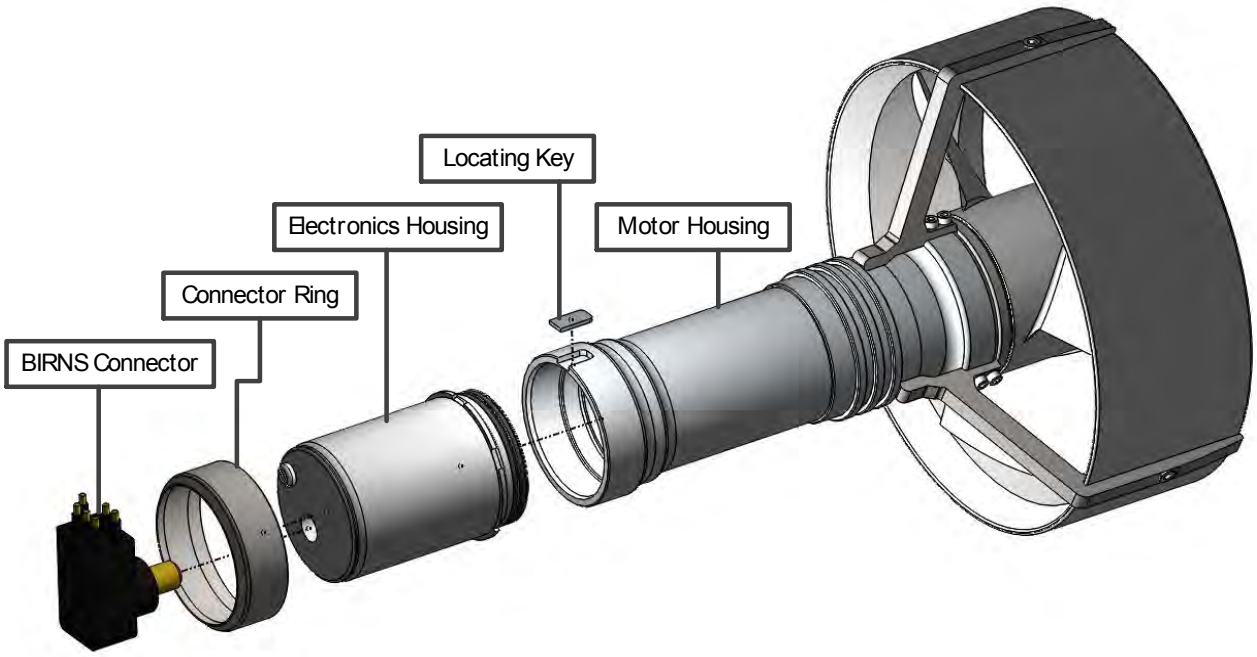

Figure 27 - Thruster Housing - Exploded View of Connection Design

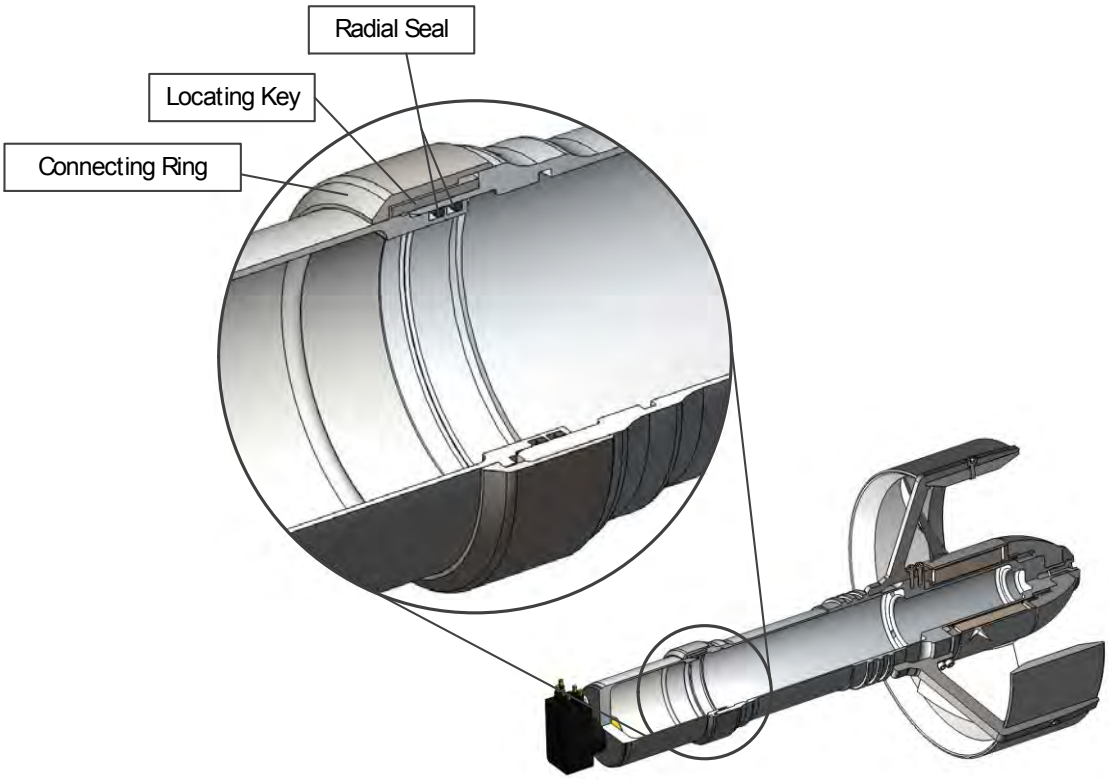

Figure 28 – Thruster Housing - Modified Connection Design Diagram

Six keyways were milled into the electronics housing to allow for the same flexibility of the electronics housing's orientation as the original design.

5.4.4 Total Mass Reduction of the Housing

The consequential weight saving from recalculating the thruster housing wall thickness and modifying the connection design is shown in Table 10. Additionally Table 10 details the weight saved on the ROV due to these modifications.

Table 10 - Modified Housing Weight Summary

Part	Original Weight		Modified Weight	
Motor Housing	1465	g	996	g
Electronics Housing	515	g	286	g
Fasteners	10	g	-	
Connection Ring	-		51	g
Locating Key	-		2	g
Total	1990	g	1335	g

Summary	Weight	
Total Saving per Thruster Module	655	g
Total Saving for Propulsion System	3275	g
Weight of Buoyancy Material no Longer Required	890	g
Total Weight Saving for ROV	**4165**	**g**

This modification resulted in a 33% and 13.6% weight saving for the thruster housing and thruster module respectively. Because of this an indirect weight saving of 890 g of buoyancy material was achieved (material no longer required to provide buoyancy for the previous housing design). This therefore reduced the ROV's total weight by 4.8%.

5.5 Conclusion to the Thruster Module's Mechanical Modifications

Figure 29 shows the cross-section of the final thruster module design. The change in gearbox resulted in the drivetrain being longer than in the previous thruster module. A new heatsink was designed to be solid and to heatsink the gearbox as opposed to the ribbed heatsink in the original thruster module (this can be seen in Section 4.2) that only provided heatsinking to the motor.

With the new housing connection, modified housing, gearbox change and new heatsink the thruster module has a mass of 4.2 kg.

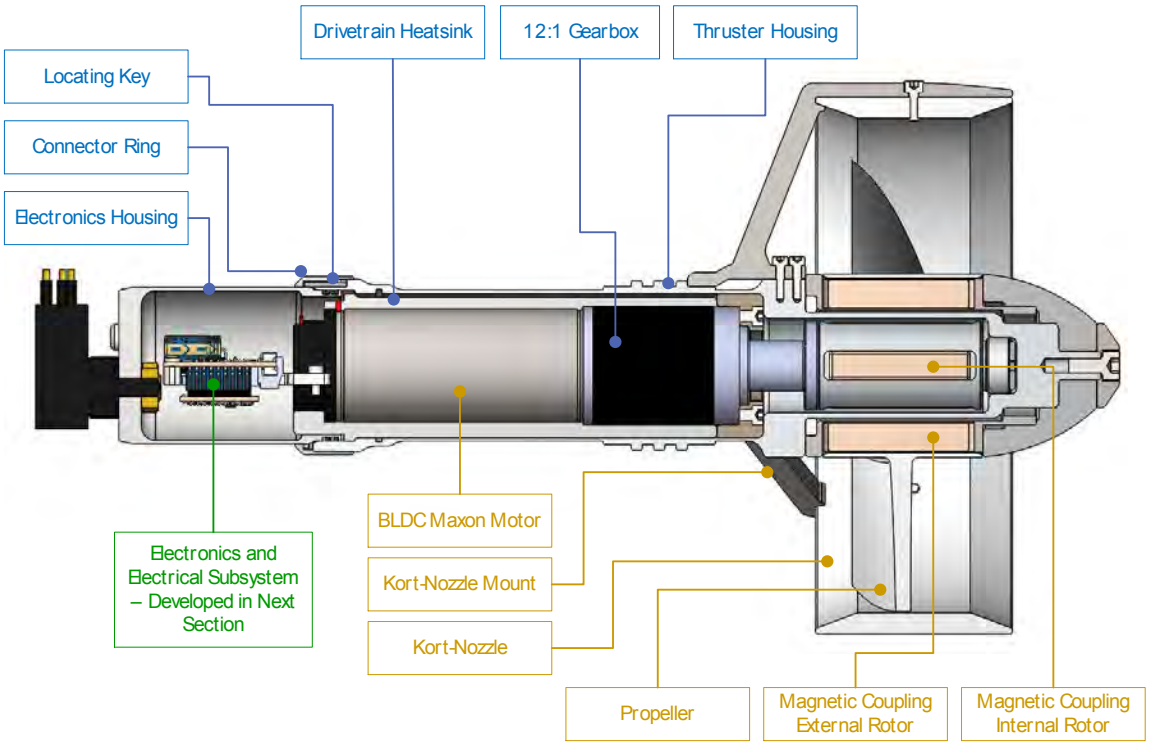

Figure 29 - Thruster Module Cross-Section

5.6 Thruster Electronics and Electrical Subsystem

5.6.1 Introduction

The thruster electronics are situated in the electronics housing of the thruster module behind the motor assembly as seen in Figure 30. The electronics comprises of two PCBs; one custom built communications and control board and one Maxon DEC 50/5 motor controller board.

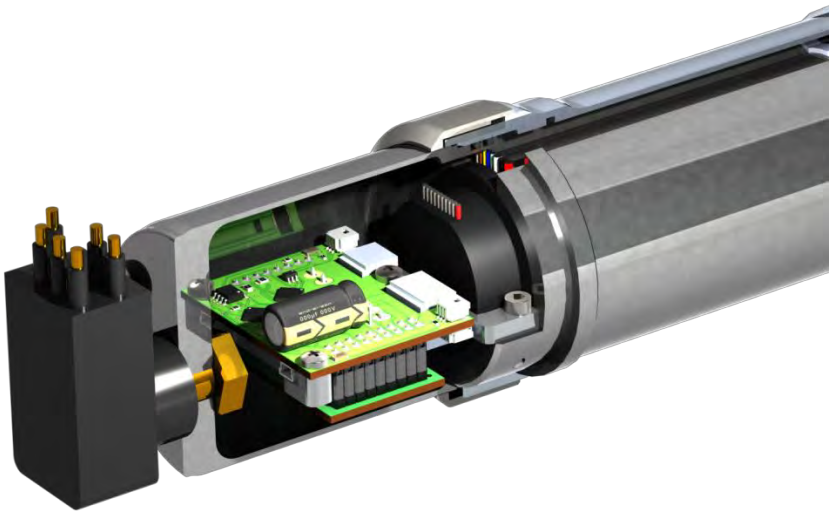

Figure 30 - Thruster Module Electronics System

This section shows the design process used to develop the communications and control board that interfaces the Maxon motor controller board with the ROV. In the beginning of the chapter the initial specifications for the electronics of the thruster module are discussed followed by the motor controller selection. Then the development of a prototype communications and control PCB to interface with the Maxon motor driver board is detailed. The final communications and control PCB is presented followed by the software flow diagram for the embedded microcontrollers.

5.6.2 Thruster Electronics Specifications

Table 11 details the thruster electronics' specifications expanding on the thruster module specifications table found in Section 5.2. The specifications below are a combination of essential and desired functions that the electronics should have for the thruster module. Each specification choice is explained to justify the design decisions made.

Table 11 - Thruster Electronics Specifications

Index	Design Requirement	Value
Motor Driver Board		
5.6.1	BLDC Motor Driver	Yes
5.6.1	Power Rating	>120 W
5.6.1	Voltage Supply	48 V
5.6.1	Continuous Current Supply	4.1 A
5.6.1	Maximum Speed	>10 100 rpm
5.6.2	Capable of Fitting Inside Thruster Housing	Yes
Communications and Control Board		
5.6.3	Voltage Supply	12 V / 15 V
5.6.4	Over Voltage Protection	Yes
5.6.5	Over Current Protection	Yes
5.6.6	Reverse Bias Protection	Yes
5.6.7	Communications Protocol	RS-485
5.6.7	Addressable Communication	Yes
5.6.8	Speed Feedback	Yes
5.6.8	Closed Loop Control Capable	Yes
5.6.9	Temperature Sensing Feedback	Yes
5.6.2	Capable of Fitting Inside Thruster Housing	Yes

5.6.1 The thruster module's motors are the Maxon 120W BLDC EC-Max. 40 motor with the following specifications listed in Table 12.

Table 12 - Maxon EC-max. 40 Motor Specifications [22]

EC-max. 40 BLDC Maxon Motor	
Specification	**Value**
Part Number	283870
Power Rating	120 W
Voltage Supply	48 V
Max. Continuous Current	4.06 A
No Load Speed	10100 rpm

Therefore a BLDC motor controller board capable of powering the EC-max. 40 motor is required

5.6.2 All the thruster electronics must fit inside the existing housing. It was essential that the electronics be located inside the thruster module. The Seahog was designed to have distributed intelligence and the thruster modules must adhere to this design philosophy.

5.6.3 The voltage supplies available from the electronics pod designed by R. de Smidt are:

- +5 VDC
- +12 VDC / +15 VDC (on the same conductor and configured by the operator)
- 48 VDC (motor power supply)

With +5 VDC being susceptible to noise generated along the cables that run to the thruster module from the electronics pod and being more likely to drop below the

threshold of the voltage regulators for the embedded microcontrollers it was decided that either the +12 VDC or +15 VDC supplies be used. With the flexibility of either being used it eliminates the possibility of an operator damaging the board if the wrong voltage supply is selected.

5.6.4 The thruster electronics must be capable of withstanding an over-voltage occurrence without the entire board being replaced.

5.6.5 If a short circuit condition occurs due to either a mechanical short, failed component or partial water ingress it is desired that the electronics is recoverable.

5.6.6 The electronics must not be damaged in the case of the accidental reverse connection of the power supplies.

5.6.7 The ROV's current communication protocol uses RS-485 serial communication between modules. The thruster modules must conform to the Seahog's communication network. Each thruster module must be individually addressable for control purposes.

5.6.8 The ROV control system and the operator must have access to accurate speeds of the thruster modules. The thrusters must incorporate closed loop speed control that is adjustable either through re-programming of the embedded microcontrollers or remotely by the operator during thruster initialisation.

5.6.9 The temperatures of the motor and electronics (gearbox optional) must be available to the operator in the case of the thruster module overheating. An automatic over-temperature shut down sequence is essential to avoid damage to the motor or electronics.

5.6.3 Thruster Electronics Overview

The exploded assembly view of the thruster electronics in Figure 31 shows the mounting and placement of the thruster electronics' PCBs. All the power and signal lines from the ROV are connected to the communications and control PCB. The communications and control PCB serves as the motherboard for the Maxon motor controller.

All RS-485 communications from the ROV are processed by the communications and control PCB. The pertinent information is processed and an appropriate desired motor speed and direction is passed onto the Maxon motor controller. All of the Maxon motor control board configuration options are controlled by the communication and control PCB. The Maxon motor controller outputs a speed signal that is captured by the communications and control PCB and sent back to the ROV and operator. This speed value is also used for speed feedback and closed loop speed control. The thruster electronics do not include current sensing; the thruster current is measured inside the electronics pod of the ROV and relayed back to the operator.

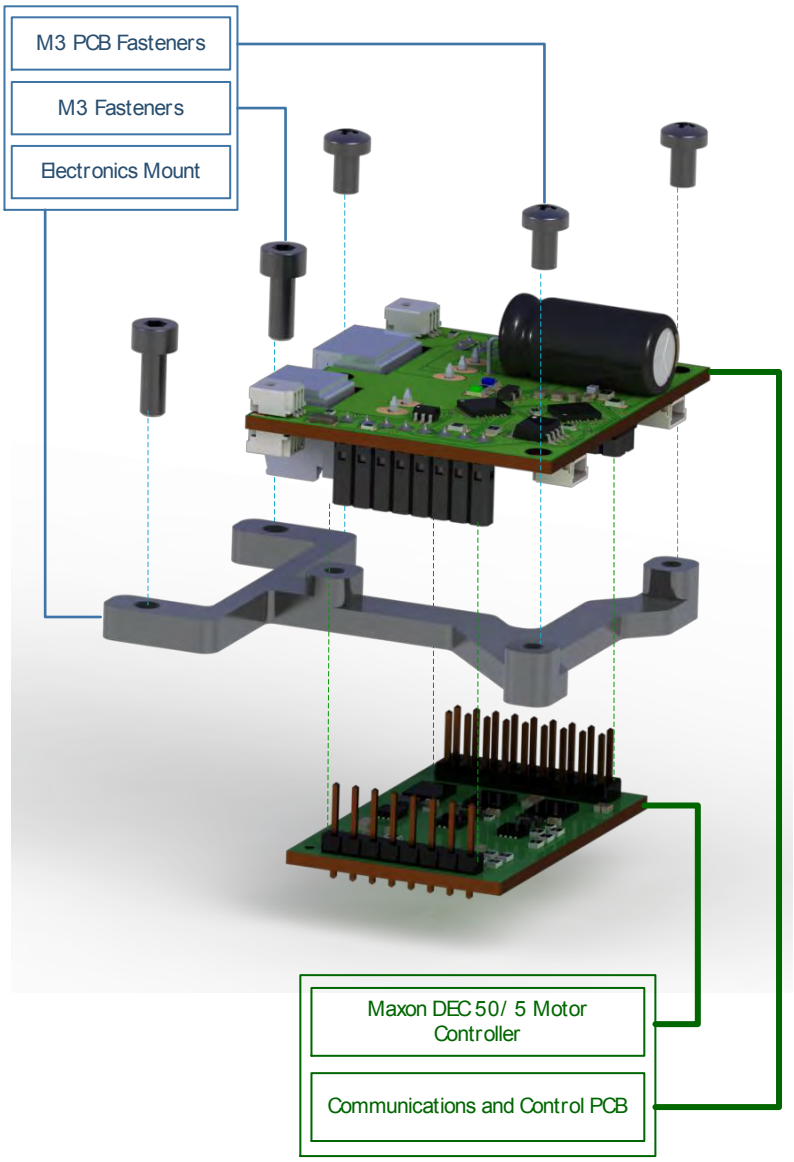

Figure 31 - Exploded View of Thruster Electronics Assembly

5.6.4 The Maxon Motor Controller PCB - DEC Module 50/5

When the thruster module was first developed, all the Maxon motor controller boards suitable for the BLDC motor were too big to be located in the thruster housing. Therefore custom built controller boards were developed however these boards proved to be inefficient and unreliable. In 2014 Maxon released the DEC Module 50/5 Motor Controller which was capable of being located inside the existing thruster electronics housing, the dimensions are shown in Figure 32. As can be seen in Table 13, the DEC Module 50/5 Motor Controller is perfectly suited to the EC-max. 40 motor's requirements.

Table 13 - Controller and Motor Compatibility [22]

Specification	EC-max. Motor		DEC 50/5 Controller	
Part Number	283870		380200	
Type	BLDC		BLDC	
Power Rating	120	W	250	W
Voltage Supply	48	VDC	50	VDC
Max. Continuous Current	4.06	A	5	A
Maximum Speed	10100	rpm	80000	rpm

The DEC Module 50/5 Motor Controller has the following features:

- closed loop speed control
- protective features:
  - under and over voltage protection
  - voltage transient protection
  - short-circuits in motor cables
  - blockage protection
- two analogue inputs to control:
  - motor speed
  - operating current limit
- four digital inputs that control:
  - enable
  - direction
  - and speed range
- two digital outputs that feedback:
  - motor speed
  - ready status

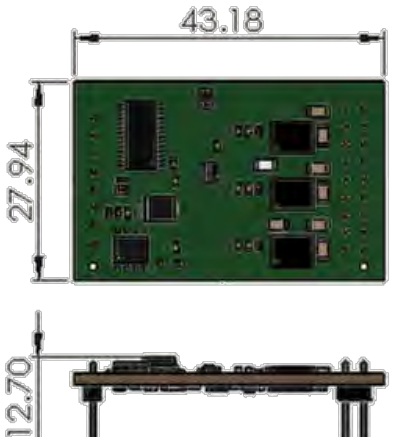

Figure 32 - DEC 50/5 Maxon Motor Controller Dimensions (mm)

5.6.5 The Communications and Control PCB

In order to interface the Maxon motor controller board with the predefined ROV system the PCB had to be capable of:

- receiving addressable RS-485 communications
- sending speed, temperature and status values via RS-485
- reading speed values from the Maxon motor controller
- perform closed loop speed control
- control and operate all the features available on the Maxon motor controller board

The communications and control board features include:

- power supply conditioning for the Maxon motor control board
- over current protection for the Maxon control board
- power regulation for the microcontrollers
- over current protection for the microcontrollers
- RS-485 serial communication IC
- passive filters for temperature sensor signals
- 10-bit **D**igital-to-**A**nalogue **C**onverter (**DAC**) for motor speed control

Figure 33 shows a schematic of the thruster electronics system and the various functions and subsystems within it. This is followed by summarised descriptions of the subsystems.

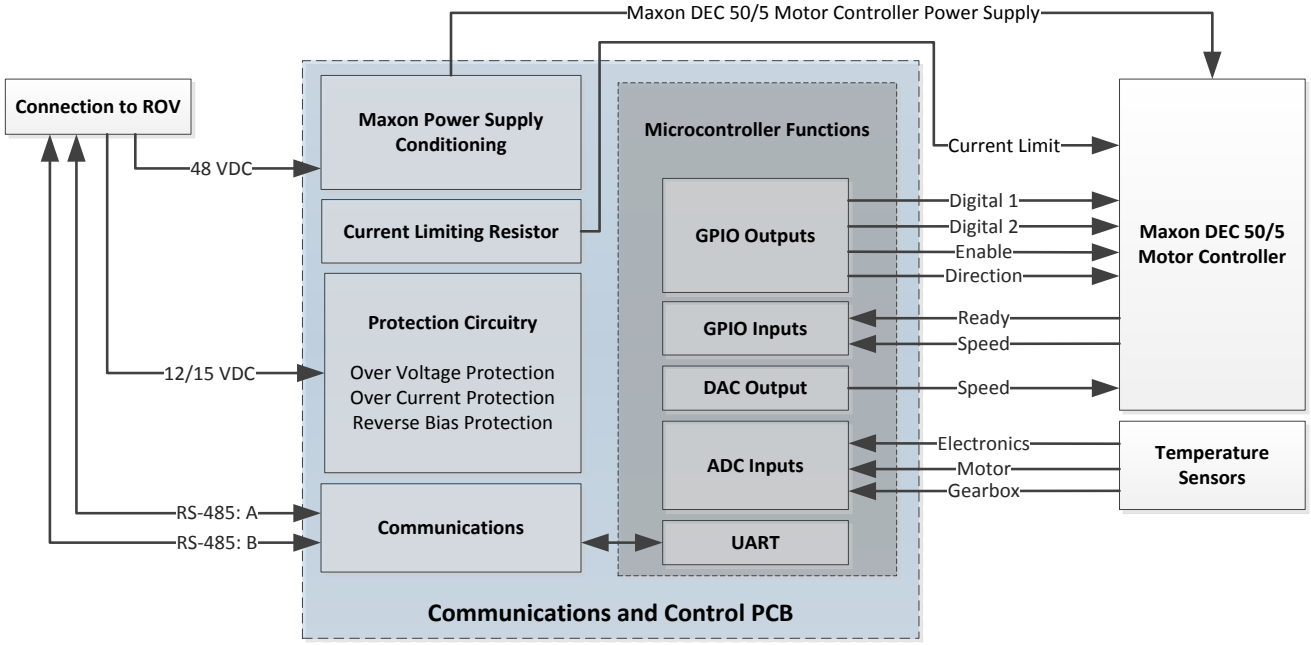

Figure 33 - Schematic of Thruster Electronics System

5.6.6 Maxon Power Supply Conditioning

The DEC50/5 motor controller power supply conditioning circuitry consists of a 7 A fuse with a capacitor and transient voltage suppressor connected to ground. This is the protection circuitry recommended by Maxon and taken directly from the motor controller's operation manual.

5.6.7 Current Limiting Resistor

The DEC 50/5 motor controller board has an option to limit the current draw of the motor by connecting a resistor to the respective analogue input on the board.

5.6.8 Protection Circuitry

The protection circuitry for the rest of the communications and control PCB consists of a 125 mA fuse connected to a crowbar circuit that activates for supply voltages above 16 VDC. The reverse bias protection is achieved with a diode. The schematic for this circuit can be seen in Figure 34. In the case of an over voltage occurrence the Zener diode will conduct current that will activate the thyristor and consequently connect the supply to ground. This condition will rapidly raise the current and blow the fuse therefore severing the circuit from the supply and protecting the electronics beyond this point.

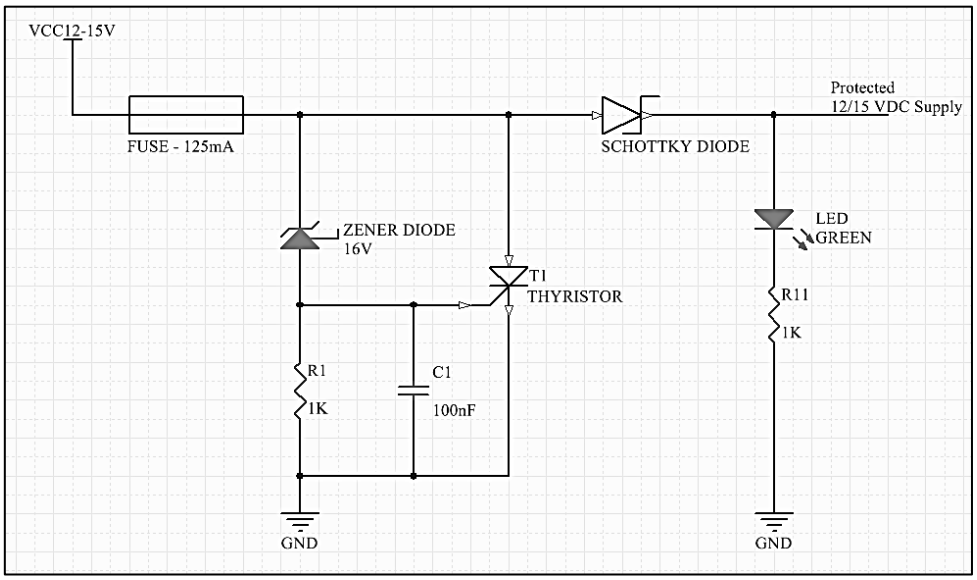

Figure 34 - Protective Circuitry - Crowbar Circuit

5.6.9 Communications

The network method chosen to communicate data amongst the modules of the ROV was the RS-485 multipoint network. The transmission lines are differential in nature and consist of two twisted wires A and B. Being a multipoint network, multiple transmitters and receivers can be connected to the line (in this case the various modules and subsystems of the Seahog). With the signals on A and B being differential and the wires being a twisted pair this allows an RS-485 network to transmit data on cables up to 1500 m long and at transfer speeds of up to 100 kbps. Higher transmission rates can be achieved with shorter cables. Only one transmitter may be active at any given time. All the nodes on the communication line that are not transmitting can access and receive the transmission [26].

A MAX3485 IC was used to convert the RS-485 differential signals into 0-3 V UART serial signals. UART is a common serial communication module built into many microcontrollers. With multiple nodes on an RS-485 network, the communication protocol used has to incorporate addressed packages allowing the nodes to identify the relevant messages from the messages intended for other nodes. This results in the node (in this case a thruster module) being interrupted every time a byte is received via the RS-485 IC, even though the information relevant for that nodes is only sent periodically.

5.6.10 Microcontroller Functions

The microcontroller functions entailed:

- communicating with the ROV via UART
- controlling the **G**eneral **P**urpose **I**nput / **O**utput (**GPIO**) inputs into the motor controller
- reading the GPIO outputs from the motor controller
- reading the analogue signals from the temperature sensors
- producing an analogue voltage to control the motor speed

GPIO Outputs

The microcontroller must control the four digital inputs into the motor controller board. These control the enabling of the motor controller, the direction of the motor and the speed control method used.

GPIO Inputs

The microcontroller must be able to read a 'ready' GPIO input from the motor controller. This state will be set high in the case of either an overheating situation, problem with the power supply or a motor fault. The second GPIO input must be able to capture the speed signal from the motor controller. The speed signal is sent in the form of a square wave with the frequency being a function of motor speed. This requires a timer module to capture the period of the signal and calculate the motor speed.

DAC Output

An analogue voltage ranging from 0 V-5 V was used to control the speed of the motor. The motor controller accepts 0 V -5 V with 10-bit resolution.

ADC Inputs

Three **a**nalogue-to-**d**igital **c**onverter (**ADC**) channels are required to read in the outputs from the temperature sensors. LM60 temperature sensors were selected to monitor the motor, gearbox and the electronics temperature.

5.6.11 Microcontroller Selection

The two processor intensive functions were identified as receiving, processing and transmission on the RS-485 communication bus and the closed loop control of the motor. Therefore for reliability and robustness it was decided to use two embedded microcontrollers; one dedicated to communications and temperature sensing, the other to motor control.

The microcontroller selected was the MSP430 manufactured by Texas Instruments. The specifications are listed in Table 14.

This microcontroller does not have a built in DAC module therefore it was decided to use an external DAC IC and commands were sent to the DAC IC via SPI.

Non-specification factors that contributed to the chip selection were the relative low cost of the microcontroller (five times cheaper than the LM3S8962 used in the original thruster module) and the fact that it was a processor being used at RARL for other robots therefore maintaining hardware consistency and standardisation of the equipment used at RARL.

Table 14 - MSP340-G2 Summarised Specification Table

General Information		
Manufacturer: Texas Instruments Product Code: MSP430 G2553 IRHB32R Supply Voltage Range 1.8 - 3.6 V 16-Bit RISC Architecture 62.5 ns Instruction Cycle Time 16 MHz Internal Clock Package Selected: QFN 32 Pin		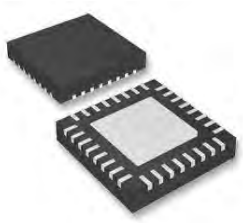
Module Summary		
Module	Number per Microcontroller	Additional Information
GPIO	24	Capacitive-Touch Enabled
UART	2	Auto Baudrate Detection
SPI	2	
I^2C™	1	
ADC	1	10-Bit at 200 ksps, 8 Channels
16-Bit Timers	2	3 Capture Registers per Timer
All information obtained from the MSP430G2x53 Datasheet [27]		

5.6.12 Communications and Control PCB Layout

Figure 35 shows the functional schematic of the thruster electronics with emphasis on the communications and control PCB. It is followed by the pin-out diagrams for the communications and control board in Figure 36.

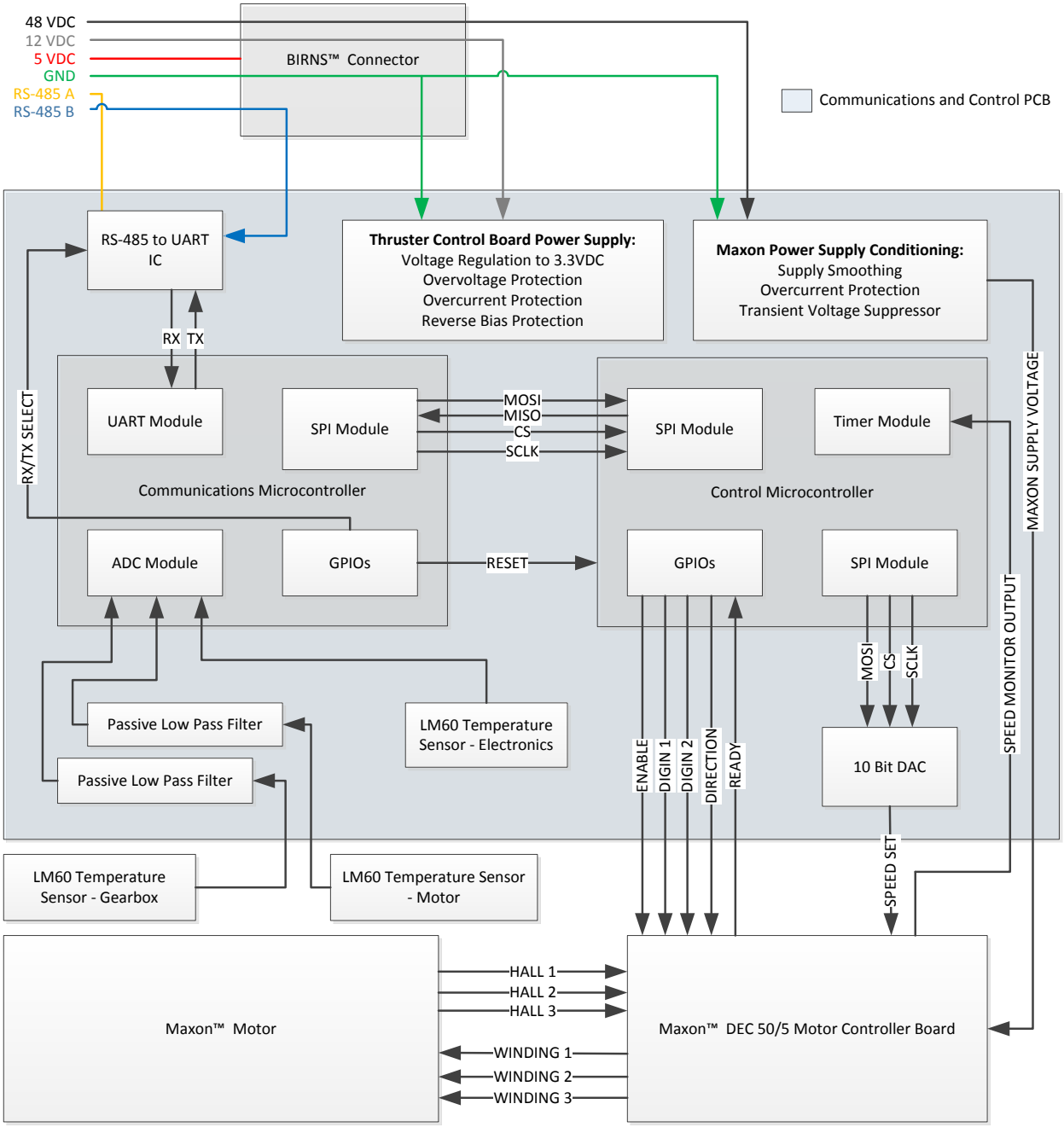

Figure 35 - Functional Schematic of Thruster Electronics

As can be seen in Figure 35 two additional features were added to the communications and control PCB:

- two passive filters to remove the noise generated along the temperature sensor wires that run to the motor and gearbox
- the communications microcontroller can reset the control microcontroller remotely

The pin-out diagram for the communications and control PCB can be seen in Figure 36.

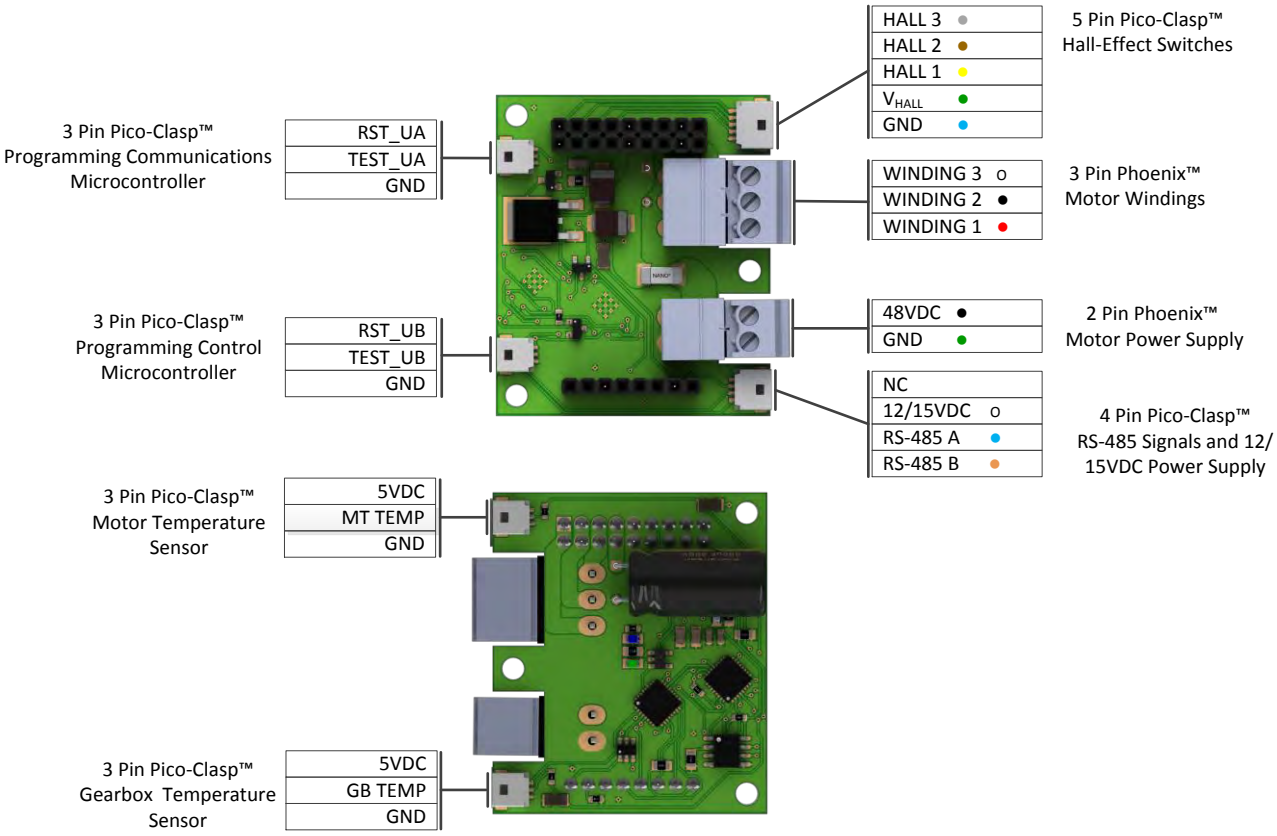

Figure 36 - Communications and Control PCB Pin-out Diagram

5.6.13 Programming of the Two Embedded Microcontrollers

The programming connectors for the two microcontrollers were designed to be easily accessible to the operator in the need of code modification or reprogramming. Figure 37 shows the communications microcontroller being reprogrammed. Only the electronics housing has to be removed. Both microcontrollers can be programmed using Texas Instrument's MSP430G2 development board.

Figure 37 - Programming of the Communications and Control PCB

5.7 Thruster Communications and Control Software

5.7.1 Introduction

This section details the data flow and format for the communication to the thruster module. An overview of how the system integrates with the ROV is discussed and compared to the system used for development. The data flow is shown from the operator console through to the control processor and back. Error checking of the communications is discussed and a flow diagram presented. The chapter ends with the control method used and presents speed test results that contributed to the control system's development.

5.7.2 Communication System Overview

Figure 38 shows how a thruster module is integrated into the ROV system regarding communications. The operator console communicates via Ethernet to a fibre optic media converter that sends the information along the fibre optic tether. The fibre optics pass through a junction box and into the electronics pod (E-Pod) of the ROV. A fibre optic media converter installed in the electronics pod converts the communications into RS-485. The RS-485 network is connected to all sub-systems except the sonar unit (that is connected to a separate RS-232 network). Each module has its own two byte unique identification that is used to address it. This system was developed by R. de Smidt and is under continued development by M. Finbow at the time of this dissertation.

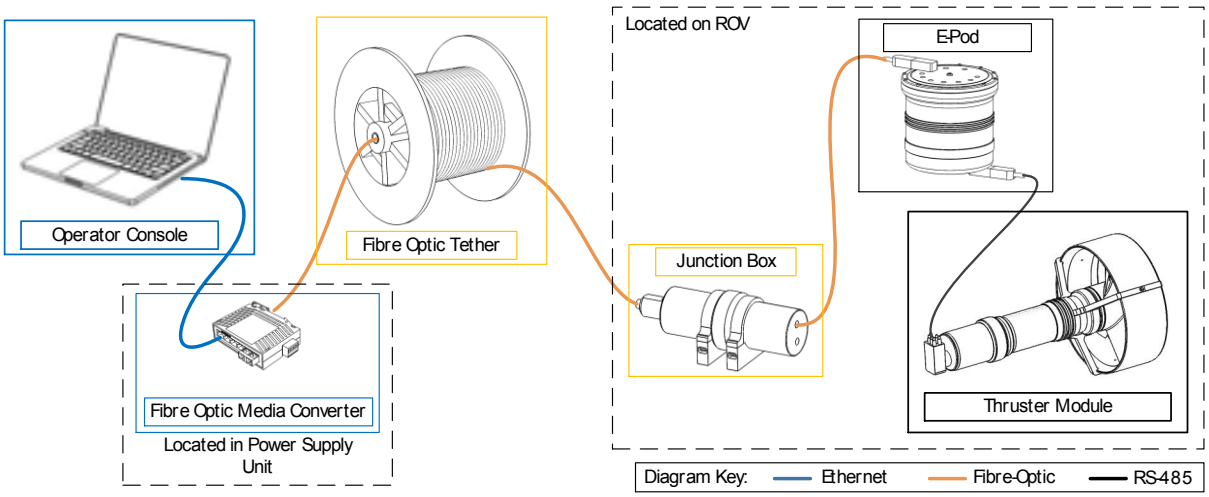

Figure 38 - Thruster Module Communication Diagram with respect to ROV System

Figure 39 shows the simplified system used for development of the thruster modules. This simplified setup removes the fibre optics and electronics pod. The information is converted from the USB serial port to RS-485 with a 'USB2Dynamixel' converter.

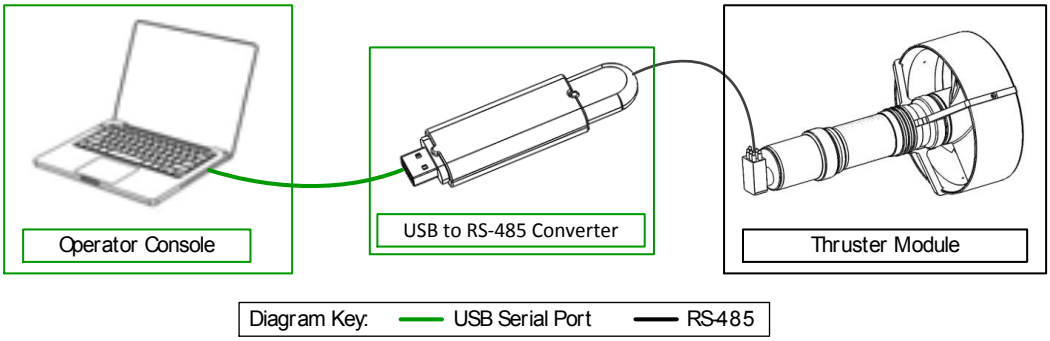

Figure 39 - Simplified Communication Network for Thruster Module Development

5.7.3 Data Flow and Communication Protocol

The data flow diagram shown in Figure 40 is applicable to both the simplified communication layout in Figure 38 and the ROV communication network in Figure 39. Blue data lines represent information being sent to the thruster module and the red data lines represent the information being sent from the thruster module to the operator console.

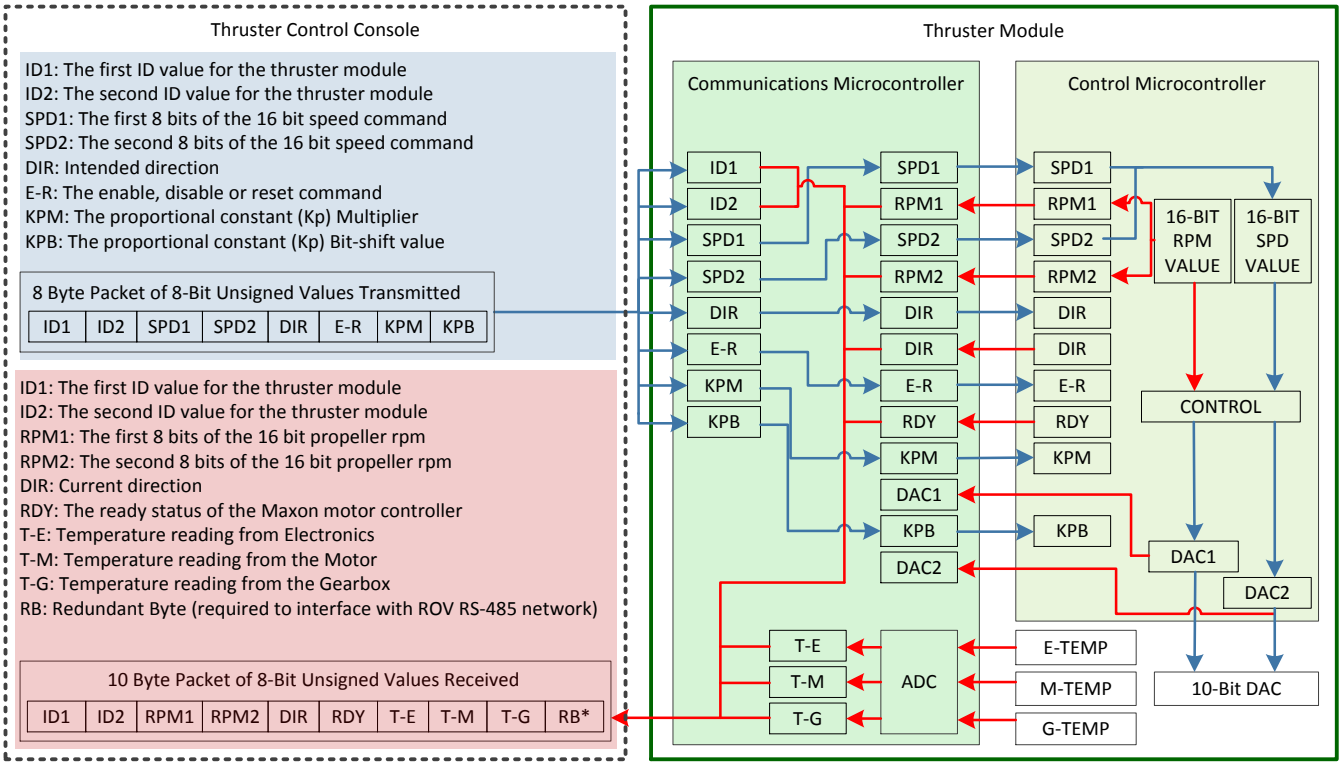

Figure 40 - Data Flow Diagram between Operator Console and Thruster Module

An eight byte addressed packet is sent to the thruster module. The communications microcontroller receives this data only if the address matches its preprogramed identification. The communications microcontroller replies with the information it has received from the control microcontroller. The direction, speed and control information is sent via SPI to the control microcontroller. Because of the synchronous setup of SPI communications the motor controller data is sent to the communications microcontroller at the same time. Once the new data has been processed and added to the control loop the control microcontroller sends two 8-bit values (that

combine into one 10-bit value) to the 10-bit DAC IC via SPI. In the event that a communication was not received by the control microcontroller for a period of 3 seconds the control-processor sends a zero speed value and a disable command to the Maxon motor controller board.

5.7.4 Estimated Communication Speed

Table 15 shows the communication speeds and calculated times for each step, which is based on baud-rate alone and does not include processing time with regards to error-checking and general processing functions. Additionally this only includes the communication steps within the scope of this dissertation therefore removing the fibre optics system featured in Figure 38. A communication's speed test is completed in Section 6.3.2.

Table 15- Estimated Communication Time

Network	Transmitter	Receiver	Bytes	bps	ms
RS-485/UART	Operator Console	Thruster Module	8	115200	0.556
UART/RS-485	Thruster Module	Operator Console	10	115200	0.694
SPI	Between Microcontrollers		6	500000	0.096
SPI	Microcontroller	DAC IC	2	500000	0.032
Total					**1.378**

5.7.5 Error-Checking

The thruster module performs error checking at each step of communication shown in Figure 40. The RS-485 communications received from the ROV and transferred into UART levels are checked once the whole packet has been received by the communications microcontroller.

The SPI communications between the microcontrollers required error-checking after every received byte to decrease the overall time required to transmit a correct packet of data. This step-wise error-checking is shown in the flow chart in Figure 43. Once a bad value has been received the entire transmission is restarted. This method was quicker than waiting for all the bytes to be exchanged to begin the error-checking process. This is the reason 8-bit **c**yclic **r**edundancy **c**heck (**CRC**) was not implemented as this requires the entire packet to be received before the check-sum polynomial can be applied. Each value was assigned its own range of valid values in which the transmitted value must be within. Figure 41 and Figure 42 show the patterns the data has to achieve to be accepted. These patterns drastically reduce the chances of errors being transmitted and accepted via SPI.

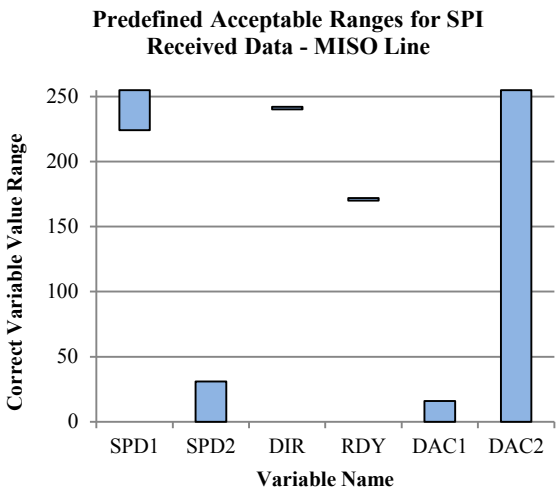

Figure 41 - Accepted MISO Values

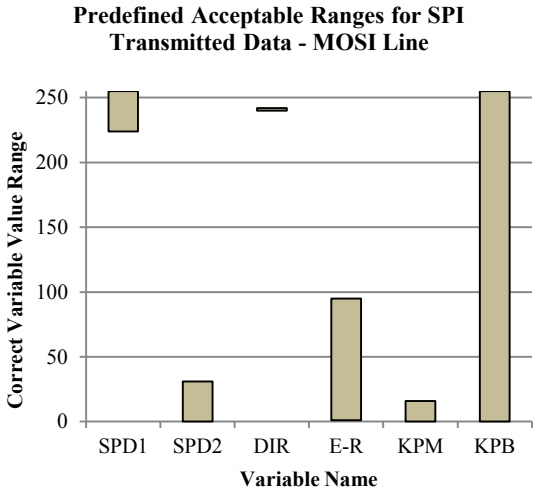

Figure 42 - Accepted MOSI Values

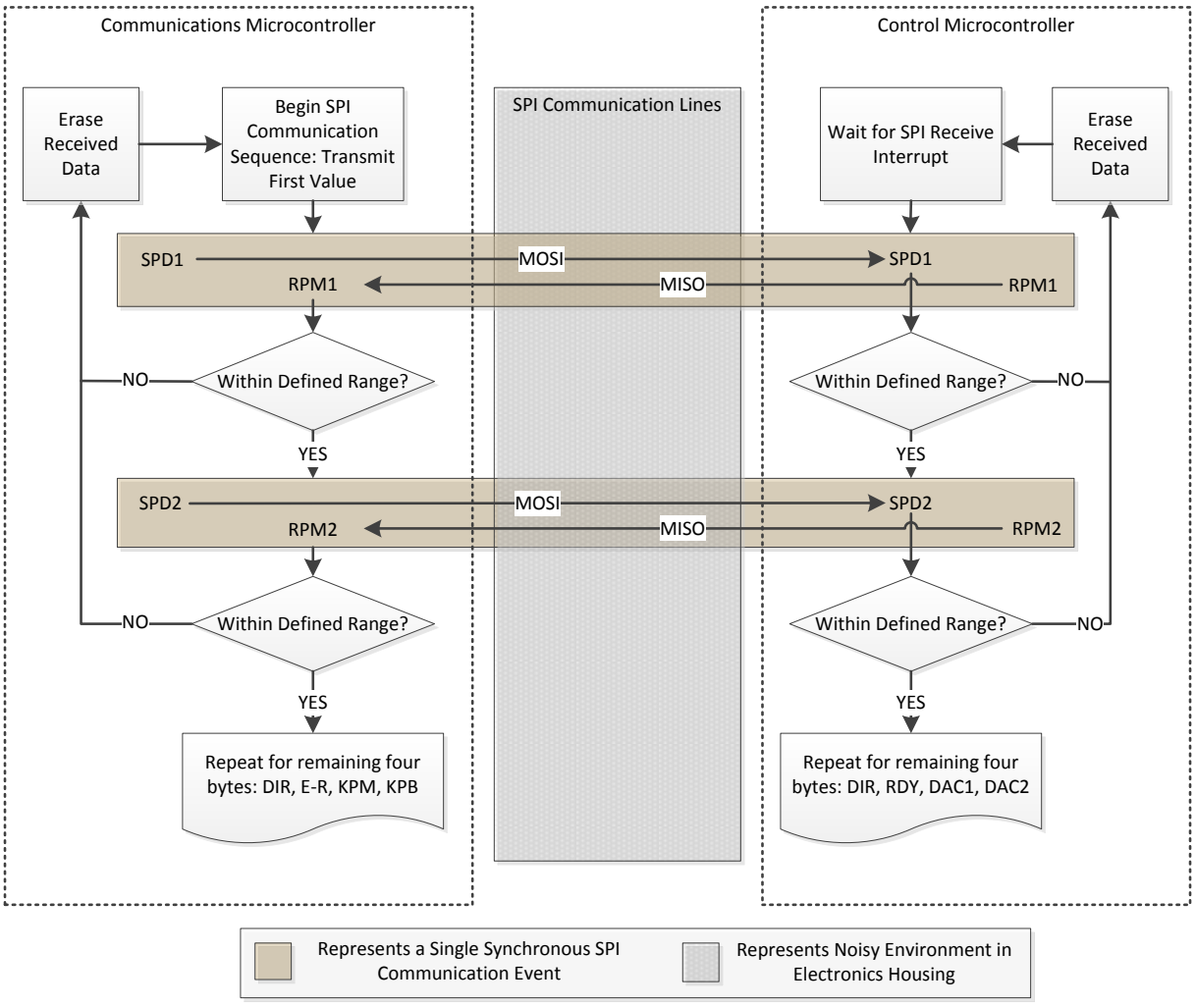

Figure 43 - SPI Error-Checking Flow Chart

5.7.6 Closed Loop Speed Control

Introduction

Specification 5.2.4 stated that the difference between the thruster module's output speed and input speed (speed error) must be below 1% of the input speed. When operating the thruster module using the motor controller's closed loop speed control it was noticed that the speed error was greater than 1% of the input speed. It was decided to calibrate the analogue input into the motor controller according to the output speed to achieve more accurate speeds. However a simple gain and offset calibration was insufficient to produce accurate speeds for the entire speed range of the thruster module. Because of the irregular error in the output speed produced it was decided to achieve accurate speeds by applying closed loop control to the input analogue voltage.

As mentioned before the Maxon motor controller is operated in closed loop control mode, however the input into this system does not have negative feedback. The control microcontroller reads the speed output by the motor controller and this output has no effect on the analogue speed control input into the Maxon motor controller. In essence this section is open loop. This is shown in Figure 44.

The aim is to introduce closed loop speed control on the control microcontroller to read the speed feedback from the Maxon motor controller and closed loop control to determine the next appropriate value to be sent to the motor controller. The change in the control system is shown in Figure 44.

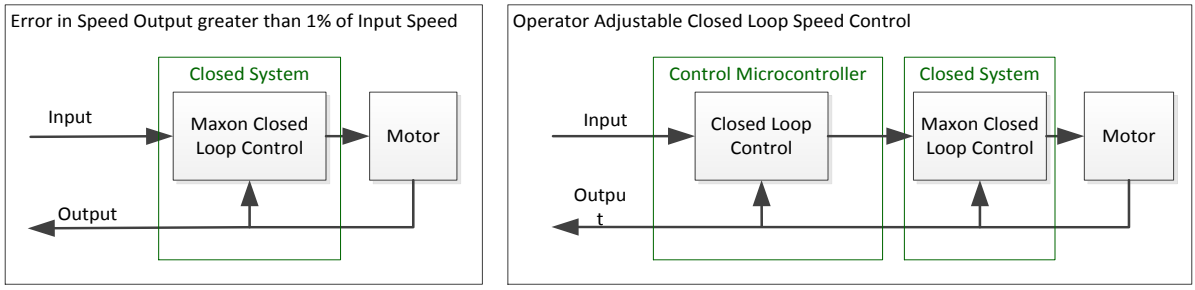

Figure 44 - Maxon Closed Loop Speed Control compared to Operator Adjustable Closed Loop Speed Control

Required Closed Loop Control

The acceleration and response to changes in speed input controlled by the Maxon motor controller board were satisfactory. The issue presented itself in the steady-state speed that was offset from the set-point speed, therefore the scope of the control loop was deemed to only be near the desired set-point speed. Figure 45 shows an example of the motor outputting an incorrect speed and an example of the upper and lower control limits that defined the range the additional closed loop control was applied in.

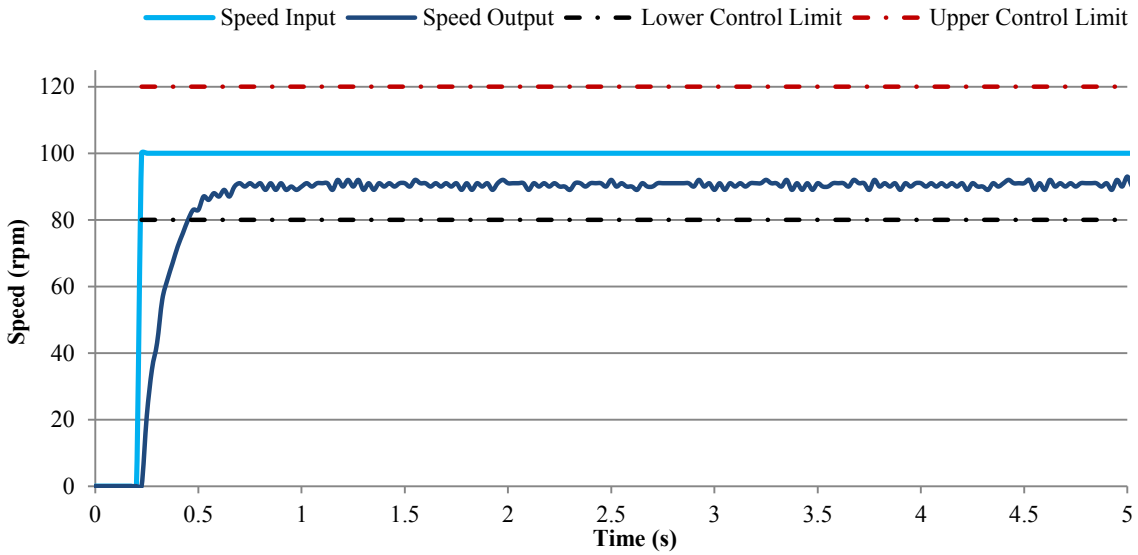

Figure 45 - Example of Erroneous Speed Output and Identified Control Range

The goal of the closed loop control design was to adjust the input into the motor controller to correct for this offset.

Initially a **PI** (**P**roportional-**I**ntegral) controller was implemented, however for all the feasible values of proportional constant (K_p) and integral constant (K_i) the controller caused the output to be oscillatory and sometimes the output oscillated about an arbitrary value as opposed to the set-point. This anomaly was due to the fact that the control loop was only applied in a band above and below the set-point and not over the entire response of the output. Figure 46 shows the functioning of a typical PI controller in a standard situation and Figure 47 shows the response of the standard PI controller when applied to the thruster module's specific situation. As can be seen at point 1 in Figure 47 the PI control loop begins to control the input however the proportional and integral control values produced (at point 2) cause the input signal to decrease and therefore decrease the output, at point 3 the output drops below the control range and the Maxon control resumes at point 4. This pattern repeats and therefore causes the output to oscillate.

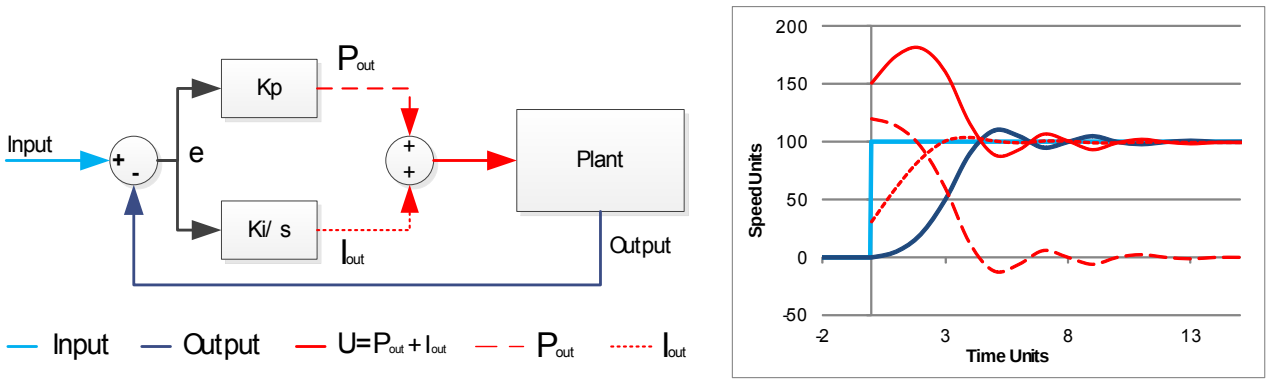

Figure 46 - PI Controller Diagram and Typical Response

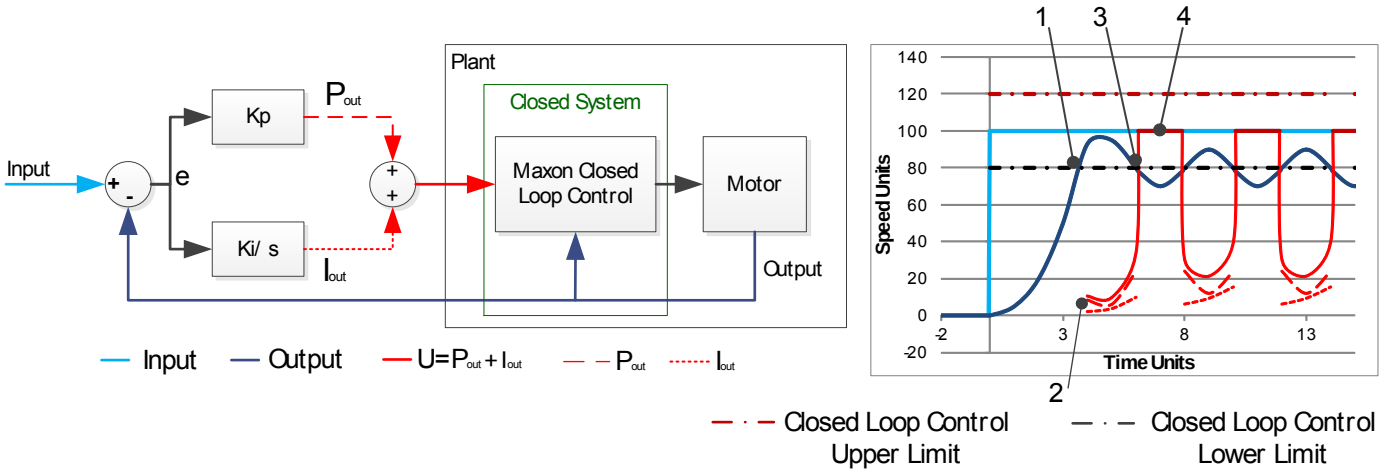

Figure 47 - Implemented PI Controller with Limits and Consequential Oscillation

A review of the system was required and instead of implementing the control system for an uncontrolled system it was decided to correct the offset generated by a controlled system. Figure 48 shows the control implemented to correct for the offset. By summing the adjustment made by the product of the error (e) and the proportional factor (K_p) to the input. The input is therefore corrected to compensate for the offset.

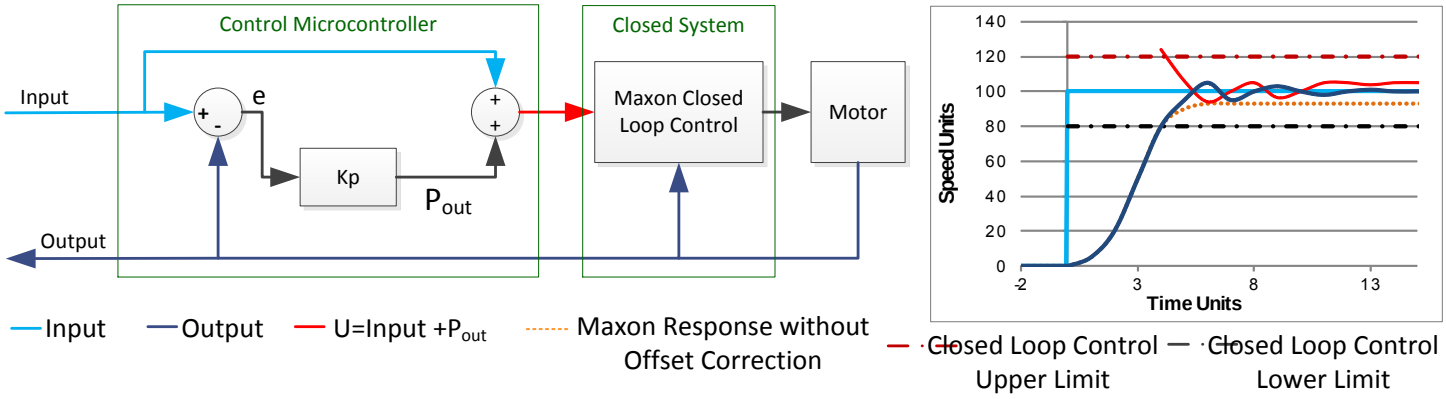

Figure 48 - Offset Correction Implemented on Thruster Module

A low pass filter was added to the output speed to prevent oscillations caused by variance in the output signal.

The K_p was tuned using the Ziegler-Nichols method. This method required the K_p value to be increased until the output began to oscillate, as denoted as K_u. The Ziegler-Nichols method recommends to set K_p to $0.5K_u$ for a P controller [28]. The results of the tuning can be seen in Figure 49. The final recommended K_p was 0.75. This offset correction method is tested in Section 6.2.4.

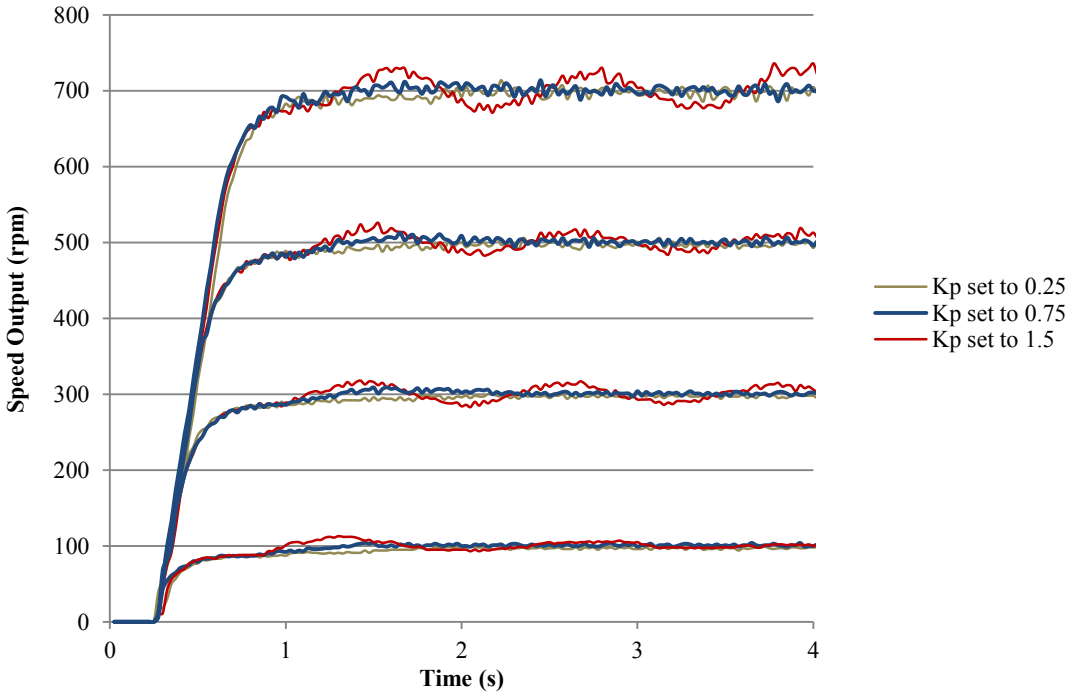

Figure 49 - K_p Tuning of the Thruster Module Offset Correction Control Loop for Multiple Propeller Speeds

6 Thruster Module Tests and Results

6.1 Introduction

This section details the tests done on the thruster module and on its sub-systems. The tests are split into two broad categories; mechanical and electronics performance tests. The results are presented after each test.

6.2 Mechanical Performance Tests

6.2.1 Thruster Housing Pressure Test

Aim

The modification of the thruster housing required that a pressure test equivalent to an ocean depth of 450 m be performed. The pressure test assessed the sealing capability of the two radial O-ring seals and the structural integrity of the housing.

Method

The housing was sent to Marine Solutions (a Cape Town based ROV operator company) to be tested in their pressure test vessel featured in Figure 50.

The housing was tested to the same standard as the pressure tests performed by R. de Smidt for the other pressure vessels on the ROV. The housing was sealed in the pressure test rig and the pressure was increased in 5 bar increments with 10 second pauses to check that the increased pressure was being maintained. The tank was pressurised to 45 bar for 60 minutes.

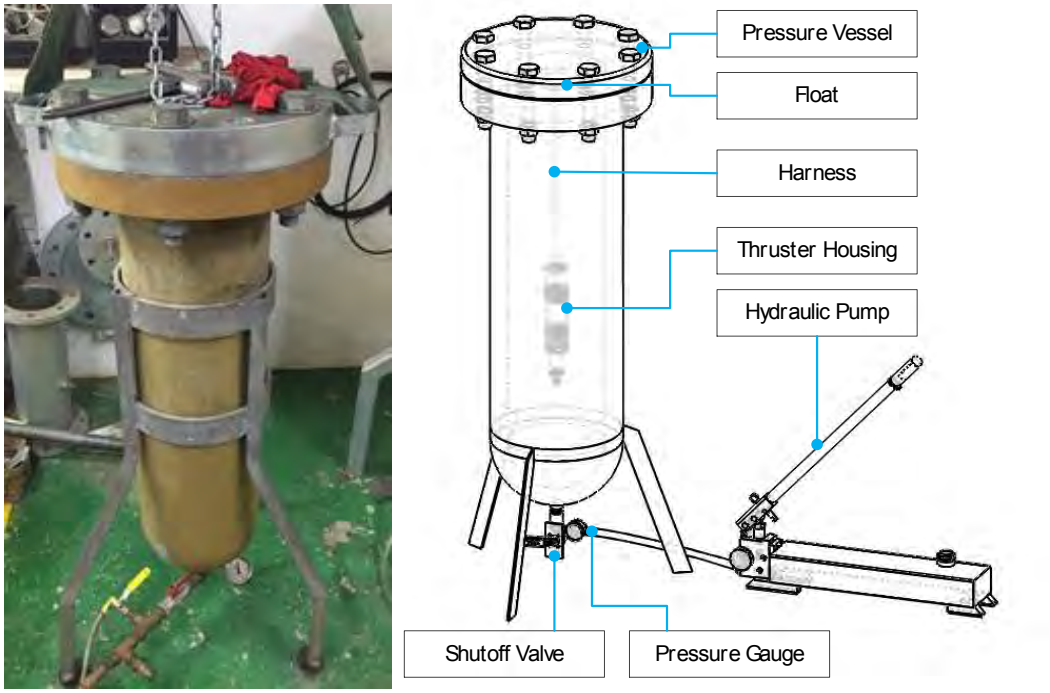

Figure 50 - Pressure Test Equipment

Pressure Test Result

The pressure of 45 bar was maintained for the entire 60 minutes. The housing showed no evidence of deformation or collapse. When opening the housing no trapped pressure was found.

No water was found to have penetrated past the static radial O-ring seals therefore concluding that the modified housing passed the pressure test.

6.2.2 Full Power Thermal Test

Aim

The previous thruster module could not be operated at full power due to the overheating of the electronics. With a new communications and control board as well as a Maxon DEC 50/5 motor controller board now powering the thruster module a full power thermal test was done to establish how long the modified thruster module can be operated at full power. The aim of the test was to obtain the temperature curves for the electronics, motor and gearbox. The maximum allowable temperature for the motor and gearbox is 100 °C and the maximum temperature for the electronics is 60 °C.

Method

The thruster was fully assembled and suspended in the thruster test tank. The tank's water temperature was noted and the thruster was operated at full power from ambient internal temperatures. The temperatures were logged until they plateaued and were considered constant. The temperatures were logged with LM60 temperature sensors installed in the thruster module and the values were sent to the operator console via the RS-485 network. Calibrations for the LM60 sensors can be found in Appendix C. The test was done for both forward and reverse directions. The reason for this being that in the reverse direction the water flow is pushed over the thruster housing and this would increase the cooling of the thruster module compared to being operated in the forward direction.

Full Power Thermal Test Results

The thruster was operated at full power (48 VDC and 4 A) for 20 minutes. The tank water was 22 °C throughout both tests. The temperature curves for both the reverse and forward tests can be seen in Figure 51. All the temperatures plateaued within the 20 minutes. The electronics obtained the highest temperature of 45 °C in the forward direction. The motor and gearbox temperatures peaked at 38 °C and 33 °C respectively. The cooling benefit from the forced water flow over the housing in the reverse test can clearly be seen. In the reverse direction test, the closer the temperature sensor placement to the propeller, the greater the rate of cooling as can be seen by the larger separation in the corresponding curves; this is due to the increased water flow rate closer to the propeller. The electronics temperature started higher than the gearbox and motor temperatures because when the thruster module is idle yet powered some heat is created from the electronics' power regulators.

The reason for the incremented temperature values was that the temperature sensor readings were rounded to the nearest integer value for the simplification of communicating the value to the operator console. Therefore the resolution of the readings was 1 °C.

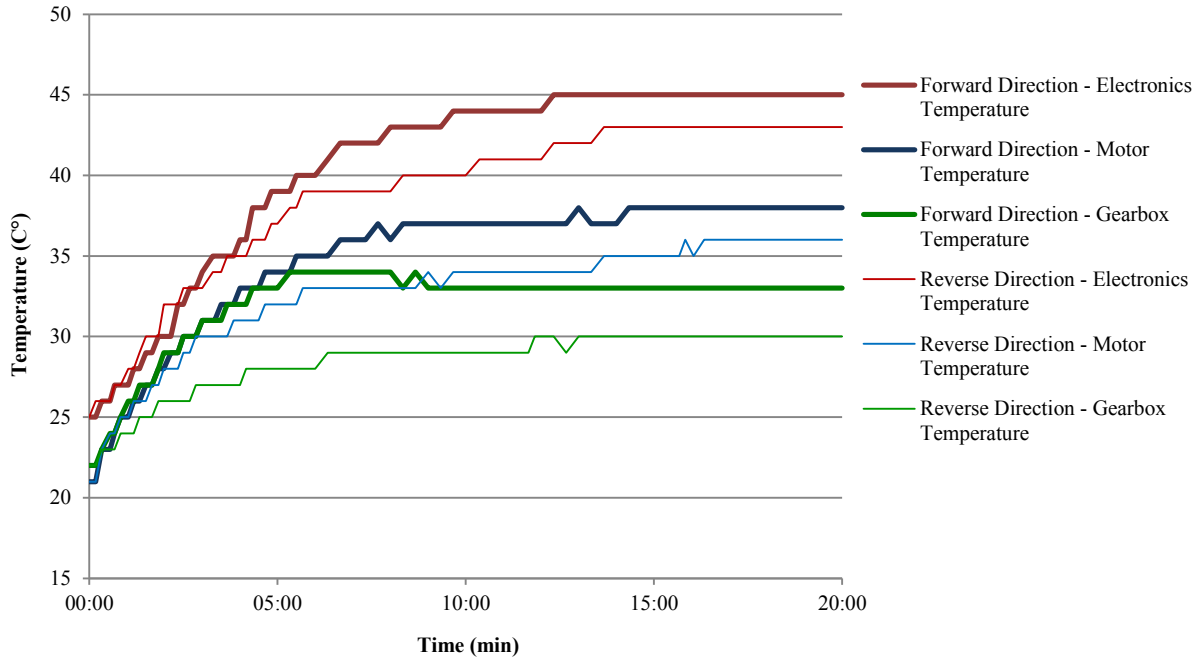

Figure 51 - Full Power Thermal Test

This result shows the thruster modules can be operated at full power in 22 °C water. It was deemed adequate as the maximum seawater temperature between June 2014 and June 2015 along the Western Cape coast was 20.4 °C [29].

6.2.3 Thruster Module Speed Tests

Introduction

This section begins with the calibration of the propeller speed reading that is sent back to the operator console. After the thruster unit was reading accurate propeller speeds the offset correction speed control detailed in Section 5.7.6 was tested. Figure 52 shows the differences between the tests.

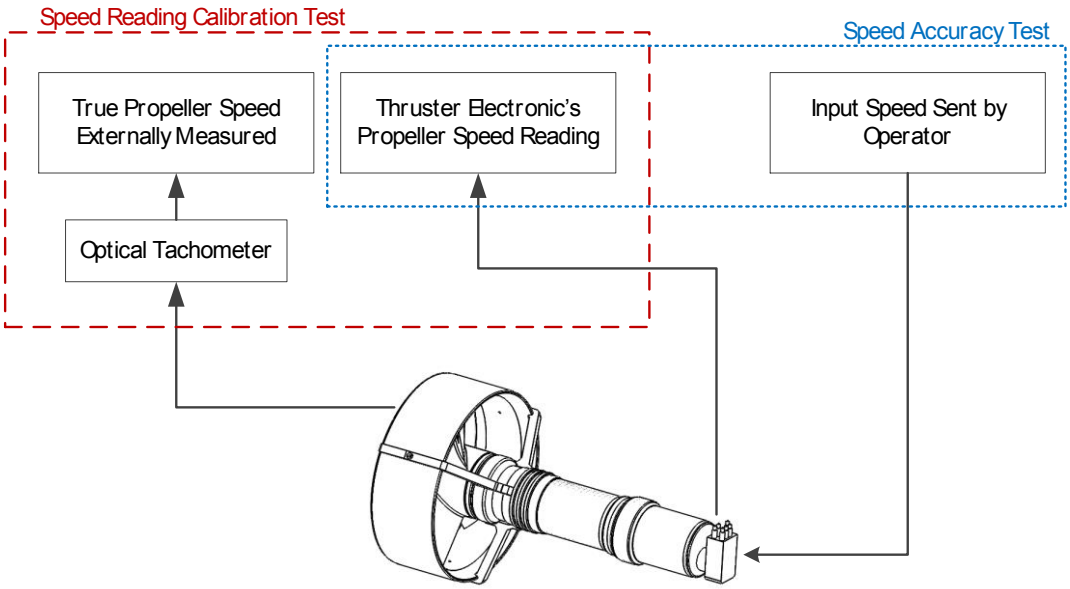

Figure 52 - Different Scopes of Thruster Module Speed Tests

Speed Reading Calibration and Test

During the initial development of the thruster electronics a square wave signal was generated using a signal generator to represent the square wave speed signal being produced by the Maxon motor controller board. The frequency *(f)* of this square wave was a function of the motor speed (S_M) as seen in equation 10 below.

$$S_M = f.20 \tag{10}$$

When the gearbox reduction ratio (r) was factored in the propeller speed was given as:

$$S_P = \frac{f.20}{r} \tag{11}$$

Equation 11 is used by the control microcontroller to calculate the propeller speed which is sent back to the operator console.

Aim

The aim of this test is to calibrate and test the accuracy of the speed readings produced by the thruster module electronics. This test does not aim to improve the control of the speed but merely calibrate the reading of the actual propeller speed.

Method

The thruster module was operated at seven different speeds over its 700 rpm speed range at intervals of 100 rpm. An input speed was sent to the module and once at a constant speed the

speed reading received back was logged and averaged over a 10 second period. During this speed logging a calibrated optical tachometer was positioned to externally read the propeller's rpm. From these values a gain and offset was calculated and applied to the readings obtained from the thruster module. The test was conducted again and the calibrated speed values were validated with regards to the tachometer readings to determine the accuracy of the propeller speed readings. Figure 53 shows the propeller speed being monitored by the optical tachometer.

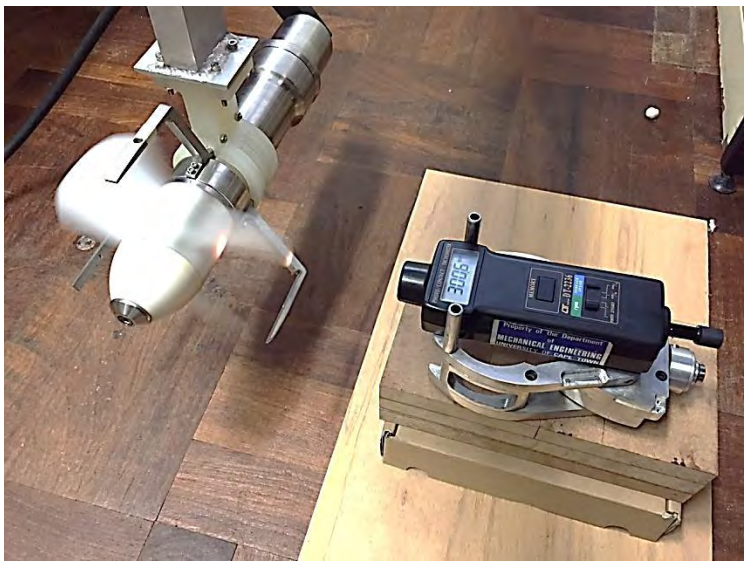

Figure 53 - Propeller Speed Calibration and Speed Test Setup

Results

The values for the logged speed were compared to the tachometers readings. The error in the thruster speed readings can be seen in Figure 54. The resolution of the speed reading from the thruster module is 1 rpm, a higher resolution was deemed unnecessary. Best fit trend lines were used to obtain a gain and offset. The gain and offset values can be seen in Table 16.

The gain and offset was applied and the test procedure redone to verify the calibration. The results can be seen in Figure 54. The average error obtained was 0.4 rpm with the maximum error being 0.7 rpm. This was deemed satisfactory as the speed reading from the thruster module has a resolution of 1 rpm. Table 16 shows the summary of the calibration.

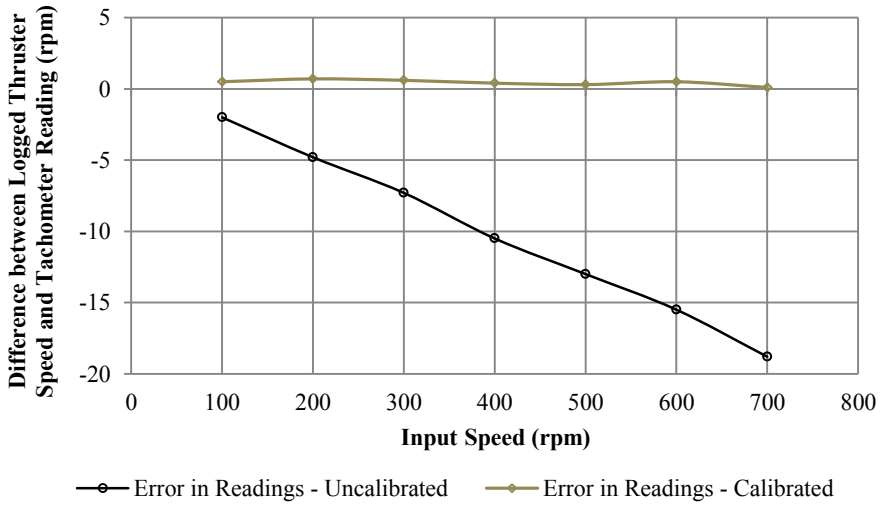

Figure 54 - Error in Calibrated Readings compared to the Error in Calibrated Readings

Table 16 - Summary of Thruster Speed Reading Calibration

Description	Value
Maximum Un-calibrated Error	-18.8 rpm
Average Un-calibrated Error	-10.3 rpm
Maximum Calibrated Error	0.7 rpm
Average Calibrated Error	0.4 rpm
Gain	0.973
Offset	0.538 rpm

This procedure must be done for each assembled thruster module and every time the electronics module (the communications and control board or Maxon motor controller board) is replaced to obtain the correct gain and offset for the respective thruster module.

6.2.4 Speed Accuracy Tests

Aim

The aim of this test is to determine whether the thruster module outputs accurate speeds. The test results will be compared to Specification 5.2.4 that states the thruster module must produce speeds within 1% of the desired speed.

Method

The test method uses the same setup as stated in the speed reading calibration test in Section 6.2.3. The thruster was operated using the offset correction closed loop control designed in Section 5.7.6. The proportional constant used was 0.75.

Results

The results from the offset correction closed loop speed control versus the calibrated DAC analogue input voltage (input in accordance with Maxon's recommended closed loop 0-5 V speed control) can be seen in Figure 55. Specification 5.2.4 is plotted on Figure 56 to show that the thruster module meets the specification stated. By testing a thruster module that did not have the DAC calibrated it was determined that the offset correction eliminates the need for the DAC output to be calibrated to the output speed.

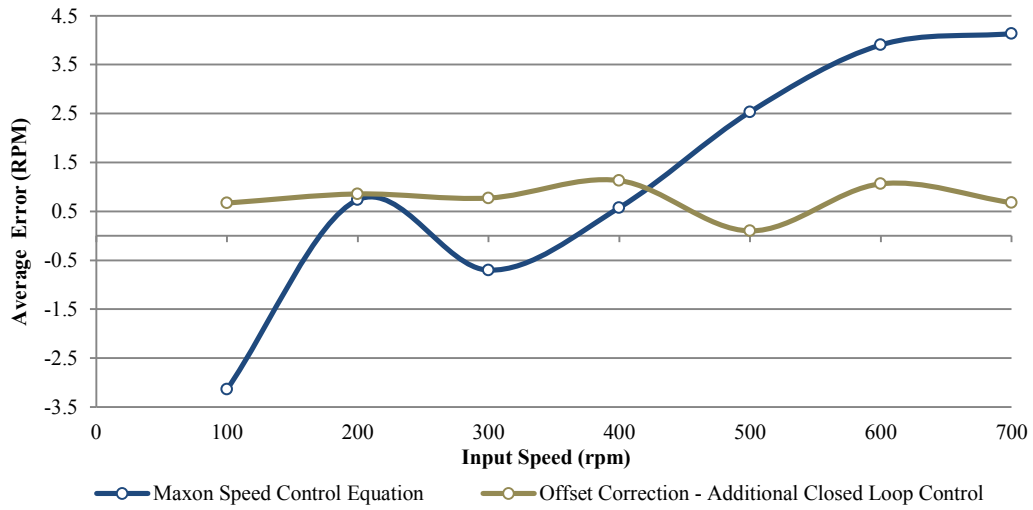

Figure 55 - Average Speed Error: Maxon Speed Control & Offset Correction

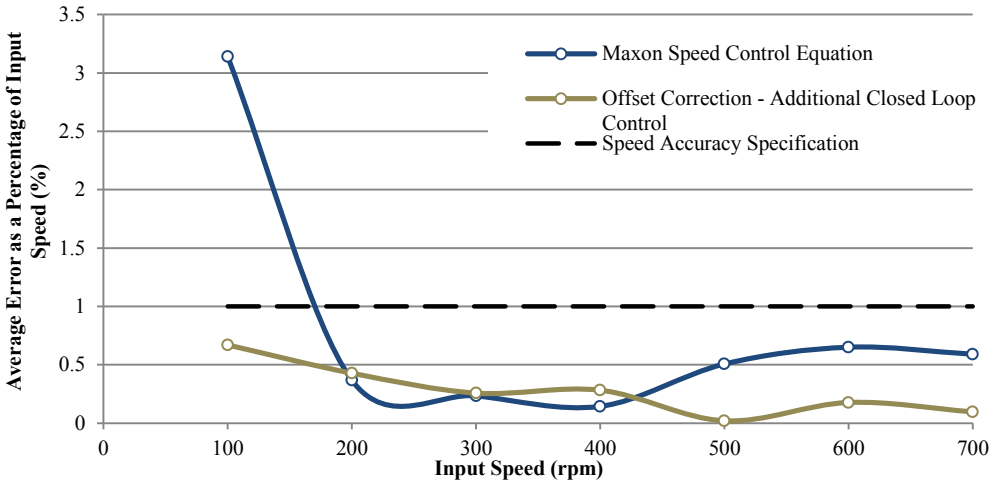

Figure 56 - Average Output Speed Error as Percentage of Input Speed

6.2.5 Magnetic Coupling Power Consumption Test

The magnetic coupling used in the thruster was designed by T. Knight and was not modified. In Section 5.3.2 the load was defined as the magnetic coupling and the propeller. To better define the performance of the thruster module and for future work into the modelling of the thruster module's performance for control purposes it was decided to test the efficiency of the magnetic coupling.

The magnetic coupling membrane is manufactured from stainless steel 316. This material has excellent corrosion properties as discussed in Section 5.4.1 and it has an **I**nternational **A**nnealed **C**opper **S**tandard (**IACS**) conductivity of 2.3%. This conductive property of the material is crucial for the efficient operation of the magnetic coupling. As discussed in Section 9.1.5 eddy currents are induced in the magnetic coupling membrane as the magnetic coupling rotates relative to the membrane. The magnitude of these eddy currents and hence the retardation force applied to the magnetic coupling is relative to the strength of the magnetic field, the rate of change of the magnetic field (in this case the speed at which the coupling is rotating) and conductivity of the membrane. While stainless steel 316 has a lower conductivity than the majority of metallic housing materials available it is conductive and therefore eddy currents will be generated in the membrane during operation. These eddy currents exert a torque that oppose the drivetrain and therefore consume power during operation. It is expected that this power consumption is related to the speed of the thruster module. The torque generated by the eddy currents is independent of the torque being transmitted to the propeller.

Aim

This test aims to define the power consumed by the magnetic coupling over the thruster modules speed range.

Method

The drivetrain was operated without the magnetic rotor connected and in a no load condition. For the entire thruster module speed range the current was logged with a multi-meter connected in series along the 48 VDC power supply cable. The second test was performed with the thruster module fully assembled except for the propeller as seen in Figure 57. This removed the torque caused by the propeller operating in air. Once again the thruster modules current was logged for the entire speed range. By obtaining the difference in power consumption with and without the magnetic coupling an estimation of the magnetic coupling's power consumption can be made. All measurements were taken at constant speeds therefore eliminating the effects of the inertia from the magnet coupling components. By using the motor's torque constant a function for the magnetic coupling's torque-speed relationship can be estimated.

Figure 57 - Magnetic Coupling Power Consumption Test Setup

Results

The results from the two tests can be seen in Figure 58. The current readings fluctuate while the thruster module is operating at a constant speed therefore the ranges of maximum and minimum current readings are displayed. For torque estimations and power estimations the average current values were used.

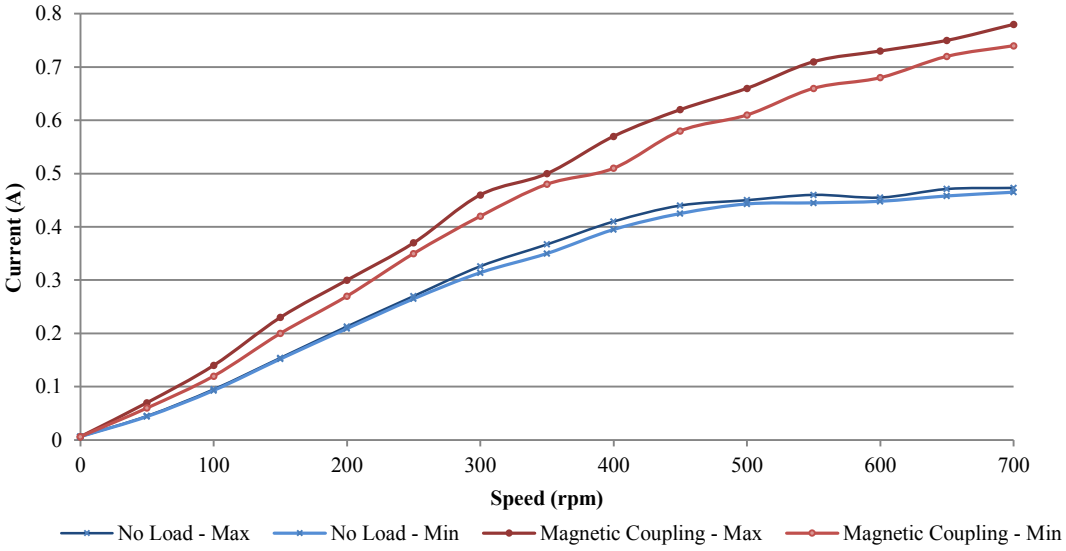

Figure 58 - Magnetic Coupling Power Consumption Test Results

The torque-speed curve and the total electrical input power consumption for the magnetic coupling are shown in Figure 59 and Figure 60 respectively. This is shown to be linear in nature.

The prediction that the power consumption of the magnetic coupling was related to speed is correlated by the results obtained. It is approximately 2 W/100 rpm.

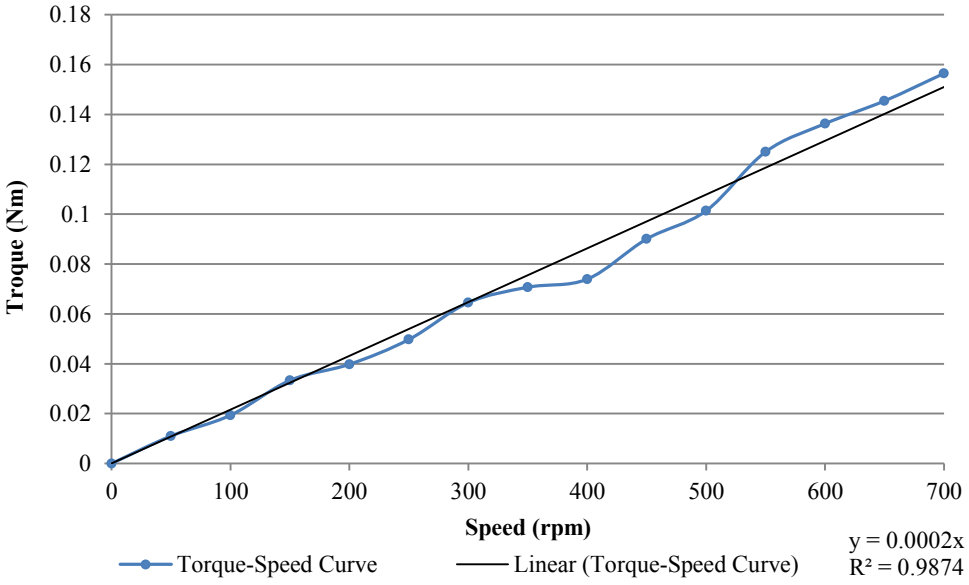

Figure 59 - The Torque-Speed Curve for the Magnetic Coupling

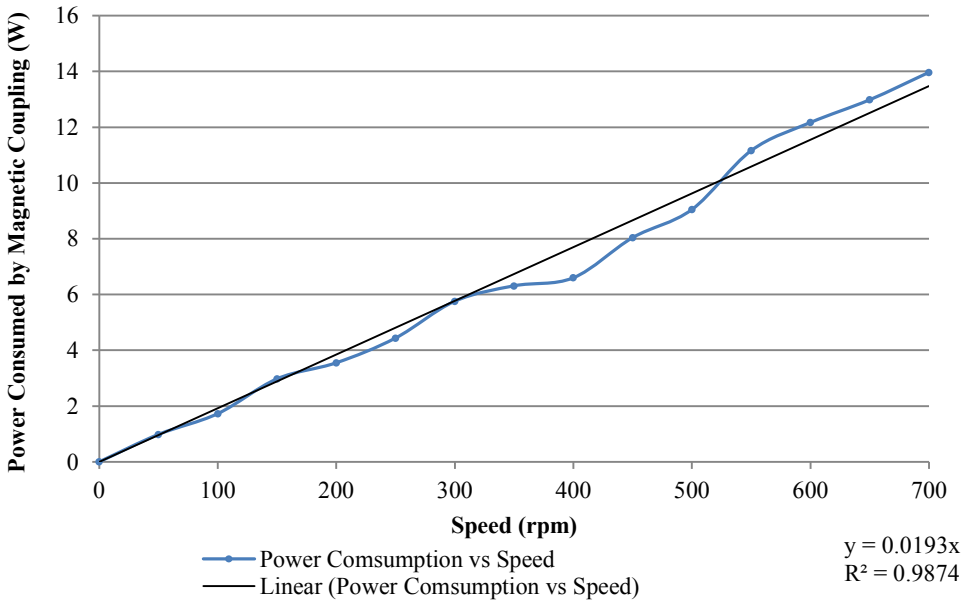

Figure 60 - The Electrical Power Consumption of the Magnetic Coupling at Various Speeds

6.2.6 Thruster Module Thrust Performance Tests

Aim

The aim is to determine the thrust-speed curves for the thruster module and to determine the maximum thrust achievable. This test will provide information used to calculate the efficiency of the thruster module.

Method

The method used was very similar to the method used by T. Knight [20]. The thruster module was mounted onto the thrust test rig and suspended into a tank as seen in Figure 61. A spring scale mounted to a lever arm was used to gauge the thrust produced by the thruster module. The thruster was operated to maximum power and the lever arm was adjusted to be vertical by using an adjustable turnbuckle hook. Once the force readings from the spring scale and the current readings from the power supply unit were read the thruster was slowed down to the next speed value and the turnbuckle hook was adjusted to make the lever arm vertical again.

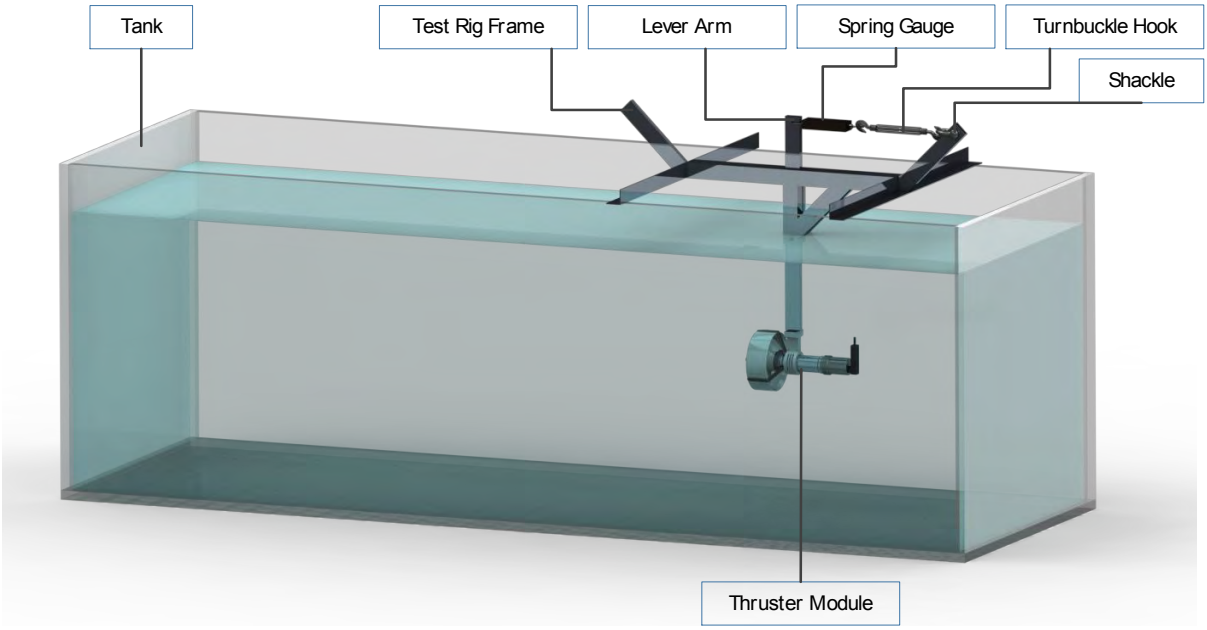

Figure 61 - Diagram of Thrust Test Setup

Ideally the thruster module should be tested in an infinitely large body of stagnant water to eradicate the reaction forces created by the water flow off the walls of the tank and to eradicate currents generated by the thruster module within the tank. However for the thruster test the only tank available was 3 m long, 1 m deep and 1 m wide. It was decided to position the thruster unit to maximise the distance for the water current created by the propeller to dissipate and reduce the reaction forces off the walls of the tank. Therefore the thruster unit was positioned at one end of the tank as shown in Figure 62 and rotated to face the other way for the reverse test.

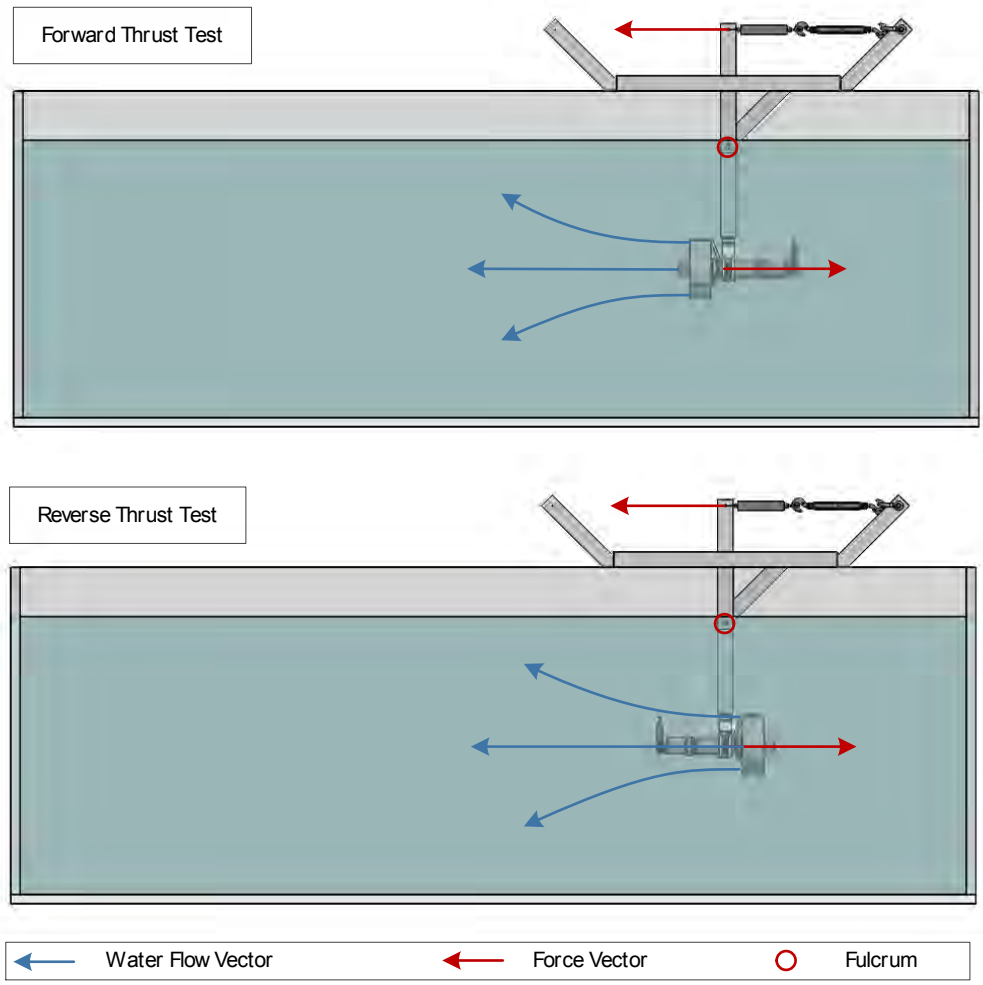

Figure 62 - Forward and Reverse Thruster Positioning Diagram

Results

For both directions the thruster module reached a maximum speed of 700 rpm at 4 A (the maximum continuous current for the motor). For the forward direction the results can be seen in Figure 63. The maximum thrust produced was 66 N with an average thrust of 63 N at 700 rpm. The thrust and current values varied and therefore the maximum and minimum values were recorded with the average values being used for specifying the performance of the thruster module. The reverse direction produced greater thrust than the forward direction, the thrust performance curve can be seen in Figure 64. The maximum thrust achieved was 70 N with an average of 67 N at 700 rpm. Even though the propeller and kort-nozzle are symmetrical, more thrust was achieved in the reverse direction than the forward direction. Table 17 summarises the thrust test results.

Table 17 - Thruster Module Thrust Performance Test – Maximum Values

Result	Value	
Forward Thrust	63	N
Reverse Thrust	67	N
Propeller Speed	700	rpm
Motor Speed	8400	rpm
Motor Current	4	A

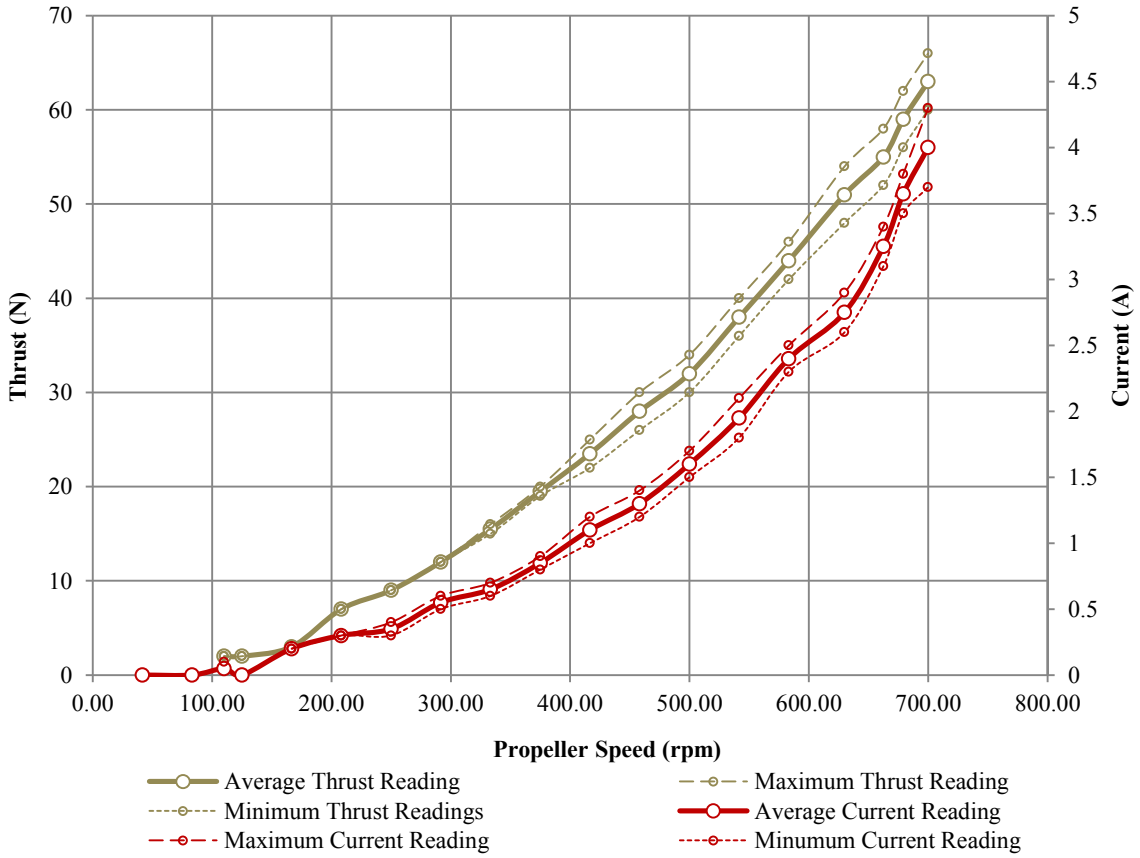

Figure 63 - Thrust Performance Test - Forward Direction

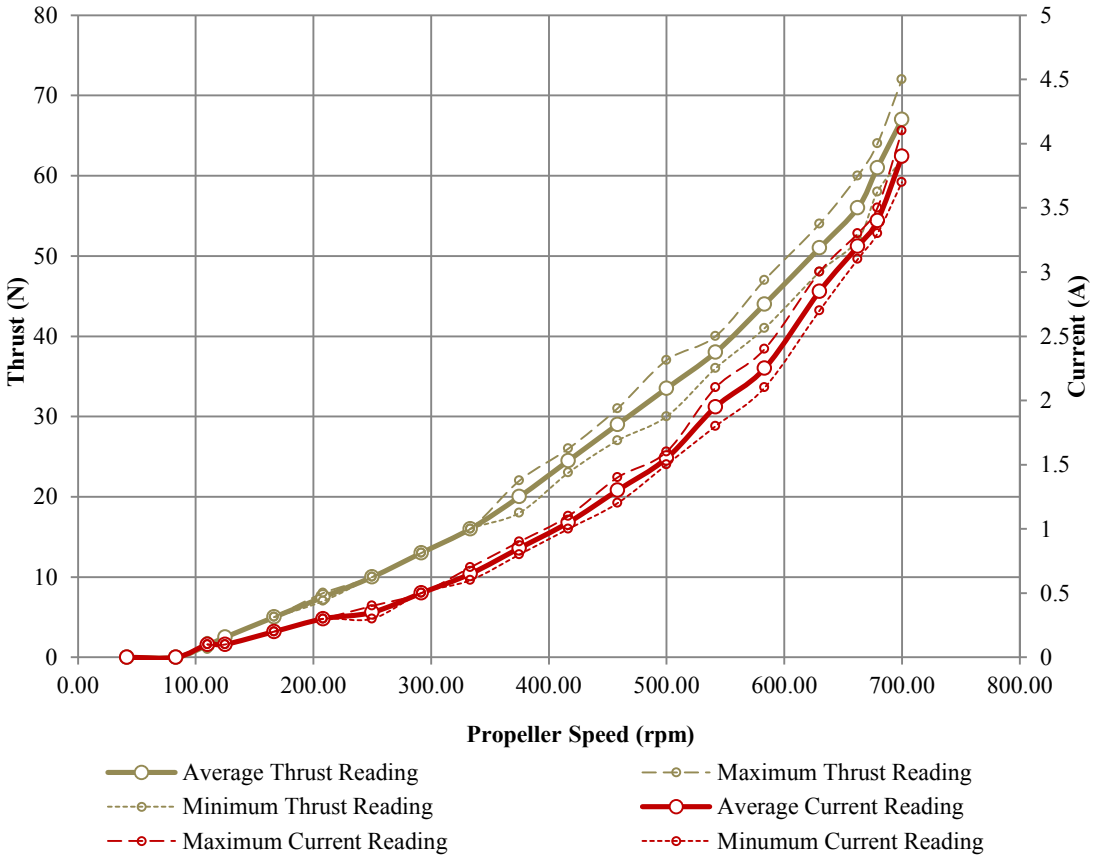

Figure 64 - Thrust Performance Test - Reverse Direction

6.3 Electronics and Software Tests

6.3.1 24 Hour Communications Test

Aim

The thruster modules provide the Seahog with mobility and are essential to the robot's operation. The communication with the thruster modules is therefore vital in order to keep the ROV functional. This test aims to evaluate the thruster module's communication performance over the span of 24 hours. This test will evaluate the hardware and method used to transmit the data as mentioned in section 5.6.9 and the error checking detailed in Section 5.7.5.

Method

The communications to the thruster module were sent every 25 milliseconds for 24 hours. The code on the thruster modules was modified to count the number of times there was an error in the packet of data received. This value is sent back to the operator console. The operator console monitored the data received and counted the number of times a received packet contained an error.

EMI was identified as a potential cause of communication errors for the thruster module. Possible sources of radiated EMI are the conductors that carry the motor currents and the motor control board. These currents are rapidly changing and large compared to the communication signals. The motor power lines are twisted with the RS-485 lines in the Birns™ subsea cable that connects to the thruster module. Inside the housing these wires and the motor winding wires are bunched above the communications and control PCB therefore potentially affecting the UART and SPI communication networks.

In order to simulate this environment the communications test was done with the thruster fully assembled and with the thruster module operating at various speeds (to vary the rate of change of voltage and currents therefore changing the frequency of the EMI). To constantly change the speeds over a 24 hour period without overheating the thruster module was operated for one minute out of every five minutes. The speed sent to the thruster module was determined by the value of the minute of the hour. This is further explained by Figure 65.

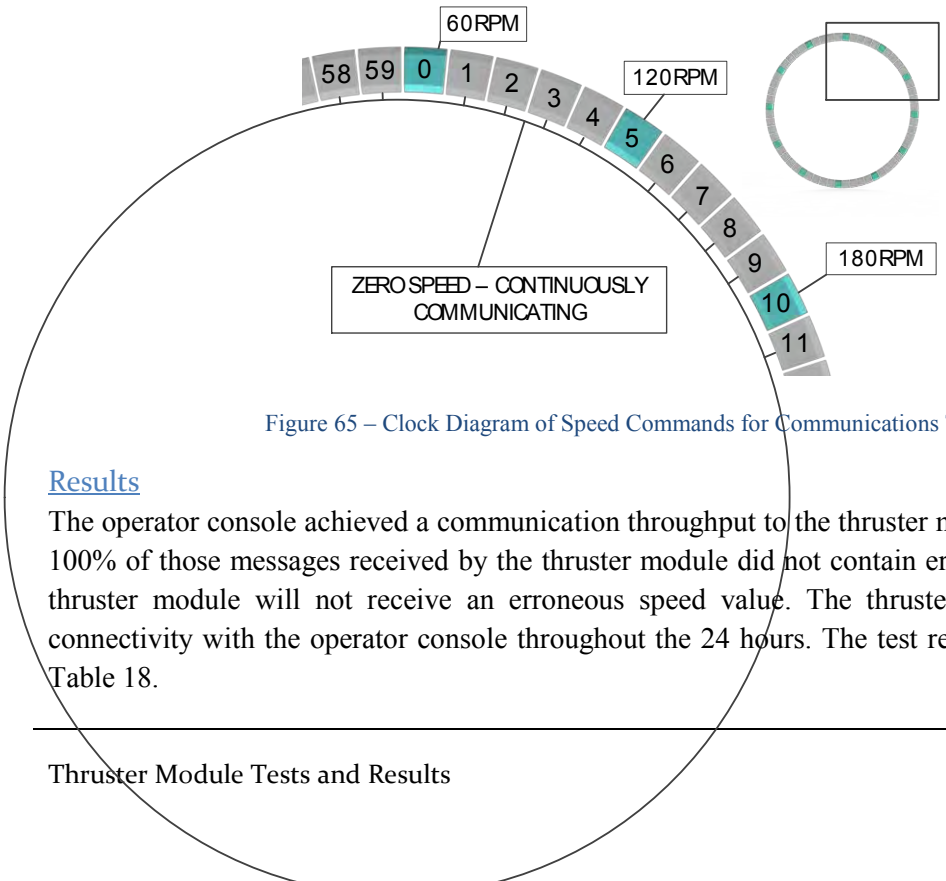

Figure 65 – Clock Diagram of Speed Commands for Communications Test

Results

The operator console achieved a communication throughput to the thruster module of 99.73% and 100% of those messages received by the thruster module did not contain errors. This ensures the thruster module will not receive an erroneous speed value. The thruster module maintained connectivity with the operator console throughout the 24 hours. The test results are presented in Table 18.

Table 18 - 24 Hour Communication Test Results

Description	Result		
Packages Transmitted by the Operator Console to the Thruster Module	3450522		
Packages Received by Control Microcontroller	3441156	99.73	%
Packages Either not Received or Filtered out by Error-Checking	9366	0.27	%
Error Packages Received by Control Microcontroller	0	0	%
Error Packages Received by Operator Console from Thruster Module	11	≈0.00	%

6.3.2 Communication Speed Test

Aim

To determine the duration of time required to communicate with the thruster module.

Method

The electronics of the thruster module were exposed and oscilloscope probes placed onto the three different stages of communication. This test does not include communication time for the entire communication network as shown in Figure 38 of Section 5.7 as the various communications stages regarding the ROV are not within the scope of this dissertation. Only the communication stages within the thruster module are tested. Figure 66 shows the diagram for the test.

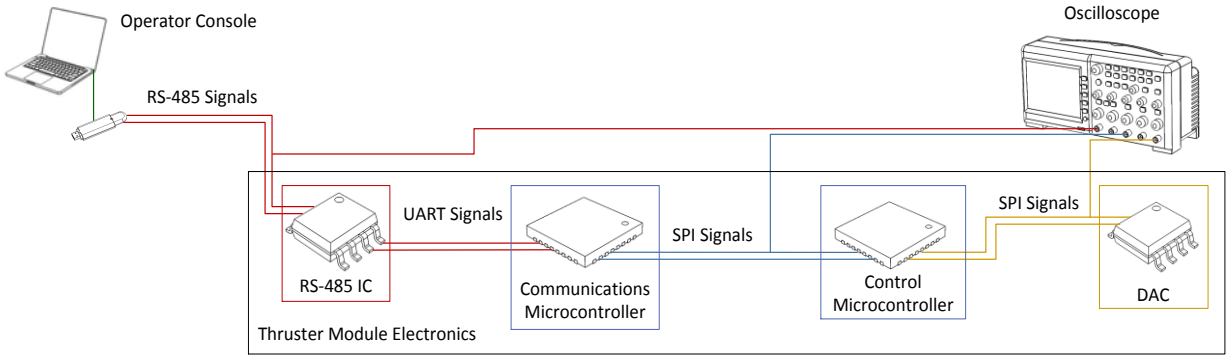

Figure 66 - Schematic for Communication Speed Test of Thruster Module Electronics

Results

The total time taken for the thruster module to receive communications, reply and send the corresponding control value to the DAC was measured to be 1.8 ms. The estimated time without considering processing time and dead time between bytes was 1.38 ms. The waveforms for the communication processes measured can be seen in Figure 67. The waveform is analysed in Figure 68. The RS-485 communications take the majority of time; the rate of communication for this network cannot be increased as this was the determined speed of communications for the ROV system. After the value is communicated via SPI to the DAC the DAC outputs the respective analogue voltage within 5 µs [30]. This analogue output is passed to the Maxon motor controller board and controls the speed of the motor.

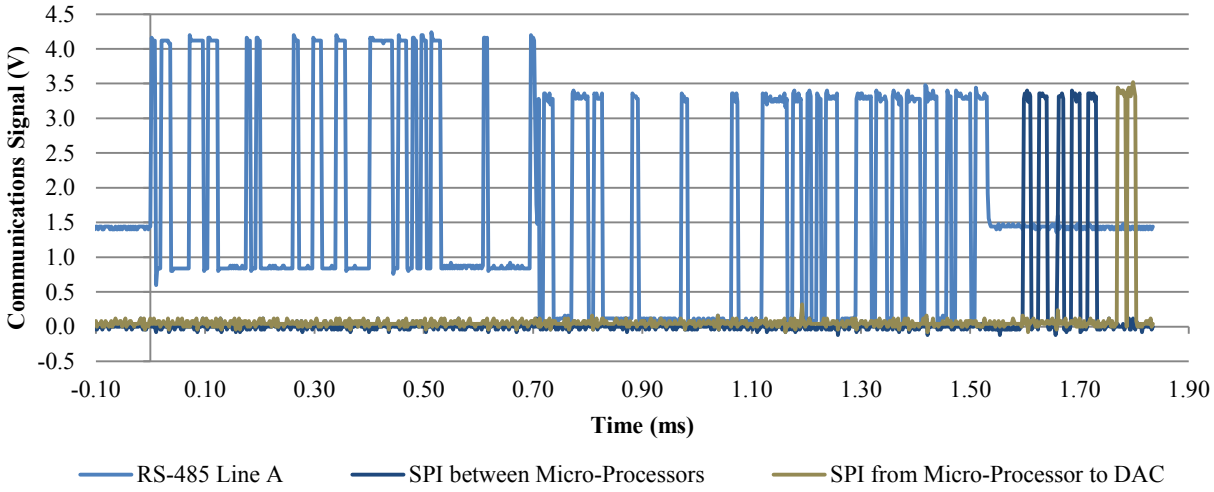

Figure 67 - Waveforms for the Communications in the Thruster Module

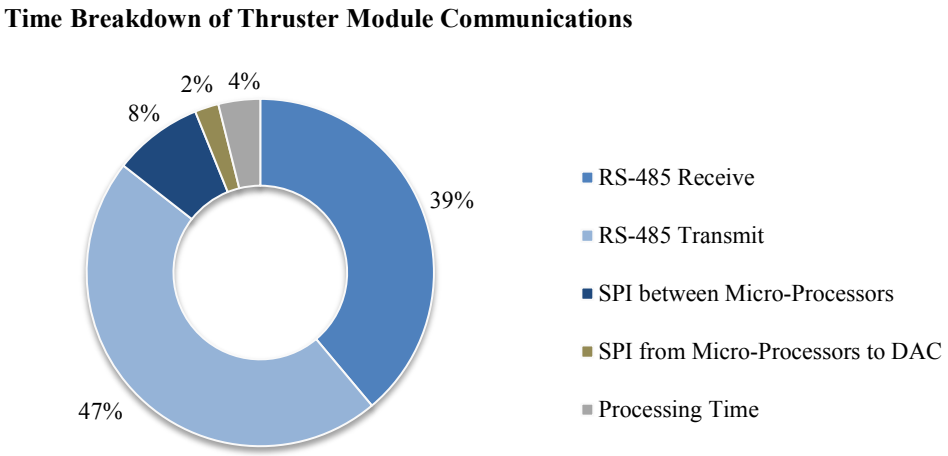

Figure 68 - Time Breakdown of Thruster Module Communications

7 Thruster Module - Conclusions

7.1 Introduction

This section initially draws conclusions on the mechanical modifications and the electronics subsystem of the thruster module. The overall performance increase of the thruster module is examined and the desired specifications for the thruster module are compared to the achieved results. Finally the thruster module is compared to the three commercial thruster modules examined in Section 3.

7.2 Mechanical Modifications

7.2.1 Housing Modifications

The housing modification resulted in a 33% weight reduction of the housing and a 4.8% weight reduction for the ROV. The assembly of the housing was simplified and the assembly time reduced. The housing withstood the test pressure specified for the ROV system and protected the thruster module from water ingress and collapse.

7.2.2 Drivetrain Modification

The drivetrain modification resulted in an approximately four times increase in the drivetrain's efficiency and a 97% increase in thrust produced. The thrust and efficiency increase was not as large as expected from the estimated results. A comparison of the previous, estimated and measured drivetrain performance can be seen in Table 19.

Table 19 - Thruster Drivetrain Performance

Property	Previous	Estimated	Measured	Units
Drivetrain Torque Output	0.558	1.206	1.742	Nm
Propeller Speed	550	800	700	rpm
Mechanical Output Power of Drivetrain	32	101	128	W
Current	4.00	2.77	4.00	A
Thrust Output	35	68	63	N
Drivetrain Efficiency	17	76	66	%

Figure 69 shows the measured load curve plotted on Figure 25 from Section 5.3.5 that was used to select the gearbox reduction ratio. The discrepancy between the estimated load and the measured load could be due to:

- the difference in efficiencies of the electronics
- the magnetic coupling load characteristics not known at the time of load estimation
- differences in test equipment

Regardless of the difference between the estimated and measured loads the 12:1 gearbox selected was the optimum gearbox available to improve the drivetrain's efficiency and performance.

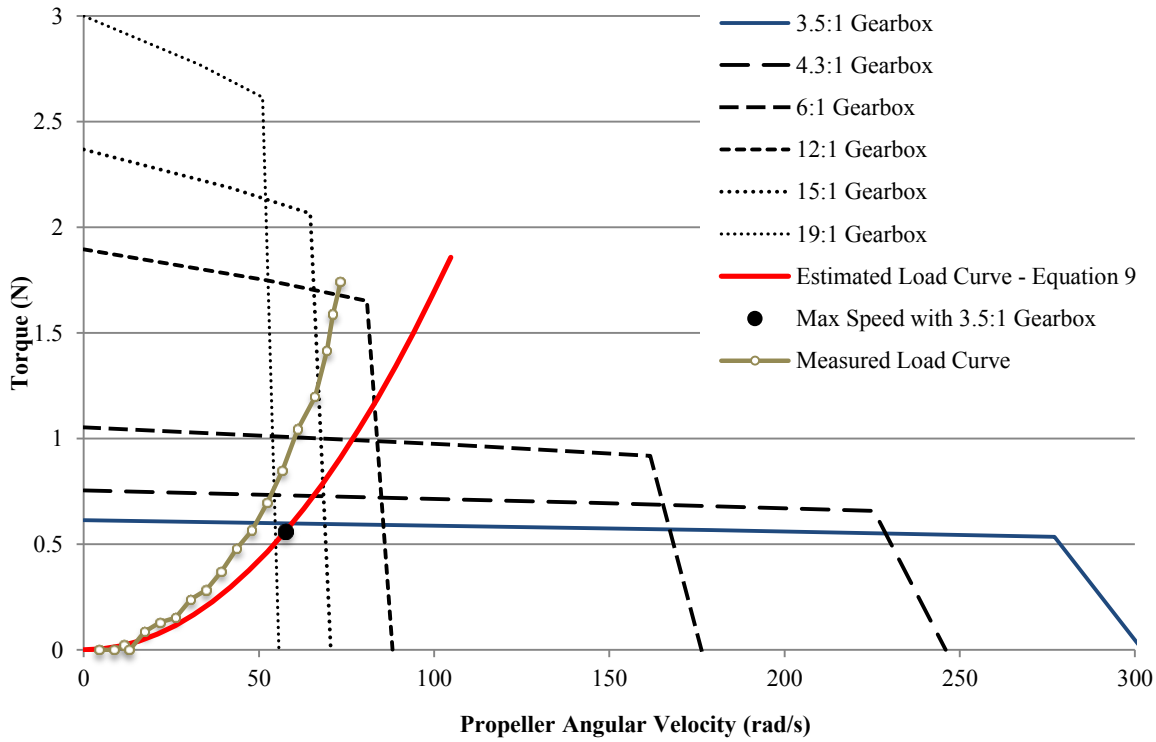

Figure 69 - Measured Load Compared to Estimated Load and Gearbox Selections

7.2.3 Electronics Subsystem

The electronics subsystem fitted into the electronics housing with adequate space for wiring. Bolting the electronics to the electronics frame prevented the electronics from contacting the housing. When the thruster module was operated at full power the electronics did not overheat and it can be operated indefinitely in local coastal waters.

The dual embedded microcontroller design of the control and communications PCB proved to be adequate in maintaining communication and discriminating between addressed packets of data while performing closed loop control of the motor. The interrupt based communications proved to be robust to EMI and reliable.

7.2.4 Performance Summary of the Thruster Module

Table 20 shows the specification table featured in Section 5.2 and details whether they were achieved. All but Specification 5.2.2 was achieved. The thruster module's thrust-to-weight ratio fell short of the desired ratio of 2.2. Recommendations to improve this are made in Section 8.1.

Table 20 - Thruster Module Specification Table - Desired vs. Achieved

Index	Design Requirement	Value	Achieved
	Quantitative Specifications		
5.2.1	Thrust-to-Power Ratio	>0.28	0.33
5.2.2	Thrust-to-Weight Ratio	>2.2	1.51
5.2.3	Max. Reverse Thrust within % of Max. Forward Thrust	10%	6.30%
5.2.4	Speed Accuracy as % of Speed	<1%	0.67%
5.2.5	Communication Response Time	<10ms	1.8ms
	Qualitative Specifications		
5.2.6	On-board Closed Loop Speed Control	Yes	Yes
5.2.7	Interrupt Based Communications	Yes	Yes
5.2.8	Can Operate at Max. Power Indefinitely	Yes	Yes
5.2.9	Temperature Feedback	Yes	Electronics, Motor, Gearbox
5.2.10	Communication Failure Shutdown Procedure	Yes	Yes, after 3s
5.2.11	Over Voltage, Over Current, Reverse Bias Protection	Yes	Yes

The thruster module's performance summary can be seen in Table 21. This table details performance improvements and additional performance indicators for the thruster module.

Table 21 - Thruster Module Specifications

Specification	Previous	Modified	Units	% Increase
Forward Thrust at Maximum Power	32	63	N	+97%
Reverse Thrust at Maximum Power	33	67	N	+103%
Maximum Power	190	190	W	0
Weight in Air	4.8	4.2	kg	-12.5%
Weight in Seawater	3.4	2.8	kg	-17.6%
Thrust-to-Power Ratio	0.17	0.33		+97%
Thrust-to-Weight Ratio	0.68	1.51		+122%
Drivetrain Efficiency	0.17	0.66		+388%
Propeller Speed Reading Accuracy	Undefined	1	rpm	NA
Propeller Speed Accuracy as % of Input Speed	Undefined	1	%	NA
Communication Speed	9600	115200	bps	+1100%

The thruster module was compared to the commercial thruster modules featured in Section 3. Figure 70 shows the thruster module's thrust-to-power ratio is now competitive with commercial thruster modules second only to the Saab Seaeye's MCT01. This improvement is due to the drivetrain modification and change in motor controller electronics.

Due to the increase in thrust and the decrease in weight the thruster module's thrust-to-weight ratio has more than doubled compared to the original thruster produced at RARL. However it is not greater than any of the three commercial thruster modules examined in this dissertation.

The thruster module has nearly doubled its thrust-to-power ratio and its thrust-to-weight ratio. It is nearly 4 times more efficient and can be operated indefinitely at full power.

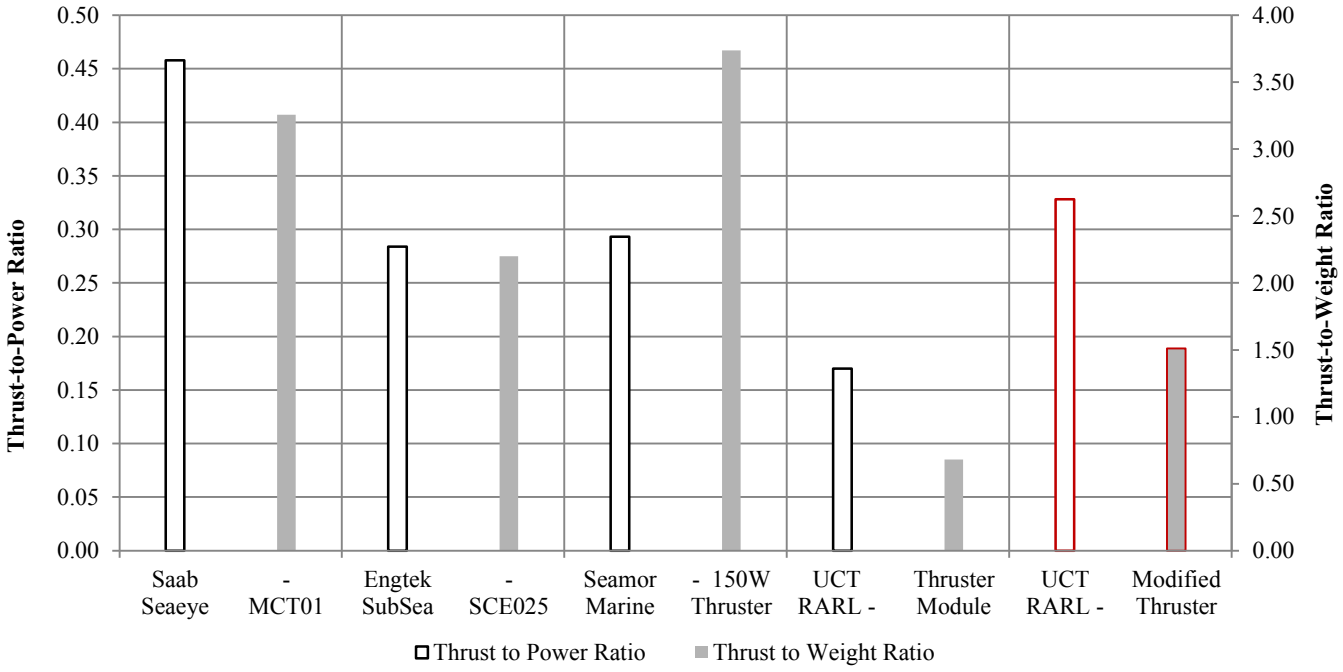

Figure 70 - Thruster Performance Comparison Chart

8 Thruster Module - Recommendations

8.1 Mechanical Modifications

The thruster module housing is a design that still has the potential to be streamlined and to have the weight reduced. It is recommended that a new housing be designed that is smaller and fits directly around the motor and gearbox therefore removing the heatsink. **F**inite **E**lement **A**nalysis (**FEA**) can be done for the housing to further reduce the weight. MBARI have developed FEA methods that are specific to cylindrical housings exposed to external pressure [31]. All thrust performance tests conducted on the thruster module were done in shallow water, therefore it is unknown how an increase in depth, and consequently pressure, will affect the thruster module's performance. It is suggested that **C**omputational **F**luid **D**ynamics (**CFD**) aided analysis is done to investigate the potential performance changes that may occur due to an increase in depth. A final design recommendation is made at the end of the dissertation in Chapter 13 that incorporates the knowledge gained from the magnetic coupling tests.

8.2 Electrical Modifications

The electronics performed adequately but for continuous development of the thruster modules at UCT it is recommended that the MSP340 embedded microcontrollers be replaced with the STM32F0. The STM32 has a built in DAC therefore reducing the number of components required [32]. Additionally the STM32 is currently being used for educational purposes at UCT with development boards and a supply of the microcontrollers becoming abundant. If the communications and control PCB is redesigned it should be made narrower (to the same width as the motor) in order to fit in a narrower housing should the changes suggested in the previous paragraph be made.

8.3 Concluding Remarks

The recommendations made in this section are not essential and the final thruster module design is satisfactory. The recommendations are only required if increased weight saving is crucial and the resources are available to make the modifications.

A consolidated and final recommendation for the thruster module is made in Chapter 13. This includes the knowledge gained from the modelling and testing of the magnetic couplings.

9 Background Research – Magnetic Couplings

9.1 Magnetic Couplings

9.1.1 Introduction

A magnetic coupling uses magnetic forces to transmit work from one mechanical system to another without mechanical contact. The work can be transmitted in a linear or rotary fashion. The coupling is comprised of two parts; the driver and the follower [33].

Several benefits exist when using magnetic couplings. Mechanical vibrations generated in the load and the drivetrain are reduced through magnetic damping. Magnetic couplings allow for a membrane to exist between the driver and the follower therefore separating the operating environments and allowing the coupling to transmit work across a pressure differential without the need for dynamic sealing. This makes them very useful for torque transmission in extreme environments and are therefore well suited for use on the ROV [34].

The couplings are highly tolerant of axial, radial and angular misalignment between the driver and follower. If designed correctly the magnetic coupling can protect the drivetrain by slipping when excessive torque is applied.

Three classes of magnetic couplings exist; synchronous, eddy current and hysteresis couplings.

9.1.2 Synchronous Magnetic Couplings

Synchronous couplings have an input to output ratio of 1:1 between the driver and follower. Like magnetic poles (North-North or South-South) repel each other and conversely opposite poles (North-South) attract each other. Using this phenomena and arranging the permanent magnets in alternating pole pairs on the driver and follower, synchronous magnetic couplings can transmit torque (see Figure 71). The inner and outer rotor of a magnetic coupling can either be the driver or follower depending on which one is connected to the drivetrain or the load.

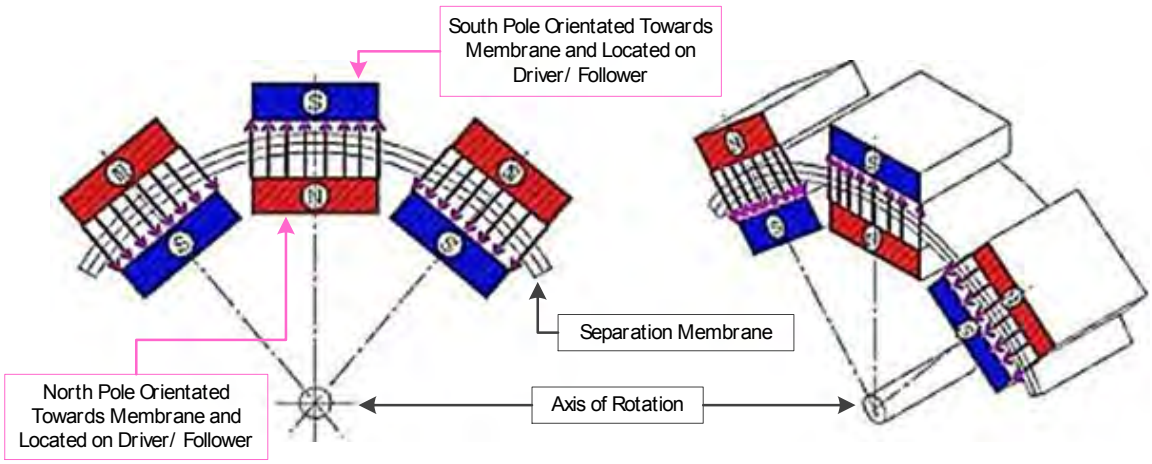

Figure 71 - Magnetic Coupling Torque Transmission - Magnet Orientation [35]

By arranging the magnets in this pattern a coupled magnetic circuit is achieved between the pole pairs. As the driver moves relative to the follower a misalignment is created and a push and pull effect is induced on the follower and hence torque and motion is achieved. The resultant torque is determined by the amount of overlap and is not constant for the change in angle of the driver. The magnetic material used, distance of separation between the driver and follower and the number of

pole pairs determine the torque and slip characteristics of the coupling [36]. At a specific angular displacement between the driver and follower the maximum transmission torque of the coupling is achieved, this is called the pull-out torque, if the pull-out torque is exceeded the pole pairs are decoupled and a ratcheting action is created as the coupling continuously slips [37]. This does not cause damage to the coupling.

Synchronous magnetic couplings provide the greatest pull-out torques for their size and weight [33].

Synchronous Magnetic Coupling Arrangements

Synchronous magnetic couplings come in two setups; axial and coaxial permanent magnetic couplings.

Axial Magnetic Couplings

Axial couplings consist of two opposing disks with permanent magnet arrays installed. The disks are separated by a non-magnetisable and non-conductive membrane. This setup results in large compressional forces on the membrane from the attraction of the two disks, these forces have to be taken up using thrust bearings. The magnetic field that transmits the force through the membrane is orientated along the axis of the shaft [33]. An example of an axial magnetic coupling is shown in Figure 72.

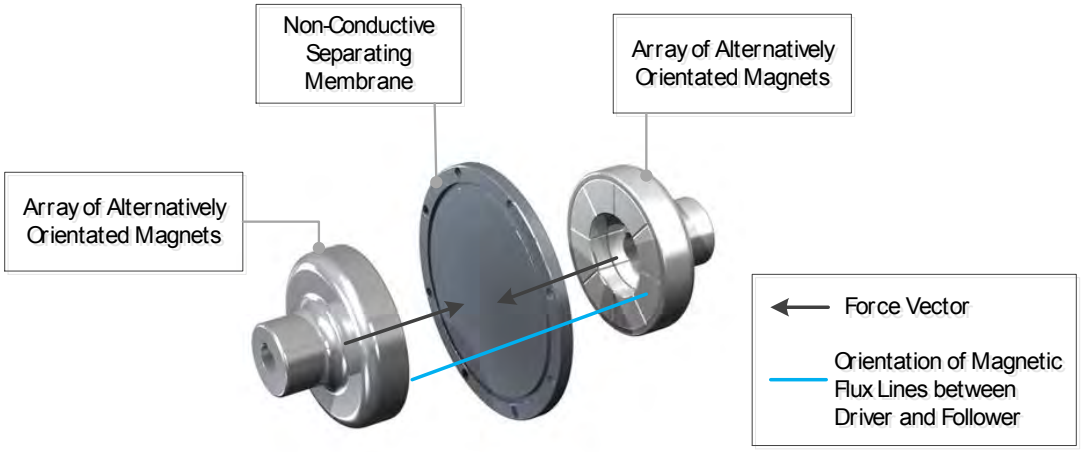

Figure 72 - Axial Magnetic Coupling [33]

Coaxial Magnetic Couplings

Coaxial concentric couplings are configured so the magnetic field is orientated in the radial direction of the coupling shaft. The internal component of the coupling (driver or follower) has alternating permanent magnet pole pairs installed on the outside and sits inside the separating membrane (or shroud). The external component has the corresponding magnetic pole pairs on the inside. The magnetic fields are transmitted through the membrane in the same direction as the radius of the coupling; Figure 73 shows the mechanical layout and Figure 74 shows magnetic field lines in a coaxial magnetic coupling. This arrangement eliminates the compressional forces experienced in axial magnetic couplings. For a given diameter coaxial magnetic couplings can transmit more power than axial magnetic couplings [33].

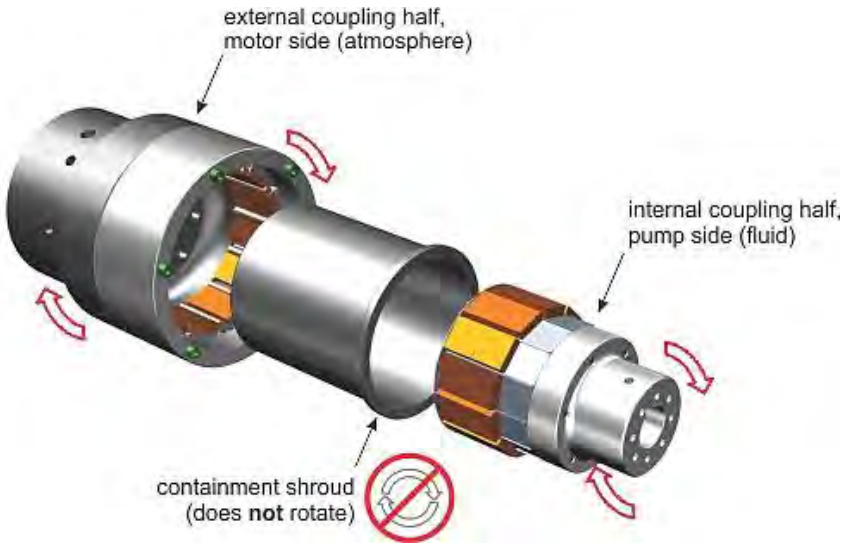

Figure 73 - Radial Concentric magnetic Coupling [35]

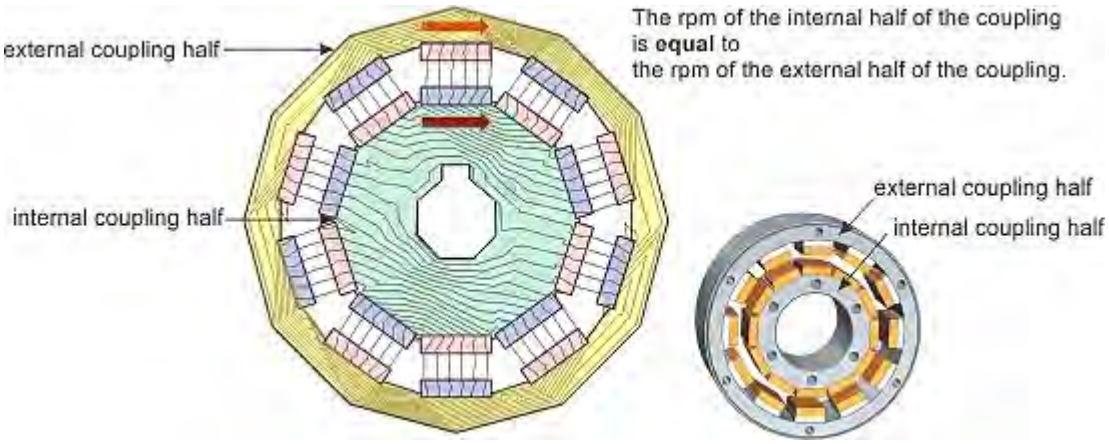

Figure 74 - Principle of Operation [35]

9.1.3 Eddy Current Magnetic Couplings

Eddy current magnetic couplings provide asynchronous transmission between the driver and follower. A speed mismatch is required to create the torque that rotates the follower. An array of alternating pole permanent magnets is placed on either the driver or follower, the other component is made from an electrically conductive material such as aluminium or copper. When there is a relative angular velocity between the follower and the driver an eddy current is induced in the rotor without the magnets (the conductive rotor). This eddy current is induced because of the changing magnetic field the rotor experiences. The resultant magnetic field created by the eddy current opposes the motion of the magnets on the other rotor, creating a resultant torque. Ampere's Law determines the relationship between the induced current and the resultant magnetic field. The resultant torque is determined by:

- the magnetic materials used in the permanent magnet array
- the speed differential between the driver and follower
- the conductivity of the conductive element in which the eddy currents are induced
- the separation distance between the driver and follower

A disadvantage of eddy current couplings is the loss of energy through ohmic heating caused by the induced current. These couplings are mainly used in braking devices [33].

9.1.4 Hysteresis Magnetic Couplings

Hysteresis couplings are a hybrid of the synchronous and eddy current couplings. Once again either the driver or follower has a permanent magnet array of alternating poles, however the other mating part is made from an easily magnetised/demagnetised material. When the applied torque is below the slip threshold for the coupling the coupling acts as a synchronous coupling would, transmitting the torque without slip. However when the torque increases beyond this threshold the coupling slips causing a speed differential between the driver and the follower. This speed differential causes the permanent magnets to magnetise and demagnetise the corresponding part. This results in a continuous transmitted torque regardless of the applied torque on the coupling. No ratcheting occurs as is experienced by synchronous couplings when exposed to a torque greater than designed for. This makes hysteresis couplings useful for continuous torque applications and torque limiting applications without ratcheting [38]. By using permanent magnets on one rotor and an easily magnetised/demagnetised material on the other rotor hysteresis magnetic couplings produce less torque than synchronous magnetic couplings of the same size and weight.

9.1.5 Membrane Characteristics

Most magnetic couplings feature a membrane to separate the drivetrain and load environments. The membrane material must be able to maintain this separation and therefore withstand any pressure differentials between the environments and be chemically resilient to any corrosive fluids that it comes into contact with. The membrane is fixed and therefore remains stationary when the rotors of the magnetic coupling are rotating. Rotating magnetic fields induce eddy currents in electrically conductive materials. The eddy currents generate magnetic fields that oppose the motion of the changing magnetic field that originally induced them, therefore retarding the rotors of the coupling. This requires the membrane material to have a low conductivity to reduce these eddy currents.

Stainless steel 316 was identified by T. Knight as the most feasible material to use as the membrane for the magnetic couplings on the ROV. It has an IACS percentage of 2.3% which means that its conductivity is 2.3% that of copper [39]. This relatively low conductivity reduces the strength of the eddy currents generated by the magnetic coupling. The mechanical and chemical properties of stainless steel 316 were discussed in Section 5.4.

9.1.6 Concluding Remarks

Synchronous magnetic couplings produce the most torque for their size and weight of the three types of magnetic couplings discussed and they suit the requirements of the ROV. The efficiency advantages the coaxial magnetic couplings have over the axial magnetic couplings make them the focus of this dissertation. It is desired that the majority of actuation on the ROV (whether that be the thrusters, a manipulator, the camera tilt unit or future customised sampling equipment) be statically sealed and not require dynamic seals or oil filled pressure compensated housings.

9.2 Magnetic Materials and Their Properties

The type of magnets used for the Seahog's couplings have been neodymium rare earth magnets. Neodymium magnets (commonly referred to as NdFeB magnets) are composed of neodymium (Nd), iron (Fe) and boron (B) and are the strongest commercial permanent magnets currently invented. Neodymium magnets have a high resistance to demagnetisation and will not become demagnetised when in the presence of other magnets or when dropped. However their magnetisation can decrease if they are heated above their operating temperature of approximately 80 °C [40].

Neodymium magnet naming convention consists of the letter 'N' followed by a two digit number, this number represents the magnetic energy product of the material and it is given in the unit Mega-Gauss Oesteds (MGOe) [41]. The grade of the magnet gives an insight into the residual magnetisation (measured in Teslas, T) of the magnet. The residual magnetism (also known as remanence or remanent magnetisation) is the magnetisation left behind in a ferromagnetic material after an external magnetic field has been removed [42]. The saturation remanence (Br) is the term used to describe the residual magnetism left in the ferromagnetic material after it was exposed to an external magnetic field (H) which is strong enough to achieve magnetic saturation. Saturation is achieved when an increase in the applied magnetic field cannot further increase the magnetisation of the material [43]. In Figure 75 the residual magnetism (Br) can be seen on the hysteresis curve at point b.

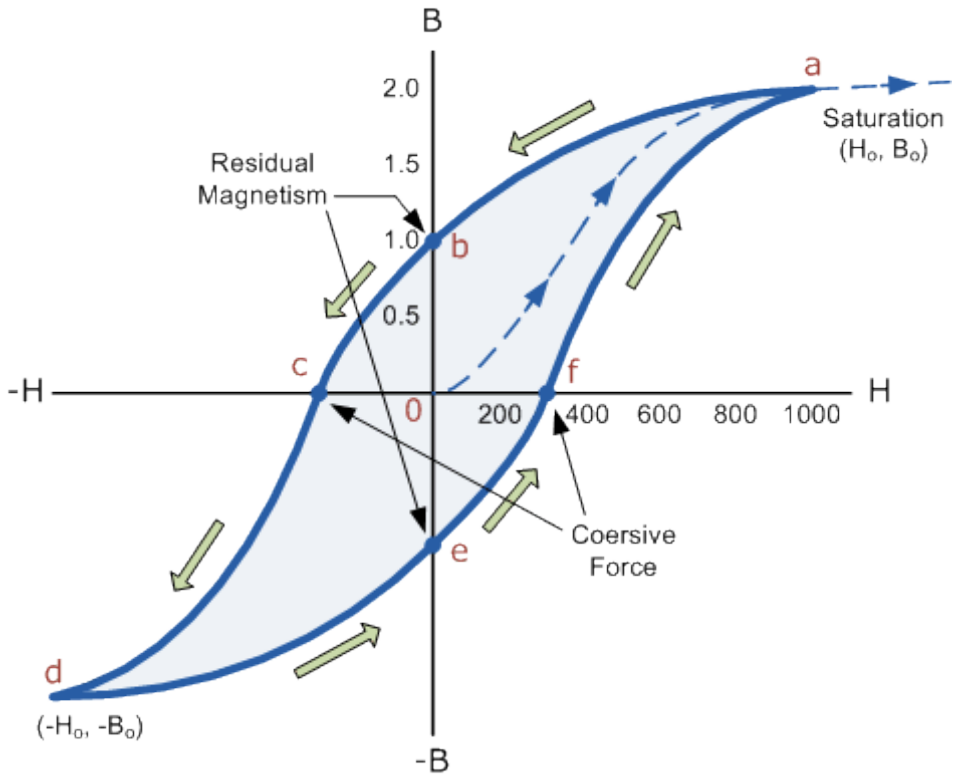

Figure 75 - Magnetic Hysteresis Loop [44]

Table 22 shows the relative residual magnetism range for various grades of Neodymium magnets.

Table 22- Neodymium Permanent Magnet Specifications [45]

	Maximum Energy Product (BHmax) (MGOe)		Residual Magnetism (Br) (T)	
Grade	**Minimum**	**Maximum**	**Minimum**	**Maximum**
N35	34	36	1.18	1.23
N38	36	39	1.23	1.26
N40	38	41	1.26	1.29
N42	40	43	1.30	1.32
N45	43	46	1.33	1.37
N48	45	49	1.37	1.41

10 Magnetic Couplings

10.1 Previous Magnetic Couplings at RARL

Two coaxial synchronous magnetic couplings have been developed at RARL. The first coupling was developed by Thomas Knight in 2012 for the thruster modules and the second coupling was developed for the manipulator module on the ROV by M. Finbow in 2013. No modelling of potential torque vs. slip properties of the couplings were attempted beforehand. The design criteria were practical and influenced by the available magnets, size limitations and the weight of the coupling.

10.1.1 Thruster Module Coaxial Magnetic Coupling

Design

The thruster module magnetic coupling design featured two pole pairs and used 50 mm x 10 mm x 10 mm cuboid magnets made from grade N38 Neodymium. A schematic for the coupling can be seen in Figure 76.

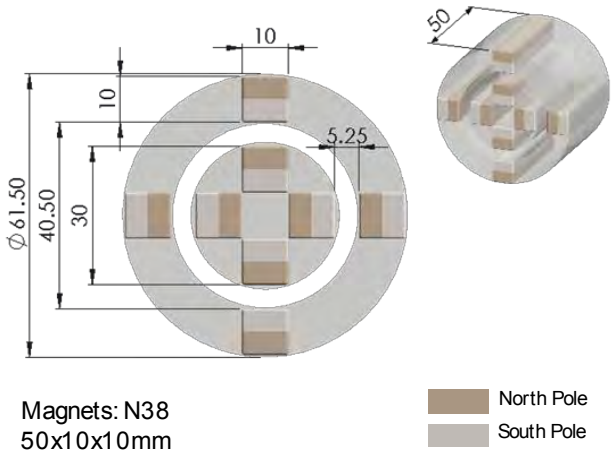

Figure 76 - Thruster Coupling Schematic

Test Method

Figure 77 shows the test rig used to determine the torque vs. slip curve. The inner rotor of the magnetic coupling was clamped using the dividing head on the left and the membrane, made from **H**igh-**d**ensity **P**oly**e**thylene (**HDPE**) for the test, was clamped by the dividing head on the right. The outer rotor (not constrained and left to rotate) had a PVC shroud to which a rope was attached. Weights placed on the rope provided constant torque to the coupling regardless of the angle of slip. A protractor was placed on the stationary inner rotor to measure the degree of slip between the two rotors.

Test Results

Figure 78 shows the torque vs. slip test results obtained during this test. The maximum torque achieved was 2.98 Nm (the pull-out torque) at a slip angle of 25°. This proved sufficient for the thruster module as the drive train produced 1.78 Nm of torque at full power.

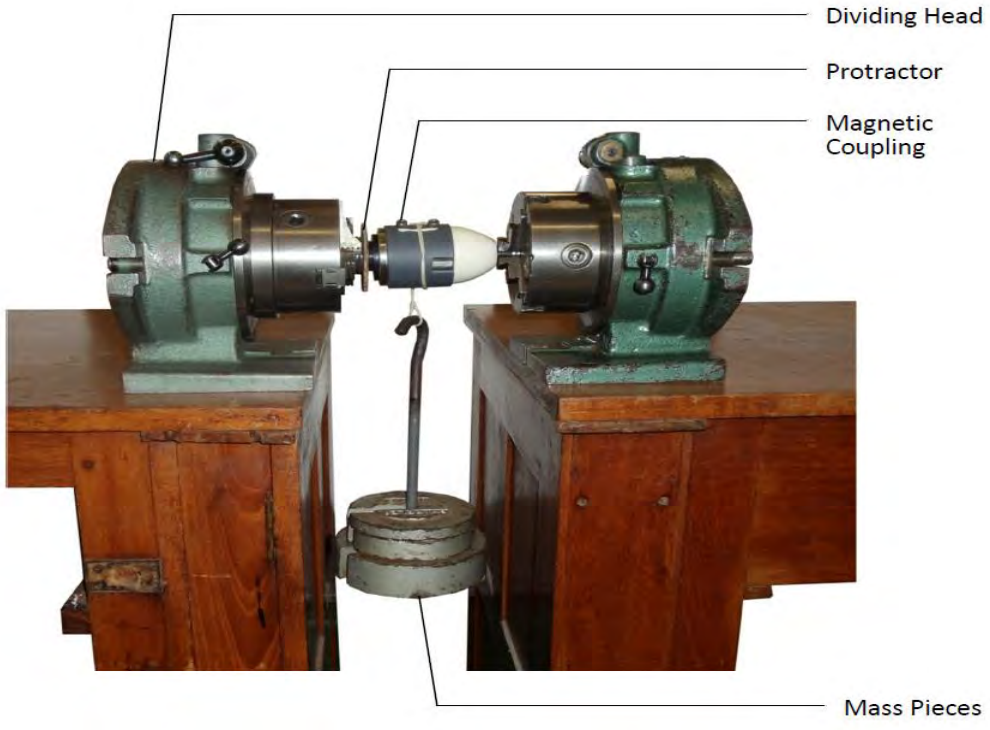

Figure 77 - Thruster Module Magnetic Coupling Test Setup [20]

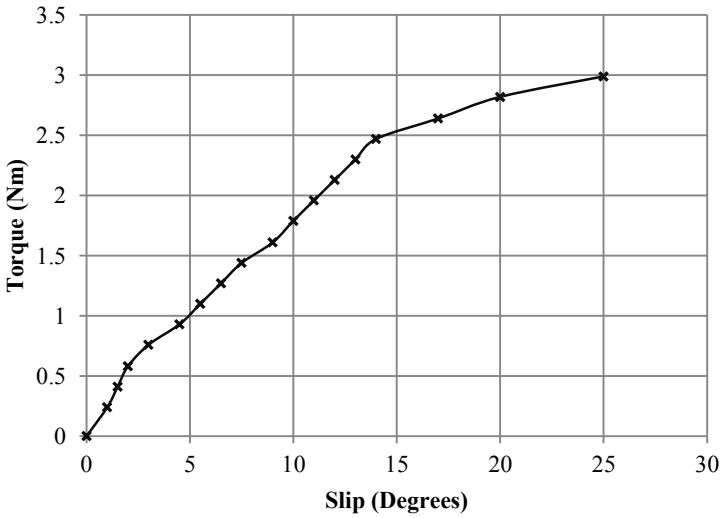

Figure 78 - Thruster Magnetic Coupling Torque vs. Slip Results [20]

Test Method Remarks

Possible causes of error in this method were the potential misalignment of the two dividing heads and the error in reading the slip angle from the protractor due to parallax caused by the awkward viewing angle. The last value in the test results is the most difficult to measure as this is the point at which the coupling completely slips and is no longer stable, when the pull-out torque of the coupling is reached the slip value can no longer be monitored using a protractor.

10.1.2 Manipulator Module Magnetic Coupling

Design

The manipulator module's magnetic coupling developed in 2013 featured three pole pairs and used the same N38 50 mm x 10 mm x 10 mm cuboid magnets as the thruster coupling. The original specification for this coupling was for it to have a pull out torque of 3.5 Nm. The number of pole pairs was increased by one from that in the thruster coupling therefore guaranteeing a higher pull-out torque. The coupling schematic is shown in Figure 79.

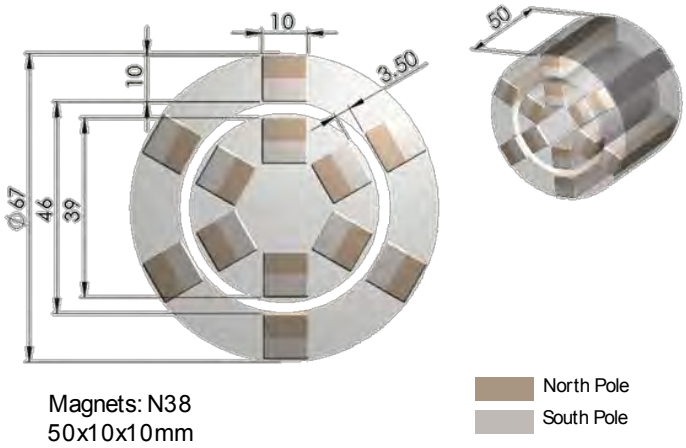

Figure 79 - Manipulator Coupling Schematic

Test Method

The test method used to obtain the torque vs. slip curve for this magnetic coupling was very different to the method used to test the thruster coupling. The test setup can be seen in Figure 80. The outer rotor was held stationary and a lever arm was attached to the inner rotor through which the torque was applied by hanging various weights. A protractor was attached to the inner shaft to measure the angle of slip between the inner and outer rotors. The lever arm only provided the calculated torque when horizontal and for every new value of applied torque the coupling's orientation had to be changed to ensure the lever arm was horizontal. A stainless steel 316 membrane was used between the two rotors.

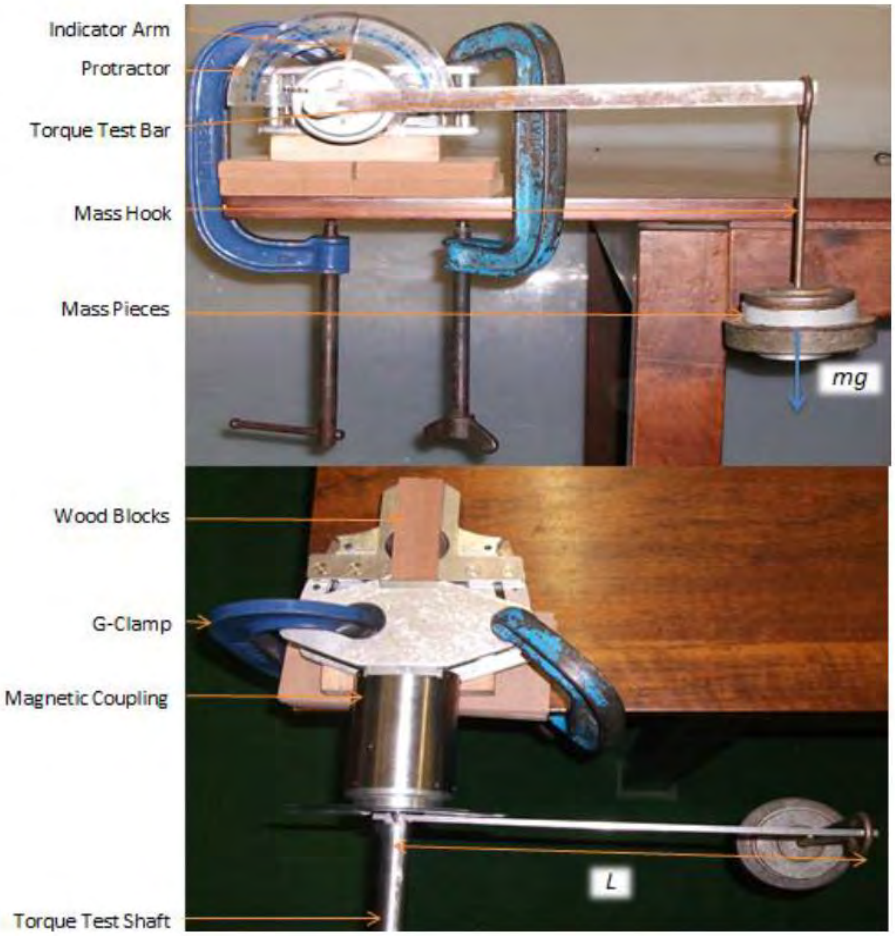

Figure 80 - Manipulator Module Test Setup [46]

Test Results

Figure 81 shows the torque vs. slip curve from the manipulator magnetic coupling. The pull-out torque proved to be 7.9 Nm at 24°, this was over double the intended pull-out torque. Clearly the effects of including a stainless steel membrane and increasing the number of pole pairs (therefore increasing the coupling's respective radial dimensions) were not well understood and thus resulted in an over designed magnetic coupling.

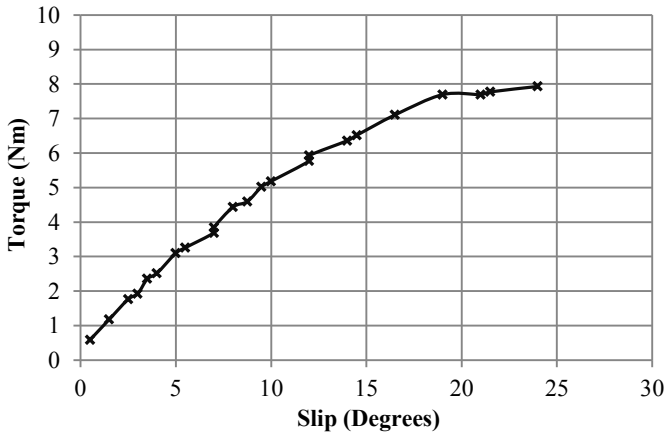

Figure 81 - Manipulator Module Magnetic Coupling Torque vs. Slip Results [46]

Test Method Remarks

The constant adjustment of the coupling for every applied torque value could have been a source of error in this test. The membrane material of stainless steel 316 does have a higher relative magnetic permeability (1.02) compared to HDPE (1.00) as used in the thruster module magnetic coupling test.

10.2 Magnetic Coupling Design Method Required

Knowing the methods used to design the previous couplings and considering the gross underestimation made in predicting the pull-out torque of the manipulator coupling it was identified that a validated design method was required in order to achieve efficient designs in magnetic couplings for the ROV's subsystems.

11 The Modelling of Magnetic Couplings

Two main methods were found to model magnetic couplings; analytical models and **F**inite **E**lement **M**ethods (**FEM**).

11.1 Analytical Models

The first analytical models of magnetic couplings involved simplified 2D scenarios that ignored end effects, included soft-iron yokes and used magnets that were trapezoid-arch shaped (as seen in Figure 82). Optimisation of these models focused on minimising the magnetic material required to transmit a given torque [47]. The soft-iron yokes helped to complete the magnetic circuits formed in the coupling between adjacent pole pairs.

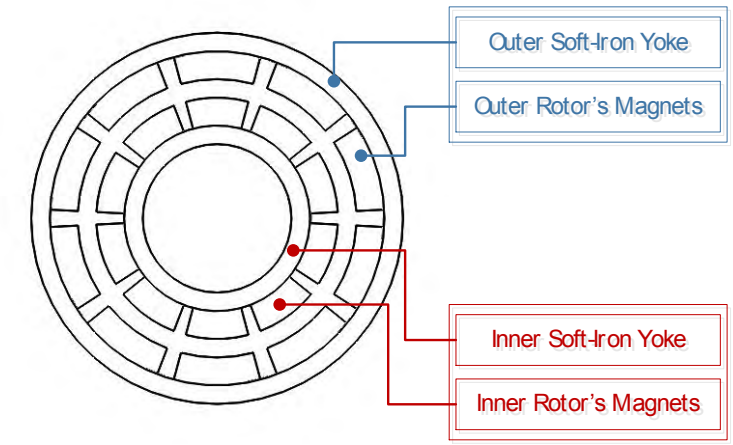

Figure 82 – Trapezoid-Arch Shaped Coaxial Magnetic Coupling Diagram

Furlani was the first to propose a 3D analytical model for the torque of coaxial magnetic couplings [48]. However, these models were restrictive due to the fact that to design an optimal coupling a custom trapezoid-arch magnet would have to be manufactured.

Due to magnet availability, the magnetic couplings would utilise cuboid magnets and because the couplings will be used in sea water, the soft-iron yokes would be excluded. The yokes would add weight, corrode and create a galvanic reaction with the other metals they would contact.

In 1984 G. Akoun and J. Yonnet developed a 3D analytical model to calculate the forces exerted between two parallel cuboid magnets [49]. This model was further expanded by Lemarquand to take into account an angular offset between the magnets that would occur in a mechanism such as a coupling. Lemarquand and Elies applied this to coaxial magnetic couplings and therefore established an analytical model applicable to the couplings that have been and will be designed for the ROV [50].

11.2 FEM Modelling of Magnetic Couplings

Similarly with analytical models, FEM analysis of magnetic couplings began with 2D methods. These 2D methods greatly reduced computation time and simplified the optimisation process compared to 3D methods, therefore being useful to approximate the optimum range of the coupling design and then 3D methods were implemented to further optimise the solution. [51]

Two methods can be used to calculate the torque of the coupling relative to slip; the Maxwell stress method and the virtual work method. The virtual work method calculates the force exerted on a pole by determining the work done when the pole is slightly displaced from the initial position. The energy stored in the air-gap is calculated and compared to the energy once the air gap has increased in volume. The difference between these energies is the work done and hence the torque can be determined. The Maxwell stress method computes local stresses at all points of a bounding surface, these stresses are summed by means of a surface integral. The component of the force that is tangential to the surface is determined and the torque derived. These two methods were detailed by Nagrial et al. The virtual work method has proved to be more accurate than the Maxwell stress method [36].

Wang et al. [34] and Wu et al. [51] provide considerations that must be taken when constructing the mesh and boundary conditions specific to coaxial magnetic couplings.

11.3 Conclusion

Wu et al. show a single comparison for an axial coupling between an analytical model, 2D FEM, 3D FEM and test results. The analytical model used was developed by Hornreich [47] and the 2D and 3D FEM methods were developed by Wu et al. [51]. The comparison is shown in Figure 83. The analytical model and the 2D FEM showed similar results as both methods ignored end-leakage effects. The 3D FEM obtained the most accurate result however it was the most intensive and difficult method regarding programming and computation [51].

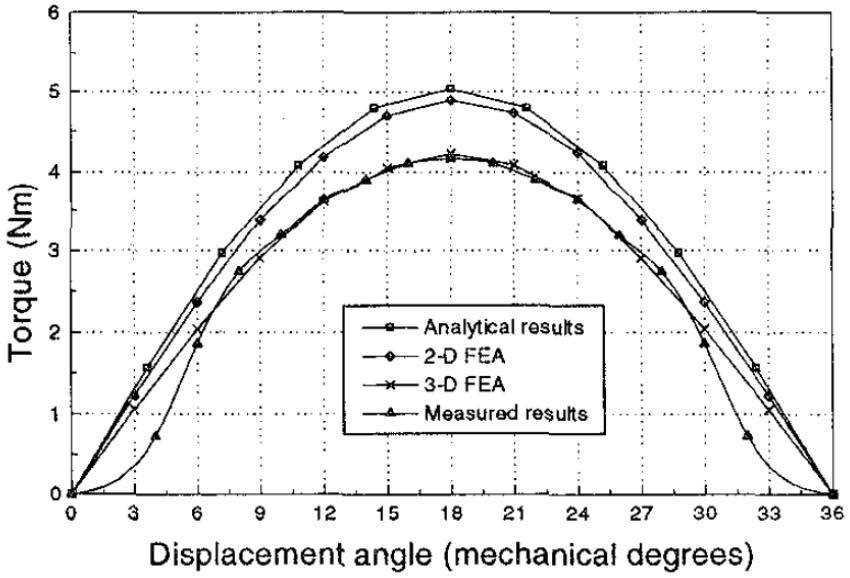

Figure 83 - Torque vs. Slip Comparisons of Multiple Modelling Techniques [51]

The comparison in Figure 83 shows an error of approximately 25% between the analytical model's result and the test result. Achieving this magnitude of error, although not optimal, would be an improvement in the design method used to design magnetic couplings for the ROV.

When having to select which method to develop several considerations such as the required accuracy of the model, the ease of development and the availability of software were taken into account. The magnetic couplings on the ROV do not have to provide precise and specific torques. However the couplings should be designed to be adequate for their respective function without being grossly overdesigned or under designed. The manipulator magnetic coupling was over designed and produced a pull-out torque 226% above what it was designed to produce. Producing a model that allows the final coupling to produce a torque ±25% of the designed torque (as the analytical model in Figure 83 did) is a significant improvement.

Without the availability of **c**omputer-**a**ided **d**esign (**CAD**) integrated electromagnetic FEM packages such as SolidWorks' EMS (also known as ElectroMagneticWorks) and ANSYS Maxwell producing an accurate 3D FEM model would have been developed from first principles and implemented using LS-DYNA's Maxwell solver. This task was considered out of the scope of this project and although a potentially very accurate model could have been developed (potentially to within ±2% of test results) it was deemed unnecessary for this application.

It was decided to implement the analytical model with the aim of it being used as a design tool when designing magnetic couplings for the ROV and simple enough for future students working on the ROV to use irrespective of their experience in FEM.

11.4 Magnetic Coupling Analytical Model

11.4.1 Introduction

An analytical model of cuboid coaxial magnetic couplings was developed using the paper by Elies and Lemarquand titled: '*Analytical Optimization of the Torque of a Permanent-Magnet Coaxial Synchronous Coupling'* [50]. This section steps through the stages required to build the model. The tangential force between two magnets is discussed and the geometry related to magnetic couplings is explained. This is combined to model the tangential forces magnets experience when rotating relative to each other and is applied to multipole magnetic couplings.

11.4.2 Tangential Forces between Two Magnets

Figure 84 shows the arrangement and symbols used to describe the situation of two magnets in proximity to each other. Magnet 0 is used as the reference position and its dimensions are noted by *a,b,c*. The dimensions of magnet 1 are *a',b',c'* and its position is given by the co-ordinate system *x', y', z'*. Magnet 1's position relative to magnet 0 is given by (x_{01},y_{01},z_{01}). The angle between the two planes X0Y and X'0Y' is θ. The magnets modelled are assumed to be parallelepiped and have a uniform residual magnetisation of J measured in Tesla.

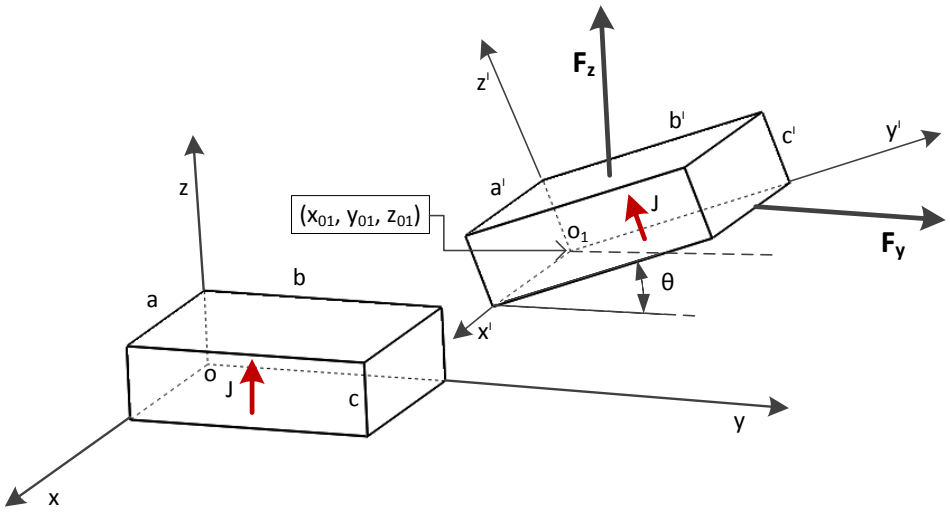

Figure 84 - Magnet Configuration and Magnetic Force Components

The force between the two magnets is broken into z and y components F_z and F_y. The tangential component is noted as F_y. The equation for the tangential component of the force is given in Appendix B.

11.4.3 Magnetic Coupling Geometry

Rotation of Magnet 1 around Magnet 0

In a magnetic coupling, magnet 1 will rotate around magnet 0 (as shown in Figure 85), therefore a function defining magnet 1's position relative to magnet 0 is required. This function shows the relation between two magnets as two rotors in a coupling are rotated relative to each other.

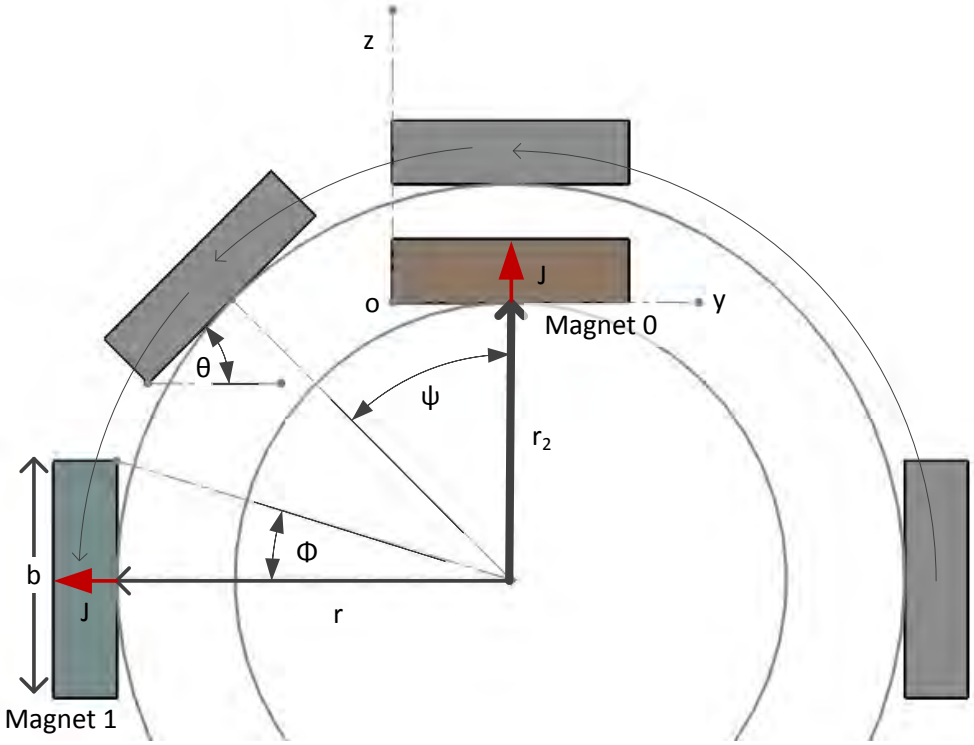

Figure 85 - Magnet 1 Rotating around Magnet 0

Magnet 1's motion is two dimensional and located in the Y0Z plane. Geometry is used to obtain functions for the y_{01} and z_{01} positions of magnet 1. These are derived as equations 12 and 13.

$$y_{01} = -\frac{r}{\cos\Phi}\sin(\psi + \Phi) + \frac{b}{2} \tag{12}$$

$$z_{01} = -\frac{r}{\cos\Phi}\cos(\psi + \Phi) - r_2 \tag{13}$$

The angular displacement is the same as the angle between the two magnets. The angle Φ is the polar half-spread of magnet 1 and is given by equation 14.

$$\Phi = arctan\left(\frac{b}{2r}\right) \tag{14}$$

The equation for the tangential force F_y was coded using LabVIEW and equation 12 and 13 were used to input y_{01} and z_{01} for a displacement of -180° to +180°. Table 23 shows the inputs used to replicate the example shown by Elies and Lemarquand. Figure 86 provides the comparison between the LabVIEW result and Elies and Lemarquand's result.

Table 23 - Inputs Used to Calculate Tangential Force

Description	Symbol	Value	
Magnet Depth	a	1	m
Magnet Width	b	30	mm
Magnet Height	c	10	mm
Radius of Magnet 1	r	90	mm
Radius of Magnet 0	r_2	70	mm
Magnetisation Strength	J	1	T

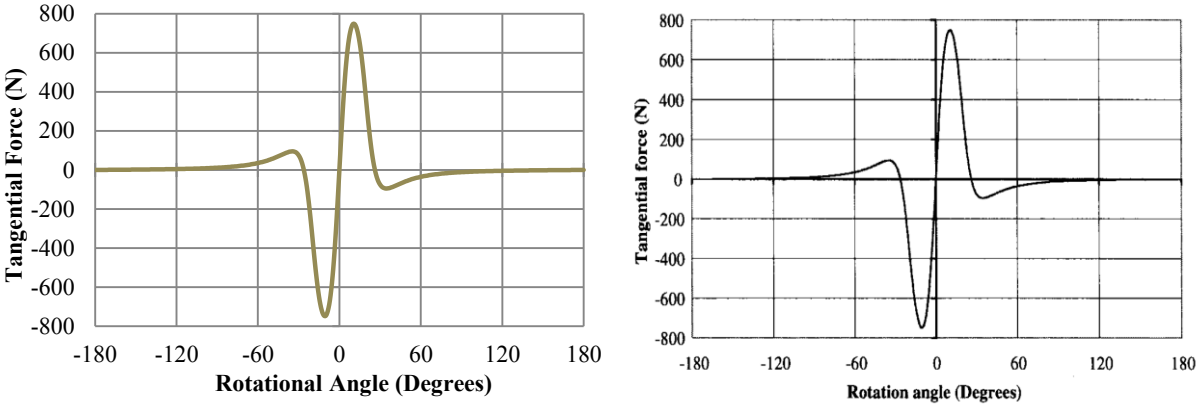

Figure 86 – LabVIEW Result (to the right) compared to Elies and Lemarquand's Result (to the left)

When magnet 1 is facing magnet 0, the tangential force is zero. As the magnet rotates the tangential force rapidly increases and reaches a maximum. As the magnet continues to rotate, the tangential force changes direction, as the rotating magnet is gradually exposed to the other pole of the stationary magnet. When magnet 1 is 180° from its original position, there is zero tangential force.

11.4.4 Multiple Pole Magnetic Coupling Geometry

To calculate the torque transmitted by a magnetic coupling, the tangential force equation was applied to a multiple pole magnetic coupling to determine the total torque.

Figure 87 shows the coupling example used to derive expressions to describe the geometry of the magnetic coupling. The outer rotor's radius is noted as r, the air-gap, e, is defined as the minimum distance between the outer and inner rotor magnets and is shown in Figure 88. The number of pole pairs is noted as p. A coupling with p pole pairs will have 2p magnets per rotor and 4p magnets in total. The other variables in Figure 87 can be expressed as functions of those discussed.

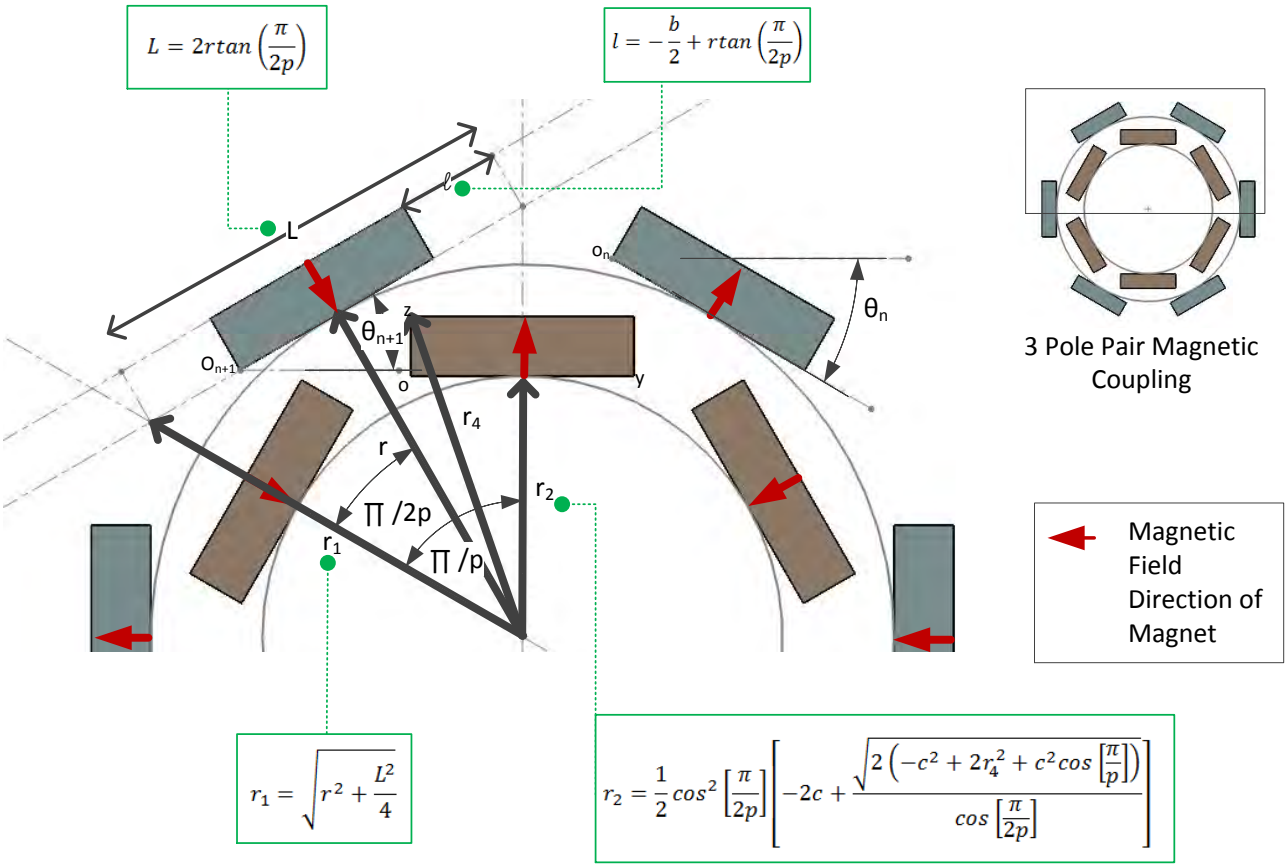

Figure 87 - The Geometry of the Magnetic Coupling

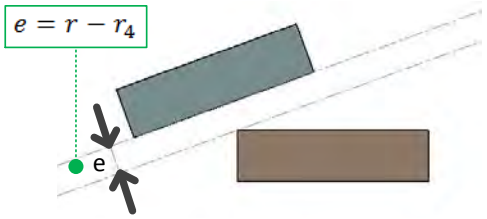

Figure 88 - Definition of Air Gap

11.4.5 Applying the Tangential Force to a Multiple Pole Magnetic Coupling

The tangential force relation between two magnets in a coupling arrangement has been discussed and the geometry of multiple magnets has been defined. These two are brought together to calculate the torque produced by a magnetic coupling with multiple pole pairs.

Coordinates of the Magnets

The coordinates of the outer magnets with respect to one of the inner magnets *(i)* in the YZ plane can be described by equations 15 and 16. These are adapted from equation 12 and 13 to include the position of the inner magnets. Each of these inner magnets in the inner rotor is represented by *i* which is an integer and varies from zero to 2p.

$$y_i = -\frac{r}{\cos\Phi}\sin\left(\psi + \Phi + i\frac{\pi}{p}\right) + \frac{b}{2} \qquad (15)$$

$$z_i = \frac{r}{\cos\Phi}\cos\left(\psi + \Phi + i\frac{\pi}{p}\right) - r_2 \quad (16)$$

$$\theta_i = i\frac{\pi}{p} + \psi \quad (17)$$

The angular shifting between the inner and outer rotor is defined as ψ and the angle of rotation between the magnets remains as θ.

Calculation of the Torque

The torque exerted by one inner magnet *(i=0)* on one outer magnet was calculated for a range of rotation angles. This calculation was similar to the calculation of the tangential force in the setup described in Figure 85. To obtain the torque created by the next inner magnet *(i=1)* on the same outer magnet the previous curve of the torque created by the outer magnet and magnet *(i=0)* was then shifted by an angle of π/p, and multiplied by $(-1)^i$ to take into account the change in magnetisation direction. This process was repeated for each inner magnet. The sum of these torque curves represent the torque experienced by one outer magnet from all the inner magnets. These curves are shown in Figure 89. This torque multiplied by 2p (the number of outer magnets in a complete coupling) provides the total transmitted torque. A 2 pole pair magnetic coupling with the parameters shown in Table 24 was used as an example to show this method for calculating the torque one outer magnet experiences from all the inner magnets.

Table 24 - Parameters of Two Pole Pair Magnet

Description	Symbol	Value	
Magnet Depth	a	1	m
Magnet Width	b	11	mm
Magnet Height	c	10	mm
Radius of Magnet 1	r	90	mm
Mechanical Air Gap	e	2	mm
Magnetisation Strength	J	1	T

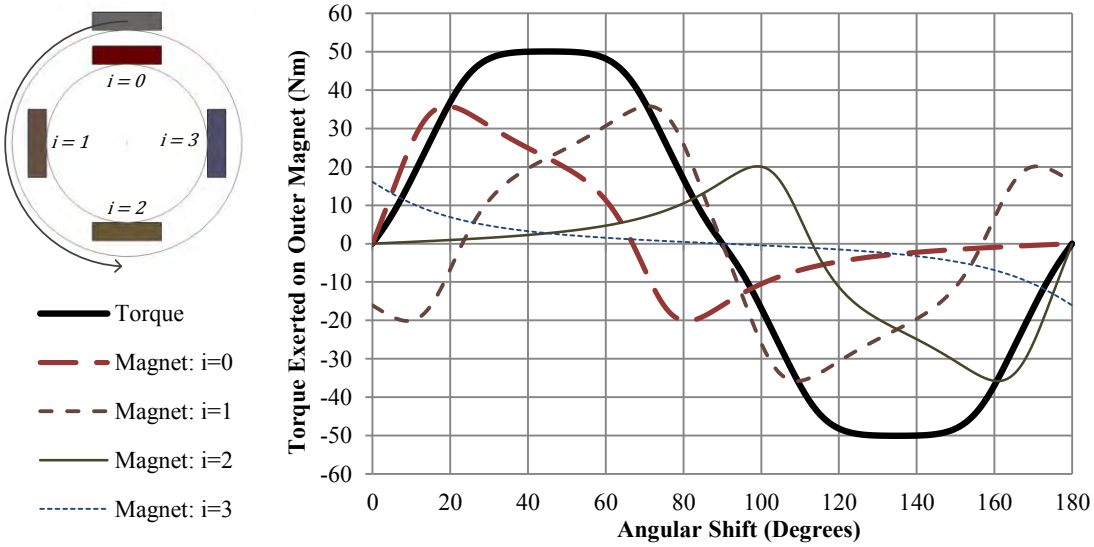

Figure 89 - Torque on One Outer Magnet from All Inner Magnets

From Figure 89 it can be seen that the period of the torque is 2π/p. When the angular shift between rotors is zero the magnets' faces are parallel therefore the torque is zero, their magnetisations are in the same direction therefore this position is stable. At the angle π/p the magnets' faces are once again parallel and the torque is zero but their magnetisations are in opposite directions and therefore this position is unstable.

11.4.6 Optimisation of the Analytical Model

Various parameters were compared to determine optimum ranges for magnetic coupling designs. For a given air gap the maximum torque can be achieved for an optimum number of pole pairs and optimal magnet angular width. For an air gap of 2 mm it was found that the maximum torque was always achieved when the magnet width was set to the maximum width possible to fit within the internal rotor. Many of the optimum values determined form the analytical model provided parameters above what was achievable for, or applicable to the magnetic coupling designs required for the ROV.

11.4.7 Optimal Magnetisation Arrangements of Coaxial Magnetic Couplings

In the paper *"Optimal Design of Cylindrical Air-Gap Synchronous Permanent Magnetic Couplings"* [52] by Charpentier and Lemarquand the analytical model previously discussed was expanded to include the change of each magnet's magnetisation direction. Three types of couplings were examined; the first type was the subject of the analytical model discussed, the second type has tangentially orientated magnets and the third type is a combination of the two. Figure 90 shows these three types of coaxial couplings.

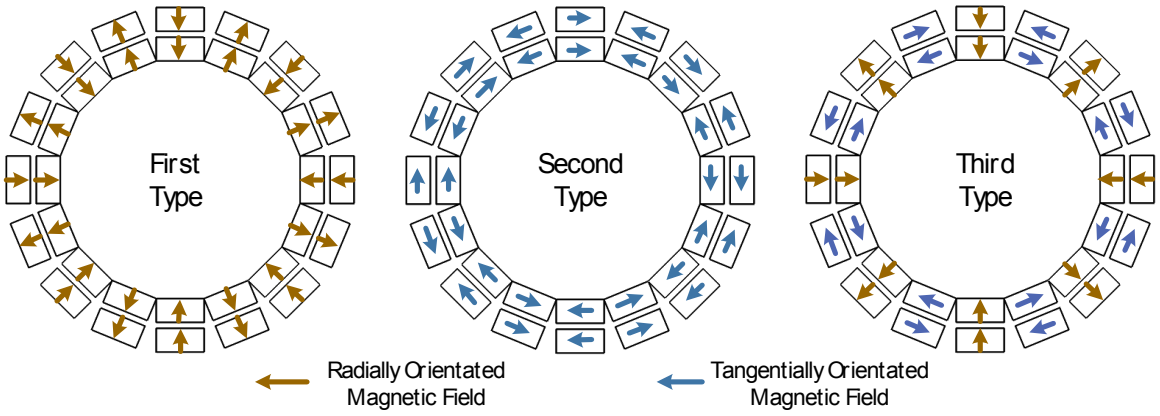

Figure 90 - Three Types of Coaxial Magnetic Couplings

The third type provided the largest pull-out torque for magnet volume minimisation and inertia reduction. Charpentier and Lemarquand concluded that this arrangement was superior to the traditional arrangement featured in the analytical model.

11.4.8 Coupling Designs Applicable to ROV

Even though the third type of coupling featured in Figure 90 was the optimum arrangement of the magnets' magnetisation orientations, two factors made this type of coupling unfeasible for the coupling designs applicable to the ROV. The first factor was that obtaining magnets with different magnetisation directions relative to their dimensions was not possible. The second factor was that the couplings required for the ROV had too few pole pairs to implement the third type of magnetic coupling. For these reasons the first type of coupling was selected as the arrangement to model and validate.

11.4.9 Assumptions in the Model

The model assumes the magnets are ideal parallelepipedic cuboids and are ideally and uniformly magnetised. Additionally the model assumes the magnets are perfectly aligned in all dimensions and orientations within the coupling and that the two rotors of the coupling are perfectly concentric to each other.

In reality and in the test couplings the magnets have rounded edges, are not ideally and uniformly magnetised, and the magnets are not perfectly aligned in all directions and orientations.

It was expected that these assumptions would contribute to a greater modelled torque than the test results as all these assumptions would lead to a decrease in coupling performance.

11.5 Previous Couplings at RARL Compared to Analytical Model

11.5.1 Thruster Coupling Test Results vs. Analytical Coupling Model

Figure 91 shows the coupling torque vs. slip output of the model for the thruster coupling developed by T. Knight in 2012. This was a two pole pair magnetic coupling with a cross section seen in Figure 91. The magnets used were neodymium (grade N38) permanent magnets, the residual magnetism of N38 magnets ranges from 1.23 T – 1.26 T [45]. These magnetisation values were input into the model to produce a maximum and minimum torque value.

From zero slippage to 90° of slip two pull out torques can be seen with a local minimum at 45°. At 90° the resultant torque is zero however this position is unstable as the force between opposing magnets is repelling them from each other.

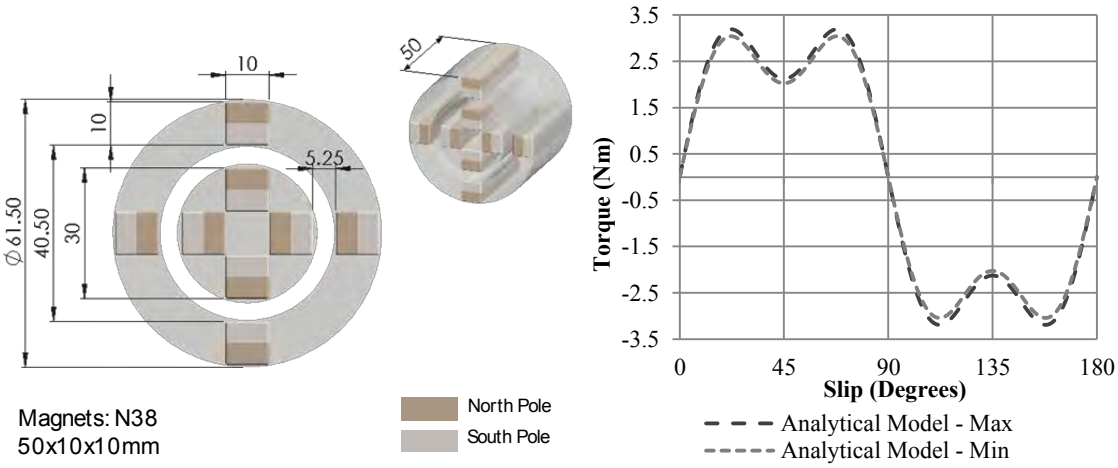

Figure 91 - Thruster Module Coupling Diagram and Analytical Model Output

The test results vs. the model output (in Figure 92) show a correlation with the measured results being less than the model output. This was expected as the model relies on several assumptions stated in Section 11.4.9 that will produce a test result less than the model calculation. These assumptions contribute to the model producing results larger than those measured.

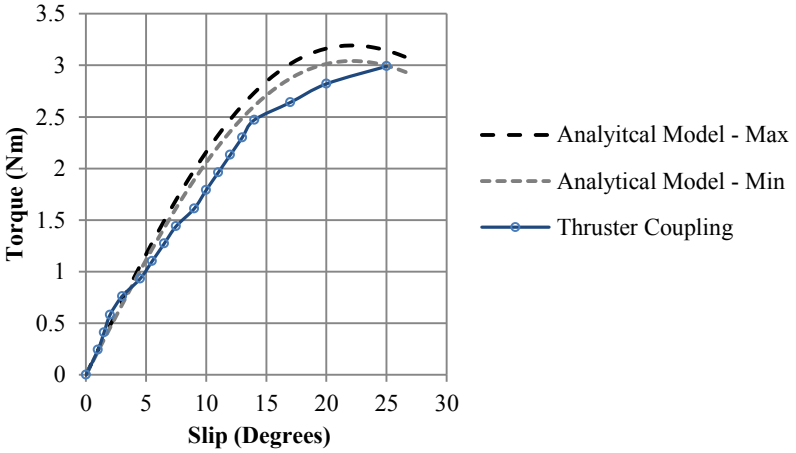

Figure 92 – Analytical Model Output Compared to Measured Torque vs. Slip for the Thruster Module Coupling

11.5.2 Manipulator Coupling Test Results vs. Analytical Output

The 3 pole pair magnetic coupling designed to actuate the manipulator mechanism was modelled. The diagram for the coupling and the output from the model can be seen in Figure 93. The same N38 magnets found in the thruster coupling were used in this coupling. The period for the torque-slip curve is 120° for a three pole pair coupling.

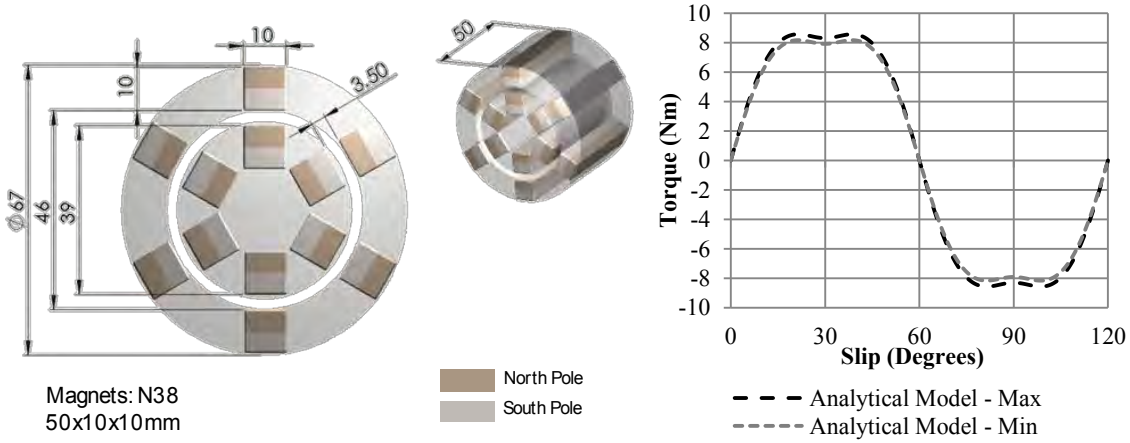

Figure 93 - Manipulator Coupling Diagram and Analytical Model Output

The measured results obtained by M. Finbow are compared to the analytical model output in Figure 94. Similarly to the thruster module results the measured values are lower than the model output. Again this was attributed to assumptions made in the model.

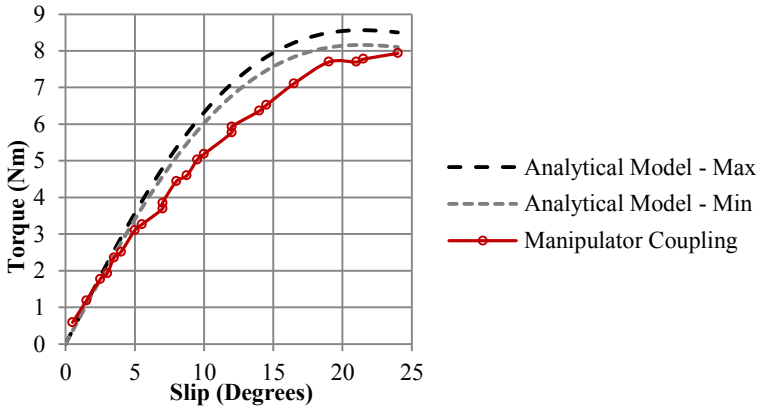

Figure 94 - Analytical Model Output Compared to Measured Torque vs. Slip for the Manipulator Coupling

11.6 Concluding Remarks

The analytical model chosen and developed fulfilled the requirement identified in Section 10.2 which stated that a method was needed to efficiently design magnetic couplings for the ROV. The analytical model suited the types of magnetic couplings that can be produced at RARL. These magnetic couplings have the following characteristics:

- Coaxial and synchronous magnetic couplings.
- No soft iron yokes are used in order to reduce weight and corrosion.
- The magnets used are cuboid (not custom made trapezoidal-arch shaped magnets).

The analytical model output correlated with the torque-slip tests done on the previous magnetic couplings built at RARL. However this was insufficient to validate the analytical model because it was only two results and the accuracies of the test methods used were questionable.

12 Validation of the Analytical Model

12.1 Introduction

A correlation between the analytical model's output and the previous tests done on magnetic couplings in the RARL was shown in the previous section. To be able to use the model as a design tool for future couplings the model needed to be further validated. Several factors influenced the manner in which the validation was done, these were the:

- validation of couplings within the range of future coupling designs
- use of magnets that were readily available and cost effective
- minimisation of the number of parts and magnets required for validation

Several parameters required validation in the model, these were identified as the:

- effect of the number of pole pairs in the coupling
- use of different magnet grades
- relationship between torque and mechanical air gap
- effect of a stainless steel 316 membrane

This section begins with a look at available magnets and the torque range in which future couplings will be designed for the ROV. The test couplings are then shown. A standardised test method is detailed which produced accurate torque-slip curves for all the test couplings, the thruster coupling and the manipulator coupling. The results are analysed and the validation of the analytical model is concluded.

12.2Coupling Torque Range

Two modules that will require magnetic couplings are the manipulator module and the tilt module.

12.2.1 Manipulator Module and Sampling Tools

As determined by M. Finbow the manipulator module can grip rocks and cut through kelp and fishing nets with 1.7 Nm applied to the mechanism [46]. This torque is specific to the mechanism however it indicates what is capable with 1.7 Nm of torque transmitted. Future sampling equipment and manipulators may require larger torques.

12.2.2 Tilt Module

The tilt module utilises a Dynamixel RX-64 servo motor that produces 5.3 Nm stall torque [53]. The pull-out torque of the magnetic coupling must be less than the stall torque of the servo motor. If an object were to become entangled in the mechanism the coupling must slip before the stall torque is reached. This ensures the gearbox and motor are protected from being overloaded and it protects the drivetrain from rapid shock loading that could occur if the tilt tray collides with an object.

12.2.3 Torque Range

The torque range of the couplings was chosen to be 1 Nm – 10 Nm. This range was deemed adequate to validate the model in the correct range for the thruster coupling, the tilt module coupling and future coupling designs (for manipulators and sampling tools) which may require additional torque.

12.3Available Magnets

Figure 95 shows the magnets that are available locally and in small quantities. The N38 50 mm x 10 mm x 10 mm magnet was the one used in the thruster and manipulator coupling. The three magnets in the centre of the range with the labels above the magnets were chosen as the magnets with which to develop the test couplings. The magnets on either side were deemed too large or too small. The three magnets selected are made from different grades of neodymium.

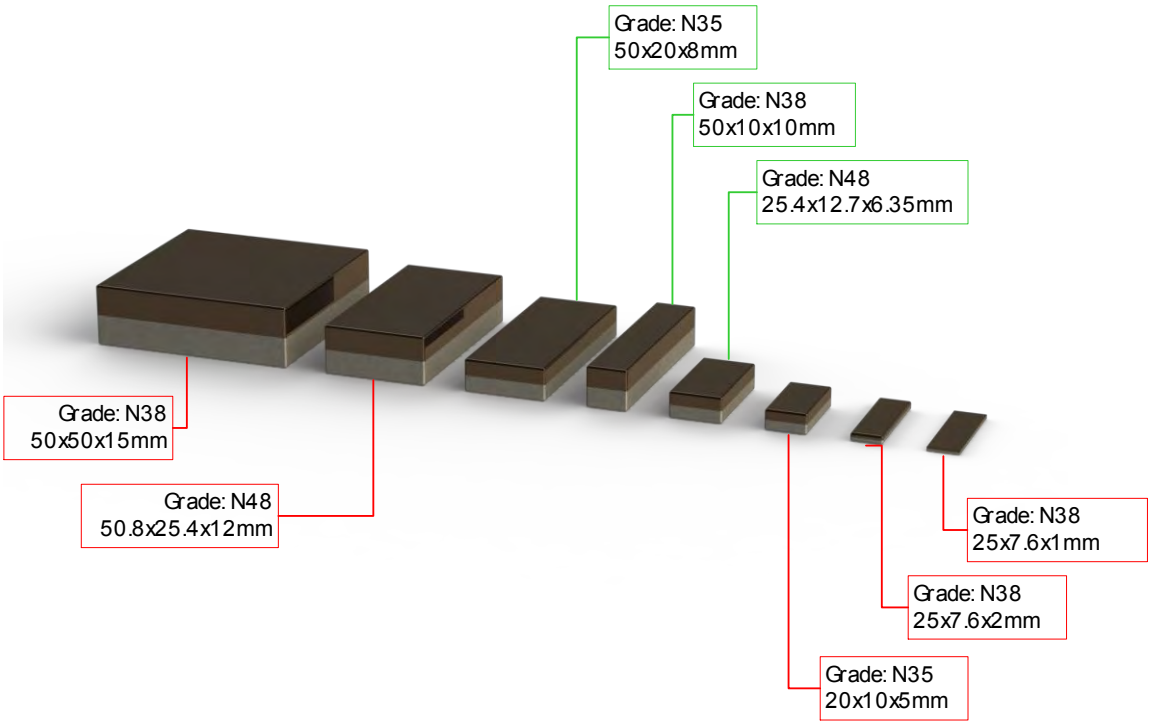

Figure 95 - Available Neodymium Magnets

12.4 Validation Couplings

All the validation couplings were designed to use the maximum magnet width possible for the inner rotor. This is done to maximise the magnetic field density in the air gap between the rotors. As stated by Elies and Lemarquand the maximum torque achieved for all couplings with a 2 mm air gap utilised the largest magnet width possible for the diameter of the inner rotor [50].

12.4.1 N48 Magnetic Couplings

The first set of couplings used the N48 25.4 mm x 12.7 mm x 6.35 mm magnets and ranged from two to four pole pairs. The model inputs and outputs are shown in Table 25 and predicted torque-slip curves are shown in Figure 96. The pull-out torques of the couplings were expected to range from 1.44 Nm – 8.73 Nm.

Table 25 - Analytical Model Inputs and Torque Outputs for N48 Series of Couplings

Magnet Properties			Two Pole Pair			Three Pole Pair			Four Pole Pair		
J	1.37 - 1.41	T	Air Gap - e	3.5	mm	Air Gap - e	3.5	mm	Air Gap - e	3.5	mm
a	25.4	mm	Radius - r	18	mm	Radius - r	23.5	mm	Radius - r	26.5	mm
b	12.7	mm	Maximum	1.52	Nm	Maximum	4.75	Nm	Maximum	8.73	Nm
c	6.35	mm	Minimum	1.44	Nm	Minimum	4.49	Nm	Minimum	8.24	Nm

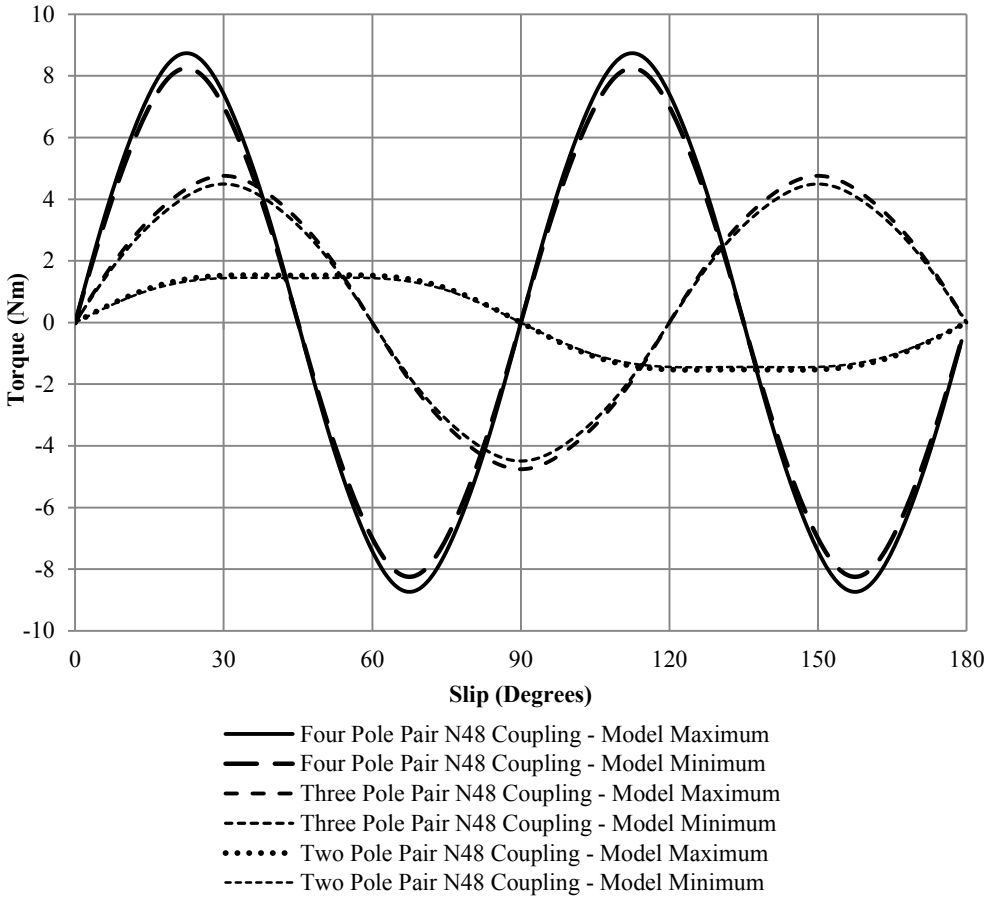

Figure 96 – Analytical Model Output Curves for N48 Series of Couplings

12.4.2 N38 Magnetic Couplings

The second set of couplings was a repeat of the thruster coupling and the manipulator coupling. Because the results for these couplings were obtained using two different apparatuses and two different test methods they required retesting using the same apparatus as the other couplings studied. A four pole pair coupling using these magnets was not tested as it would have produced torques beyond the design range of 10 Nm.

12.4.3 N35 Magnetic Coupling

The N35 magnetic coupling is a two pole pair coupling and it uses the largest of the selected magnets. A three and four pole pair coupling were not developed because these would have produced pull-out torques exceeding the design range of 1 Nm– 10 Nm. The model inputs and outputs are shown in Table 26 and the modelled torque vs. slip curve is shown in Figure 97.

Table 26 - Analytical Model Inputs and Torque Outputs for N35 Series of Couplings

Magnet Properties			Two Pole Pair		
J	1.18 - 1.23	T	Air Gap - e	3.5	mm
a	50	mm	Radius - r	24.5	mm
b	20	mm	Maximum	5.86	Nm
c	8	mm	Minimum	5.39	Nm

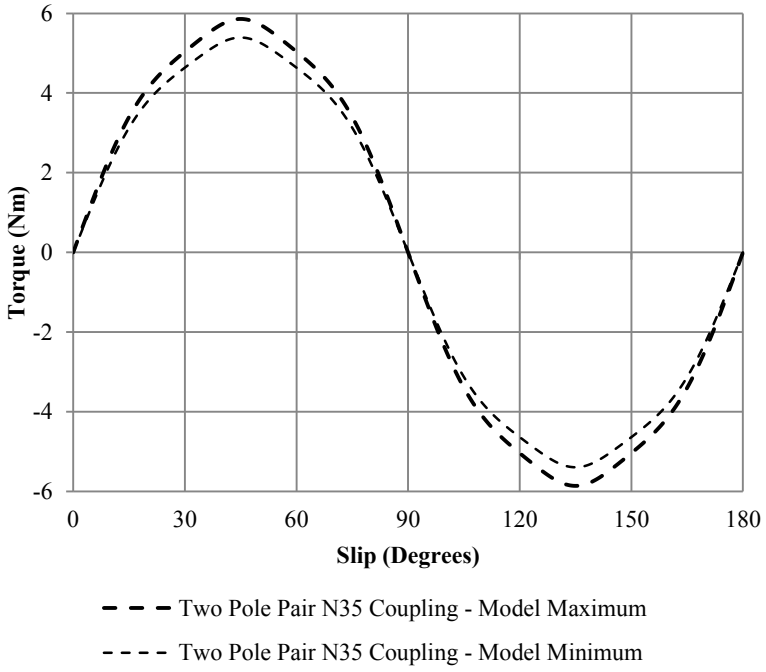

Figure 97 - Analytical Model Output Curves for the Two Pole Pair N35 Coupling

12.4.4 Summary of Test Couplings

The test couplings were designed to validate various parameters. The number of pole pairs was changed for the same magnet and the magnet was changed for the same number of pole pairs, this is shown in Figure 98. The N48 three pole pair coupling was used to test the effect that varying the air gap has on the pull-out torque. The manipulator coupling was tested with and without the membrane to see the effect the membrane had on the pull-out torque.

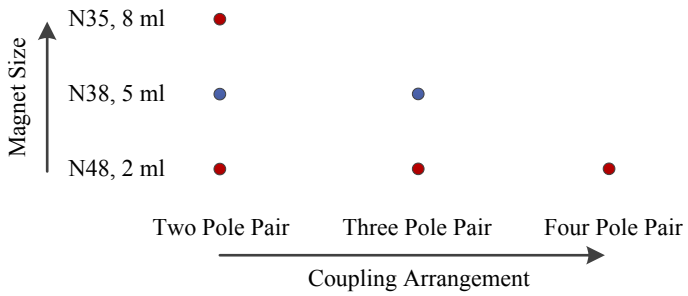

Figure 98 - The Number of Pole Pairs and the Magnet Grades of the Test Couplings

12.5 Standardised Test Method

The objective of testing the couplings was to obtain the torque-slip curve therefore the torque generated on the stationary rotor and the angular displacement of the rotating rotor needed to be measured simultaneously. Figure 99 shows this diagrammatically.

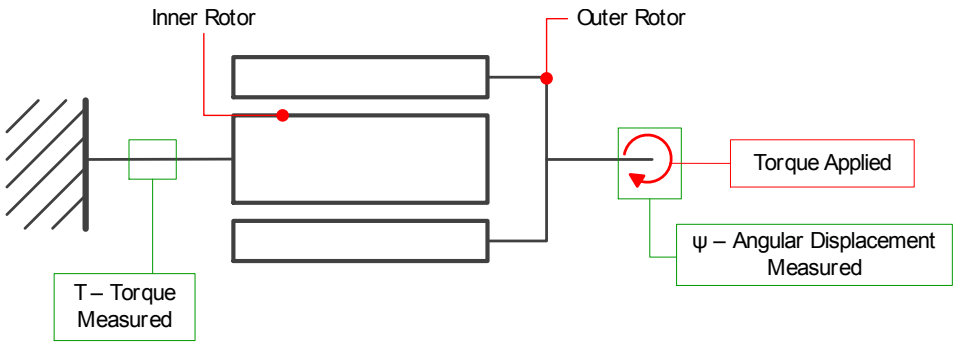

Figure 99 - Coupling Test Schematic

12.5.1 Angular Displacement Measurement

Three common encoders used to measure the rotation of a shaft are optical, magnetic and mechanical contact encoders. Optical and magnetic encoders produce digital outputs, are well suited for continuous turn applications and have long service lives. Mechanical contact encoders are better suited to slow movement applications and produce and analogue output. Due to the mechanical contact they are not recommended for prolonged use [54]. A form of mechanical contact encoder is a potentiometer. For this application a potentiometer was used because:

- the shaft did not rotate continuously
- the number of rotations completed was minimal
- no digital circuitry or digital processing was required
- potentiometers are economical compared to optical or magnetic encoders

The output from the potentiometer was connected to an amplifier and low pass filter to increase and smooth the measurement. The circuitry for the potentiometer is shown in Figure 100.

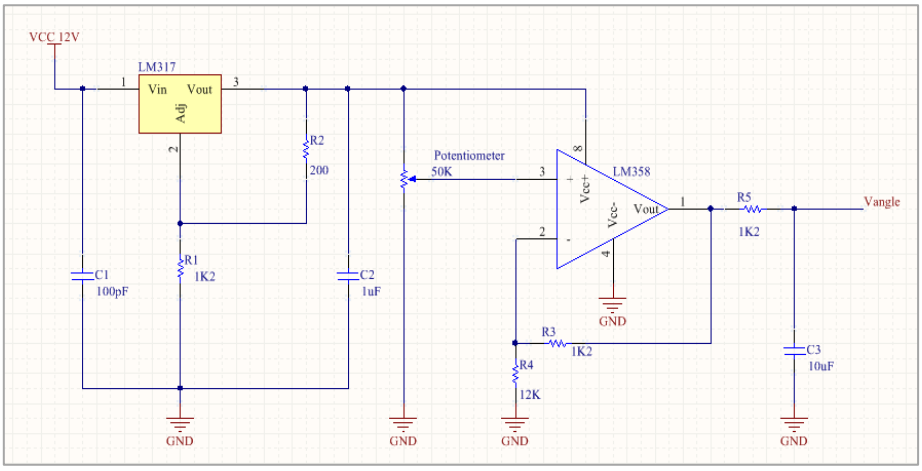

Figure 100 - Potentiometer Circuitry - Amplifier and Filter

12.5.2 Torque Measurement

The torque was measured using a full bridge strain gauge attached to an aluminium tube section. This allowed the torque value to be observed up to and beyond the pull-out torque. The strain gauge was connected to a strain indicator that amplified the signal. The output from the strain indicator and output from the potentiometer circuitry were connected to an analogue **d**ata **acq**uisition unit (**DAQ**) which allowed the measurements to be logged simultaneously using LabVIEW. This arrangement is shown in Figure 101.

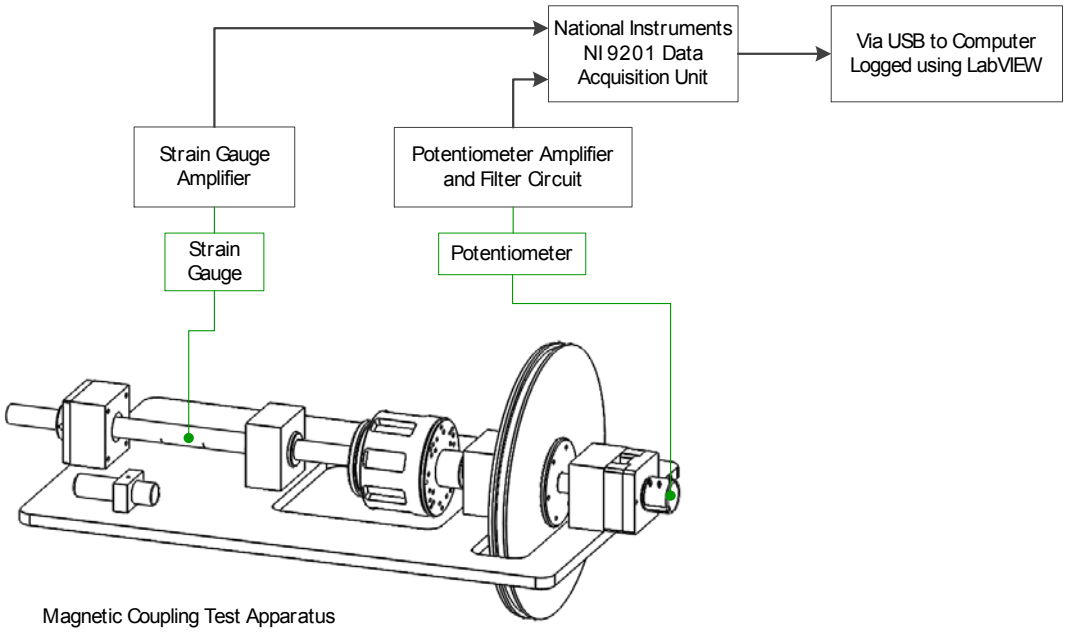

Figure 101 - Magnetic Coupling Test Setup

12.5.3 Magnetic Coupling Test Apparatus

Figure 102 shows a diagram of the test rig designed and used to acquire the torque-slip curves for the magnetic couplings. The test rig fixes the aluminium tube and strain gauge which is connected to the inner rotor of the coupling. The outer rotor is coupled to the potentiometer and rotates around the inner rotor. To generate the torque to make the couplings slip a wheel was placed onto the outer rotor's shaft.

An acrylic protractor was laser cut and placed on to the wheel and a laser pointer was installed on the base of the test rig. These two components were used to calibrate the potentiometer to produce accurate angular displacement measurements.

Calibrations for the angular displacement and the strain gauge are detailed in Appendix C.

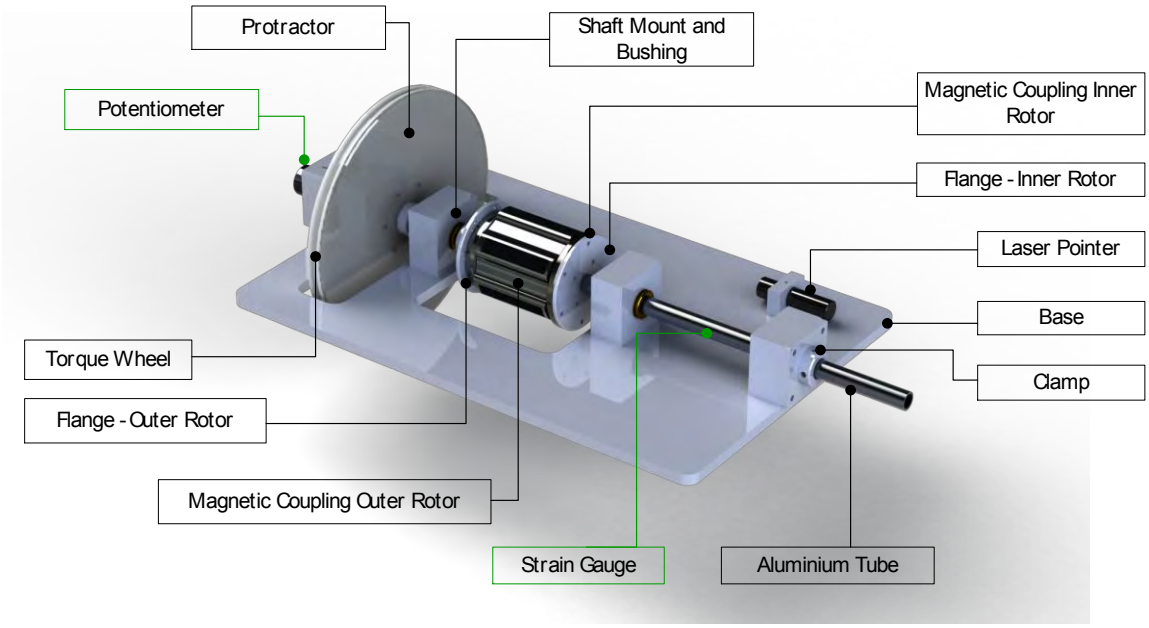

Figure 102 - Magnetic Coupling Test Apparatus

12.6 Test Results

12.6.1 Initial Results

The initial coupling test results showed a correlation with the model output. The test results for the three N48 grade magnetic couplings are plotted against the average output produced from the analytical model in Figure 103. It can be seen that at zero torque the measured curves are in phase with the model output however for increasing torque the results become out of phase with the model.

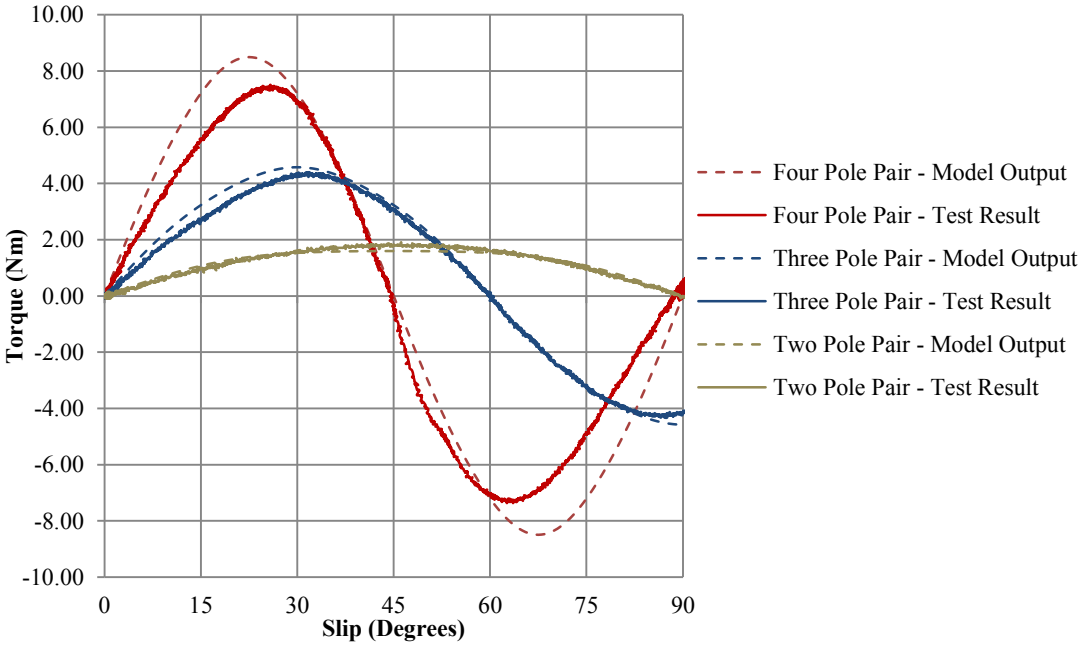

Figure 103 – N48 Magnetic Couplings - Initial Results vs. Model Output

This phase distortion that was proportional to torque was attributed to flexibility in the test rig. As the torque increased the torsion on the aluminium tube increased therefore creating twist in the tube. This twisting changed the angle of the inner rotor and therefore changed the relative angle between the two rotors.

12.6.2 Flexibility and Play in the Test Rig

To test the amount of twist in the test rig, the magnetic coupling was removed and the flanges for the inner and outer rotors were bolted together. This fastened connection created a continuously coupled shaft from the clamp to the potentiometer. The torque on the shaft was increased and decreased in both directions and the torque and angle measurements were logged and graphed in Figure 104. A linear relationship between torque and twist was expected however the result showed a nonlinear response with hysteresis occurring between increasing torque and decreasing torque.

A loose fit was observed where the flange for the inner coupling rotor connected to the aluminium tube. To remove this loose fit the two parts were welded together. The flexibility of the test rig was measured again and the response was improved (shown in Figure 105). Approximately 1° separation was measured between the increasing and decreasing torque curves. This discrepancy occurred because of a dimensional tolerance between outer coupling flange and the shaft connected to the potentiometer. This separation was considered acceptable for validating the

analytical model. The amount of twist according to torque obtained from Figure 105 was used to correct the measured slip angle and obtain the true slip angle between the rotors.

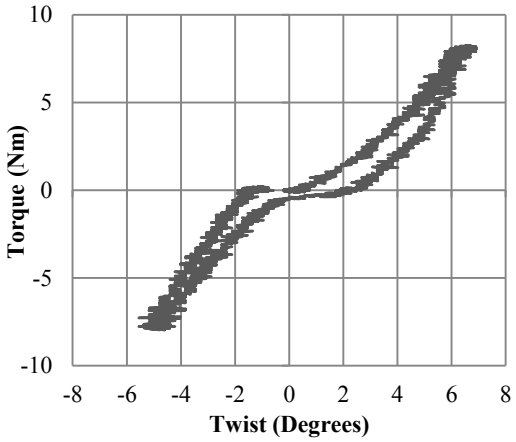

Figure 104 - Flexibility Tests Before Flange Modification

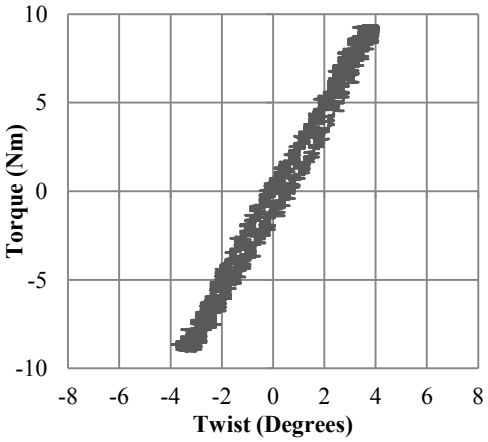

Figure 105 - Flexibility Tests After Flange Modification

12.6.3 Final Results

Coupling Test Results

The results obtained from the coupling tests are shown in Table 27. The torque vs. slip curves for each coupling test are shown from Figure 107 to Figure 113. A correlation between the analytical model outputs and the obtained test curves was evident. The most accurate test result when compared to the analytical model estimation, was the three pole pair N48 magnetic coupling that produced a pull-out torque of 1.11% below the minimum pull-out torque from the model.

The least accurate results occurred in two of the two pole pair magnetic couplings, one with the N48 magnet and the other with the N35 magnet. The respective pull-out torques were 16.34% and 23.21% greater than modelled. Figure 106 shows the percentage error in the modelled pull-out torques for each coupling.

In Figure 107, Figure 110 and Figure 111 the local minimum torque that occurred in the model's output was consistently less pronounced in the test results. Figure 112 shows the comparison between the previous test results obtained for the thruster and manipulator couplings compared to the tests completed with the coupling test rig.

Table 27 - Magnetic Coupling Test Results

Magnet Grade	Magnet Dimensions (mm)	Number of Pole Pairs	Air Gap (mm)	Pull-out Torque (Nm)			% Error in Model
				Model Maximum Output	Model Minimum Output	Test Result	
N48	25.4 x 12.7 x 6.35	2	3.5	1.53	1.44	1.78	16.34
N48	25.4 x 12.7 x 6.35	3	3.5	4.75	4.49	4.44	-1.11
N48	25.4 x 12.7 x 6.35	4	3.5	8.73	8.24	7.51	-8.86
N38	50 x 10 x 10	2	4.2*	3.21	3.06	2.88	-5.88
N38	50 x 10 x 10	3	2.9*	8.72	8.31	7.87	-5.29
N35	50 x 20 x 8	2	3.5	5.86	5.39	7.22	23.21

*Couplings were designed during previous projects

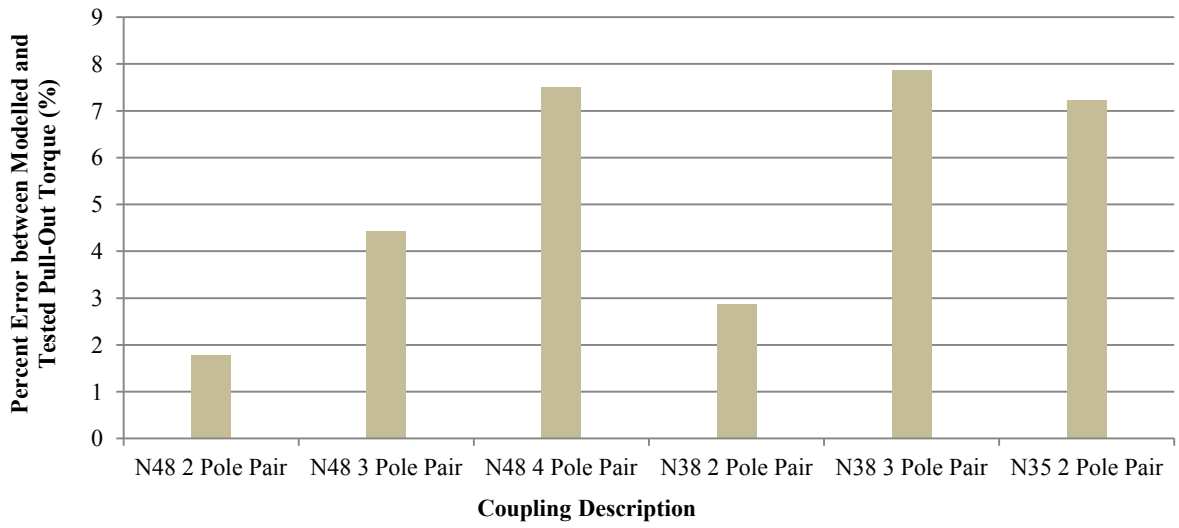

Figure 106 - Percent Error between Model and Test Results

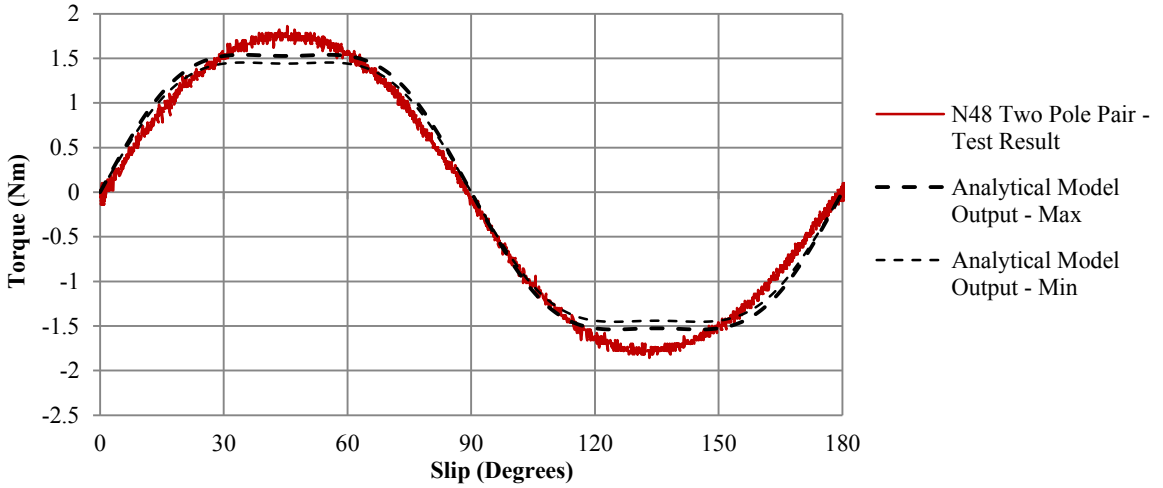

Figure 107 - N48 Two Pole Pair Magnetic Coupling Torque vs. Slip Curve

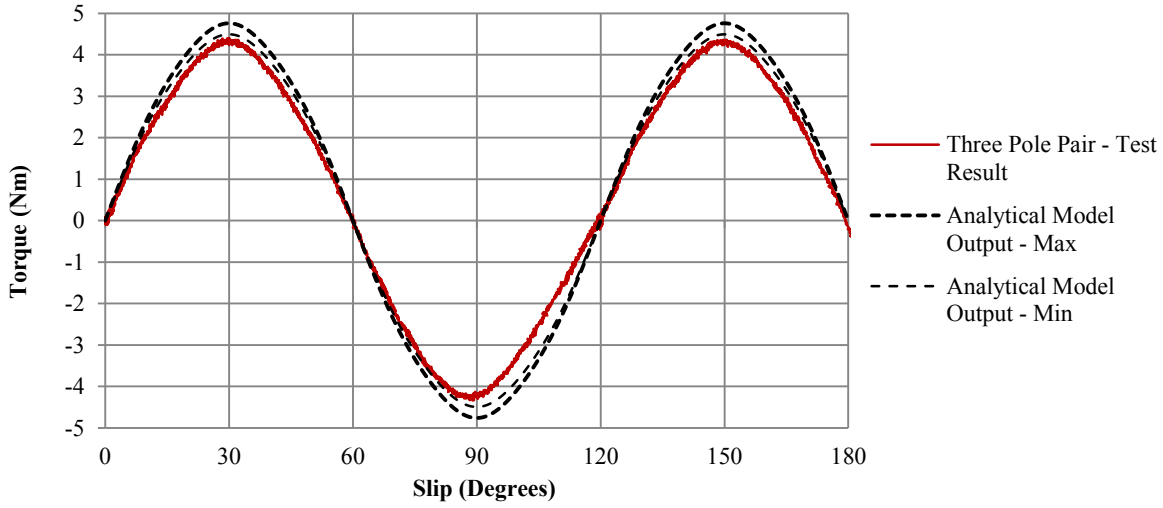

Figure 108 - N48 Three Pole Pair Magnetic Coupling Torque vs. Slip Curve

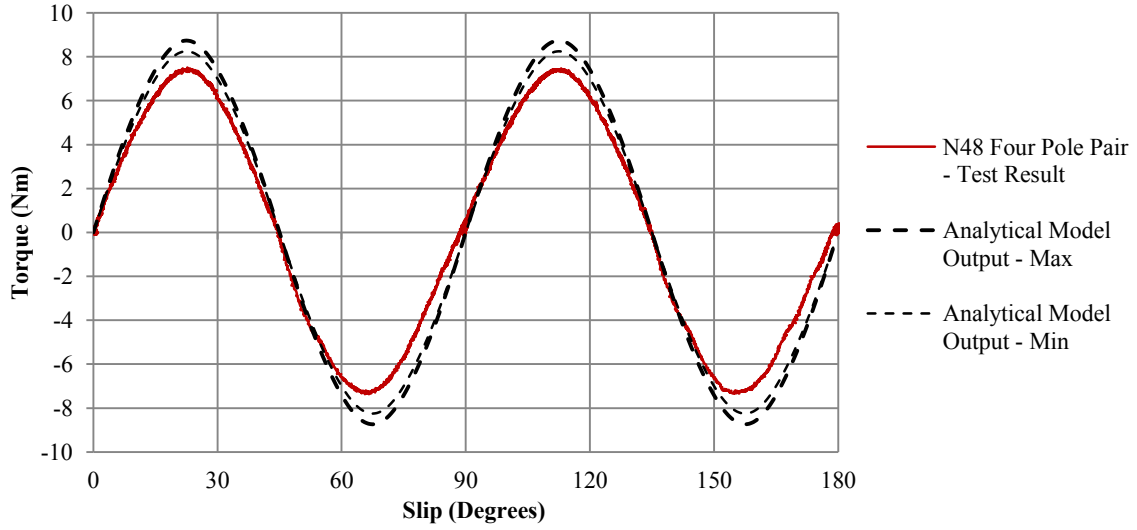

Figure 109 - N48 Four Pole Pair Magnetic Coupling Torque vs. Slip Curve

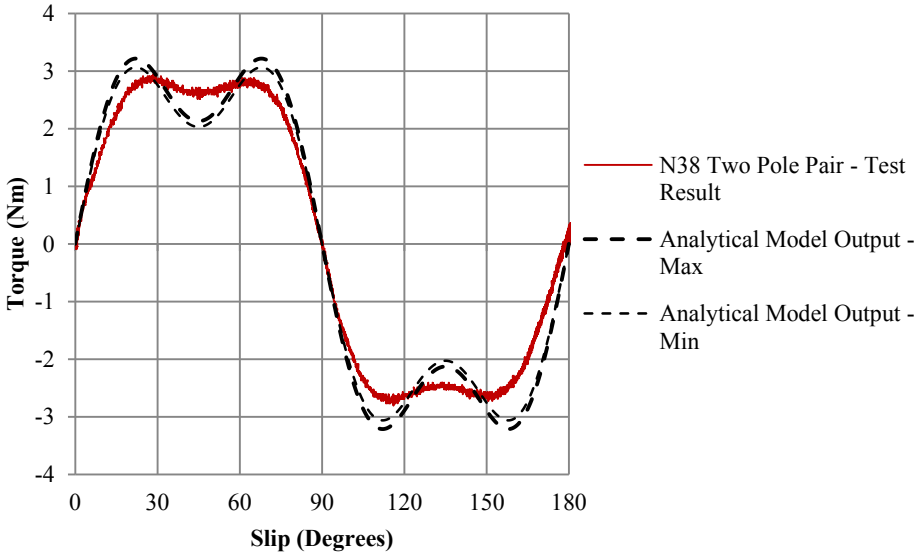

Figure 110 - N38 Two Pole Pair Coupling (Thruster Coupling) Torque vs. Slip Curve

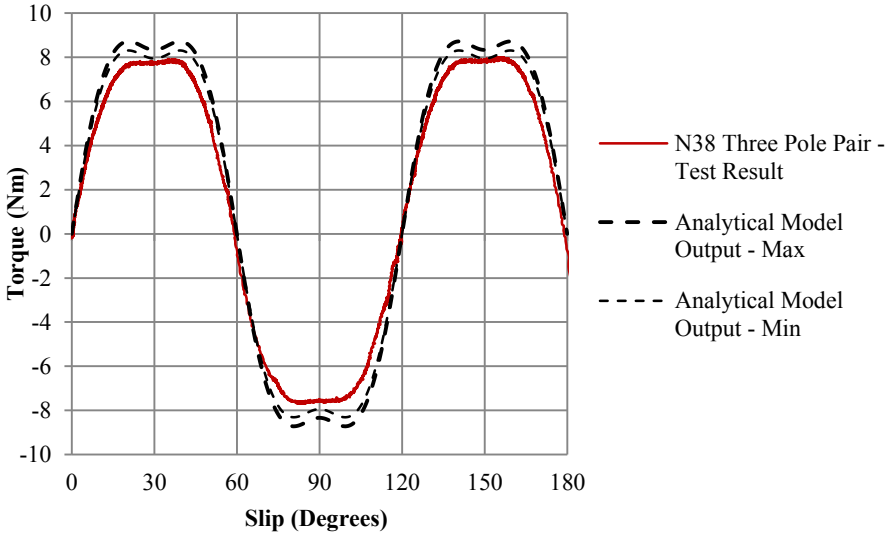

Figure 111 - N38 Three Pole Pair Magnetic Coupling (Manipulator Coupling) Torque vs. Slip Curve

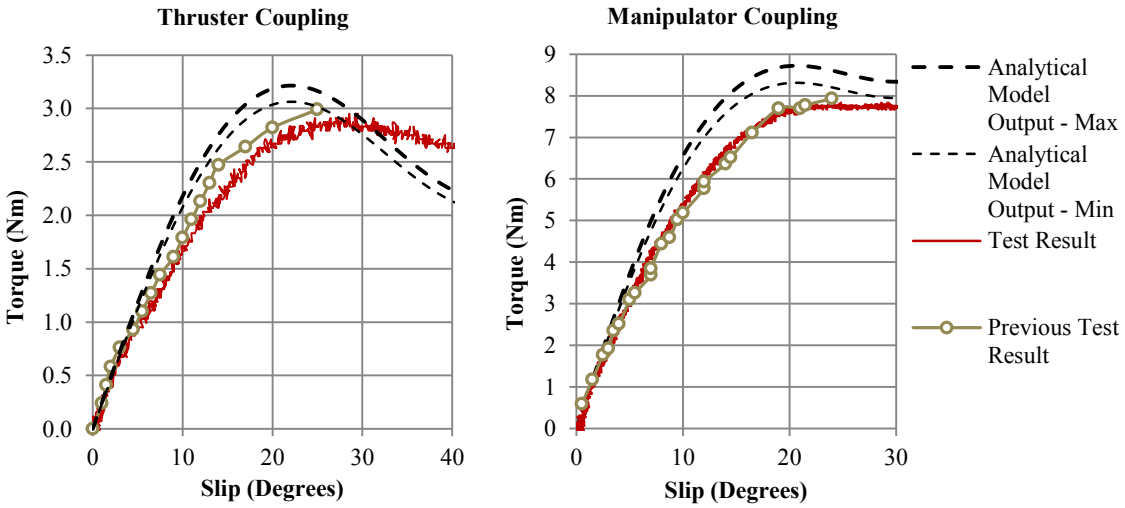

Figure 112 – N38 Magnetic Coupling Test Results Compared to Previous Test Results

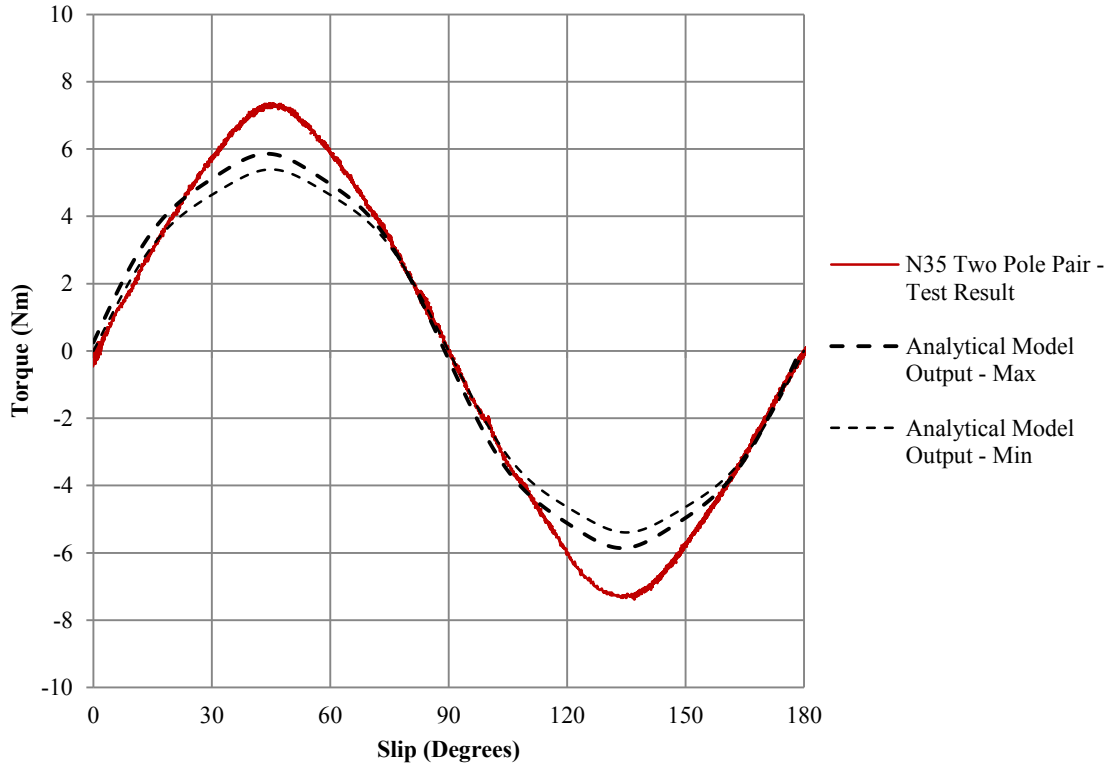

Figure 113 - N35 Two Pole Pair Magnetic Coupling Torque vs. Slip Curve

Coupling Test Analysis

The weight and size of the coupling compared to the torque it produces is essential to assess the efficiency of the coupling. To calculate which coupling arrangement was the most efficient the torque per magnet mass, torque per coupling diameter and the torque per coupling unit volume was calculated for each coupling. For the torque per magnet mass and the torque per unit volume of the coupling the N48 four pole pair magnetic coupling proved to be the most efficient. Figure 114, Figure 115 and Figure 116 show these comparisons for the six couplings tested.

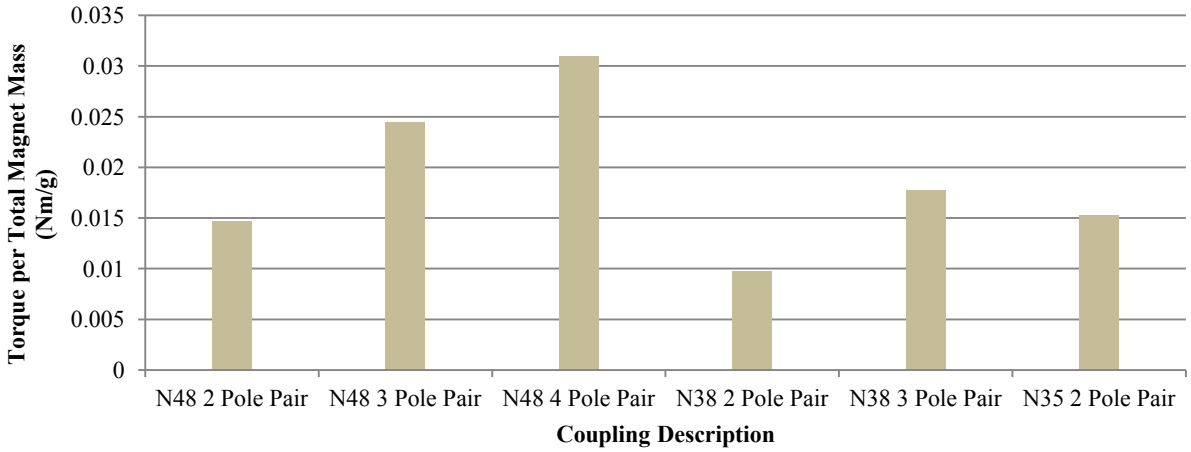

Figure 114 - Torque compared to Total Magnet Mass

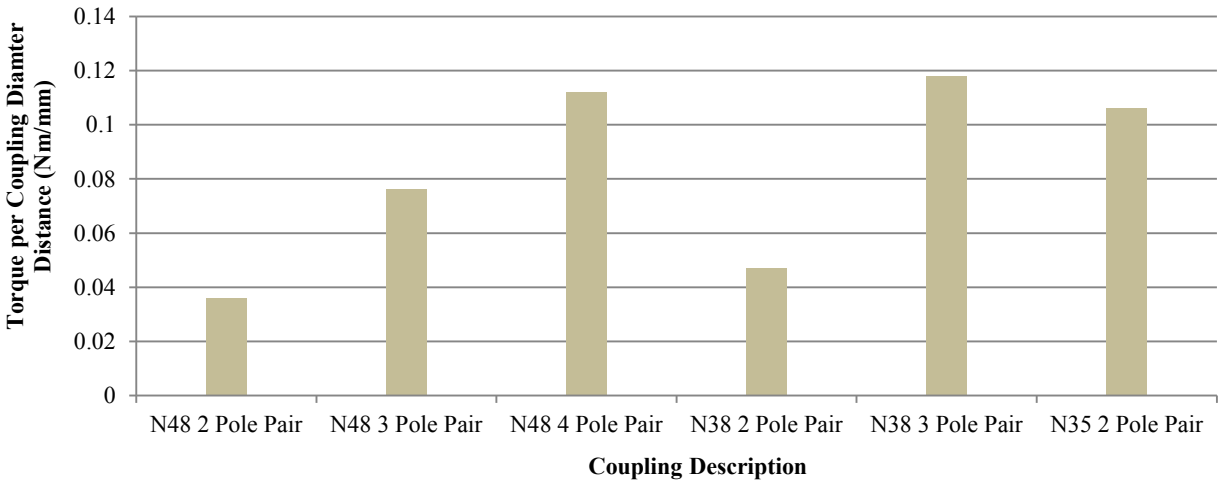

Figure 115 - Torque Compared to the Coupling's Outer Diameter

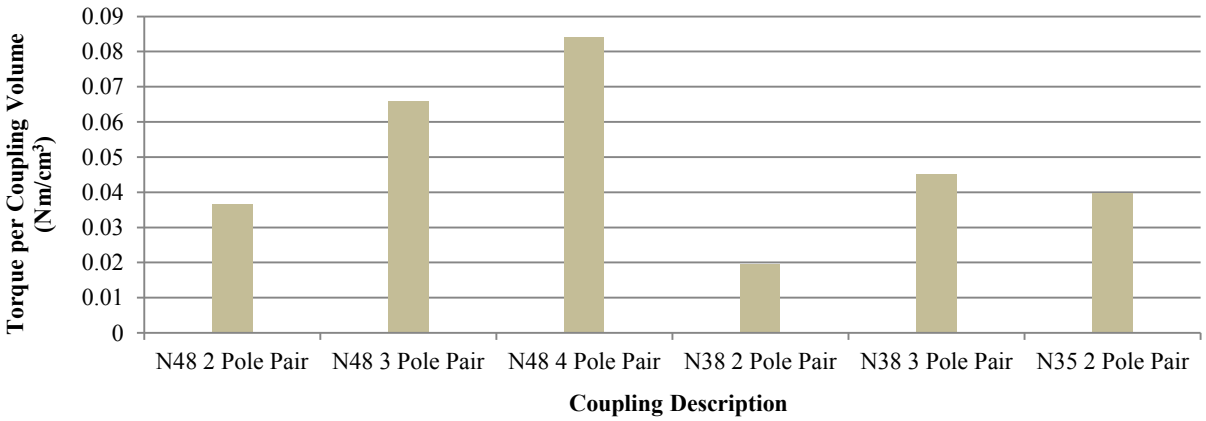

Figure 116 - Torque Compared to the Coupling's Total Required Volume

Coupling Test Conclusion

Using the results from the previous couplings developed at RARL and by knowing the assumptions made in the model it was expected that the model would produce torques larger than those measured in the tests. The model assumed the use of perfectly cuboid magnets that were ideally aligned and ideally magnetised. These factors are all attributes that would increase the pull-out torque of a magnetic coupling. However the largest discrepancy between the analytical model and the test results occurred in the N35 two pole pair coupling with the test coupling producing 23% more torque than the model's highest calculation. This was the only coupling tested with the N35 50 mm x 20 mm x 8 mm magnet. Similarly with the second largest discrepancy the torque achieved was higher than the model's calculation, this too utilised a two pole pair coupling which featured the N48 25.4x12.7x6.35 mm magnets. The other couplings tested with this magnet showed close correlation between the model's results and the test results with the error in the model being less than 10%.

Coupling Test Recommendations

To be able to draw definitive conclusions on how the accuracy of the analytical model changes with changes in specific parameters such as the number of pole pairs and the magnet grade more tests would need to be conducted. To be able to test more pole pair arrangements for a specific magnet (to be able to test five, six and seven pole pair couplings) it is suggested to use a smaller magnet than those featured to be able to keep the torque within the range of the intended application and within the limits of the test rig. Having the same magnet shape manufactured from

different grades is not currently possible but would be useful to test the model's accuracy according to different grades of magnets.

12.6.4 Varying Air-Gap Test

Without being able to custom design the magnets that will be used in future couplings or to choose their grade of neodymium the ability to vary the air gap between the inner rotor's magnets and the outer rotor's magnets was identified as a parameter that can be adjusted to achieve precise pull-out torques. Intuitively as the air gap increases the pull-out torque will exponentially decrease as the force between magnets is inversely proportional to the squared distance of separation.

Varying Air Gap – Method and Results

This test was conducted to assess the coherency of varying the air gap in the model compared to varying the air gap in the actual coupling. The air gap in the N48 three pole pair magnetic coupling was varied in 0.75 mm increments from 3.5 mm to 7.25 mm. Figure 117 shows the pull-out torques achieved compared to the modelled pull-out torques generated from the analytical model.

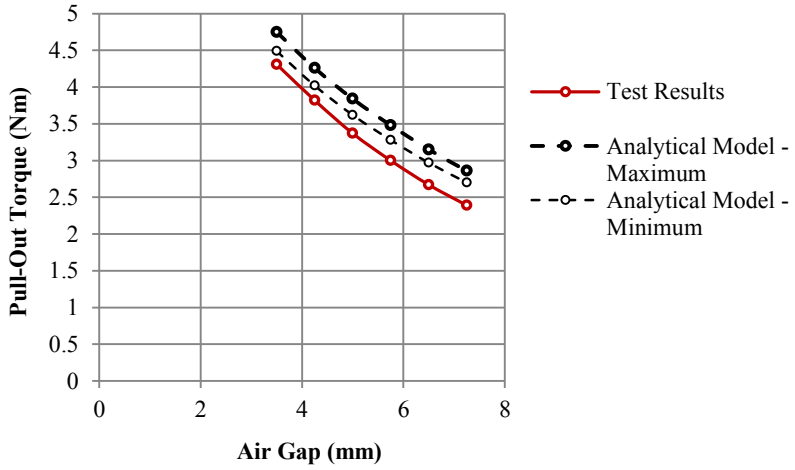

Figure 117 - Tested and Modelled Pull-out Torques vs. Air Gap

Varying Air Gap - Conclusion

The results from the model and the tests showed the expected exponential decay of the pull-out torque as the air gap was increased. The error in the modelled values for the respective air gaps are shown in Figure 118.

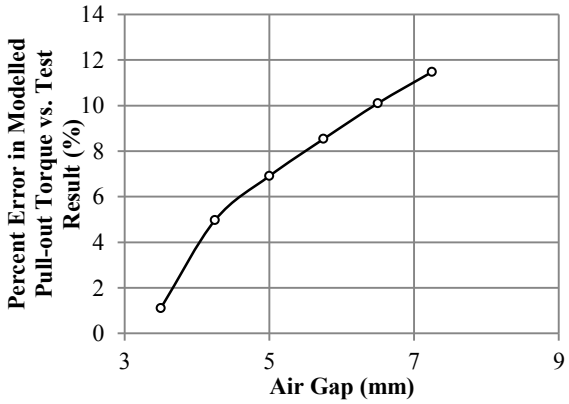

Figure 118 - Error in Modelled Pull-out Torque vs. Coupling Air Gap

The model's accuracy decreases with an increase in air gap however this decrease in accuracy is predictable and can be factored into the model's output when changing the air gap in a coupling design.

12.6.5 Torque vs. Slip with and without Stainless Steel 316 Membrane

In the magnetic couplings that will be developed for the ROV there will be stainless steel 316 membranes to separate the motor and electronics from the sea water. The effect of the presence of a membrane on the pull-out torque depends on the material of the membrane and the amount of volume the membrane occupies in the air gap between the rotors. As stated in Section 5.4, stainless steel 316 is the ideal material to manufacture magnetic coupling membranes from as it has a low conductivity compared to other metals and high corrosion resistance in alkaline solutions such as sea water. Annealed stainless steel 316 has a relative magnetic permeability close to 1 however cold working or machining the metal can increase the relative magnetic permeability to 1.02 which affects the magnetic field between the rotors of the coupling [55]. Because of this increase in magnetic permeability, it was expected that the presence of the membrane would increase the pull-out torque of the coupling.

Membrane Test – Method and Result

Only the manipulator coupling was used for this test as it was the only coupling with an existing membrane. This test parameter was not important enough to warrant the manufacturing of membranes for each coupling tested. To approximate this effect the magnetic permeability for the air gap of the manipulator coupling was adjusted to include the membrane. An averaged magnetic permeability was calculated for the cross-sectional area of the air gap between the rotors of the coupling and the cross-sectional area of the membrane. This produced a 1% increase in modelled pull-out torque and can be seen in Figure 119.

The tested pull-out torque increased by 5% with the presence of the membrane and the result is shown in Figure 119.

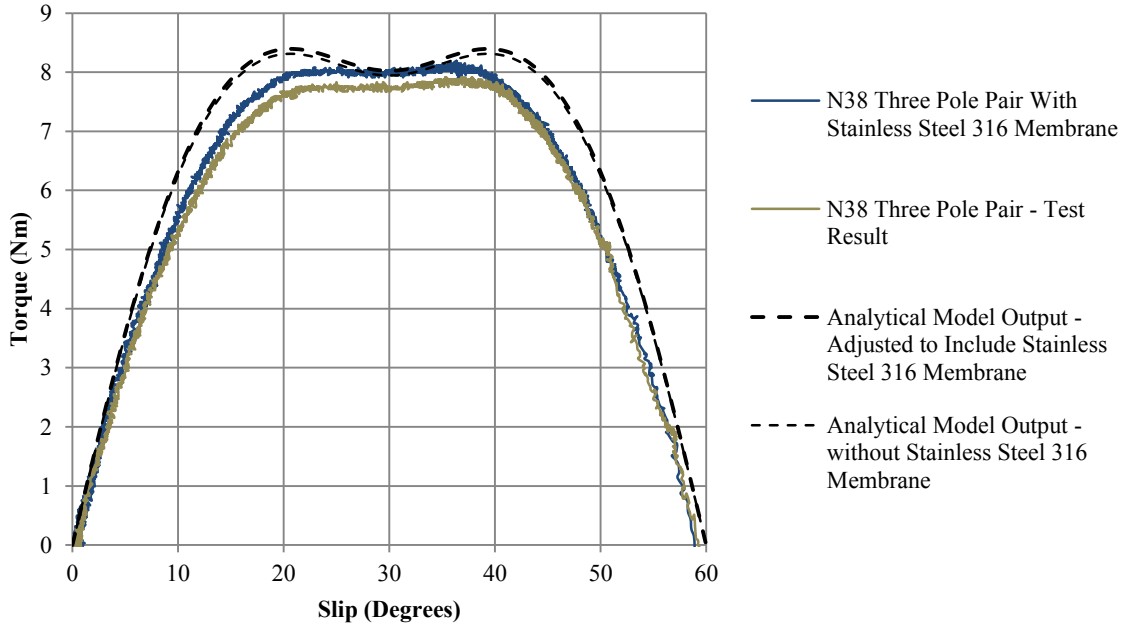

Figure 119 - Manipulator Coupling Tested and Modelled with and without Membrane

Membrane Test – Conclusion

This showed that the stainless steel 316 membrane does increase the pull-out torque as anticipated however the expected increase in pull-out torque was under estimated. The increase in pull-out torque is smaller than the accuracy of the magnetic coupling model therefore the presence of a machined stainless steel 316 membrane will not cause a major discrepancy between the model and the final coupling's pull-out torque.

Membrane Test – Recommendations

To better approximate the effect of a stainless steel 316 membrane a membrane can be manufactured for each test coupling and tested. An alternative would be to remove the effect caused by the machined stainless steel 316 by annealing the membrane after the part is machined to restore the material's relative magnetic permeability to 1.00. Both these suggestions would be costly and therefore the increased accuracy gained from these measures would have to be justified.

12.7 Conclusions

The analytical model's accuracy ranged from -8.8% to +23.21%, when compared to the test results for all the couplings tested. The largest discrepancy between the model and the tests occurred with two pole pair couplings and the most accurate results (that ranged from -8.8% to -1.1%) were achieved using three and four pole pair couplings with air gaps smaller than 5.5 mm.

From the current selection of available magnets the pull-out torques can be estimated to within a ±25% range with confidence. If the coupling designed uses similar magnets and layouts to the more accurate couplings modelled in this section then the pull-out torques can be designed to within ±10% of the designed pull-out torque.

The analytical model allows valuable insight into the magnitude and frequency of the torque-slip curve for a magnetic coupling and can be used to predict the effect of changing the air gap of a coupling to achieve precise torques. The model is adequate for the purpose of designing magnetic couplings for the ROV as it suits the design limitations and required pull-out torque accuracies for the couplings.

12.8 Recommendations

To be able to predict and analyse the error in the model, more couplings should be built and tested. It is recommended that the N35 20x10x5 mm magnet be used (the magnet to the right of the selected magnets in Figure 95). This would allow for a two to seven pole pair test range of couplings that will produce torques within the 0-10 Nm torque range. Figure 120 shows the modelled couplings that could be tested.

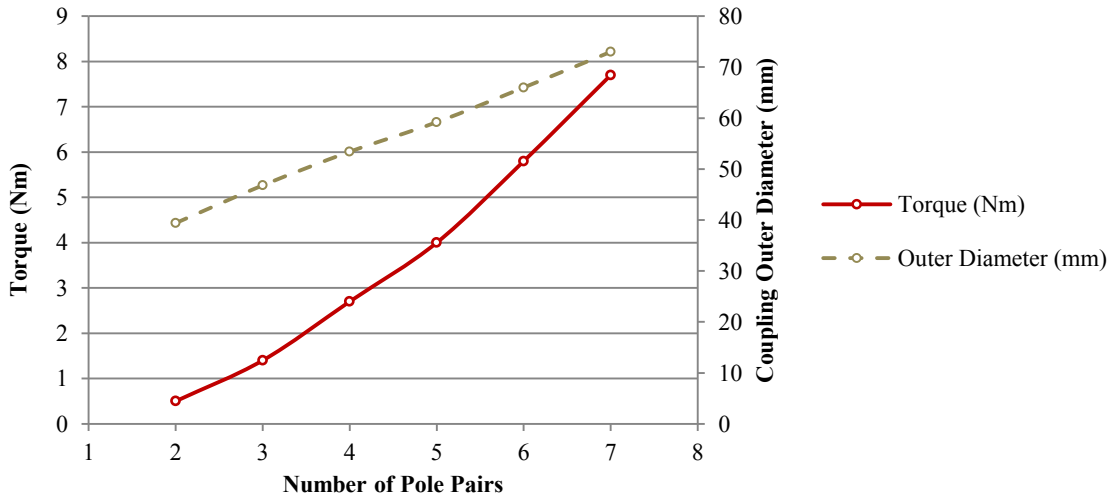

Figure 120 - Recommended N35 20x10x5 mm Magnet Coupling Tests

13 Consolidated Recommendations

13.1 Introduction

As stated in Section 7 the thruster module's efficiency is competitive with commercial thrusters however its thrust-to-weight ratio is not better than any of the commercial thrusters featured in this dissertation. The lowest thrust-to-weight ratio of the commercial thrusters was 2.2. This section recommends the modifications that are required to exceed this.

13.2 Recommended Modifications

By combining the knowledge gained in magnetic couplings with the mechanical recommendations made in Section 8.1 the thruster module can be further streamlined and designed to be lighter.

At full power the thruster's drivetrain produces 1.74 Nm of torque. The N48 two pole pair coupling tested produced 1.78 Nm with an air gap of 3.5 mm and without the presence of a stainless steel 316 membrane. To use this coupling in the thruster module and to allow additional torque for acceleration and start-up it is recommended to use a stainless steel 316 membrane and reduce the air gap to 2 mm. This will increase the torque of the coupling by approximately 25% to 2.23 Nm and therefore will be sufficient to transmit the drivetrain's power to the propeller. A concept for this design change is shown in Figure 121.

By replacing the magnetic coupling and implementing the smaller housing design recommended in Section 8 the thruster module's mass can be reduced from 4.2 kg to 2.7 kg and therefore increase its thrust-to-weight ratio by 65% to 2.5. This change would reduce the ROV's total mass by 7.5 kg (a 10% reduction). This recommendation would require the redesigning and machining of every thruster module part besides the kort-nozzle.

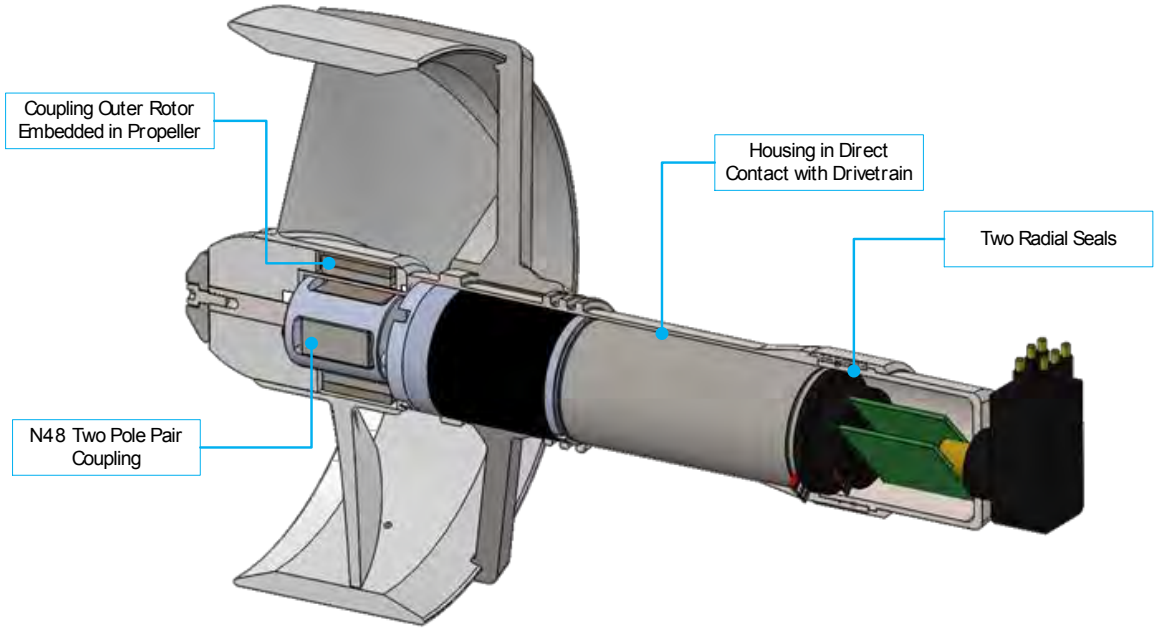

Figure 121 - Thruster Module - Recommended Modifications

This recommendation is an example showing that the ability to model the torque and slip characteristics of a magnetic coupling design can save weight, material and cost to the ROV's mechanically actuated sub-systems.

14 References

[1] C. Edmonds, B. Thomas, B. McKenzie, and J. Pennefather, "Diving Medicine for Scuba Divers," *Webpage*, 2012. [Online]. Available: http://www.divingmedicine.info/Ch 18 SM10c.pdf. [Accessed: 05-Jun-2013].

[2] R. De Smidt, "Development of the Electronics Pod for an Underwater Remotely Operated Vehicle," M.Sc. Thesis, University of Cape Town, 2014.

[3] R. D. Christ and R. L. Wernli, *The ROV Manual*, 1st Edtn. Oxford: Butterworth-Heinemann, 2007.

[4] D. R. Blidberg, "The Development of Autonomous Underwater Vehicles (AUV); A Brief Summary," *IEEE, ICRA*, vol. 6500, p. 12, 2010.

[5] U.S. Navy, "The Navy Unmanned Undersea Vehicle (UUV) Master Plan," 2004.

[6] Video Ray, "Pro 4 User Manual," *Pro 4 User Manual*, 2014. [Online]. Available: http://download.videoray.com/documentation/pro_4/html/qs_components.html. [Accessed: 08-Mar-2015].

[7] SAAB Seaeye Ltd., "Seaeye TMS Systems," 2014. [Online]. Available: http://www.seaeye.com/tms.html. [Accessed: 26-Aug-2014].

[8] Marine Technology Society, "ROV History," 2014. [Online]. Available: http://www.rov.org/rov_history.cfm. [Accessed: 05-Mar-2015].

[9] JAMSTEC, "JAMSTEC Research ROVs," 2014. [Online]. Available: http://www.jamstec.go.jp/e/about/equipment/ships/kaiko7000.html. [Accessed: 05-Mar-2015].

[10] J. R. McFarlane, "Underwater technology 2000 ROVs and AUVs: tools for exploring, exploiting and defending the ocean frontier," *Proc. 2000 Int. Symp. Underw. Technol. (Cat. No.00EX418)*, pp. 465–471, 2000.

[11] F. I. Khan and P. R. Amyotte, "Inherent safety in offshore oil and gas activities: A review of the present status and future directions," *J. Loss Prev. Process Ind.*, vol. 15, pp. 279–289, 2002.

[12] R. Bachmayer, S. Humphris, D. J. Fornari, C. L. Van Dover, J. C. Howland, a D. Bowen, R. L. Elder, T. Crook, D. E. Gleason, W. J. Sellers, and S. Lerner, "Oceanographic research using remotely operated underwater robotic vehicles: Exploration of hydrothermal vent sites on the mid-atlantic ridge at 37 degrees North 32 degrees West," *Mar. Technol. Soc. J.*, vol. 32, no. 3, pp. 37–47, 1998.

[13] SAAB Seaeye Ltd., "Seaeye - Falcon & Falcon DR," 2013. [Online]. Available: http://www.seaeye.com/falcon.html. [Accessed: 20-Mar-2013].

[14] J. B. Hinves, C. D. Douglas, and A. Purpose, "The Development of Hybrid Advanced Composite-Syntactic Foam Structural Component for Use in Undersea Vehicles," *IEEE, Ocean. '93*, pp. 468–472, 1993.

[15] J. Garus, "Optimization of Thrust Alocation in the Propulsion System of an Underwater Vehicle," *Int. J. Appl. Math. Comput. Sci.*, vol. 14, no. 4, pp. 461–467, 2004.

[16] F. R. Driscoll, R. G. Lueck, and M. Nahon, “Development and validation of a lumped-mass dynamics model of a deep-sea ROV system,” *Appl. Ocean Res.*, vol. 22, pp. 169–182, 2000.

[17] SAAB Seaeye Ltd., “Saab Seaeye Brushless DC Thrusters,” *Webpage*, 2014. [Online]. Available: http://www.seaeye.com/thrusters.html. [Accessed: 02-May-2015].

[18] SAAB Seaeye Ltd., “Thruster SI-MCT1 Instruction Manual,” no. 7. Seaeye, p. 7,8, 2006.

[19] Engtek SubSea Systems, “SubSea Propulsion Technology,” *Thruster Brochure*, 2014. [Online]. Available: http://www.ems-thrusters.com/PDF/subsea/SubSea General Catalogue.pdf. [Accessed: 26-Mar-2014].

[20] T. Knight, “Development of the Thruster, Camera and Lighting Systems for an Underwater Remotely Operated Vehicle,” M.Sc. Thesis, University of Cape Town, 2012.

[21] J. S. D. Yoerger, J. Cooke, “The Influence of Thruster Dynamics on Underwater Vehicle Behavior and their Incorporation into Control System Design,” *IEEE, Ocean. Eng.*, vol. 15, no. 3, pp. 167–178, 1990.

[22] Maxon Motor AG, “Maxon Program 2013/14,” Sachseln, 2013.

[23] AK Steel Corporation, “Product Data Sheet: Stainless Steel 316/316L,” 2007. [Online]. Available: http://www.aksteel.com/pdf/markets_products/stainless/austenitic/316_316l_data_sheet.pdf. [Accessed: 15-May-2013].

[24] E. J. Hearn, *Mechanics of Materials 1*, 3rd Editio. Oxford: Butterworth-Heineman, 1997.

[25] K. Siemon, *Manual for the Design of Ferrous and Non-Ferrous Pressure Vessels and Tanks*, 3rd Edtion. Ann Arbor, Michigan: Edwards Brothers. Inc., 1948.

[26] B. Perrin, “The Art and Science of RS-485,” Jul-1999. [Online]. Available: http://www2.htw-dresden.de/~huhle/ArtScienceRS485.pdf. [Accessed: 23-Jun-2013].

[27] Texas Instruments, “MSP430G2x53 Datasheet,” 2013. [Online]. Available: http://www.ti.com/lit/ds/symlink/msp430g2553.pdf. [Accessed: 06-May-2014].

[28] C. Purdue University, “Tuning a PID Controller using Ziegler-Nichols Method,” 2008. [Online]. Available: http://www.purduecal.edu/cpmi/NSF Courses/ECET-462/LABORATORIES/8-TuningofaPIDcontrollerusingZiegler-NicholsMethod.pdf. [Accessed: 20-Jan-2015].

[29] World Sea Temperature, “Sea Temperature,” 2015. [Online]. Available: http://www.seatemperature.org/africa/south-africa/plettenberg-bay-june.htm. [Accessed: 15-Jul-2015].

[30] Texas Instruments, “DAC101S101 / DAC101S101Q 10-Bit Micro Power , RRO Digital-to-Analog Converter,” 2013. [Online]. Available: http://www.ti.com/lit/ds/symlink/dac101s101.pdf. [Accessed: 06-May-2014].

[31] D. Heckman, “Finite Element Analysis of Pressure Vessels,” Monterey, California, 1998.

[32] ST Electronics, “STM32F0x1,” *Web Page*, 2015. [Online]. Available: http://www.st.com/web/en/catalog/mmc/FM141/SC1169/SS1574/LN7. [Accessed: 01-Jun-2015].

[33] Dexter magnetic Technologies, “Custom Magnetic Couplings,” *Webpage*, 2013. [Online]. Available: https://www.dextermag.com/products/magnetic-assemblies/magnetic-couplings. [Accessed: 07-Aug-2013].

[34] Y. L. Wang, K. Liu Pin, J. Wu, and H. Ding, “Near-optimal design and 3-D finite element analysis of multiple sets of radial magnetic couplings,” *IEEE, Trans. Magn.*, vol. 44, no. 12, pp. 4747–4753, 2008.

[35] JBJ Techniques Limited, “Permanent Magnetic Couplings,” *Webpage*, 2013. [Online]. Available: http://www.jbj.co.uk/magnetic-couplings.html. [Accessed: 08-Jul-2013].

[36] M. H. Nagrial, J. Rizk, and A. Hellany, “Design of Synchronous Torque Couplers,” *World Acad. Sci. Eng. Technol.*, vol. 5, no. 7, pp. 426–431, 2011.

[37] V. Lemarquand, J. F. Charpentier, and G. Lemarquand, “Nonsinusoidal Torque of Permanent-Magnet Couplings,” *IEEE Trans. Magn.*, vol. 35, no. 5 PART 3, pp. 4200–4205, 1999.

[38] Tridelta Magnetsysteme, “Permanent Magnetic Couplings and Brakes for Drive Technology,” 2013. [Online]. Available: http://tridelta.de/viomatrix/imgs/download/kupplungen-bremsen-gb.pdf. [Accessed: 17-Jul-2014].

[39] E. C. T. Incorporated, “Eddy Current Technology Incorporated,” 2013. [Online]. Available: http://eddy-current.com/conductivity-of-metals-sorted-by-resistivity/. [Accessed: 01-Feb-2014].

[40] K&J Magnetics Inc., “Neodymium Magnet Information,” *Webpage*, 2014. [Online]. Available: https://www.kjmagnetics.com/neomaginfo.asp. [Accessed: 08-Jul-2014].

[41] Dura Magnetics Inc, “What is Maximum Energy Product,” *Webpage*, 2014. [Online]. Available: http://www.duramag.com/techtalk/tech-briefs/what-is-maximum-energy-product-bhmax-and-how-does-it-correspond-to-magnet-grade/. [Accessed: 06-Oct-2014].

[42] S. Chikazumi, *The Physics of Ferromagnetism*. Oxford: Clarendon Press, 1997.

[43] M. S. Vijaya and G. Rangarajan, *Materials Science*, 3rd Editio. New Dehli: Tata McGraw-Hill Publishing Company Ltd, 2006.

[44] W. Storr, “Magnetic Hysteresis,” *Basic Electronics Tutorials*, 2014. [Online]. Available: http://www.electronics-tutorials.ws/electromagnetism/magnetic-hysteresis.html. [Accessed: 08-Sep-2014].

[45] Dura Magnetics Inc, “Available Neodymium Magnet Grades,” *Webpage*, 2014. [Online]. Available: http://www.duramag.com/neodymium-magnets-ndfeb/available-neodymium-magnet-grades/. [Accessed: 12-Dec-2014].

[46] M. Finbow, “Development of a Magnetic Coupling for the Gripper Module on the 3rd Generation ROV at RARL,” B.Sc. Final Year Project, University of Cape Town, Cape Town, 2013.

[47] R. M. Hornreich and S. Shtrikman, “Optimal Design of Synchronous Torque Couplers,” *IEEE, Trans. Magn.*, vol. MAG-14, no. 5, pp. 800–802, 1978.

[48] E. P. Furlani, R. Wang, and H. Kusnadi, “Three-dimensional Model for Computing the Torque of Radial Couplings,” *IEEE, Trans. Magn.*, vol. 31, no. 5, pp. 2522–2526, 1995.

[49] G. Akoun and J. Yonnet, “3D Analytical Calculation of the Forces Exerted between Two Cuboidal Magnets,” *IEEE, Trans. Magn.*, vol. MAG-20, no. 5, pp. 1962–1964, 1984.

[50] P. Eliès and G. Lemarquand, “Analytical Optimization of the Torque of a Permanent-Magnet Coaxial Synchronous Coupling,” *IEEE, Trans. Magn.*, vol. 34, no. 4, pp. 2267–2273, 1998.

[51] W. Wu, H. C. Lovatt, and J. B. Dunlop, “Analysis and Design Optimisation of Magnetic Couplings using 3D Finite Element Modelling,” *IEEE, Trans. Magn.*, vol. 33, no. 5, pp. 4083–4085, 1997.

[52] J.-F. Charpentier and G. Lemarquand, “Optimal Design of Cylindrical Air-Gap Synchronous Permanent Magnet Couplings,” *IEEE, Trans. Magn.*, vol. 35, no. 2, pp. 1037–1046, 1999.

[53] Robotis, “Dynamixel RX-64 Manual,” 2014. [Online]. Available: http://support.robotis.com/en/techsupport_eng.htm#product/dynamixel/rx_series/rx-64.htm. [Accessed: 25-Oct-2014].

[54] E. Eitel, “Basics of Rotary Encoders,” *Machine Design*, 2014. [Online]. Available: http://machinedesign.com/sensors/basics-rotary-encoders-overview-and-new-technologies-0. [Accessed: 03-Mar-2015].

[55] J. R. Davis, *ASM Specialty Handbook: Stainless Steels*, 3rd ed. Ohio: Materials Park: ASM International, 1999.

Appendix A

Pressure Vessel Theory and Calculations

A.1 Cylindrical Vessels under External Pressure

A.1.1 Nomenclature

D – Diameter of tube
L – Length of tube
L_c – Critical length
t – Wall thickness
p – Pressure
E – Modulus of elasticity
μ - Poisson's ratio

A.1.2 Theory

This section is a summary from chapter 7 (Cylindrical Vessels under External Pressure) of the *"Manual for the Design of Ferrous and Non-Ferrous Pressure Vessel and Tanks"* by K. Siemon [1].

The behaviour of a vessel under external pressure can be compared to the behaviour experienced by a solid rod when in compression. A rod, when in tension, can withstand a force after the yield point has been reached however a rod in compression may buckle and fail below the yield point due to the structure being compromised. This is exacerbated by irregularities in the material or imperfections in the part. This comparison is similar to when vessels are under internal or external pressures. A vessel under internal pressure can continue to contain the pressure once the yield point has being reached however when externally pressurised the vessel can buckle and collapse below the yield point of the material.

The diameter, wall thickness and length of a vessel determine its stability under external pressures. Short, small and thick walled vessels are stable and fail closer to the yield point than long, large and thin walled vessels.

Several formulas have been developed to calculate the external pressures that a vessel can withstand. Of those formulas the most accurate was developed by von Mises. This method was useful to check the integrity of a vessel as it could not derive the required wall thickness therefore the wall thickness had to be approximated first.

The US Experimental Model Basin formula (given by equation 1) deviates from von Mises formula for tube exposed to both radial external pressure and axial external pressure by an average of 1%. This solution provides a simplified formula (compared to von Mises' solution) and is recommended for vessel designs that have a length below the critical length.

$$p = \frac{2.42E\left(\frac{t}{D}\right)^{2.5}}{(1-\mu^2)^{0.75}\left[\frac{L}{D} - 0.45\left(\frac{t}{D}\right)^{0.5}\right]} \quad (1)$$

The critical length is defined as the length beyond which the structural integrity of the vessel with regards to external pressure is independent of the length of the vessel. The critical length is given by equation 2.

$$L_c = \frac{4\sqrt{6}\pi}{27}\sqrt[4]{1-\mu^2} \quad (2)$$

A.1.3 Application to Thruster Housing

The thruster housing's two parts (the motor housing and the electronics housing) were redesigned using the dimensions from Figure A1 as inputs into the US Model Basin equation. The material of the housings was stainless steel 316 and the material properties are shown in Table A1. The housing was designed to withstand a pressure that would be experienced at a depth of 300 m in sea water. A safety factor of 2.5 was included as this was the standard used by R. de Smidt to design the other module housings on the ROV. The parameters are listed in Table A2.

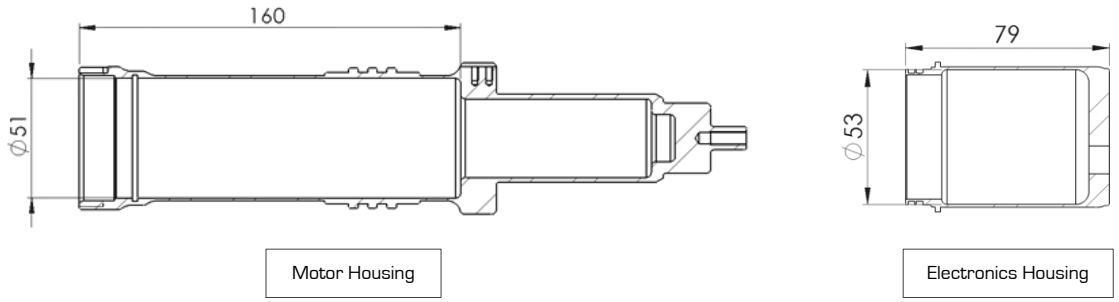

Figure A1 - Thruster Housing Components and Dimensions

Table A1 - Material Properties of Stainless Steel 316[2]

Stainless Steel 316		
Yield Strength	290	MPa
Ultimate Tensile Strength	579	MPa
Young's Modulus	193	GPa
Poisson's Ratio	0.27	

Table A2 - Design Parameters for Thruster Housing Parts

Design Parameters		
Depth in Sea Water	300	m
Density of Sea Water	1029	kg/m3
External Pressure (Bar)	30.3	bar
Safety Factor	2.5	
Pressure with Safety Factor	75.7	bar

The thruster housing wall thickness required was calculated to be 0.95 mm. The wall thickness chosen was 1.2 mm as this allowed for any misalignment that could occur during re-machining. Table A3 details the results from the calculation.

Table A3 - Results from US Experimental Model Basin Formula

Part Description	**Internal Diameter - D**	**Wall Thickness - t**	**Length - L**	**Critical Length - Lc**
Motor Housing	51	0.95	160	425.15
Electronics Housing	53	0.73	79	506.31

A.1.4 References

[1] K. Siemon, *Manual for the Design of Ferrous and Non-Ferrous Pressure Vessels and Tanks*, Thrid Edit. Ann Arbor, Michigan: Edwards Brothers. Inc., 1948.

[2] AK Steel Corporation, "Product Data Sheet: Stainless Steel 316/316L," 2007.

Appendix B

Magnetic Coupling Analytical Model

-

Tangential Force Expression

B.1. Tangential Force Expression

Figure B1 shows two cuboid magnets rotated relative to each other with their respective co-ordinate systems. The tangential force between the two magnets is given by the function F_y. The variables used in the following equations refer to the variables in Figure B1. The variables u, v, w, y′ and z′ are intermediate variables (placeholders) and the functions f_1, f_2, f_3, f_4, f_5 and f_6 are intermediate functions. All the equations detailed in this appendix are from Elies and Lemarquand's *"Analytical Optimization of the Torque of a Permanent-Magnet Coaxial Synchronous Coupling"* [1].

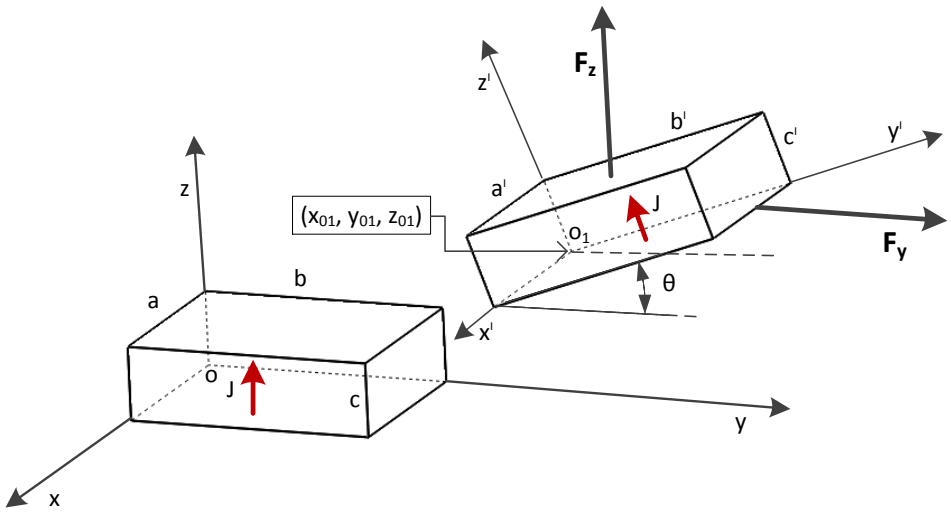

Figure B1-Magnet Configuration and Magnetic Force Components [1]

$$
\begin{aligned}
F_y(\theta, x_{01}, y_{01}, z_{01}, a, b, c, a', b', c', J) \\
&= -f_1(x_{01}, x_{01}+a', y_{01}, z_{01}, \theta, 0,0, b', c', J) \\
&+ f_1(x_{01}-a, x_{01}-a+a', y_{01}, z_{01}, \theta, 0,0, b', c', J) \\
&- f_1(x_{01}-a, x_{01}-a+a', y_{01}, z_{01}, \theta, b, 0, b', c', J) \\
&+ f_1(x_{01}, x_{01}+a', y_{01}, z_{01}, \theta, b, 0, b', c', J) \\
&- f_1(x_{01}-a, x_{01}-a+a', y_{01}, z_{01}, \theta, 0, c, b', c', J) \\
&+ f_1(x_{01}, x_{01}+a', y_{01}, z_{01}, \theta, 0, c, b', c', J) \\
&- f_1(x_{01}, x_{01}+a', y_{01}, z_{01}, \theta, b, c, b', c', J) \\
&+ f_1(x_{01}-a, x_{01}-a+a', y_{01}, z_{01}, \theta, b, c, b', c', J)
\end{aligned} \tag{1}
$$

$$
\begin{aligned}
f_1(v, w, y_{01}, z_{01}, \theta, b, c, b', c', J) \\
&= \frac{J^2}{4\pi\mu_0}[f_2(v, w, y_{01}, z_{01}, \theta, b, c, b', c') \\
&- f_2(v, w, y_{01}, z_{01}, \theta, b, c, b', 0)]
\end{aligned} \tag{2}
$$

$$
\begin{aligned}
f_2(v, w, y_{01}, z_{01}, \theta, b, c, b', z') \\
&= +f_4(w, y_{01}, z_{01}, \theta, b, c, b', z') \\
&- f_4(v, y_{01}, z_{01}, \theta, b, c, b', z') \\
&- f_4(w, y_{01}, z_{01}, \theta, b, c, 0, z') \\
&+ f_4(v, y_{01}, z_{01}, \theta, b, c, 0, z')
\end{aligned} \tag{3}
$$

$$
\begin{aligned}
f_3(y_{01}, z_{01}, \theta, b, c, y', z') \\
&= \sqrt{u^2 + f_5^2(y_{01}, z_{01}, \theta, b, c, z') + f_6^2(y_{01}, z_{01}, \theta, b, c, y')}
\end{aligned} \tag{4}
$$

$$
\begin{aligned}
&f_4(u, y_{01}, z_{01}, \theta, b, c, y', z') \\
&= u f_6(y_{01}, z_{01}, \theta, b, c, y') \ln[(-u + f_3(y_{01}, z_{01}, \theta, b, c, y', z')] - u f_6(y_{01}, z_{01}, \theta, b, c, y') \\
&- u^2 \ln[f_3(y_{01}, z_{01}, \theta, b, c, y', z') + f_6(y_{01}, z_{01}, \theta, b, c, y')] \\
&+ u f_5(y_{01}, z_{01}, \theta, b, c, z') \arctan\left(\frac{-f_5^2(y_{01}, z_{01}, \theta, b, c, z') - u^2 + u f_3(y_{01}, z_{01}, \theta, b, c, y', z')}{f_5(y_{01}, z_{01}, \theta, b, c, z') f_6(y_{01}, z_{01}, \theta, b, c, y')}\right) \\
&+ \frac{1}{2} u\pi |f_5(y_{01}, z_{01}, \theta, b, c, z')| sign[f_6(y_{01}, z_{01}, \theta, b, c, y')] \\
&+ \frac{1}{2} f_6(y_{01}, z_{01}, \theta, b, c, y') f_3(y_{01}, z_{01}, \theta, b, c, y', z') \\
&+ \frac{1}{2}[u^2 + f_5^2(y_{01}, z_{01}, \theta, b, c, z')] \ln[f_3(y_{01}, z_{01}, \theta, b, c, y', z') + f_6(y_{01}, z_{01}, \theta, b, c, y')]]
\end{aligned} \tag{5}
$$

$$
f_5(y_{01}, z_{01}, \theta, b, c, z') = -y_{01} \sin[\theta] + z_{01} \cos[\theta] + b \sin[\theta] - c \cos[\theta] + z' \tag{6}
$$

$$
f_6(y_{01}, z_{01}, \theta, b, c, y') = y_{01} \cos[\theta] + z_{01} \sin[\theta] - b \cos[\theta] - c \sin[\theta] + y' \tag{7}
$$

B.2. References

[1] P. Eličs and G. Lemarquand, "Analytical Optimization of the Torque of a Permanent-Magnet Coaxial Synchronous Coupling," *IEEE*, vol. 34, no. 4, pp. 2267–2273, 1998.

Appendix C

Calibrations

C.1. Temperature Sensor Calibrations

C.1.1 Sensor Details and Circuitry

The temperature sensors used in the thruster modules were the LM60BIZ from Texas Instruments. The LM60 can sense temperatures between -40°C and +125°C which covers the required range for the thruster module of 0 - 100°C. The output is linearly proportional to degrees Celsius. The LM60 is calibrated to provide an accuracy of ±2°C at room temperature (20°C) and ±3°C over the sensor's operating range [1].

The sensor used to monitor the electronics' temperature was a surface mount variant (SOT-23 package) of the LM60 and was directly soldered to the communications and control PCB. The LM60 sensors used to monitor the gearbox and motor temperatures were in a cylindrical plastic package (TO-92) and connected to the PCB via wires and board-to-wire connectors. The gearbox and motor temperature sensor wires ran along the length of the BLDC motor and the output signals were susceptible to noise generated by the motor therefore low pass filters were placed on the PCB to smooth the signals.

The outputs from the LM60 on the PCB and the filtered outputs from the motor and gearbox sensors were connected to ADC channels on the communications micro-processor. The micro-processor sampled these channels, applied a conversion to the read value and communicated the result via RS-485 to the operator station. The result sent to the operator station was an integer value representing degrees Celsius therefore the resolution of the reading was to the nearest degree. This resolution was adequate to monitor the thruster module in the case of overheating.

C.1.2 Aim

The aim of the calibration was to obtain accurate temperature readings from the LM60 sensors used to monitor the thruster module's temperatures.

C.1.3 Method and Apparatus

The thruster module communications and control PCB and the two temperature sensors were secured to a board and monitored with a calibrated thermal camera. In the monitor for the camera, three spot temperature indicators were placed on the three sensors which provided the temperatures of each sensor. The temperatures from the communications and control PCB were logged with LabVIEW. The PCB and the sensors were heated to 100°C with a hot air gun. As the PCB and sensors cooled the images from the thermal camera were recorded and the values from the sensors were logged. From this data a gain and offset were calculated and implemented in the code of the communications micro-processor. The test repeated and the calibration was validated. Figure C1 shows an image from the thermal camera during the calibration with spot one on the LM60 on the PCB and the other two spots on the motor and gearbox LM60 temperature sensors.

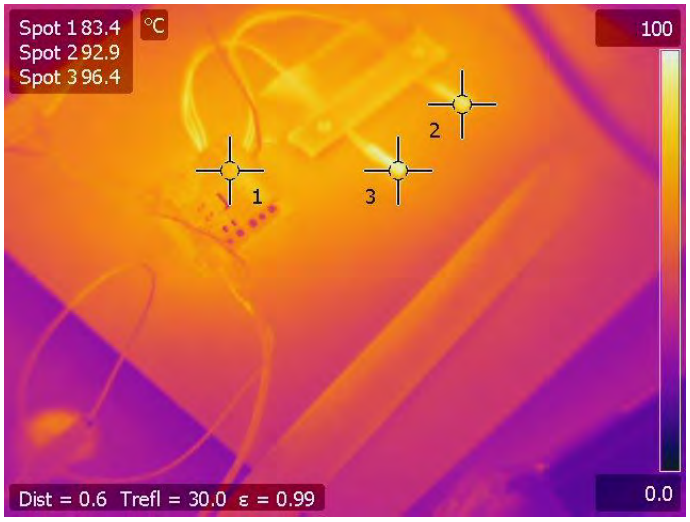

Figure C1 - Temperature Sensor Calibration - Thermal Image

C.1.4 Calibration Results and Information

Table C1 shows the gains and offsets calculated for all the temperature sensors in the thruster module. Figure C2 shows the error in the readings before and after the calibration was applied.

Table C1 - Thruster Module Temperature Sensor Calibration Results

Electronics Temperature Sensor	Gain	0.91
	Offset	4.24
Motor Temperature Sensor	Gain	0.88
	Offset	7.44
Gearbox Temperature Sensor	Gain	0.85
	Offset	6.70

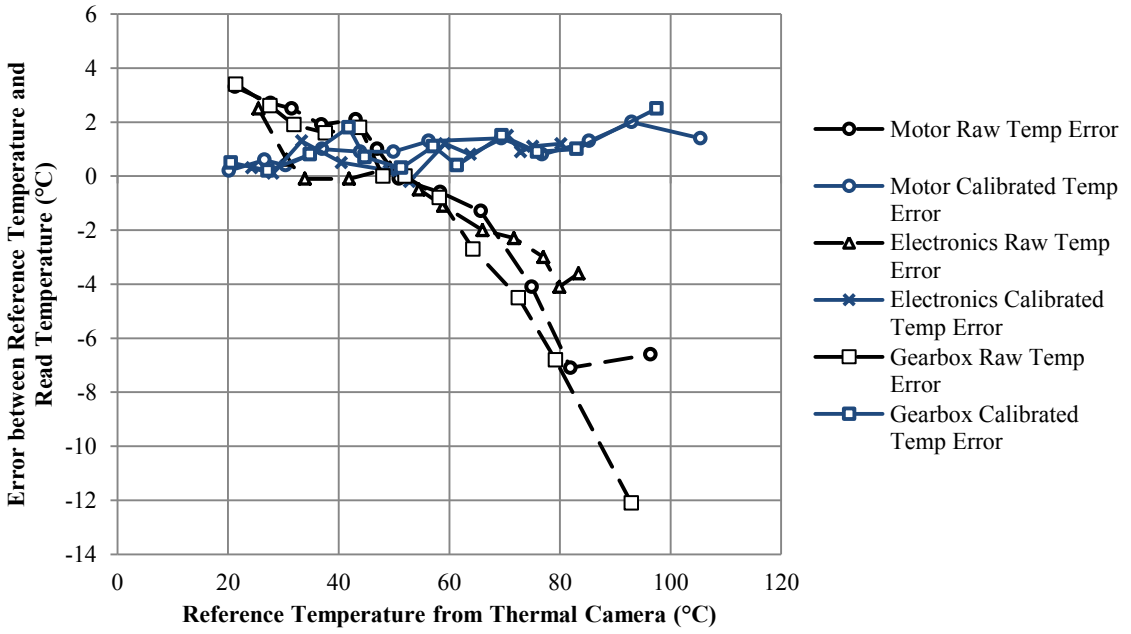

Figure C2 - Error in Temperature Readings Before and After the Calibration

C.2. Angle Measurement Calibration

C.2.1 Sensor Details and Circuitry

To measure the angle of the rotating shaft in the test rig the shaft was coupled to a potentiometer. The potentiometer selected was a 50 KΩ multi-turn potentiometer. The angle range that was measured was only 5% of the potentiometers rotation range therefore the signal from the potentiometer was amplified. A low pass filter was connected to the output of the amplifier to reduce noise in the output signal. The circuitry can be seen in Figure C3.

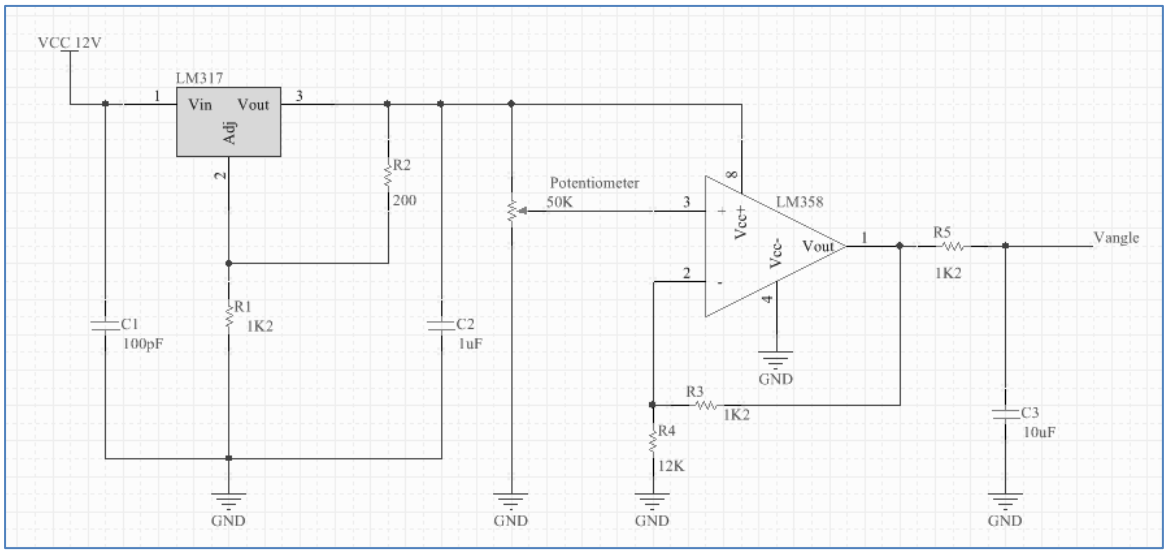

Figure C3 - Potentiometer Circuitry

C.2.2 Aim

The aim of the calibration was to convert the signal received by the DAQ from the potentiometer circuitry into an angle measurement.

C.2.3 Method and Apparatus

A laser was mounted to the test rig's base plate and a laser cut acrylic protractor was fitted to the wheel mounted to the rotating shaft. The wheel was rotated in 10° increments with the voltage from the potentiometer circuitry recorded by the DAQ for each angle. After the calibration was completed this sequence was repeated to validate the calibration. The angle range for calibration was 0-180° as this was the test range for the couplings. Figure C4 shows the setup on the test rig and the protractor manufactured for the calibration.

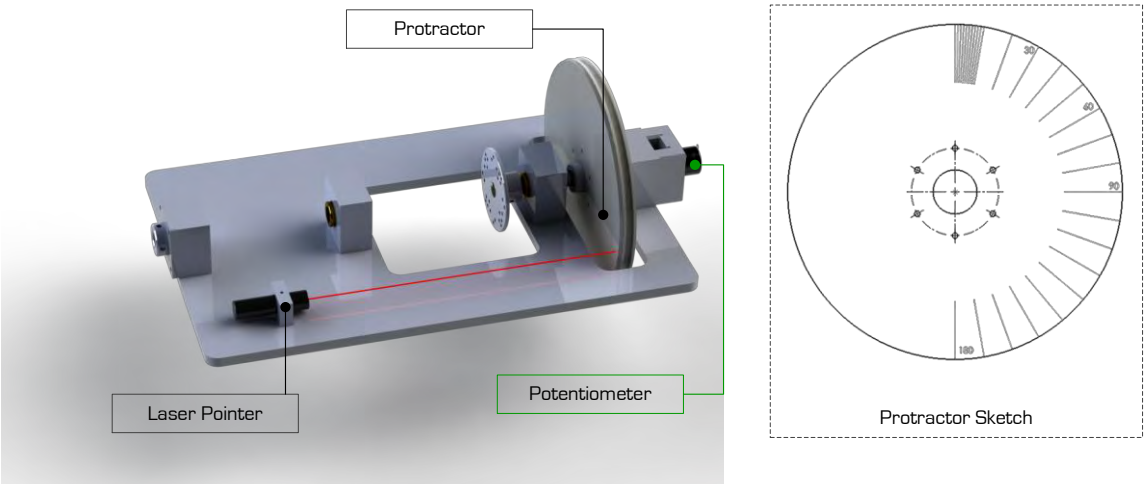

Figure C4 - Angle Measurement Calibration Setup

C.2.4 Calibration Results and Information

The conversion from read voltage to degrees was described by the linear function in equation 1 with the angle of rotation represented as ψ and the read voltage as V. Figure C5 shows the results from the calibration.

$$\psi = 37.292V - 37.649 \quad (1)$$

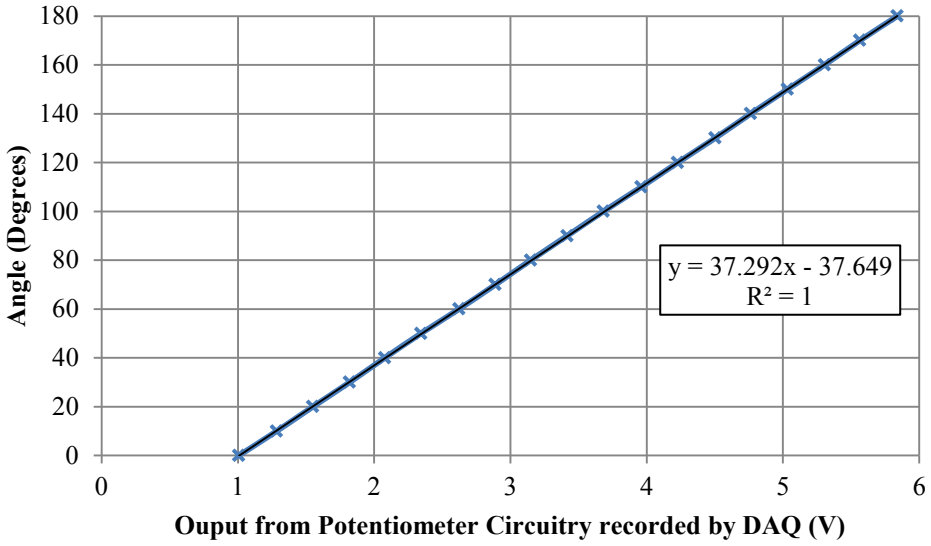

Figure C5 - Angle Measurement Calibration Result

C.3. Strain Gauge Calibration

C.3.1 Sensor Details and Circuitry

The strain gauges used were Kyowa biaxial KFG 120 Ω 0°/90° gauges (KFG-2-120-D2-23) designed to measure torque on aluminium bars [2]. Two gauges were used in a full-bridge setup. The bar specimen selected was large enough for the strain gauges to be bonded to the bar and allowed the strength to prevent the bar from plastically deforming when the maximum torque was applied.

The strain gauge was connected to a strain indicator amplifier (Vishay P-3500 Portable Strain Indicator). The analogue output from the strain indicator was fed into the NI 9201 Data Acquisition Unit.

C.3.2 Aim

The aim of the calibration was to convert the signals recorded by the DAQ into accurate torques. The torque applied was known by knowing the weight of the mass used and the radius of the wheel from which the mass was suspended.

C.3.3 Method and Apparatus

To calibrate the strain gauge the aluminium tube was clamped and bolted directly to the shaft that applies torque to the test rig. The strain indicator was zeroed when no torque was applied. Weighed masses were connected to the torque wheel to apply a known torque to the aluminium tube (this is shown in Figure C6). To calibrate the strain gauge for the entire torque range (-10 to +10 Nm) torques were applied in both the clockwise and counter-clockwise directions. The voltages were recorded using LabVIEW and plotted against the known applied torques. From this a conversion from voltage to torque was calculated. This method was repeated and the calibration was validated.

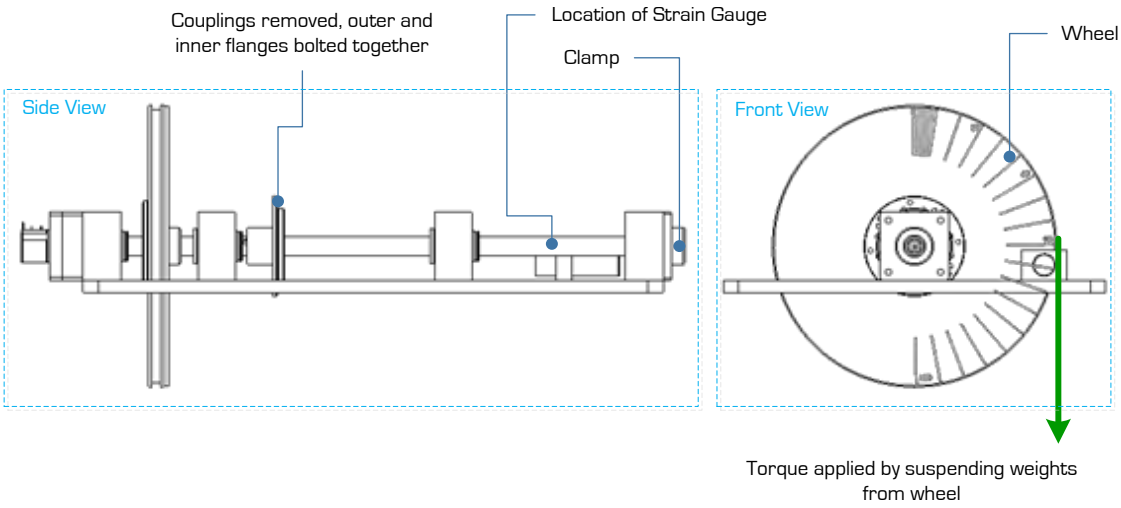

Figure C6 - Strain Gauge Calibration Method

C.3.4 Calibration Results and Information

The result for the calibration can be seen in Figure C7. The conversion from voltage read and torque was 7.7794 Nm/V.

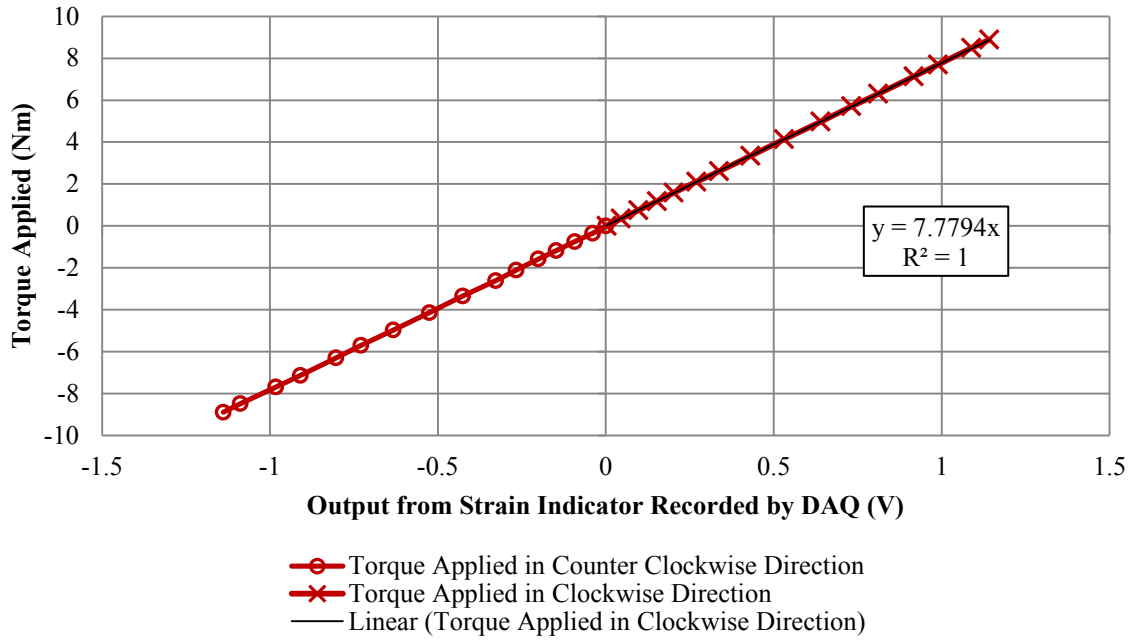

Figure C7 - Strain Gauge Calibration Results

C.4. References

[1] Texas Instruments, "LM60/LM60-Q1 2.7V Temperature Sensor," Dallas, 2012.

[2] Kyowa, "General-Purpose Foil Strain Gauges," *Webpage*, 2015. [Online]. Available: http://www.kyowa-ei.com/eng/product/category/strain_gages/kfg/index.html. [Accessed: 27-Feb-2015].

Appendix D

Technical Drawings

Contents

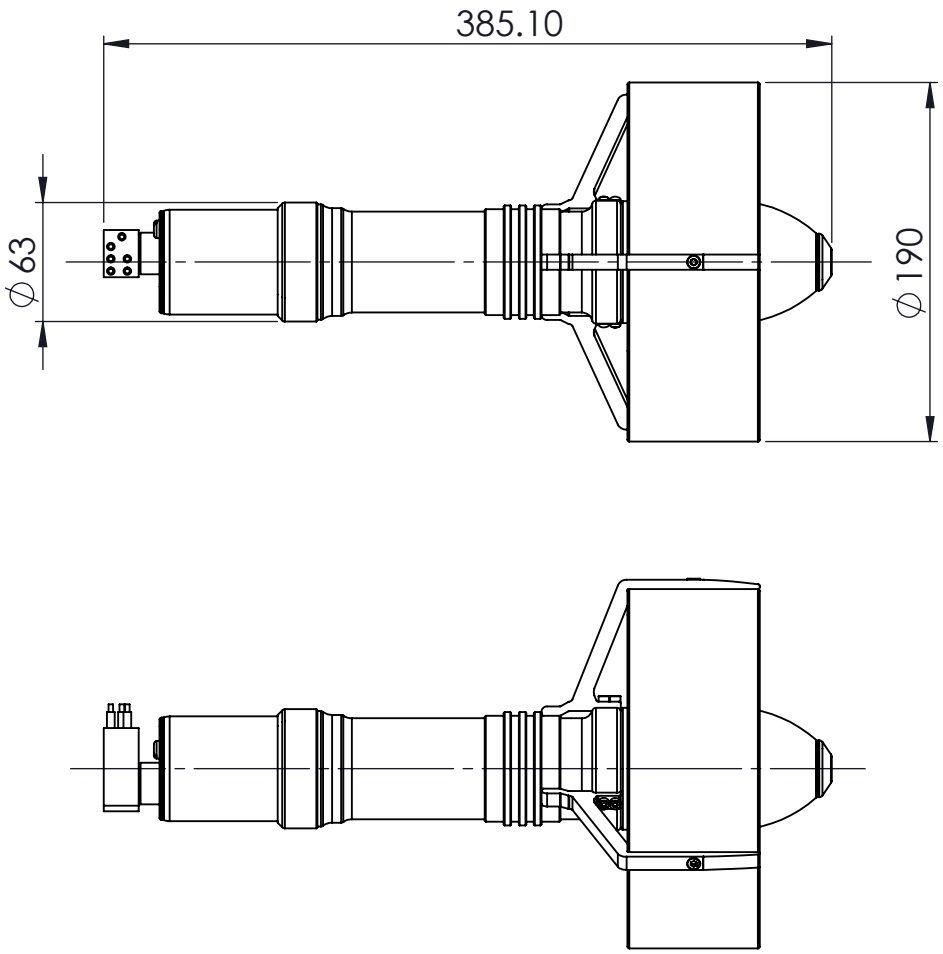

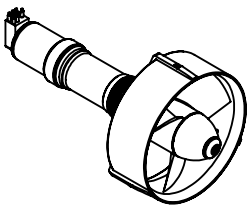

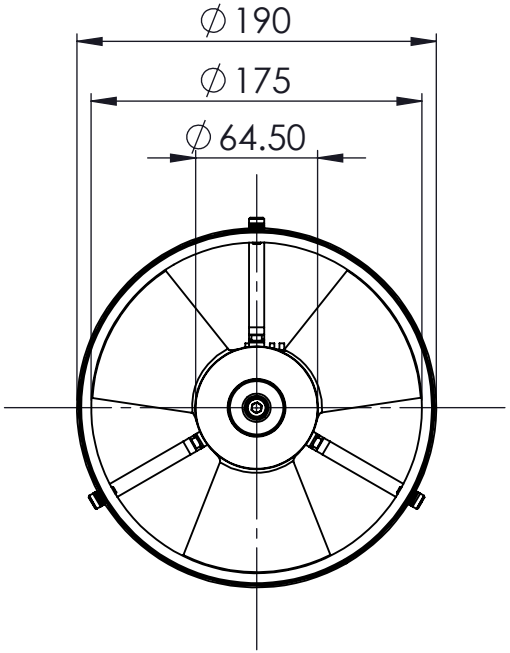

A4 Landscape	University of Cape Town Department of Mechanical Engineering			
	Title: THRUSTER - GENERAL DIMENSIONS			
Assembly Drawing	Scale: 1:4	Date: 2015/09/05	Sheet 1	of 4
	Drawn By: T P HOPE		Drawing Number D-THR-1	

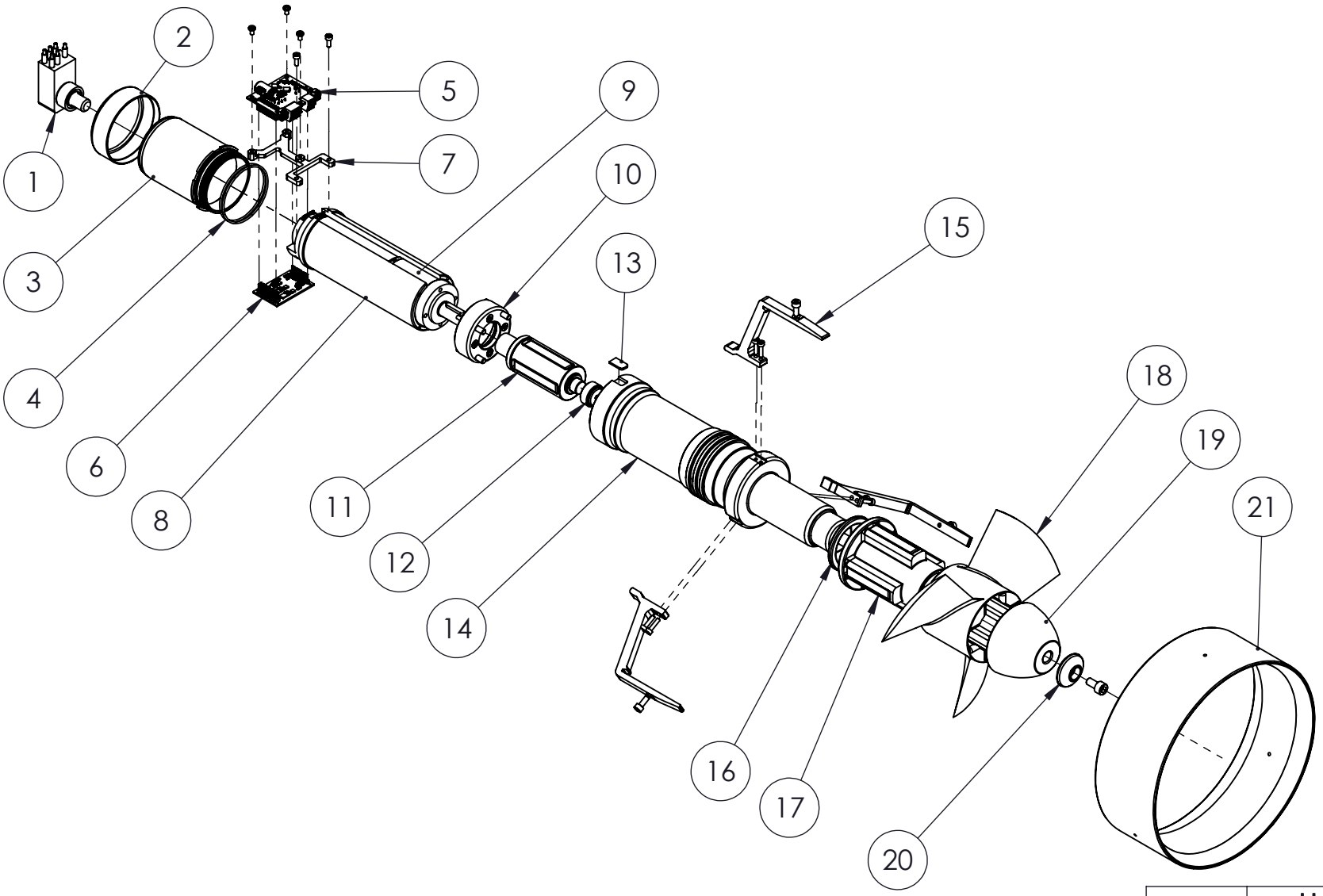

	PART NAME	QTY
1	CON-BRINS-LPBH6	1
2	THR-CONRING	1
3	THR-EHOUSING	1
4	THR-ORING	2
5	THR-CCPCB	1
6	THR-MXPCB	1
7	THR-EMOUNT	1
8	THR-HEATTSINK	1
9	THR-DRIVETRAIN	1
10	THR-MOTORMNT	1
11	THR-INNERRTR	1
12	THR-INNERBRN	1
13	THR-LOCTKEY	1
14	THR-HOUSING	1
15	THR-KNBRACKET	3
16	THR-OUTERBRN	1
17	THR-OUTERRTR	1
18	THR-PROPELLER	1
19	THR-ENDCONE	1
20	THR-ENDDISK	1
21	THR-KORTNOZZ	1

A4 Landscape	**University of Cape Town** Department of Mechanical Engineering			
	Title: THRUSTER EXPLODED VIEW			
Assembly Drawing	Scale: 1:5	Date: 2015/09/05	Sheet 2	of 4
	Drawn By: T P HOPE		Drawing Number D-THR-2	

	PART NAME	QTY
1	CON-BIRNS-LPBH6	1
2	THR-VENTPLUG	1
3	THR-BIRNSSPACER	1
4	THR-CONRING	1
5	THR-EHOUSING	1
6	THR-ORING	2
7	THR-MXPCB	1
8	THR-HEATSINK	1
9	THR-DRIVETRAIN	1
10	THR-HOUSING	1
11	THR-LOCTKEY	1
12	THR-EMOUNT	1
13	THR-CCPCB	1

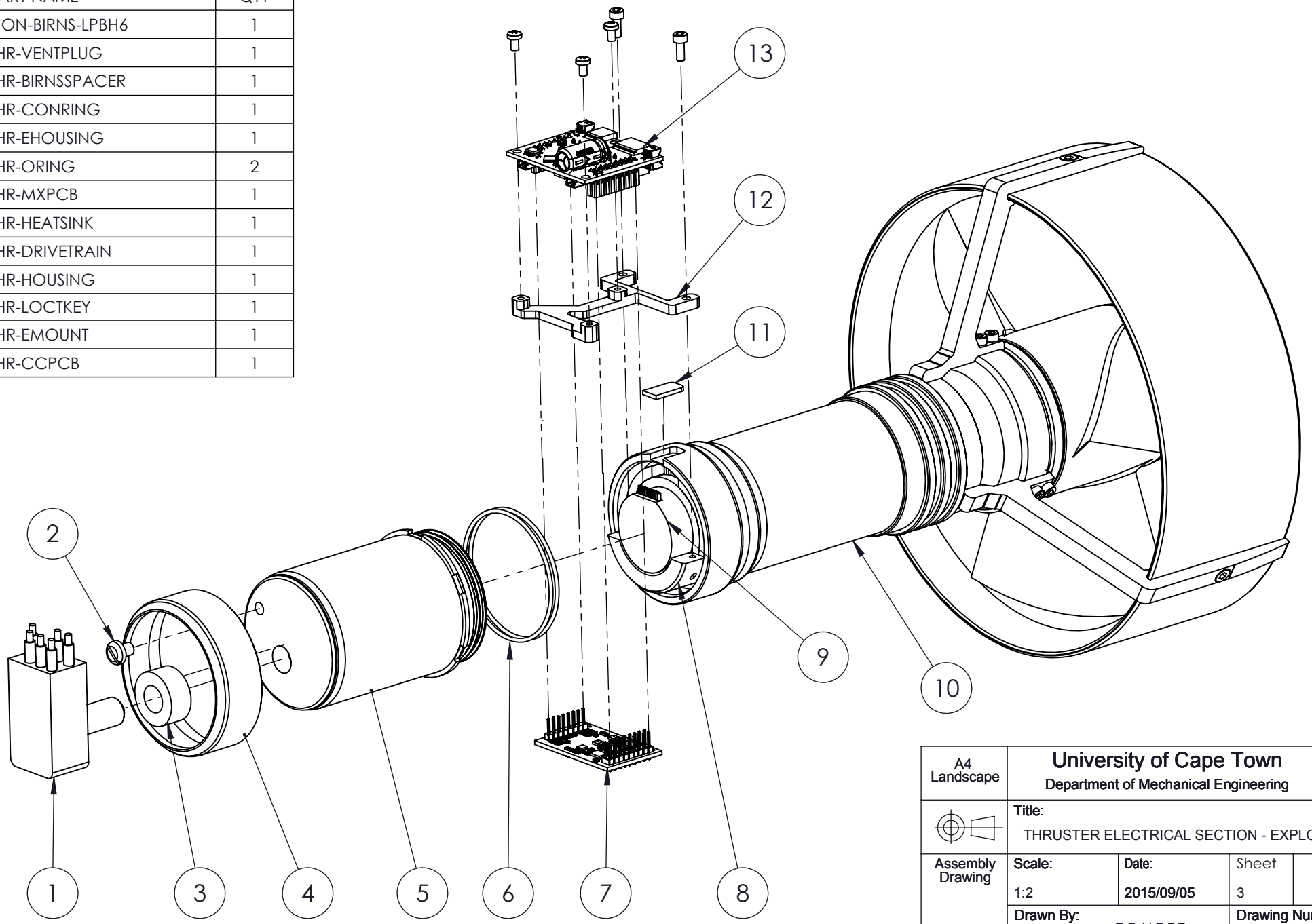

A4 Landscape	**University of Cape Town** Department of Mechanical Engineering			
	Title: THRUSTER ELECTRICAL SECTION - EXPLODED			
Assembly Drawing	Scale: 1:2	Date: 2015/09/05	Sheet 3	of 4
	Drawn By: T P HOPE		Drawing Number D-THR-3	

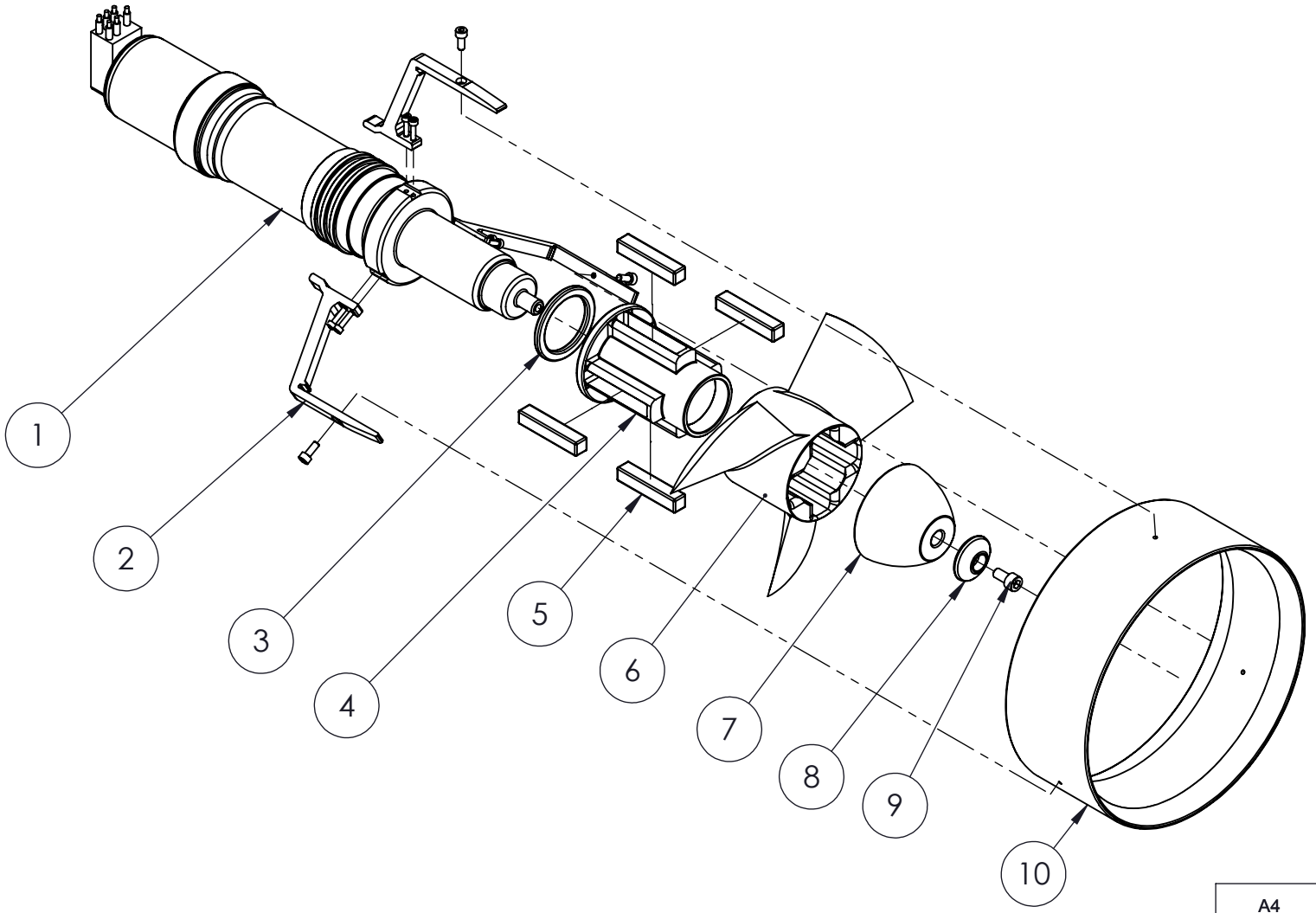

	PART NAME	QTY
1	THR-HOUSING	1
2	THR-KNBRACKET	3
3	THR-OUTERBRN	1
4	THR-OUTERRTR	1
5	THR-NEOMAGNET	4
6	THR-PROPELLER	1
7	THR-ENDCONE	1
8	THR-ENDDISK	1
9	M6BOLT-HEXSOCKET	1
10	THR-KORTNOZZ	1

A4 Landscape	**University of Cape Town** **Department of Mechanical Engineering**			
	Title: THRUSTER PROPELLER SECTION - EXPLODED			
Assembly Drawing	**Scale:** 1:4	**Date:** 2015/09/05	Sheet 4	of 4
	Drawn By: T P HOPE		**Drawing Number** D-THR-4	

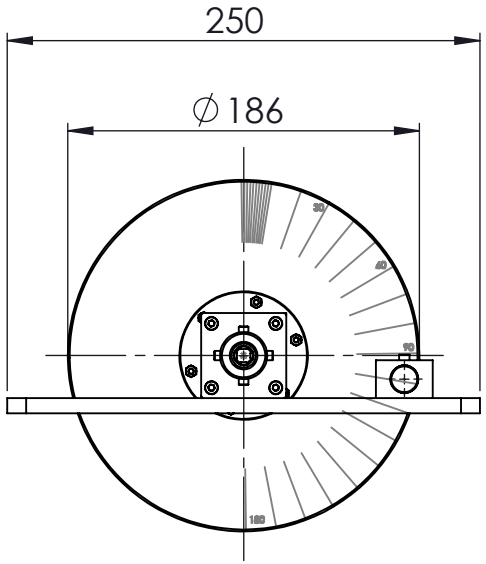

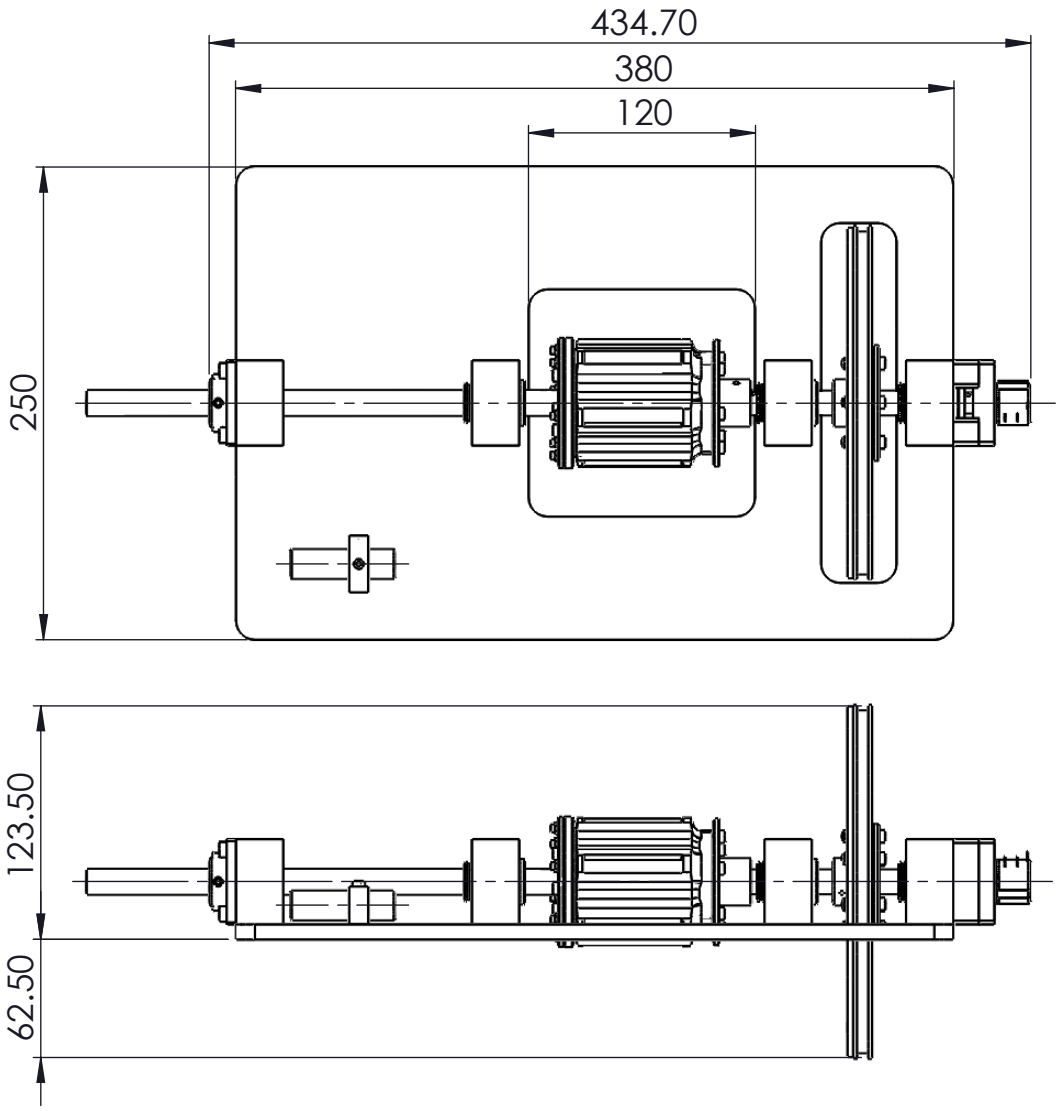

A4 Landscape	**University of Cape Town** **Department of Mechanical Engineering**			
	Title: MAGNETIC COUPLING TEST RIG GENERAL DIMENSIONS			
Assembly Drawing	**Scale:** 1:4	**Date:** 2015/09/05	Sheet 1	of 3
	Drawn By: T P HOPE		**Drawing Number** D-MCTR-1	

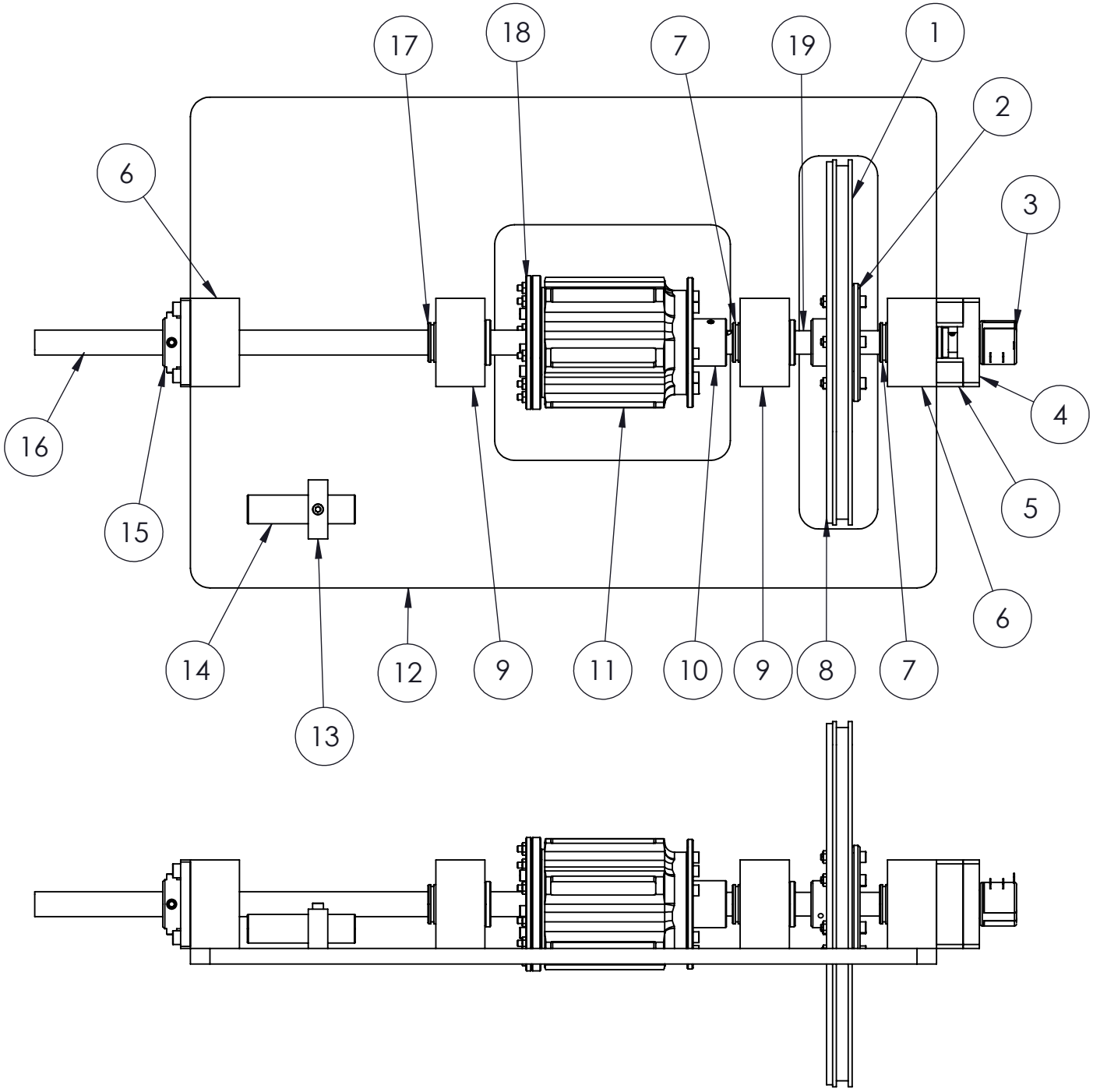

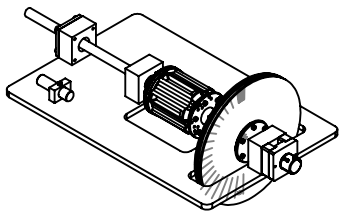

	PART NAME	QTY
1	MCTR-TORQUEWHEEL	1
2	MCTR-TWHEELHUB	1
3	MCTR-POTENTIOMETER	1
4	MCTR-POTMUONT	1
5	MCTR-POTSPACER	1
6	MCTR-SHAFTMOUNT-1	2
7	MCTR-BRASSBUSHING-1	2
8	MCTR-ACRYLICPROTAC	1
9	MCTR-SHAFTMOUNT-2	2
10	MCTR-OUTERROTORFLANGE	1
11	MANIPYULATOR COUPLING ASSEMBLY	1
12	MCTR-BASEPLATE	1
13	MCTR-LASERMOUNT	1
14	MCTR-LASER	1
15	MCTR-CLAMP	1
16	MCTR-GAUGESHAFT	1
17	MCTR-BRASSBUSHING-2	1
18	MCTR-INNERROTORFLANGE	1
19	MCTR-TORQUESHAFT	1

A4 Landscape	**University of Cape Town** Department of Mechanical Engineering			
	Title: MAGNETIC COUPLING TEST RIG			
Assembly Drawing	Scale: 1:3	Date: 2015/09/05	Sheet 2	of 3
	Drawn By: T P HOPE		Drawing Number D-MCTR-2	

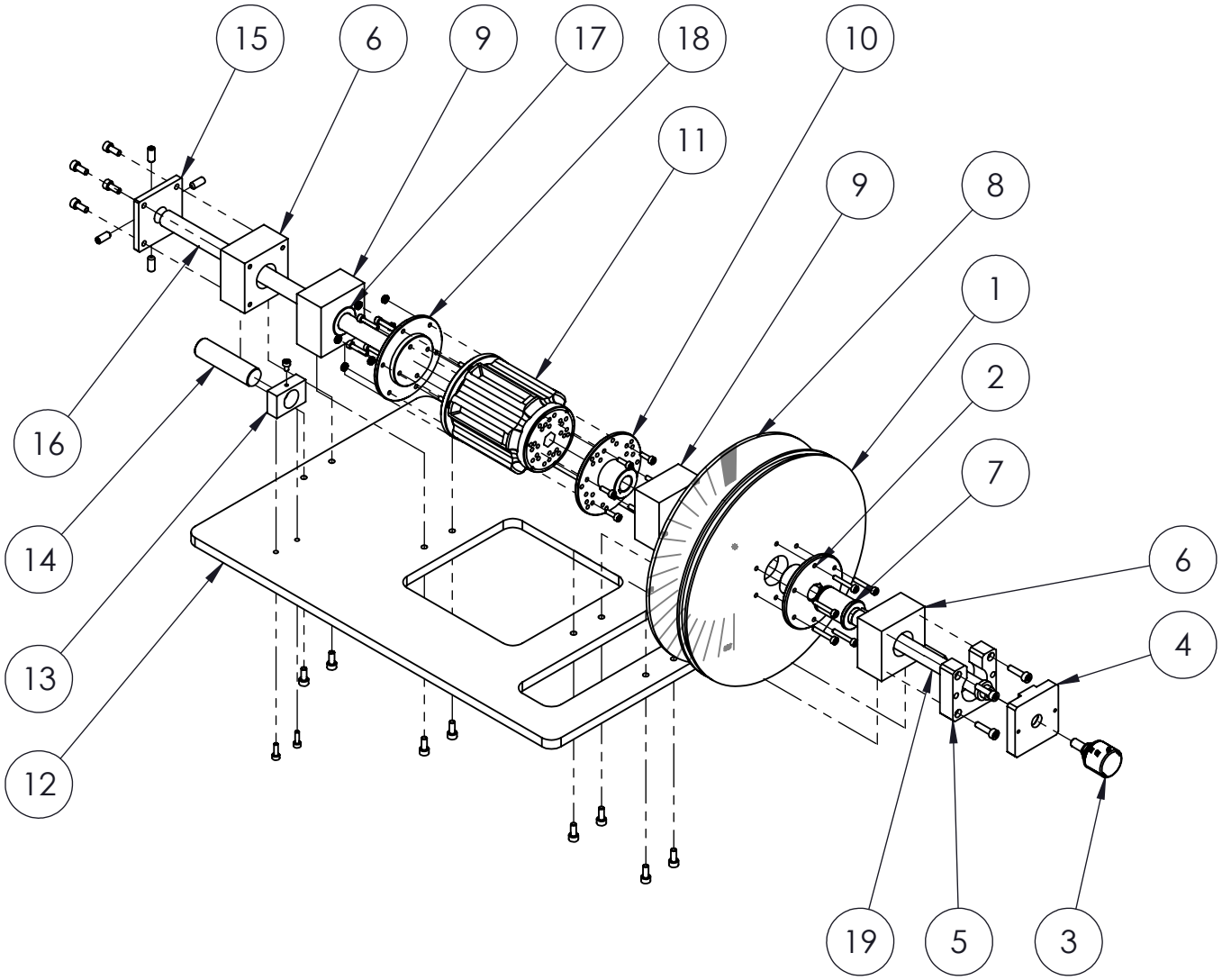

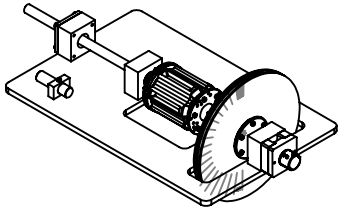

	PART NAME	QTY
1	MCTR-TORQUEWHEEL	1
2	MCTR-TWHEELHUB	1
3	MCTR-POTENTIOMETER	1
4	MCTR-POTMUONT	1
5	MCTR-POTSPACER	1
6	MCTR-SHAFTMOUNT-1	2
7	MCTR-BRASSBUSHING-1	2
8	MCTR-ACRYLICPROTAC	1
9	MCTR-SHAFTMOUNT-2	2
10	MCTR-OUTERROTORFLANGE	1
11	MANIPULATOR COUPLING ASSEMBLY	1
12	MCTR-BASEPLATE	1
13	MCTR-LASERMOUNT	1
14	MCTR-LASER	1
15	MCTR-CLAMP	1
16	MCTR-GAUGESHAFT	1
17	MCTR-BRASSBUSHING-2	1
18	MCTR-INNERROTORFLANGE	1
19	MCTR-TORQUESHAFT	1

A4 Landscape	University of Cape Town Department of Mechanical Engineering			
	Title: MAGNETIC COUPLING - EXPLODED VIEW			
Assembly Drawing	Scale: 1:5	Date: 2015/09/05	Sheet 3	of 3
	Drawn By: T P HOPE		Drawing Number D-MCTR-3	

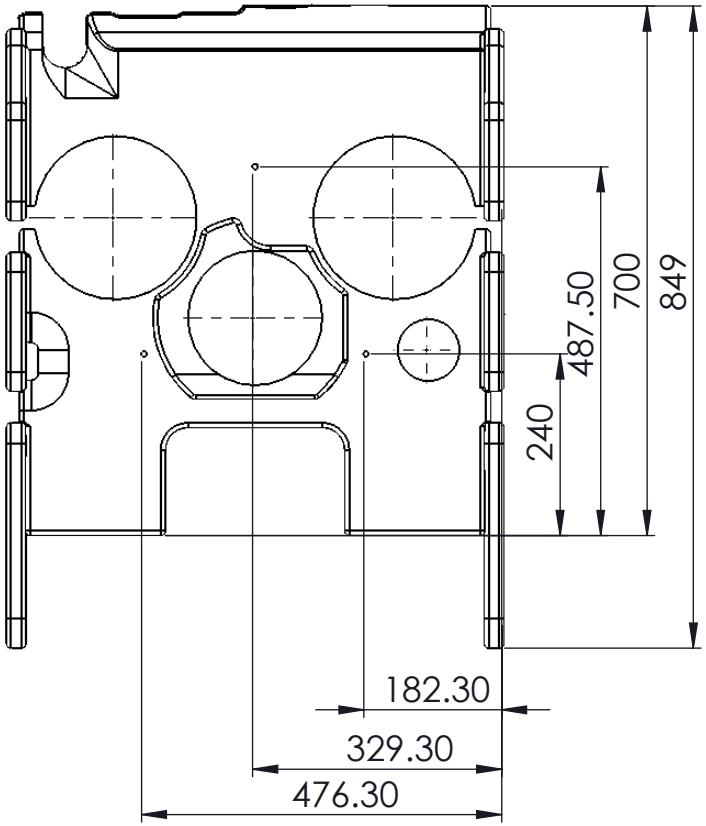

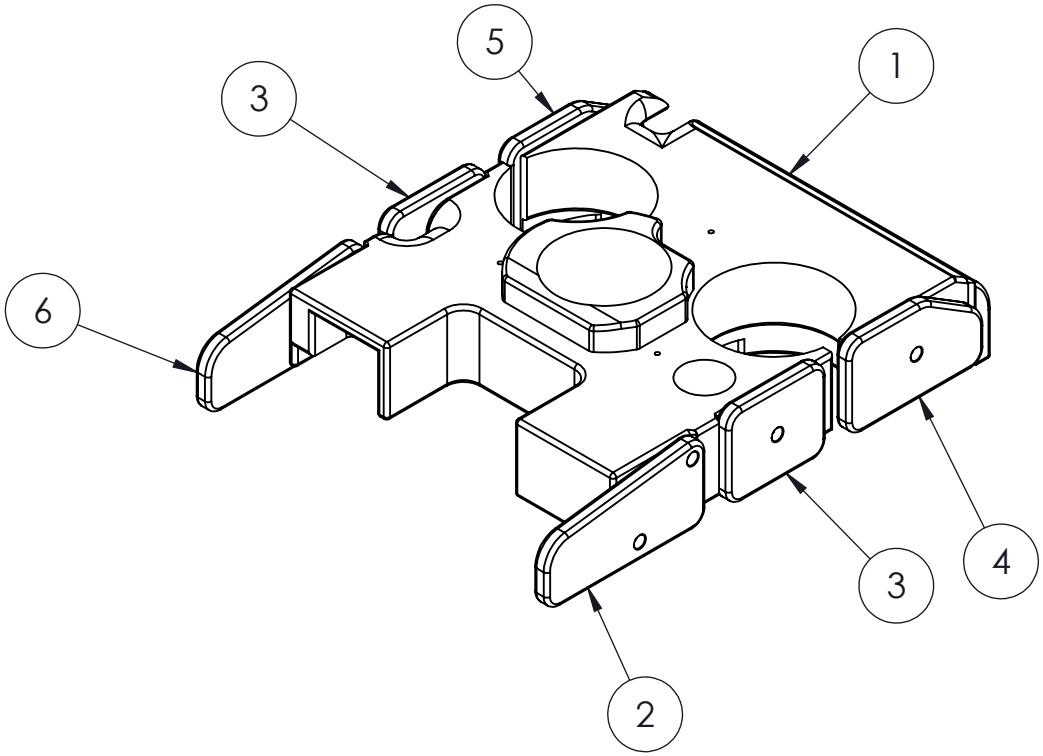

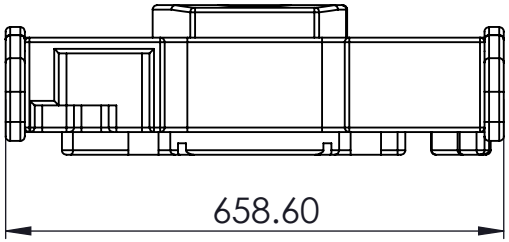

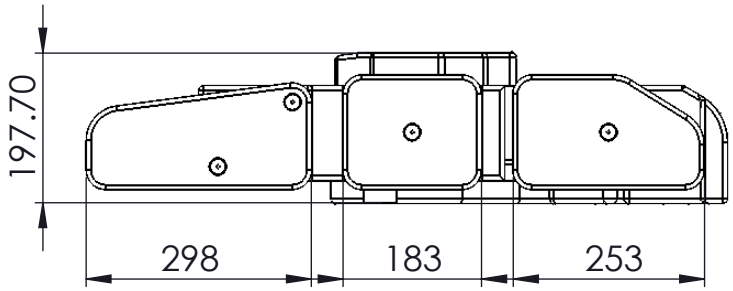

	PART NAME	QTY
1	FLTB-MAIN BLOCK	1
2	FLTB-PORTFORWARD	1
3	FLTB-PORTANDSTARBD	1
4	FLTB-PORTAFT	2
5	FLT-STARBDAFT	1
6	FLTB-STARBDFRONT	1

A4 Landscape	**University of Cape Town** Department of Mechanical Engineering			
	Title: BUOYANCY SYSTEM - GENERAL DIMENSIONS			
Assembly Drawing	Scale: 1:10	Date: 2015/09/05	Sheet 1	of 2
	Drawn By: T P HOPE		Drawing Number D-FLTB-1	

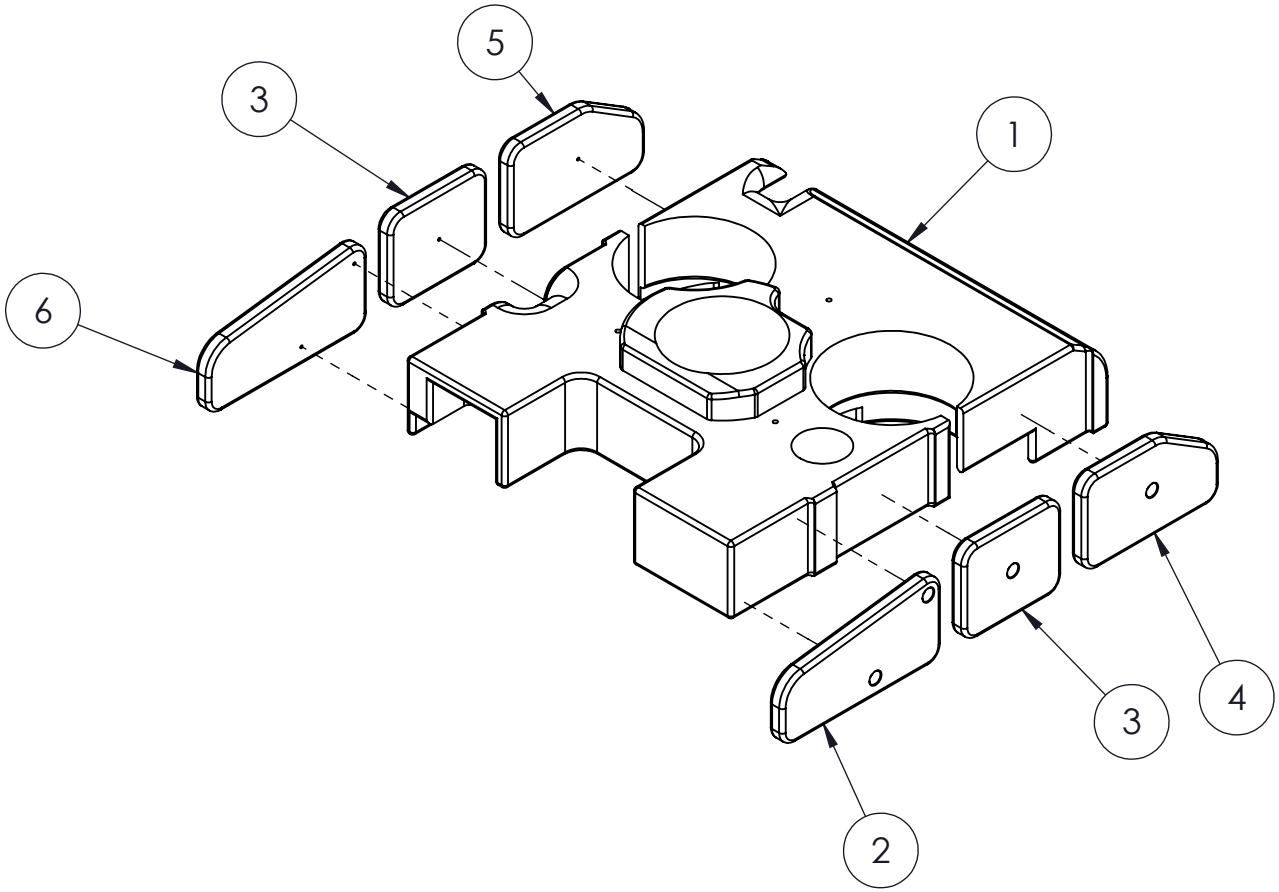

	PART NAME	QTY
1	FLTB-MAIN BLOCK	1
2	FLTB-PORTFORWARD	1
3	FLTB-PORTANDSTARBD	1
4	FLTB-PORTAFT	2
5	FLT-STARBDAFT	1
6	FLTB-STARBDFRONT	1

A4 Landscape	**University of Cape Town** **Department of Mechanical Engineering**			
	Title: BUOYANCY SYSTEM - EXPLODED			
Assembly Drawing	**Scale:** 1:10	**Date:** **2015/09/05**	Sheet 2	**of** 2
	Drawn By: T P HOPE		**Drawing Number** D-FLTB-2	

Appendix E

Electrical Schematics

Contents

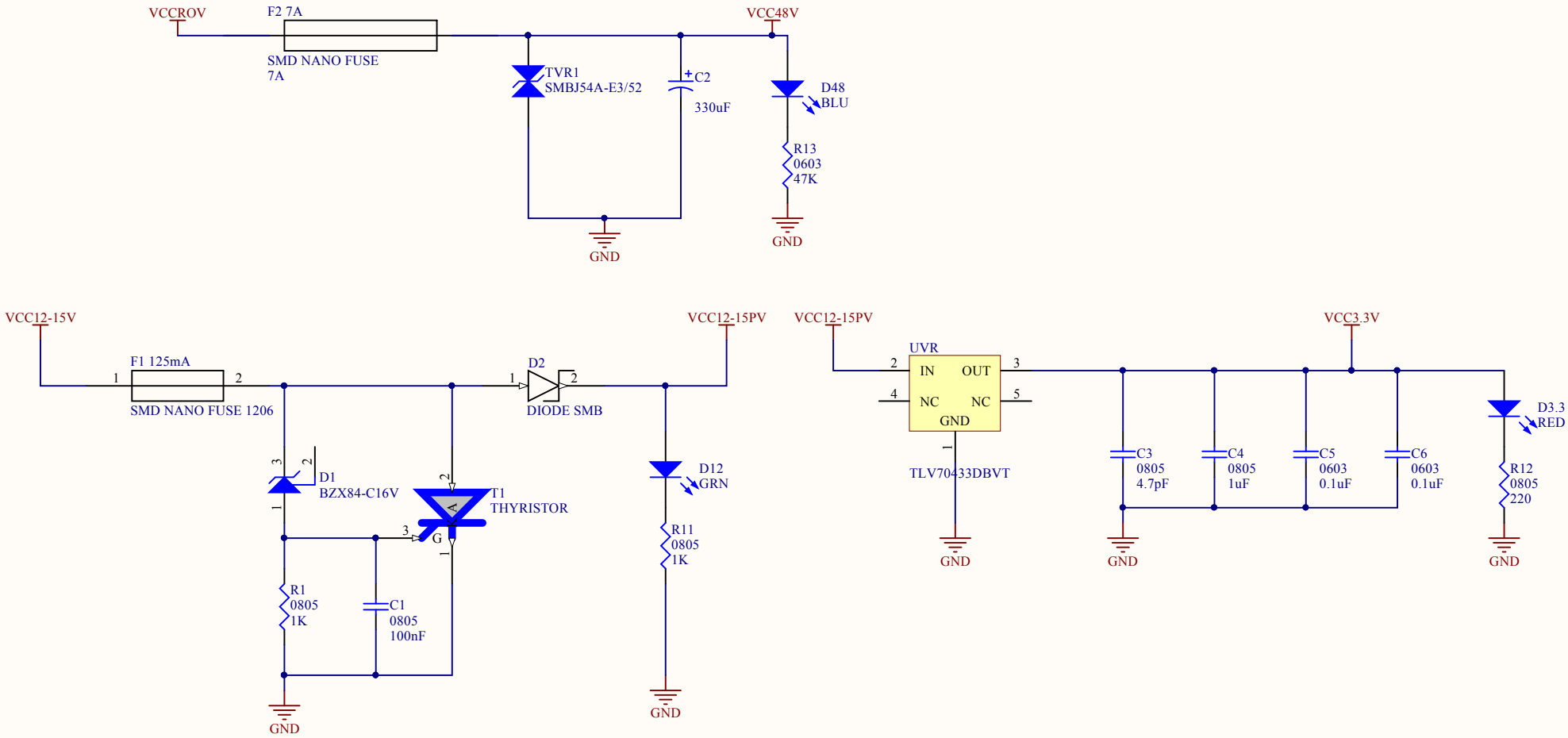

Title	Communications and Control PCB - Power Conditioning and Regulation	
Size: A4	Number: E-CCPCB-PRW	Revision: v2.6
Date: 2015/09/05	Sheet of 1:3	
	Drawn By: T P HOPE	

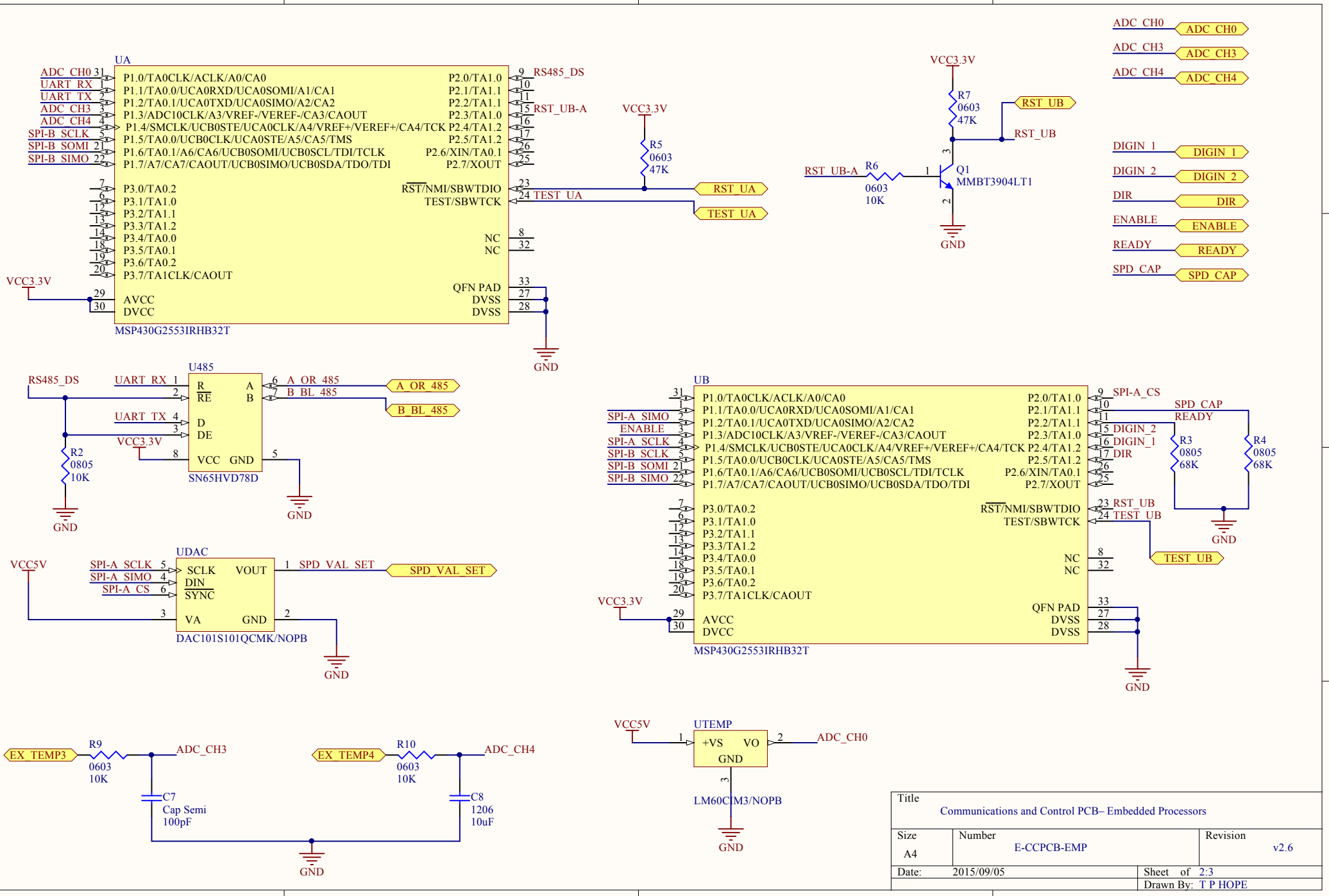
UA
ADC_CH0 31
UART_RX 1
UART_TX 2
ADC_CH3 3
ADC_CH4 4
SPI-B_SCLK 5
SPI-B_SOMI 21
SPI-B_SIMO 22
P1.0/TA0CLK/ACLK/A0/CA0
P1.1/TA0.0/UCA0RXD/UCA0SOMI/A1/CA1
P1.2/TA0.1/UCA0TXD/UCA0SIMO/A2/CA2
P1.3/ADC10CLK/A3/VREF-/VEREF-/CA3/CAOUT
P1.4/SMCLK/UCB0STE/UCA0CLK/A4/VREF+/VEREF+/CA4/TCK
P1.5/TA0.0/UCB0CLK/UCA0STE/A5/CA5/TMS
P1.6/TA0.1/A6/CA6/UCB0SOMI/UCB0SCL/TDI/TCLK
P1.7/A7/CA7/CAOUT/UCB0SIMO/UCB0SDA/TDO/TDI
P2.0/TA1.0
P2.1/TA1.1
P2.2/TA1.1
P2.3/TA1.0
P2.4/TA1.2
P2.5/TA1.2
P2.6/XIN/TA0.1
P2.7/XOUT
P3.0/TA0.2
P3.1/TA1.0
P3.2/TA1.1
P3.3/TA1.2
P3.4/TA0.0
P3.5/TA0.1
P3.6/TA0.2
P3.7/TA1CLK/CAOUT
AVCC
DVCC
RST/NMI/SBWTDIO
TEST/SBWTCK
NC
NC
QFN PAD
DVSS
DVSS
RS485_DS
RST_UB-A
RST_UA
TEST_UA
MSP430G2553IRHB32T
VCC3.3V
GND
R5
0603
47K
R7
0603
47K
RST_UB
R6
0603
10K
Q1
MMBT3904LT1
ADC_CH0
ADC_CH3
ADC_CH4
DIGIN_1
DIGIN_2
DIR
ENABLE
READY
SPD_CAP
U485
RS485_DS
UART_RX 1
UART_TX 4
R
RE
D
DE
A
B
VCC
GND
A_OR_485
B_BL_485
SN65HVD78D
R2
0805
10K
UDAC
VCC5V
SPI-A_SCLK 5
SPI-A_SIMO 4
SPI-A_CS 6
SCLK
DIN
SYNC
VOUT
VA
SPD_VAL_SET
DAC101S101QCMK/NOPB
UB
SPI-A_SIMO 2
ENABLE 3
SPI-A_SCLK 4
SPI-B_SCLK 5
SPI-B_SOMI 21
SPI-B_SIMO 22
SPI-A_CS
RST_UB
TEST_UB
DIGIN_2
DIGIN_1
DIR
R3
0805
68K
R4
0805
68K
MSP430G2553IRHB32T
EX_TEMP3
EX_TEMP4
R9
R10
C7
Cap Semi
100pF
C8
1206
10uF
UTEMP
+VS
VO
GND
LM60CIM3/NOPB
Title
Communications and Control PCB– Embedded Processors
Size
A4
Number
E-CCPCB-EMP
Revision
v2.6
Date:
2015/09/05
Sheet of 2:3
Drawn By: T P HOPE

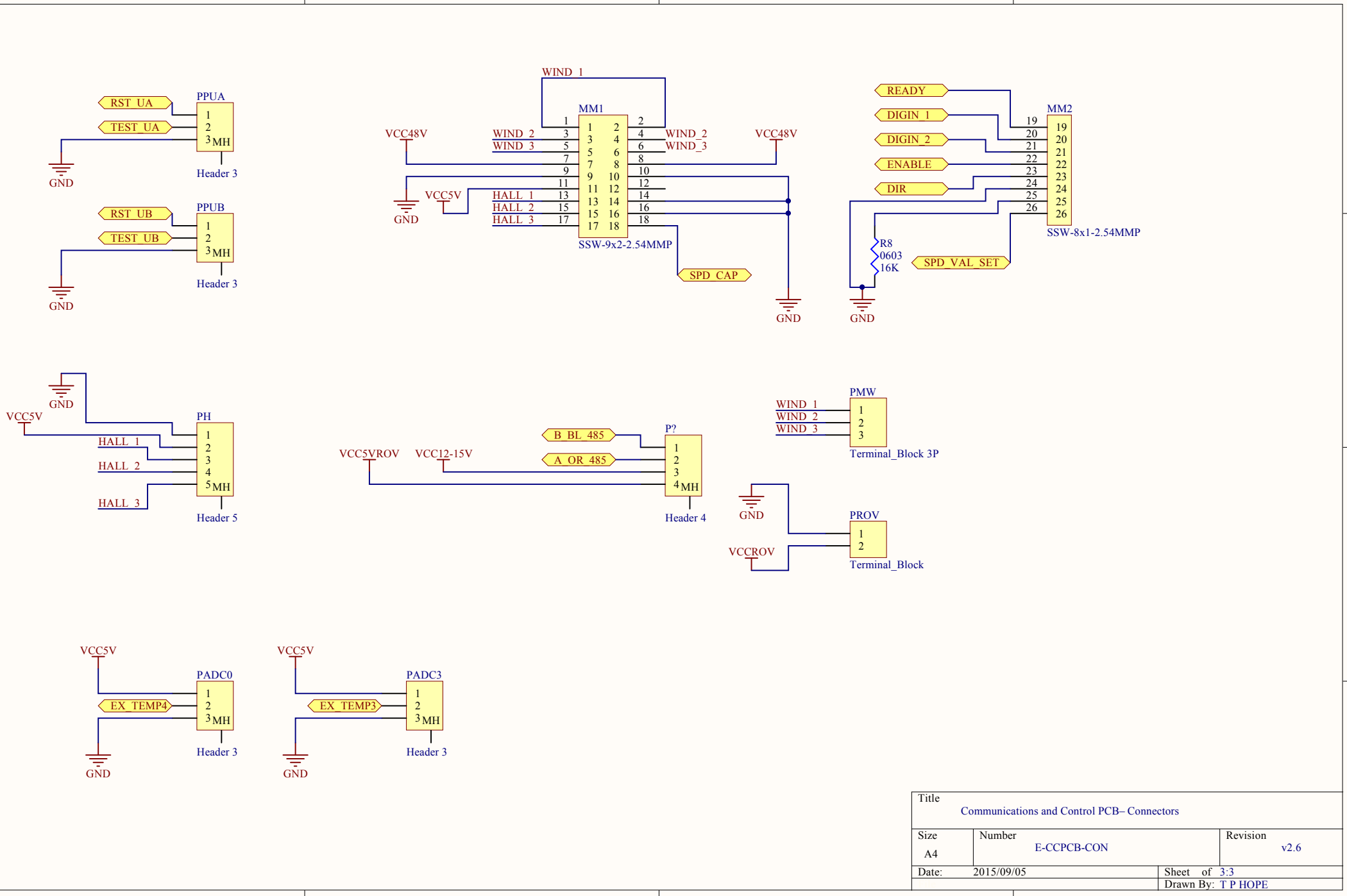

Title: Communications and Control PCB– Connectors		
Size: A4	Number: E-CCPCB-CON	Revision: v2.6
Date: 2015/09/05	Sheet of 3:3	
	Drawn By: T P HOPE	

Appendix F

Buoyancy System

F.1 Buoyancy System

F.1.1 Introduction

This section discusses the relationship between buoyancy and stability with regards to ROVs. The properties of the buoyancy system are detailed and different types of buoyancy systems are explained.

F.1.2 Buoyancy and Vehicle Stability

Archimedes principle states that the buoyant force that is exerted on a body immersed in a fluid, whether fully or partially submerged is equal to the weight of the fluid that the body displaces. This principle is a law of physics which is fundamental to fluid mechanics [1]. The collective parts of an ROV (excluding the buoyancy system) are negatively buoyant therefore without a buoyancy system an ROV would sink. Buoyancy systems on ROVs allow the vehicle to control its depth.

Any vehicle, such as an ROV, can move in six degrees of freedom, those being three translations: surge, heave and sway and three rotations; roll, yaw and pitch (these are shown in Figure F1). The ROV designed at RARL was designed similar to most commercial ROVs with the ability to control movement in only four degrees of freedom (surge, heave, sway and yaw). This meant that the ROV cannot control its pitch or roll [2]. The camera was designed with the ability to tilt therefore allowing the operator to view in front of, above and below the ROV however the ROV itself does not change its pitch. Because the ROV cannot control its pitch and roll it had to be designed to be stable with regards to these degrees of freedom.

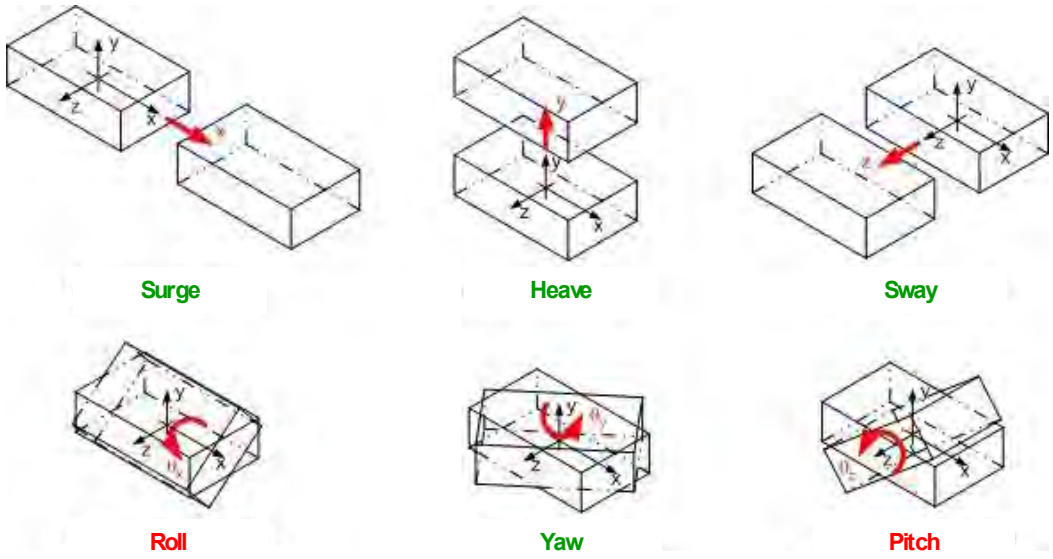

Figure F1 - Six Degrees of Freedom

For a totally submerged vessel in a fluid (as an ROV) the weight acts through the centre of gravity while the buoyancy acts through the centre of buoyancy which is the centroid of the vessel (the centre of volume). Regardless of the orientation of the vessel these two points will remain in the same positions relative to the vessel (this is only true for totally submerged vessels) [1]. The vehicle is considered to be in hydrostatic equilibrium when the centre of buoyancy and centre of gravity are aligned with the centre of buoyancy being above the centre of gravity. When they are

not aligned a righting moment is created that is proportional the separation distance between the centre of buoyancy and centre of gravity. Therefore the greater this separation the greater the righting moment and the quicker the vehicle rights itself after being disturbed [2]. This is shown in Figure F2.

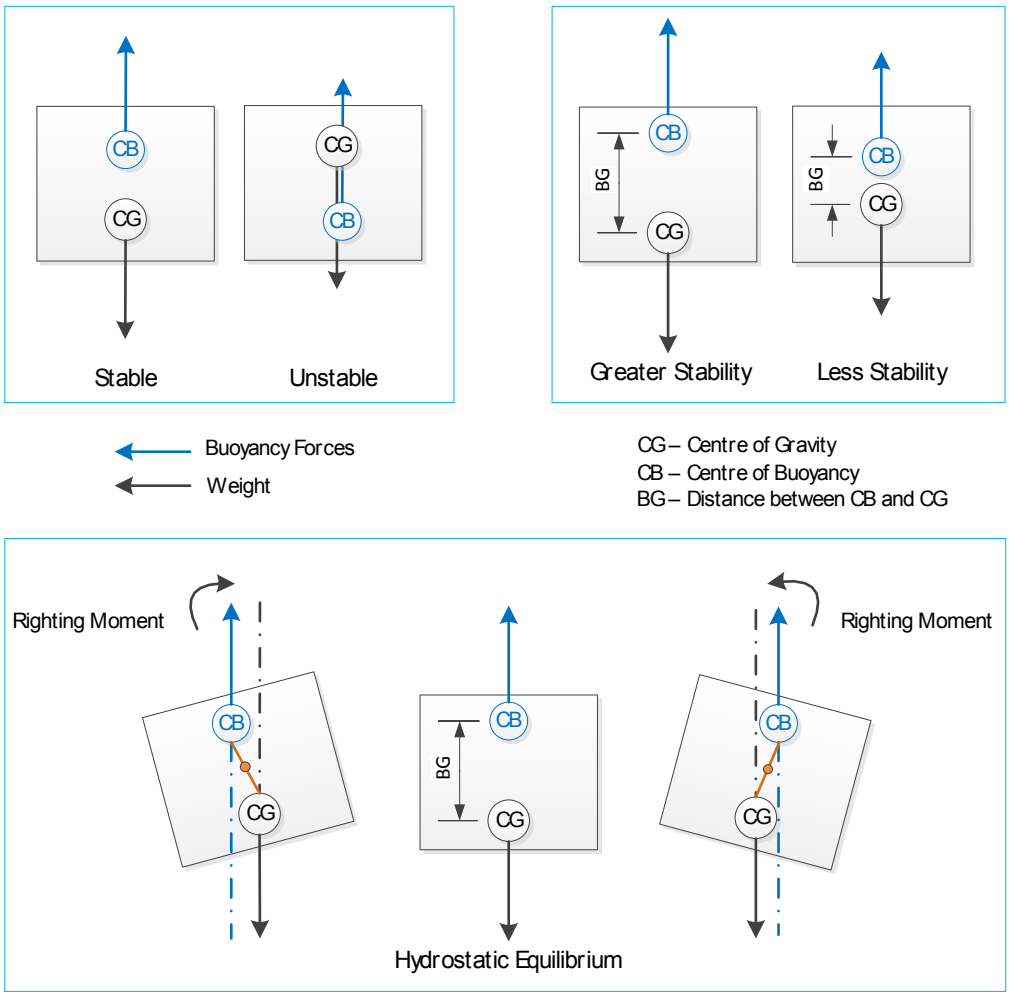

Figure F2 - Buoyancy, Weight and ROV Stability

For observation class ROVs lead or stainless steel ballasts are often placed on the bottom of the ROV frame to trim the pitch and the roll of ROV. By placing the ballasts on the bottom and to the extremities of the ROV frame the stability of the vehicle is increased as this brings the centre of gravity lower relative to the centre of buoyancy [2].

F.1.3 Buoyancy Systems

Two broad categories of buoyancy systems are dynamic buoyancy ballasts and passive float blocks. Dynamic buoyancy ballasts change the overall buoyancy of the ROV by compressing/decompressing air and allowing water to flow in and out of the ballast therefore changing the net buoyancy of the vessel. Float blocks add a fixed buoyancy to the ROV, this buoyancy cannot be changed and the vertical movement of the ROV is controlled by vertical thrusters [3]. The majority of observation class ROVs utilise float blocks exclusively. Float blocks eliminate the need for additional moving parts therefore providing a simpler solution than dynamic buoyancy modules. It is conventional operating procedure to have the ROV setup up to be positively buoyant therefore in the case of thruster failure or power failure the ROV will return to the surface [2]. A slightly positively buoyant ROV can hover over the ocean floor with the

vertical thruster propelling water through the top of the ROV as opposed to the bottom therefore reducing the amount of sediment stirred up, this is explained in Figure F3.

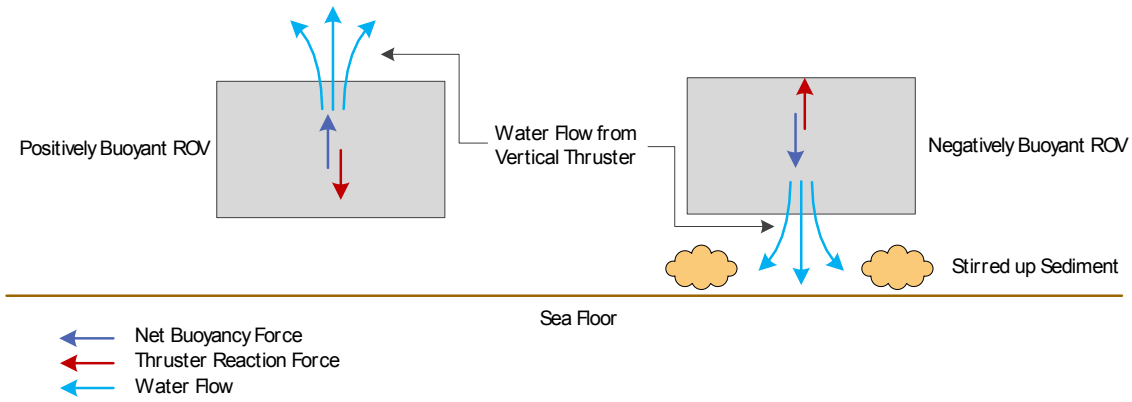

Figure F3 - Benefit of Positively Buoyant ROV in Proximity to the Sea Floor

F.1.4 Static Buoyancy Systems

Static buoyancy systems comprise of one or several float blocks attached to the ROV. The float block has to be less dense than water (in order to provide buoyancy) and it must be able to withstand the hydrostatic pressure experienced at the ROVs maximum operating depth. Several foams and composites are used to manufacture float blocks.

F.1.5 Float Block Materials

Polyurethane and Polyisocyanurate Foams

The rigid polyurethane foam group can be further divided into two sub groups: polyisocyanurate formula and polyurethane formula. Both of these polymer foams are extruded in large blocks and are cut into sheets. They are generally low density, insulation grade foams. ROV manufacturers cut and shape these sheets and either cover them in fibre glass or thick paint in order to prevent water intrusion and to protect the foam from cuts and abrasions. Covered float blocks have been tested to depths of 300 m in sea water and provide an inexpensive floatation system for shallow water applications [2].

Styrene-Acrylonitrile Foam

Styrene-**A**crylo**n**itrile copolymer (**SAN**) is manufactured from the copolymerisation of styrene and acrylonitrile [4]. SAN offers superior mechanical properties and chemical resistance to polystyrene resin [5]. This material is made into a foam with an impermeable closed cell structure that forms isolated micro air pockets. These pockets reduce the density of the material. SAN foams can be made to have lower densities than syntactic foams and have been developed to withstand depths of up to 900 m without crushing [6].

Syntactic Foams

Syntactic materials are composite materials that are synthesized by dispersing hollow particle fillers in a matrix material as can be seen in Figure F4. These materials can be classified as composite materials and foams. The hollow particles give the material a lower density and higher specific strength (the strength over the composite density). The matrix can be made from materials such as polymers, metals or ceramics. Microspheres can be constructed from polymers, glass or carbon. For maritime float block material the most common syntactic foams use vinyl or epoxy resins as a matrix and are filled with either glass or polymer microspheres [7]. High strength syntactic foams can be used to full ocean depths [8].

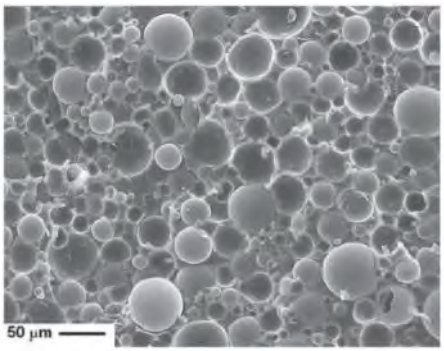

Figure F4 - Microstructure a Hollow Glass Filled Vinyl Ester Matrix Syntactic Foam [7]

F.1.6 Concluding Remarks

Due to the current design of the ROV and the mechanical simplicity of static buoyancy systems it was decided to design a float block for the ROV. By knowing the effects of the centre of buoyancy and the centre of gravity on the stability of the ROV, the design needed to maximise the vehicle's stability and align the centre of buoyancy with the centre of gravity in the vertical direction in order to keep the ROV pitched correctly during operation. The float block needed to provide enough buoyancy to make the ROV positively buoyant.

Three types of foams were available, polyurethane based foam, SAN foams and syntactic foams each one suitable to be used at different depths. The polyurethane foams could only be used to 300 m if it is enclosed in a fibre glass casing therefore adding strength to the float block. This would require pressure testing, add weight and be a limiting design factor. The SAN foams are suitable to be used at the depths the ROV is designed to operate in and have lower densities than syntactic foams therefore reducing the amount of foam required to provide the equivalent buoyancy.

F.2 Float Block Design

F.2.1 Material Selection

The float block material selected was Gurit's CoreCell S1200 SAN foam. This foam was specifically designed for subsea applications and has a higher strength, higher ductility and a finer cell size than polyurethane foams. While not as strong as syntactic foams CoreCell S foam does have a more consistent and lower density [6]. The mechanical properties of CoreCell S1200 are detailed in Table F1.

Table F1 - Gurit's CoreCell S1200 Mechanical Properties [6]

Property	Value	
Nominal Sheet Size	890 x 1830	mm
Nominal Sheet Thickness	25	mm
Nominal Density	210	kg/m3
Hydrostatic Crush Pressure*	>45	bar
Compressive Strength	4.71	MPa
Compressive Modulus	293	MPa

*Hydrostatic Crush Pressure is defined as the point in pressure in bar where the material when subjected to increasing pressure of 1-2 bar/sec has lost 5% of its initial volume

The hydrostatic crush pressure of the CoreCell S1200 foam is above 45 bar. This is equivalent to a depth of 446 m in sea water and was deemed adequate for the ROV which is rated to an operational depth of 300 m.

F.2.2 Design Method

Figure F5 shows the ROV without a float block. A float block had to be incorporated into the top section shown in Figure F5.

Figure F5 - ROV without Float Block

The first step in the design was to ensure the CAD models of the ROV and all the modules were truly representative of the actual modules in terms of weight and weight distribution. All the modules were individually weighed and where discrepancies occurred between the weighed values and the weight calculated by SolidWorks the properties of the respective module were examined and adjusted to match the weighed results. A complete and accurate model of the ROV was developed. This model was referred to as 'the real model'. The tilt module design had not been completed or built when this was done. An approximate design was made and placed onto the ROV in the appropriate position.

The float block was designed onto the real model and the density of the foam was set into the float block's material parameters. This model provided the total weight and the co-ordinates for the centre of gravity of the ROV.

A second CAD model of the ROV was developed to obtain the buoyancy force and the centre of buoyancy. According to Archimedes' principle the buoyant force of a vessel submerged in a fluid is equal to the weight of the water displaced by the vessel and it is located at the centroid of the vessel. Therefore a CAD model of the water displaced by the ROV was required. All the modules of the ROV were emptied of internal components and filled using a cavity fill function in SolidWorks. The densities of all the parts in these filled modules were changed to the density of sea water. The float block was included in this model and its density was also changed to that of sea water. This model was termed 'the water model'. This model's mass multiplied by gravity provided the magnitude of the buoyant force of the ROV and this buoyant force acted through the water model's centre of gravity (the density for the model was uniform therefore the centre of gravity equalled the centre of volume, i.e. the centroid).

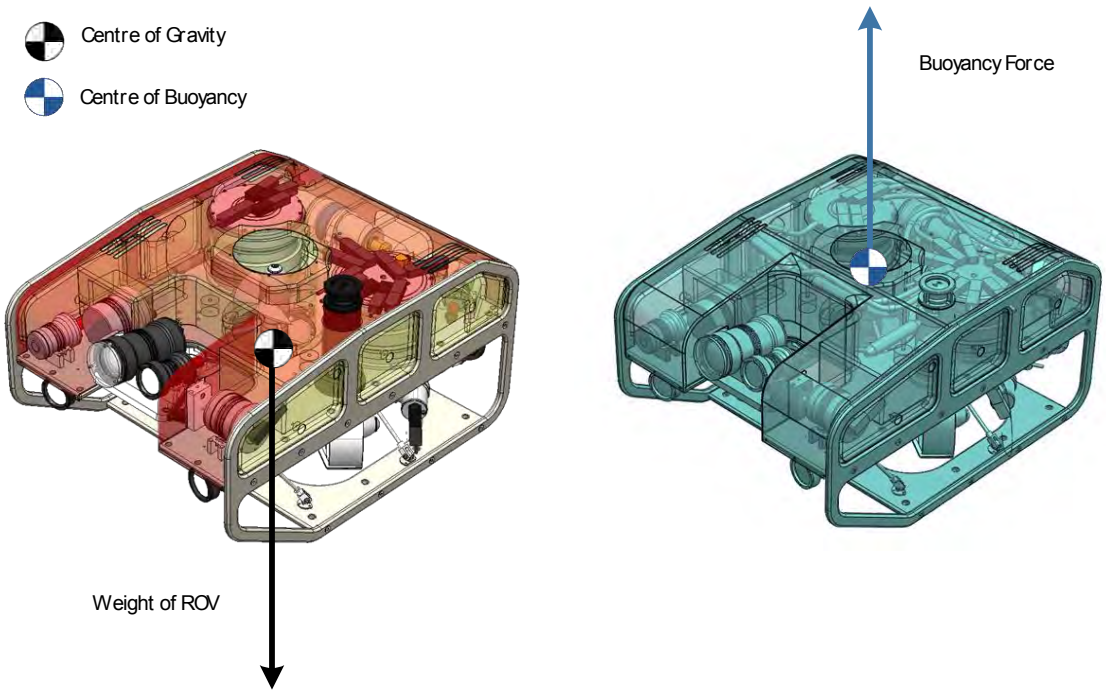

Figure F6 - Real Model vs Water Model

The aim of the float block design was to vertically align the centre of gravity of the real model with the centre of buoyancy of the water model. As stated in Section **Error! Reference source not found.** these two have to be vertically aligned (with the centre of buoyancy above the centre of gravity) for the ROV to be in hydrostatic equilibrium. An objective of the design of the float block was to maximise the separation between the centre of gravity and the centre of buoyancy to maximise the stability of the ROV.

The design process was iterative and the float block had to allow space for the modules, the modules' mounting blocks and the cables. It was intended that a single float block be designed that fitted around the modules therefore reducing the number of parts and the number of mounting points however this was not possible as there was too little buoyancy towards the rear of the ROV. The volume in the cavities in the ROV's side panels was used to provide the extra buoyancy at the rear of the ROV.

F.2.3 Final Design

The final design of the float block is shown in the exploded view of the ROV in Figure F7. Figure F8 shows the positioning of the centre of gravity and the centre of buoyancy of the ROV. Extra buoyancy was allowed to make the ROV positively buoyant and to allow the operator to trim the buoyancy using lead or stainless steel ballasts attached to the bottom of the ROV frame.

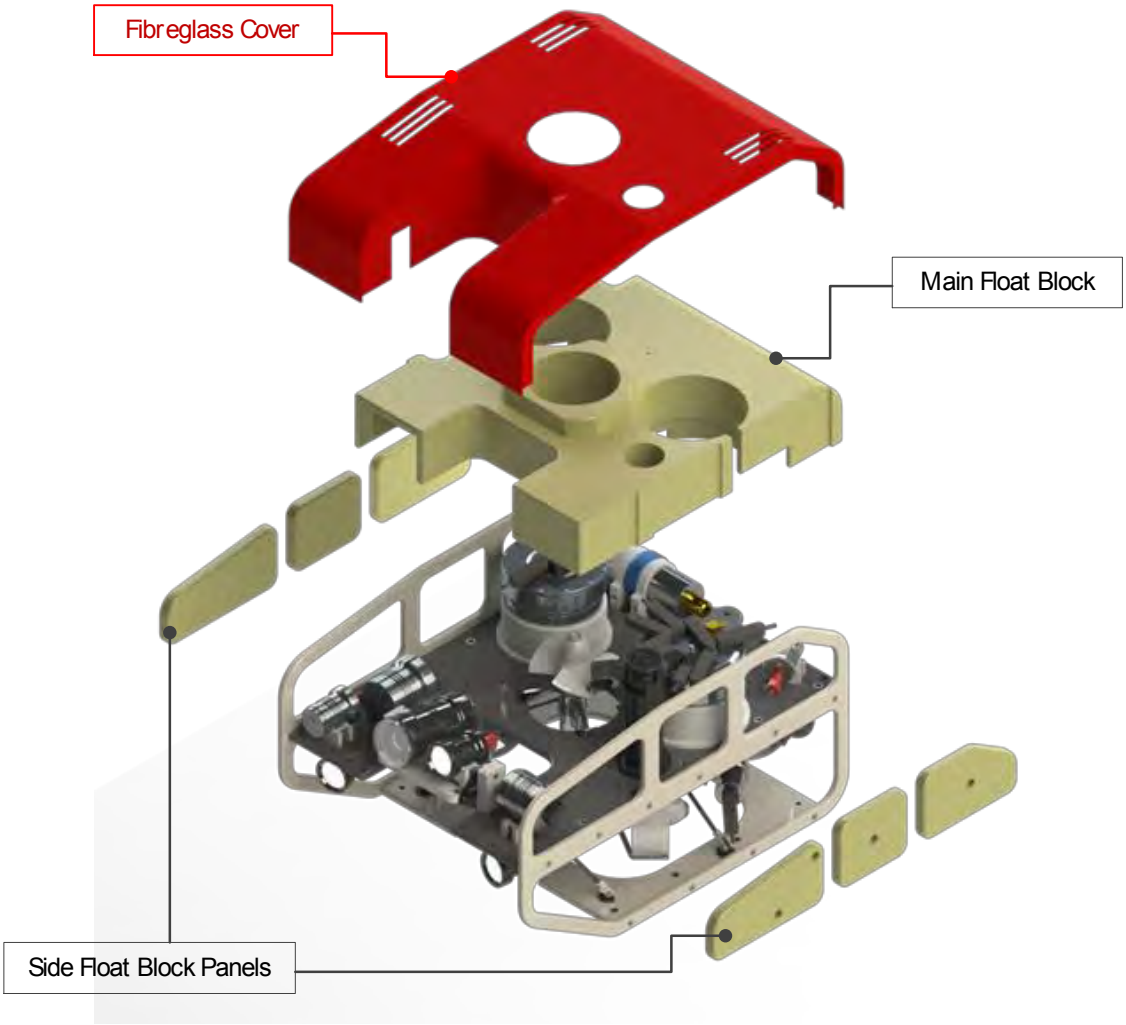

Figure F7 - Exploded View of the ROV's Cover and Float Block

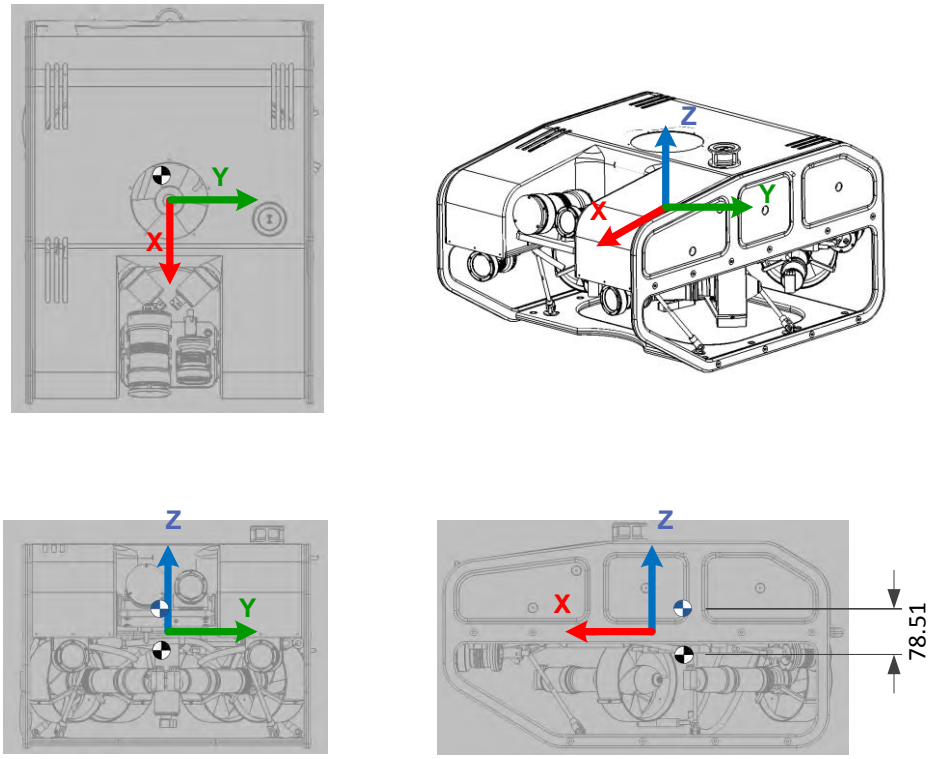

Figure F8 - The Locations of the Centre of Gravity and the Centre of Buoyancy

The float block is mounted using three stainless steel 316 rods that clamp the block to the base plate of the ROV. Table F2 shows the detailed coordinates of the centre of gravity and the centre of buoyancy. The net positive buoyancy was designed to be 2.5 kg as this allowed extra buoyancy for weight to be added in the form of ballasts on the ROV frame when the ROV's pitch and roll are trimmed. The lengthy manufacturing process detailed in the next section meant that the float block was not completed in time for this dissertation and therefore the ROV's buoyancy was not trimmed.

Table F2 - Buoyancy Details of ROV

Coordinates	CG	CB	Units
X	-43.12	-42.38	mm
Y	-5.93	-6.62	mm
Z	60.94	-17.57	mm
Vertical Separation between Centre of Gravity and Centre of Buoyancy	78.51		mm
Total mass of ROV	79.5		kg
Total Buoyancy of ROV	82		kg
Net Positive Buoyancy	2.5		kg

F.3 Float Block Manufacturing Method

F.3.1 Epoxy Selection and Lamination Recommendations

The float block material comes in 25 mm thick laminates that have to be epoxied together. The suppliers of the foam, AMT Composites, and Marine Solutions (an ROV operations company based in Cape Town) were consulted on the best method of bonding the laminates together. It was recommended that Ampreg 21 epoxy be used as it has a low viscosity and adjustable gel times that make it suitable for the wet laminating of the sheets. To ensure a good bond between the laminates and to remove any air that can get trapped during lamination it was recommended to not laminate more than four sheets at a time. Marine Solutions advised that the accurate alignment of the sheets during lamination was difficult and to achieve accuracies below several millimetres was impossible.

F.3.2 Multiple Manufacturing Stages

The six side panels of the float block were **c**omputer **n**umerical **c**ontrol (**CNC**) milled and required no laminating. However the main central float block required multiple stages of machining and laminating. The CAD model of the float block was split into eight layers of laminates and each laminate was increased in size as seen in Figure F9. The overall plan to manufacture the float block was to laminate these sheets together and CNC mill the excess material therefore producing an accurately machined float block. However eight layers could not be laminated in one session and the thickness of the float block meant that it was not possible to CNC mill the final shape as the mill bit was not long enough. If the sheets were CNC milled into their final shape before laminating poor alignment during lamination would cause the final float block to be distorted with steps between the laminates.

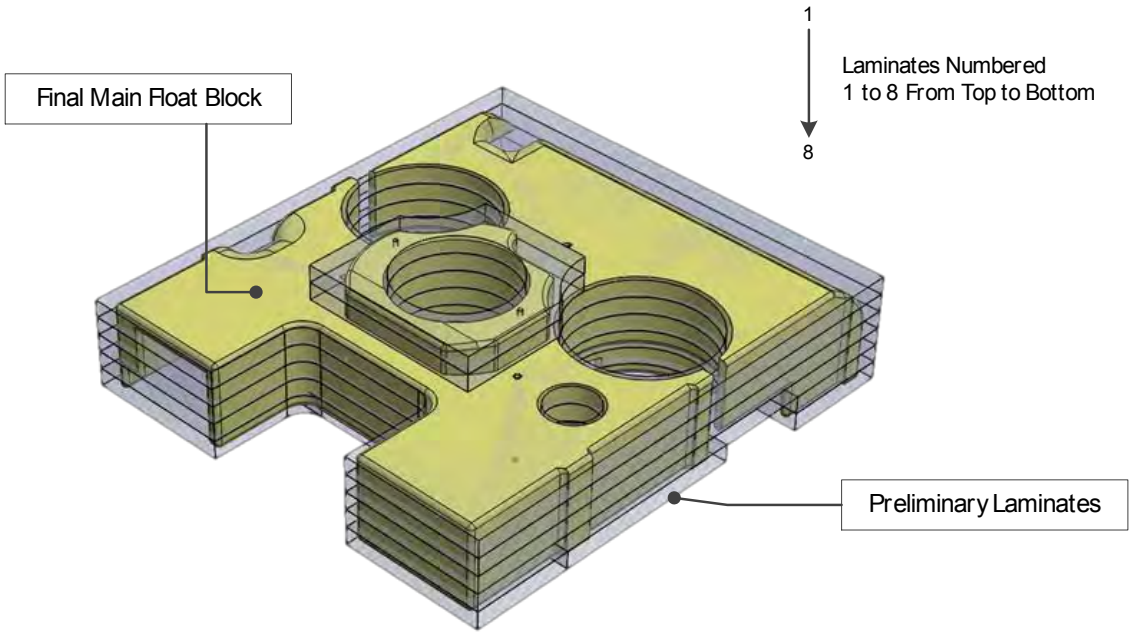

Figure F9 - Float Block Design Split into Preliminary Laminates

Taking into consideration the three limiting factors of CNC mill depth, the number of laminates bonded at a time and the alignment of laminates a multiple stage process was created.

Stage 1 – CNC Milling of Laminates

The separate laminates shown in Figure F9 were cut from the 890 mm x 1830 mm sheets and individually CNC milled.

Stage 2 – Bonding and CNC Milling of Laminates 3 to 5

Laminates 3 to 5 were epoxied and clamped into position. The clamp was comprised of two, laser cut, 6 mm thick, steel plates. Figure F10 shows the alignment method used. Three acrylic tubes were used to locate the sheets relative to each other. This tube also severed as the liner for the three stainless steel mounting rods that fasten the float block to the ROV's base plate. This bonded section was then milled into the final shape.

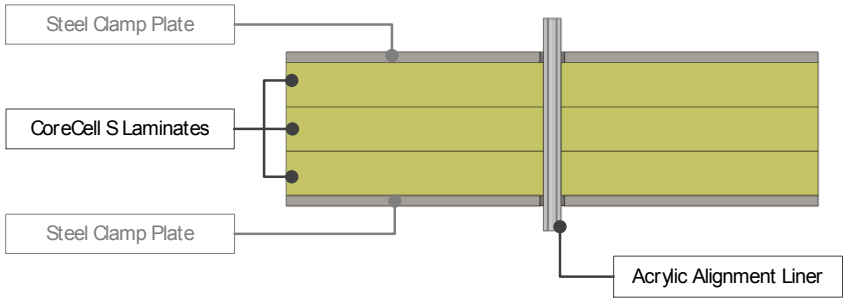

Figure F10 - Clamping of CoreCell S Laminates Showing Acrylic Liner

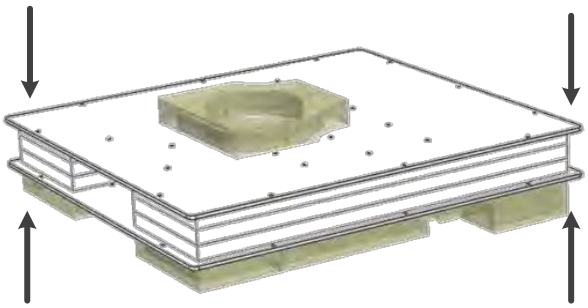

Figure F11 - Bonding of Laminates 3 to 5

Stage 3 – Bonding and CNC Milling of Laminates 6 to 8

Laminates 6 to 8 were bonded together layer by layer therefore two bonding sessions were done as the laminates in these sheets do not cover the entire clamped area. Once these three laminates were bonded they were bonded to the piece that was CNC milled in the previous step (laminates 3 to 5). The acrylic alignment liners were used as they were in the previous stage. Now that laminates 3 to 8 were a single part, the bottom of the float block (laminates 6 to 8) were CNC milled in the final shape. Figure F12 shows the laminates bonded in this section.

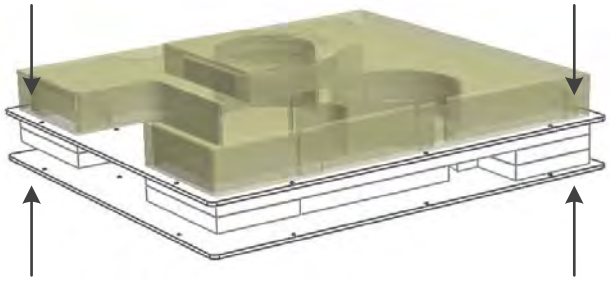

Figure F12 - Bonding of Laminates 6 to 8

Stage 4 – Bonding and CNC Milling of Laminates 1 and 2

The two top and smallest laminates were bonded together and aligned using solid acrylic dowels. They were CNC milled into their final shape before being bonded onto the top of the float block as shown in Figure F13.

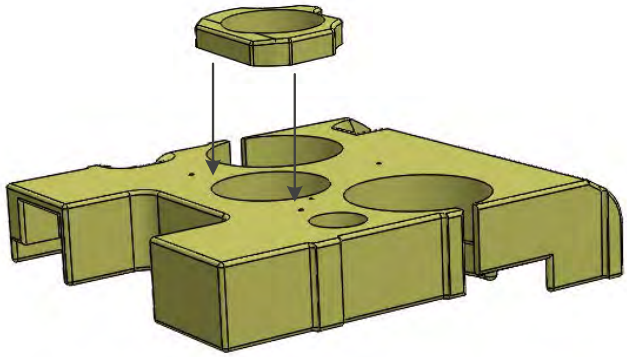

Figure F13 - Top of Float Block Bonded to Main Portion

Due to workshops delays only stage 2 of this manufacturing process had been completed when writing this dissertation.

F.3.3 References

[1] J. F. Douglas, J. M. Gasiorek, J. A. Swaffield, and L. B. Jack, *Fluid Mechanics*, 5th Editio. Essex: Pearson Education limited, 2005.

[2] R. D. Christ and R. L. S. Wernli, *The ROV Manual*, 1st Editio. Butterworth-Heinemann, 2007.

[3] Cornerstone Robotics, "Buoyancy, Stability and Ballast," *Webpage*, 2014. [Online]. Available: http://cornerstonerobotics.org/curriculum/lessons_year3/eriii10_buoyancy2.pdf. [Accessed: 02-Feb-2014].

[4] T. E. of E. Brittanica, "Styrene-acrylonitrile copolymer (SAN)," *Encyclopedia Brittanica*. Encyclopedia Brittanica, 2014.

[5] Patterson-Rothwell, "Material Information," *Webpage*, 2014. [Online]. Available: http://www.patterson-rothwell.co.uk/images/services/materialinformation.pdf. [Accessed: 03-Feb-2014].

[6] Gurit Inc, “Gurit Corecell S Data Sheet,” 2014. [Online]. Available: http://www.gurit.com/files/documents/guritcorecell-sv11pdf.pdf. [Accessed: 03-Mar-2014].

[7] N. Gupta, S. E. Zeltmann, V. C. Shunmugasamy, and D. Pinisetty, “Applications of Polymer Matrix Syntactic Foams,” *Jom*, vol. 66, no. 2, pp. 245–254, 2014.

[8] DIAB, “Syntactic Foams,” *Webpage*, 2014. [Online]. Available: http://www.diabgroup.com/en-GB/Products-and-services/Core-Material/Syntactic-Foams. [Accessed: 03-Feb-2014].